

**STUDY OF LADDER SYSTEM IN RUBIDIUM AND
DEVELOPMENT OF A COLLINEAR LASER SPECTROSCOPY
SETUP AT THE ISOL FACILITY AT VECC**

By

MD SABIR ALI

PHYS04201204001

Variable Energy Cyclotron Centre, Kolkata

A thesis submitted to the

Board of Studies in Physical Sciences

In partial fulfilment of requirements

for the Degree of

DOCTOR OF PHILOSOPHY

of

HOMI BHABHA NATIONAL INSTITUTE

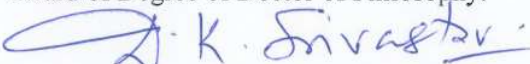


April, 2017

Homi Bhabha National Institute

Recommendations of the Viva Voce Committee

As members of the Viva Voce Committee, we certify that we have read the dissertation prepared by Md. Sabir Ali entitled "Study of ladder system in Rubidium and development of a collinear laser spectroscopy setup at the ISOL facility at VECC" and recommend that it may be accepted as fulfilling the thesis requirement for the award of Degree of Doctor of Philosophy.

 D. K. Srivastava

18/4/2018

Chairman – Dr. D. K. Srivastava

Date:

 Alok Chakrabarti

18/4/2018

Guide / Convener - Dr. Alok Chakrabarti

Date:

 Dr. B. P. Singh

APRIL 18, 2018

Examiner - Dr. B. P. Singh

Date:

 Dr. V. S. Pandit

18/4/2018

Member 1- Dr. V. S. Pandit

Date:

Member 2- Dr. Satyajit Saha

Date:

 Dr. Satyajit Saha

18/4/2018

Final approval and acceptance of this thesis is contingent upon the candidate's submission of the final copies of the thesis to HBNI.

I hereby certify that I have read this thesis prepared under my direction and recommend that it may be accepted as fulfilling the thesis requirement.

Date: 18/04/2018

Place: VECC, Kolkata

 Alok Chakrabarti

Guide

STATEMENT BY AUTHOR

This dissertation has been submitted in partial fulfilment of requirements for an advanced degree at Homi Bhabha National Institute (HBNI) and is deposited in the Library to be made available to borrowers under rules of the HBNI.

Brief quotations from this dissertation are allowable without special permission, provided that accurate acknowledgement of source is made. Requests for permission for extended quotation from or reproduction of this manuscript in whole or in part may be granted by the Competent Authority of HBNI when in his or her judgment the proposed use of the material is in the interests of scholarship. In all other instances, however, permission must be obtained from the author.

Md. Sabir Ali

Md Sabir Ali

DECLARATION

I, hereby declare that the investigation presented in the thesis has been carried out by me.
The work is original and has not been submitted earlier as a whole or in part for a degree /
diploma at this or any other Institution / University.

Md. Sabir Ali

Md Sabir Ali

Acknowledgement

This thesis is the outcome of continuous help, advice and support of my supervisor Dr. Alok Chakrabarti. His constant motivation and guidance have helped me to steer in the forward direction and I express my deep and sincere gratitude to him for that. I also take pleasure to thank my doctoral committee members, Dr. D.K. Srivastava, Dr. V.S. Pandit and Dr. Satyajit Saha for their insightful comments and advice during the entire time.

I would also like to thank Dr. Arup Bandyopadhyay and Dr. Vaishali Naik for their constant encouragement in carrying out different experiments and valuable suggestions during the course of my thesis work.

I owe a large part of my laboratory work experience to Dr. Ayan Ray. His constant enthusiasm and practical skill has helped me to learn a lot about the subject matter. I also want to thank Dr. Siddhartha Dechoudhury, Manas Mondal and rest of the RIB group members for their unconditional support. I am very much grateful to VECC nuclear electronics section and VECC workshop for being there to help us whenever we needed.

I would like to thank all journal referees for their comments, criticism and advice. They contributed a lot to improve the qualities of the published papers.

I am also thankful to Waseem Raja, Subir Rakshit and Pravas Chandra Sadhukhan for their support, engagement and cheerfulness. You made the job look much easier for me.

In the end, I would like to thank my family members and well wishers, specially my parents, my brother, my wife and son for their never ending love, support and encouragement which helped me to complete this mammoth task. I also take this opportunity to thank all my teachers. Without their blessing it would not be possible to come this far.

..... Md Sabir Ali

Dedicated to the memory of my father

List of Publications arising from the thesis

A. Journal

1. *Optical Switching in a Ξ system: A comparative study on DROP and EIT*; Ayan Ray, **Md. Sabir Ali** and Alok Chakrabarti, Eur. Phys. J. D (2013) 67: 78
2. *Tunable Offset Locking in a Ξ system: An Experimental Study on Rubidium Atom*; **Md. Sabir Ali**, Ayan Ray and Alok Chakrabarti, Phys. Scr. 88 (2013) 065301
3. *Atomic Line Filter: A study on the effect of Repump laser*; Ayan Ray, **Md. Sabir Ali** and Alok Chakrabarti, JOSA B 30, 2436 (2013)
4. *Application of repumping laser on optical switching*; Ayan Ray, **Md. Sabir Ali** and Alok Chakrabarti, Optics and Laser Technology 60 (2014) 107-110.
5. *Control of coherence in a ladder type system with double resonance optical pumping and electromagnetically induced transparency*; **Md. Sabir Ali**, Ayan Ray, Alok Chakrabarti, The European physical journal D (2015) 69: 41
6. *Double dark resonance in inverted Y system and its application in attenuating optical switching action*; **Md. Sabir Ali**, Ayan Ray, Alok Chakrabarti, The European physical journal D (2016) 70:27
7. *Development of A Collinear Laser Spectrometer Facility at VECC: First test result*, **Md. Sabir Ali**, Ayan Ray, Waseem Raja, Arup Bandyopadhyay, Vaishali Naik, Asish Polley, Alok Chakrabarti, Pramana, 90:47, April 2018.

B. Publications/presentations in conferences/symposium:

1. *Coherence control in a E system and its utility in optical switching*; Ayan Ray, **Md. Sabir Ali**, and Alok Chakrabarti, Proceedings of 2nd International Conference and Exhibition on Lasers, Optics & Photonics, September-08-10, 2014, USA, Volume 1, issue 3, p-69
2. *EIT in all optical switching*, **Md. Sabir Ali**, Ayan Ray and Alok Chakrabarti, Proceedings of International Conference on Light Quanta: Modern Perspectives and Applications, University of Allahabad, December 14-16, 2015 (p. no. 24).

Other Publications:

1. *Design and development of a radio frequency quadrupole linac postaccelerator for the variable energy cyclotron center rare ion beam project*; S Dechoudhury, V Naik, M Mondal, A Chatterjee, HK Pandey, TK Mandi, A Bandyopadhyay, P Karmakar, S Bhattacharjee, PS Chouhan, **S Ali**, SCL Srivastava, A Chakrabarti, Review of Scientific Instruments 81, 023301 (2010).
2. *Design of the medium energy beam transport (MEBT) line for the rare ion beam (RIB) project at VECC*; **Md S Ali**, S Dechoudhury, YC Chao, PS Chauhan, SCL Shrivastava, Arup Bandyopadhyay, A Chakrabarti., Nuclear Instruments and methods in Physics Research A 636 (2011) 1-7
3. *A gas-jet transport and catcher technique for on-line production of radioactive ion beams using an electron cyclotron resonance ion-source*; V. Naik, A. Chakrabarti, M. Bhattacharjee, P. Karmakar, A. Bandyopadhyay, S. Bhattacharjee, S. Dechoudhury, M. Mondal, H. K. Pandey, D. Lavanyakumar, T. K. Mandi, D. P. Dutta, T. Kundu Roy, D. Bhowmick, D. Sanyal, S. C. L.

Srivastava, A. Ray and **Md. S. Ali**, Review of scientific instruments 84, 033301 (2013).

4. *Design of medium Energy beam Transport (MEBT) line for the rare ion beam project at VECC*; **Md. Sabir Ali**, Arup Bandyopadhyay, Siddhartha Dechoudhury, Alok Chakrabarti, Book of abstracts of DAE-BRNS Indian Particle Accelerator Conference, November 19-22, 2013, p-167
5. *The blue light indicator in rubidium 5S-5P-5D cascade excitation*; Waseem Raja, **Md Sabir Ali**, Alok Chakrabarti and Ayan Ray, Applied Physics B, 123:202, 2017

Md. Sabir Ali

Md. Sabir Ali

Table of Contents

Table of Contents	i
List of figures	v
List of Tables	viii
Synopsis	ix
Chapter 1 Introduction	1
Chapter 2 Basics of laser spectroscopy and related concepts	5
2.1 Rubidium electronic structure.....	5
2.1.1 Fine structure	6
2.1.2 Hyperfine structure	6
2.1.3 Isotope shift	7
2.2 Effect of external magnetic field	9
2.3 Optical selection rules.....	9
2.4 Laser-atom interaction and line broadening	10
2.4.1 Einstein's A and B coefficients	10
2.4.2 Line-width and lifetime	11
2.4.3 Line broadening.....	12
2.5 Dipole matrix element	14
2.6 Rabi frequency.....	15
2.7 Optical pumping	16
2.8 Saturation intensity	17
2.9 Lamb dip.....	18
2.10 AC stark shift.....	19
2.11 Electromagnetically Induced Transparency (EIT).....	20
2.12 Double Resonance Optical Pumping (DROP).....	22
Chapter 3 Experimental techniques: A brief introduction	24
3.1 Saturation absorption spectroscopy	24
3.1.1 Experimental schemes	24
3.1.2 Cross-over signals	25
3.2 Polarization spectroscopy	27
3.2.1 Basic working principle.....	27
3.3 Stabilization of External cavity diode lasers	29
3.3.1 Diode lasers	29

3.3.2 Basics of frequency stabilization.....	34
3.3.3 Locking schemes in vapour cell spectroscopy	39
3.3.4 Laser locking at VECC laser hut.....	45
3.3.5 Analysis of laser locking	46
3.4 Collinear laser spectroscopy (CLS) on accelerated stable ion beam.....	48
3.4.1 Doppler tuning.....	50
3.4.2 New developments in collinear laser spectroscopy.....	50
Part I. Study of ladder system in Rubidium.....	52
Chapter 4 Study of optical switching in Rubidium Ladder system	53
4.1 Introduction.....	53
4.2 Motivation.....	53
4.3 Intensity switching under EIT	55
4.4 Experimental scheme, results and discussion	56
4.4.1 First part of the experiment	57
4.4.2 Second part of the experiment.....	62
4.4.3 Final part of the experiment	67
4.5 Conclusion	69
Chapter 5 Study on the application of repump laser in optical switching	71
5.1 Introduction.....	71
5.2 Motivation.....	71
5.3 Experimental scheme.....	72
5.4 Results & discussion.....	74
5.5 Conclusion	78
Chapter 6 Controlling coherence in ladder system	79
6.1 Introduction.....	79
6.2 Motivation.....	79
6.3 Repumping in ladder system	81
6.4 Experimental schemes	83
6.5 Results and discussion.....	85
6.6 Conclusion	96
Chapter 7 Double dark resonance in inverted Y system and its effect on optical switching	97
7.1 Introduction.....	97
7.2 Motivation.....	97

7.3 Optical switching in an inverted Y level scheme	99
7.4 Experimental arrangement.....	104
7.5 Results and discussion	105
7.5.1 First part of the experiment	106
7.5.2 Second part of the experiment.....	109
7.5.3 Final part of the experiment	117
7.6 Conclusion	118
Chapter 8 Effect of repump laser on Atomic line filter.....	119
8.1 Introduction.....	119
8.2 Motivation.....	119
8.3 Controlling IDEALF using repump laser	121
8.4 Experimental arrangement.....	122
8.5 Results and discussion	125
8.6 Conclusion	132
Chapter 9 Tunable Atomic frequency offset locking in ladder system.....	133
9.1 Introduction.....	133
9.2 Motivation.....	133
9.3 Transfer of frequency modulation in a coherently driven Ξ system.....	135
9.4 Experiment, result and discussion	139
9.4.1 First part of the experiment	140
9.4.2 Second part of the experiment.....	142
9.5 Conclusion	148
Part II. Development of a collinear laser spectroscopy setup at the ISOL facility at VECC	150
Chapter 10 Development of the collinear laser spectroscopy set up at VECC-ISOL facility.....	151
10.1 Introduction.....	151
10.2 Collinear laser spectroscopy setup at the VECC-ISOL facility.....	153
10.2.1 Offline ion source	154
10.2.2 Beam transport system, diagnostics and beam tuning.....	155
10.2.3 Design of the charge exchange cell.....	158
10.2.4 Photon detection unit and PMT handling.....	160
10.2.5 Laser system	164
10.2.6 Data acquisition and experimental control.....	166

10.2.7 Beam line vacuum	168
10.3 Results and discussion	169
10.3.1 Calibration of CEC	170
10.3.2 Detection of Rb fluorescence spectra	173
10.4 Conclusion	179
Appendix A. Important formulae used in the thesis.....	181
A.1. Clebsch-Gordan Coefficients.....	181
A.2. Mean free path	181
A.3. Estimation of required laser power	182
A.4. Magnet calibration	182
A.5. Doppler shift estimation.....	183
A.6. Isotope shift estimation.....	183
A.7. Photon counting	184
References.....	185

List of figures

Fig. 1.1 Nuclide chart summarizing the isotopes studied by optical techniques.	3
Fig. 2.1 Optical pumping	17
Fig. 2.2 Energy levels show ac stark effect in dressed state picture.	20
Fig. 2.3 The basic level coupling schemes for three-level atomic system.....	21
Fig. 2.4 Ladder level coupling scheme showing OODR and DROP	23
Fig. 3.1 Saturation absorption spectroscopy set up.....	25
Fig. 3.2. Cross-over signals.....	26
Fig. 3.3 Polarization spectroscopy set up.....	28
Fig. 3.4 p-n diode band diagram	30
Fig. 3.5 ECDL configurations.....	32
Fig. 3.6 Laser stabilization scheme and error signal.....	36
Fig. 3.7 Side of the fringe lock.....	37
Fig. 3.8 Frequency modulation	39
Fig. 3.9 Schematic of DAVLL set up	40
Fig. 4.1 Ladder level scheme for optical switching	57
Fig. 4.2 Schematic of the experimental arrangement for optical switching in ladder.	58
Fig. 4.3 Experimental recording of probe absorption for pump laser frequency scan.....	59
Fig. 4.4 Recording of the probe absorption spectra for probe laser frequency scan.....	62
Fig. 4.5 Intensity switching in pump and probe laser	64
Fig. 4.6 Comparison of intensity switching	66
Fig. 4.7 Theoretical simulation of intensity switching in EIT system.	67
Fig. 4.8 Recording of the probe absorption spectra for different probe laser power	68
Fig. 5.1 Level coupling scheme for optical switching with repump laser.	73
Fig. 5.2 Schematic of the experimental arrangement to study effect of repump laser.....	74
Fig. 5.3 probe absorption spectrum showing DROP-EIT feature without repump laser....	75
Fig. 5.4 Intensity switching of pump laser and its effect on probe laser.....	76
Fig. 5.5 Gain-bandwidth response of the optical switch in ladder system.....	77
Fig. 6.1 Level scheme of $^{87}\text{Rb } 5S_{1/2} \rightarrow 5P_{3/2} \rightarrow 5D_{5/2}$ transition	81
Fig. 6.2 Schematic of experimental arrangement for coherence control in ladder system.	84
Fig. 6.3 Probe absorption spectra as a function of probe detuning.	87
Fig. 6.4 Blue fluorescence spectra recording as a function of pump detuning	89

Fig. 6.5 Coherence control of DROP-EIT medium	90
Fig. 6.6 Comparison of relative intensity (ζ) and line-width (Γ_{EIT}) of EIT	91
Fig. 6.7 Coherence control of DROP-EIT medium under detuned two-photon resonance	92
Fig. 6.8 Comparison of relative intensity (ζ) and line-width (Γ_{EIT}) of EIT	94
Fig. 6.9 Example of open system TPA.	95
Fig. 7.1 Level coupling scheme for inverted Y system.	99
Fig. 7.2 Simulation of optical switching in inverted Y system.....	103
Fig. 7.3 Schematic of experimental arrangement for DDR in inverted Y system.....	105
Fig. 7.4 Probe absorption spectra for Λ connection in inverted Y system.....	107
Fig. 7.5 Probe transmission and blue fluorescence spectra in inverted Y system.	108
Fig. 7.6 Probe transmission and blue fluorescence spectra for pump scanning.....	112
Fig. 7.7 Gain bandwidth response of the switch in inverted Y system.....	116
Fig. 8.1 Level scheme of $5S1/2 \rightarrow 5P3/2 \rightarrow 5D3/2$ transition of ^{87}Rb atom.....	123
Fig. 8.2 Schematic of experimental arrangement for ALF	124
Fig. 8.3 Experimental recording of ALF signal vs probe2 detuning	126
Fig. 8.4 ALF characteristic parameter vs pump intensity.	127
Fig. 8.5 Effect of repump detuning on ALF spectrum.....	128
Fig. 8.6 Peak transmittance and FWHM of ALF vs repump laser detuning.....	130
Fig. 8.7 Peak transmittance and FWHM of ALF vs repump laser intensity.....	131
Fig. 9.1 Ladder level coupling scheme in Rubidium-87.....	136
Fig. 9.2 Probe absorption and modulation transfer in a three level ladder system	138
Fig. 9.3 Schematic of the experimental arrangement for TAFOL.	139
Fig. 9.4 Probe absorption spectrum vs pump detuning.....	141
Fig. 9.5 Recorded fringes from a scanning FPI	143
Fig. 9.6 Probe absorption spectra for different pump frequency settings.	144
Fig. 9.7 Frequency noise spectral density ($S\Delta\nu$) vs fourier frequency (f) plot.	147
Fig. 10.1 Current status of collinear laser spectroscopy setup.....	152
Fig. 10.2 3D view of the ion beam transport system for ISOL-CLS setup.....	153
Fig. 10.3 Ion source (schematic) of the ISOL-CLS facility.....	154
Fig. 10.4 Ion beam profile simulated in TRNASPORT.....	155
Fig. 10.5. Ion beam profile in X plane as measured using wire scanner	158
Fig. 10.6 Charge exchange cell for ISOL-CLS setup:	160
Fig. 10.7 Reflector assembly and detection of second focus	162

Fig. 10.8 PMT fixed on beam line with the help of cage mount assembly.....	163
Fig. 10.9. Positioning of apertures on reflector and photograph of apertures.....	164
Fig. 10.10 Schematic overview of the laser system layout for ISOL-CLS setup	164
Fig. 10.11 Laser system layout	165
Fig. 10.12 Synchronous-mode photon counting	167
Fig. 10.13 Data acquisition layout for ISOL-CLS setup.....	169
Fig. 10.14 Neutralization efficiency vs temperature plot.....	172
Fig. 10.15 First recorded spectra of 8.0 keV Rb ion beam using ISOL-CLS setup.....	174
Fig. 10.16 Recording of ^{85}Rb ($F = 3 \rightarrow F'$) hyperfine transition in a single laser scan...	177

List of Tables

Table 6.1 Fitted fluorescence line intensities	88
Table 6.2 Fitted fluorescence line-widths	88
Table 7.1 Blue fluorescence statistics when two independent \bar{E} systems act in parallel. .	113
Table 7.2 Blue fluorescence statistics under on resonance matched DDR mode	114
Table 7.3 Blue fluorescence statistics under off-resonant DDR mode.	115
Table 10.1. Beam optics simulation results	157
Table 10.2 Ion source parameters and practical beam transport efficiency	158
Table 10.3 Experimental parameters for CLS experiment.....	170
Table 10.4 Results of the first recorded spectra on Rb using ISOL-CLS beam line	176
Table 10.5 Results of the fitting of ^{85}Rb lines.....	178

SYNOPSIS

Coherent pump-probe spectroscopy in alkali vapor media provides unique opportunity to study different aspects of coherent photon-atom interaction [1]. Such interaction leads to many interesting observations such as electromagnetically induced transparency (EIT) [2], electromagnetically induced absorption (EIA) [3], coherent population trapping (CPT) [4] etc and also finds several application in the field of metrology [5], magnetometry [6], frequency offset locking [7], slowing down of light [8] etc. Commonly, pump-probe spectroscopy consists of two or more independent lasers which connect the atomic hyperfine levels to satisfy different level coupling schemes (Λ, Ξ, V, N etc. The Ξ level coupling is very important for three step photo-ionization. Photo-ionization can be thought of as the starting point for resonant ionization spectroscopy (RIS) [9] which is also a potent method for nuclear spectroscopy using atomic physics.

Collinear laser spectroscopy is one of the various atomic physics techniques that are routinely used to study various nuclear properties [10]. The main advantage of this tool is the model independent estimation of nuclear spin, mean-square charge radius and nuclear moments. The limitation of Doppler broadening in vapor cell spectroscopy is overcome in this method by probing an accelerated the ion beam. Generally this kind of spectroscopy is performed on an isotopic chain of a particular element at the ISOL facilities. Such systematic studies for elements throughout the nuclear chart will provide physical data for further study.

The present thesis deals with coherent pump-probe spectroscopy together with the effects related to the use of one additional laser (repump laser) in Rubidium-87 (^{87}Rb) $5S_{1/2} \rightarrow 5P_{3/2} \rightarrow 5D_{5/2}$ ladder (Ξ) system and their application in the field of optical switching, atomic frequency offset locking, atomic line filter, coherence control, double dark resonance etc. It also deals with the development of a collinear laser spectroscopy setup at

ISOL facility at VECC. The thesis is divided into two parts. First part of the thesis is related to the experimental observation of different pump-probe-repump laser induced phenomena and the possible explanations based on the semi-classical treatment of atomic coherences. The other part of the thesis is dedicated to the developmental aspects of the collinear laser spectroscopy setup and the first experimental demonstration of the setup using 8.0 keV Rubidium ion beam from the VECC-ISOL facility [11]. Provisions for further developments on the collinear laser spectroscopy setup are also discussed at the end of the thesis.

The thesis is organized in ten chapters to discuss the various spectroscopic studies on the ^{87}Rb ladder system and the developmental aspects of the collinear laser spectroscopy setup at VECC-ISOL facility. Briefs for each chapter can be found in the following portions of the synopsis.

Chapter 1 provides a brief introduction to the subject matter of coherent pump-probe spectroscopy in gaseous alkali media and collinear laser spectroscopy on accelerated ion beam. The current status of the field and its important applications in the field of basic and applied sciences are also discussed at the same time. The purpose of the chapter is to present the basic motivation behind the works presented in the later chapters.

Chapter 2 presents the background theoretical knowledge relevant to the present thesis. This is required for the understanding of the experimental results presented in the subsequent chapters. In that direction, fine structure, hyperfine structure and isotopic shift of the atomic energy levels along with the effect of external magnetic field on the atomic energy levels is discussed. The concept of optical selection rules is central to any spectroscopic measurement and therefore it is discussed in the same chapter. Atomic transitions are prone to different line broadening mechanism and the common issues relevant for vapor cell spectroscopy are treated in this connection. Many optical properties such as dipole matrix element, Rabi frequency, optical pumping, saturation intensity and many more are mentioned

for later usage. Some recent experimental observations in vapor cell spectroscopy, for example, double resonance optical pumping (DROP) [12], EIT, optical switching, atomic line filter etc and their underlying principles are also discussed in brief. For the sake of completeness few nuclear physics concepts relevant to the field of the collinear laser spectroscopy is also mentioned at the end of the chapter.

Chapter 3 outlines the experimental techniques relevant for the present thesis. To this end, the basic spectroscopic setup, such as, saturation absorption spectroscopy (SAS) and polarization spectroscopy are discussed in this chapter. As the frequency of a free running diode laser shifts with time, it is necessary to keep the laser frequency stable for spectroscopic measurement during experiments. In view of this, the operation of the external cavity diode laser (ECDL), its noise characteristic and basics of the frequency stabilization scheme etc are discussed. A small review of the available laser locking schemes for vapor cell spectroscopy is also presented in this chapter. The chapter ends with the discussion of the collinear laser spectroscopy and some specialized applications in this field. The radioactive ion beam facility at VECC and the production of stable Rubidium ion beam at the VECC-ISOL facility is also discussed in this context.

Chapter 4 marks the starting point of the first part of the thesis. It presents the investigation on optical switching in ^{87}Rb ladder system under dominant DROP and EIT condition. The motivation behind the present study lies in the observation of DROP and EIT phenomena in ^{87}Rb $5S_{1/2} \rightarrow 5P_{3/2} \rightarrow 5D_{5/2}$ ladder system. Though both DROP and EIT originate from the same two-photon coherence (TPA) their difference is very subtle. Therefore it was necessary to study the coherence assisted transfer of intensity modulation in the medium under DROP and EIT conditions and to investigate for any difference in their behavior under the intensity switching. Apart from describing the experimental scheme and relevant level coupling, the chapter also discusses the procedure to prepare the system under

DROP and EIT condition. In this context, the relevant conditions for system preparation and the experimental confirmation from the probe absorption spectra are reported. In the second part of the experiment, optical intensity switching is introduced through the pump laser and the effect of the same is monitored on the probe laser. This is performed under both DROP and EIT conditions. We have found that the medium under EIT condition is more agile towards faster optical switching compared to the medium under DROP. In the last part of the experiment we have tried to find out any demarcation feature for the transition of the medium from dominant DROP to dominant EIT condition and the relevant findings are reported in this chapter. To explain the results of the experiment a phenomenological simulation based on semi-classical treatment of atomic coherence has also been provided in the chapter.

Chapter 5 deals with the experimental investigation aimed at finding the effect of one additional laser (repump) on the optical switching in $^{87}\text{Rb } 5S_{1/2} \rightarrow 5P_{3/2} \rightarrow 5D_{5/2}$ ladder system. The appearance of DROP in probe absorption spectra for the concerned level coupling scheme is due to the decay of atoms to the uncoupled hyperfine ground state $5S_{1/2} (F = 1)$ whereas EIT demands no loss of population from the particular ladder coupling scheme. This counter requirements of DROP and EIT opens up the possibility of introducing another laser which can retrieve back the population ‘lost’ to the $F = 1$ state. This has the potential to strengthen the EIT while reducing the DROP effect. As DROP and EIT were already explored for their dual mode of optical switching in our previous experiment, we wanted to see the effect of the repump laser on optical switching in the presented investigation. The beneficial aspect of repump laser is based on the manipulation of population in the ladder level coupling scheme. We have found that the presence of repump laser increases the gain throughout the switching bandwidth and the same observation is reported in this chapter. The probe absorption spectra clearly show the role of repump laser in strengthening EIT. The response of the probe laser intensity switching in response to the

pump laser intensity switching at 1 *MHz* under the presence of σ^+ repump laser is also shown for completeness. Though the system bears significant resemblance with the inverted *Y* system [13], it is markedly different from it and the possible explanations for the same is discussed.

Chapter 6 presents the experimental investigation conducted on the same ladder system to study the role of repump laser in controlling the coherence. Controlling coherence in atomic system is a well explored subject [14]. Moon et al [15,16] have also conducted systematic studies on ^{87}Rb in both open and close system. In spite of these, the use of repump laser in controlling the coherence was still unexplored. The application of repump laser helps to reduce the effect of incoherent pumping and related radiation trapping of atoms in the uncoupled $F = 1$ state. We have found experimentally that the repump laser intensity has profound effect on the EIT line-width and strength for both the resonant and detuned coupling condition. In this connection, effect of both types of repumping i.e. normal hyperfine repumping (using linearly polarized repump laser) and Zeeman sublevel repumping (using σ^+ polarized repump laser) have also been studied and possible comparison is made between the two. The effect of repump laser on both the close ladder system ($F = 2 \rightarrow F' = 3 \rightarrow F''$) and the open ladder system ($F = 2 \rightarrow F' = 2 \rightarrow F''$) were studied and the results are discussed in this chapter. The recording of the blue fluorescence ($\lambda = 420 \text{ nm}$) along with the probe absorption spectra was also simultaneously performed to understand the atomic population dynamics in the $5D_{5/2}$ state which is also reported and discussed in this context. Along with the experimental observations, possible explanations are also provided this chapter.

Chapter 7 presents the experimental investigation on inverted *Y* system in ^{87}Rb . The inverted *Y* system is closely related to the ladder system. Co-propagating probe and repump laser is used along with a counter propagating pump laser to form this kind of system. The

typical signature of this system is the appearance of a double dark resonance (DDR) [17]. The effect of DDR in optical switching is investigated in this experimental work. We have found that the DDR plays an important role in attenuating the optical switching action throughout the switching bandwidth. The working of the overall system is similar to that of a combination logic gate. In all the previous work we had used co-propagating pump-repump laser combination which is different from the current scheme. As the inverted Y system can be thought of as the combination of a ladder and Λ system, independent behavior of these subsystems are first studied and the results are discussed. Simultaneous measurement of the typical blue fluorescence was also done to understand population dynamics of the system. System behavior under the exact resonance condition (subsystems becomes coupled and forms inverted Y system) was studied in detail. Finally the effect of the matched DDR on optical switching is studied and compared with the earlier results obtained for simple ladder system.

Chapter 8 discusses the effect of repump laser on atomic line filter (ALF) realized in the $5S_{1/2} \rightarrow 5P_{3/2} \rightarrow 5D_{3/2}$ ^{87}Rb ladder system. The σ^+ repump laser couples the $5S_{1/2}$ ($F = 1$) state with the $5P_{3/2}(F')$ levels. ALF finds its application in the field of laser imaging detection and ranging, free space laser communication etc. There are many types of ALF but we have chosen an induced dichroism excited atomic line filter (IDEALF) [18] as the ALF choice to investigate. Presented investigation shows that the performance of ALF can be optimized by carefully choosing the detuning and intensity of repump laser. The peak transmittance of the ALF can be increased by $\sim 30\%$ with the use of a repump laser. We have used DROP signal for the calibration of the ALF signal. The repump action also gives rise to sidelobe for detuned repump laser frequency which can be eliminated with careful choice of repump laser frequency. Along with the experimental results possible explanations for the observed behavior are also given in this chapter.

Chapter 9 reports the experimental observation on tunable atomic frequency offset locking (TAFOL) in $5S_{1/2} \rightarrow 5P_{3/2} \rightarrow 5D_{5/2}$ ^{87}Rb ladder system. TAFOL finds its application in the field of metrology, high precision coherent spectroscopy etc and is very useful for laser locking in the excited state transitions. AFOL scheme is typically employed in situations where the system exhibits EIT. Such schemes have already been employed for Λ level coupling [19]. TPA and EIT spectra were utilized to lock the probe laser while the pump laser was locked on the fringe produced by the Fabry-Perot interferometer. The main advantage of the lock is its tunability. The lock point can be chosen anywhere on the Doppler width of the $5S_{1/2} \rightarrow 5P_{3/2}$ transition without sacrificing the precision. The chapter discusses in detail about the applied locking methodology applied and also reports its merits. A simple phenomenological explanation for the frequency modulation transfer from pump to probe laser is also given in this chapter.

Chapter 10 deals with the development of collinear laser spectroscopy setup at ISOL facility at VECC. A new collinear laser spectroscopy setup is installed at the VECC-ISOL facility for laser nuclear spectroscopy. Present chapter outlines each step of development for every part (e.g. beam transport and diagnostics, Charge exchange cell, photon detection unit, laser system layout, data acquisition etc) of the setup. First experimental test result using 8.0 keV Rb ion beam is also reported in the chapter. Results are explained and further scope of development is mentioned at the end of the chapter.

References

- [1] Bruce W. Shore, *The theory of coherent atomic excitation, Volume 1 & 2*: John Wiley & Sons, 1990.
- [2] K. J. Boller, A Imamoglu, S. E. Harris, "Observation of Electromagnetically Induced Transparency," *Physical Review Letters*, vol. 66, no. 20, pp. 2593-2596, May 1991.

- [3] A. M. Akulshin, S. Barreiro, A. Lezama, "Electromagnetically induced absorption and transparency due to resonant two-field excitation of quasidegenerate levels in Rb vapor," *Physical Review A*, vol. 57, no. 4, pp. 2996-3002, April 1998.
- [4] E. Arimondo, "Coherent population trapping in laser spectroscopy," *Progress in optics*, vol. XXXV, p. 258, 1996.
- [5] Th. Udem, R. Holzwarth T.W. Hansch, "Optical frequency metrology," *Nature*, vol. 416, pp. 233-237, 2002.
- [6] M. Stahler, S. Knappe, C. Affolderbach, W. Kemp, R. Wynands, "Picotesla magnetometry with coherent dark states," *Europhysics Letters*, vol. 54, no. 3, pp. 323-328, May 2001.
- [7] S. C. Bell, D. M. Heywood, J. D. White, J. D. Close, R. E. Scholten, "Laser frequency offset locking using electromagnetically induced transparency," *Applied Physics Letters*, vol. 90, no. 171120, pp. 1-3, 2007.
- [8] Olga Kocharovskaya, Yuri Rostovtsev, Marlan O. Scully, "Stopping Light via Hot Atoms," *Physical Review Letters*, vol. 86, no. 4, pp. 628-631, January 2001.
- [9] B Cheal, K T Flanagan, "Progress in laser spectroscopy at radioactive ion beam facilities," *Journal of Physics G: Nuclear and Particle Physics*, vol. 37, no. 113101, pp. 1-38, September 2010.
- [10] P. Campbell, I.D. Mooreb, M.R. Pearson, "Laser spectroscopy for nuclear structure physics," *Progress in Particle and Nuclear Physics*, vol. 86, pp. 127-180, 2016.
- [11] Md. Sabir Ali, Ayan Ray, Waseem Raja, Arup Bandyopadhyay, Vaishali Naik, Asish Polley, Alok Chakrabarti, Development of A Collinear Laser Spectrometer Facility at VECC: First test result, 2016, Communicated to NIMA.

- [12] H.S. Moon, L. Lee, J.B. Kim, "Double resonance optical pumping effects in electromagnetically induced transparency," *Optics Express*, vol. 16, no. 16, pp. 12163-12170, August 2008.
- [13] Amitabh Joshi, Min Xiao, "Electromagnetically induced transparency and its dispersion properties in a four-level inverted-Y atomic system," *Physics Letters A*, vol. 317, pp. 370-377, September 2003.
- [14] Wei Jiang, Qun-feng Chen, Yong-sheng Zhang, G.C. Guo, "Optical pumping-assisted electromagnetically induced transparency," *Physical Review A*, vol. 73, no. 053804, pp. 1-7, May 2006.
- [15] Han Seb Moon, Lim Lee, Jung Bog Kim, "Coupling-intensity effects in ladder-type electromagnetically induced transparency of rubidium atoms," *Journal of Optical Society of America B*, vol. 22, no. 12, pp. 2529-2533, December 2005.
- [16] Han Seb Moon, Heung-Ryoul Noh, "Resonant two-photon absorption and electromagnetically induced transparency in open ladder-type atomic system," *Optics Express*, vol. 21, no. 6, pp. 7447-7455, March 2013.
- [17] Jianbing Qi, "Electromagnetically induced transparency in an inverted Y-type four-level system," *Physica Scripta*, vol. 81, no. 015402, pp. 1-8, 2010.
- [18] Zhusong He, Yundong Zhang, Hao Wu, Ping Yuan, Shuangqiang Liu, "Theory and experiment for atomic optical filter based on optical anisotropy in rubidium," *Optics Communications*, vol. 282, pp. 4548-4551, August 2009.
- [19] Han Seb Moon, Lim Lee, Kyoungdae Kim, Jung Bog Kim, "Laser frequency stabilization using electromagnetically induced transparency," *Applied Physics Letters*, vol. 84, no. 16, pp. 3001-3003, April 2004.

Chapter 1

Introduction

The present thesis is comprised of two parts. The first part of the thesis (Part-I) deals with various types of laser spectroscopic studies carried out on Rubidium in a vapour cell. The second part of the thesis (Part-II) discusses the efforts towards developing a collinear laser spectroscopy setup for spectroscopy on atomic beam at the existing Isotope Separator On-Line (ISOL) facility at VECC. Part-I of the thesis is discussed in Chapters 4 to 9 and the Part-II of the thesis is described in Chapter 10.

Coherent pump-probe spectroscopy in alkali vapour media has yielded interesting results from the very beginning. Coherence population trapping (CPT), electromagnetically induced absorption (EIA), electromagnetically induced transparency (EIT) [1,2,3] etc are the few interesting outcome of the atomic coherence in the medium. On the application front slowing down of light [4], ultrasensitive magnetometry [5], miniaturized atomic clock [6], frequency offset locking [7,8,9] etc are a few to name. These new observations and applications together make this field interesting to the whole research community. Generally this type of spectroscopy is performed using two or more lasers in the desired configuration (V, Λ, Ξ, N etc). The resulting atomic coherence in the medium helps in modulation transfer from one laser to the other and this fact is utilized in the demonstration of optical switching [10,11,12,13,14], frequency stabilization [15] etc. In this connection the spectroscopy on Rubidium-87 $5S_{1/2} \rightarrow 5P_{3/2} \rightarrow 5D_{5/2,3/2}$ ladder (Ξ) system is of particular interest as it has application in the field of optical switching, metrology [16], frequency conversion [17] etc. Pump-probe spectroscopy in such a system reveals excited state hyperfine structure in terms of double resonance optical pumping (DROP) [18,19,20,21] and EIT [22].

Another important relevant topic is the issue of coherence control in this kind of system. In literature there are many studies available on this aspect of atomic coherence [23,24,25]. A ladder (Ξ) linkage pattern can be extended into an inverted Y system naturally by addition of another laser [26,27,28,29]. The additional laser sometimes helps to generate additional dark resonance in the system and can also act as repump laser depending upon the geometry of the linkage. A lot of studies have been carried out to understand the nature of this additional dark resonance and interplay among the dark resonances [23,30,31]. Coherent pump probe spectroscopy also finds its application in the field of narrowband optical filter which has immense technological application in the field of free space laser communication [32], generation of narrowband quantum light [33,34], laser imaging and detection [35,36,37] etc. The ^{87}Rb ladder system as mentioned above can also be used to generate an induced dichroism excited atomic line filter (IDEALF) [38,39,40]. In this connection the main focus has always been to improve the transmittance, width etc of the filter. Another important application of pump-probe spectroscopy is in the field of atomic frequency offset locking (AFOL) which is based on the generated atomic coherence in the medium. It has been well investigated with respect to the Λ linkage [7,8,41] because of its high degree of coherence [42] and is less explored in ladder system [43]. The main concern of this type of locking scheme has always been to improve the tunability and precision of the lock point.

High resolution laser spectroscopy on atomic beam is a robust experimental technique used for model independent estimation of nuclear ground state properties such as size, shape and multipole moments. Measurement of atomic hyperfine structure and isotope shifts provides useful information about the underlying nuclear structure. In this direction, ISOL (Isotope Separator On-Line) facilities provide unique opportunity to study chain of isotopes. When laser spectroscopic technique is utilized at the ISOL facilities, we get useful information about the behaviour of the nuclear ground state properties at the so called magic

numbers, at which nuclei are generally strongly bound, and also about the changes in the shape and size of the nucleus. As we shift far from the valley of β -stability, the nuclear structure changes and precise knowledge about the same is non-existent or rare. In such situation, the nuclear structural data obtained through the high resolution laser spectroscopy is highly important and can also be used to test the validity of available theoretical prediction. The theoretical models used for the prediction of nuclear ground state properties depend on the nuclear mass region. On the other hand, laser spectroscopic technique can be used on any nuclear mass region to estimate the nuclear ground state properties. The atomic hyperfine splitting (HFS) provides information about the spin and moments of the nucleus. The information about the changes in the size and shape of the nuclear charge distribution can be deduced from the measurement of isotope shift (IS). The summary of the isotopes studied by optical techniques is presented in Fig. 1.1 [44].

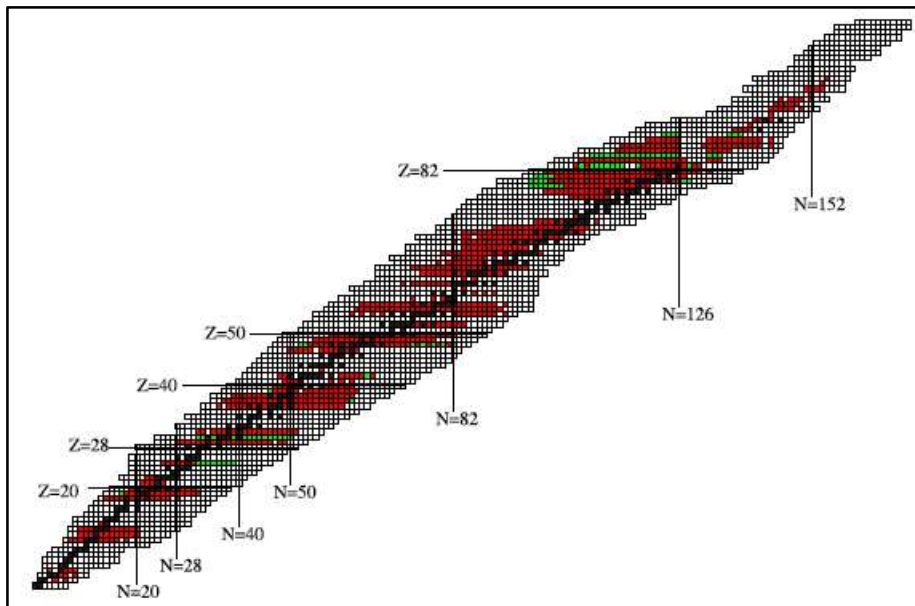


Fig. 1.1 Nuclide chart summarizing the isotopes studied by optical techniques. Black boxes represent stable or long lived nuclides and red boxes (in colour) represent the elements studied by optical techniques. Green boxes (in colour) represent currently unpublished studies.

The use of laser spectroscopy on fast ion beam can be traced back to 1975 [45]. The use of collinear geometry for this kind of spectroscopy was pioneered by Wing et al [46] and Kaufman [47,48]. Soon, collinear laser spectroscopy (CLS) became a method of choice for the study of radioactive beams [49,50]. Since then, the field has grown tremendously and many facilities have come up worldwide. The growth of the field has been reviewed from time to time by different authors [51,52,53,54,55,56]. The current status of the field can be found in several recent reviews [57,58,59,60,61,44].

Chapter 2

Basics of laser spectroscopy and related concepts

The experimental investigations presented in this thesis were all performed on Rubidium. It is a member of the alkali metal group and natural Rubidium (Rb) contains ^{85}Rb and ^{87}Rb isotopes with natural isotopic abundance of 72.17% and 27.83% [62] respectively. Rubidium vapour cell experiments were conducted on ^{87}Rb while the test of collinear laser spectroscopy set up was performed both on ^{85}Rb and ^{87}Rb . Rubidium fine structure consists of D_1 and D_2 lines (doublet) at wavelengths 795 nm and 780 nm respectively. As the available laser wavelength was ~ 780 nm, the experiments were based on D_2 transitions. As the vapour cell of Rubidium contains large numbers of atoms at room temperatures, most of the experiments were performed at room temperatures though some of the experiments involving higher excited states were performed at higher temperature to compensate for the low number of atoms at higher excited states at room temperature. It is a well known fact that the finite size, spin, magnetic moment and electric quadrupole moment of a nucleus perturb the observed optical spectra [63,64]. For a specific isotope spin, magnetic moment and electric quadrupole moment determine the hyperfine spectrum of the isotope. On the other hand isotope shift results from the finite size and mass of the nucleus. Therefore ground state nuclear properties can be estimated from the observed hyperfine spectra and isotope shift for a particular isotopic chain. This chapter discusses key concepts and important Rubidium properties which are referred throughout the rest of the thesis.

2.1 Rubidium electronic structure

The outermost electronic shell of Rubidium atom consist of only one valence electron ($1s^2 2s^2 2p^6 3s^2 3p^6 3d^{10} 4s^2 4p^6 5s$) in the 5s orbital. All the inner shell electrons therefore don't contribute to the total transition probability and orbital angular momentum of the atom. The

this thesis follows standard nomenclature used in the literature [62] to identify the different energy levels (orbital) within the atom and is discussed below.

2.1.1 Fine structure

Rubidium fluorescence spectra consist of a doublet fine structure in the near-infrared region (NIR). It results from the spin-orbit coupling between the orbital angular momentum (\vec{L}) of the outer electron and its spin angular momentum (\vec{S}). The total angular momentum of the outer electron is thus given by,

$$\vec{J} = \vec{L} + \vec{S} \quad 2.1$$

and total angular momentum (\vec{J}) should lie in the range $|L-S| \leq J \leq |L+S|$. ^{87}Rb ground state ($5S_{1/2}$) has $L = 0$, $S = 1/2$, $J = 1/2$ and therefore it has no fine structure. On the other hand the first excited state ($5P$) has $J = 1/2$ or $3/2$ (as $L=1$ and $S = 1/2$). Therefore it splits into $5P_{1/2}$ and $5P_{3/2}$ levels and shows the presence of fine structure. Transitions between these states and ground state are known as D_1 ($5^2S_{1/2} \rightarrow 5^2P_{1/2}$) line and D_2 ($5^2S_{1/2} \rightarrow 5^2P_{3/2}$) line.

2.1.2 Hyperfine structure

The nuclear magnetic dipole moment is associated with total angular momentum of the nucleus I . The electron induced magnetic field (B) interacts with nuclear magnetic moment and thus results in a coupling of angular momentum of the nucleus (I) and the electrons (J). This introduces a new total angular momentum

$$\vec{F} = \vec{I} + \vec{J} \quad 2.2$$

similar to the electron LS coupling. The value of F lies between, $|I-J| \leq F \leq |I+J|$. The hyperfine interaction produces a splitting into either $(2J+1)$ levels for $J < I$ or $(2I+1)$ levels for $J > I$. The hyperfine interaction results in an energy shift which can be written as,

$$\Delta E_{HFS} = \frac{A}{2} * C + B * \frac{\frac{3}{2} C(C + 1) - 2I(I + 1)J(J + 1)}{4I(2I - 1)J(2J - 1)} \quad 2.3$$

where $C = F(F + 1) - I(I + 1) - J(J + 1)$. The hyperfine constant $(A) = g\mu_N B(0)\hbar/J$ is the magnetic dipole constant where g is the nuclear g-factor, μ_N is nuclear magneton, $B(0)$ is the magnetic field generated at the nuclear site by electrons and B is the electric quadrupole constant. The nuclear magnetic moments for ^{85}Rb and ^{87}Rb are $5/2$ and $3/2$ respectively. This leads to a splitting of the $^{87}\text{Rb } 5S_{1/2}$ state ($J=1/2, I=3/2$) into two hyperfine levels with $F = 1$ or 2 . Similarly the excited states $5P_{3/2}$ and $5D_{5/2}$ splits into $F' = 3, 2, 1$ or 0 and $F'' = 4, 3, 2$ or 1 levels respectively. The ground state, first excited state and second excited states are denoted by F, F' and F'' respectively. It is worth to note that the ground state splitting is much higher compared to the excited state due to the greater overlap of the spherical S orbital with the atomic nucleus.

2.1.3 Isotope shift

Isotope shift is the change in the transition frequency of the characteristic spectral lines between two isotopes (of mass number $A1$ and $A2$) of a specific element and is defined as $\delta\nu^{A1,A2} = \nu_{A1} - \nu_{A2}$. The transition frequency is calculated with respect to the center of gravity of all the hyperfine components of the spectral line. Isotope shift can be explained in terms of the deviation from a point-like, infinitely heavy nucleus approximation. The mass shift and the field shift (or the volume shift) contribute to the total isotope shift of an atom.

Mass shift

Mass shift for hydrogen-like spectra can be accounted for by considering finite nuclear mass and introducing the reduced electron mass and it is given by,

$$\Delta\nu_{NMS} = (M_{A1} - M_{A2})\nu m_e / M_{A1}M_{A2} = N * (A1 - A2)/A1A2 \quad 2.4$$

where $M_{A1,A2}$ are the mass of the isotopes and $N = \nu m_e$ is the normal mass shift constant (m_e = electron mass in amu). The transition frequency is proportional to the reduced mass and so is the shift in transition frequency. In case of a many electron system, the different electron momentum may be correlated. This leads to a collective effect on the nuclear motion and causes the specific mass shift which is expressed as,

$$\Delta\nu_{SMS} = S * (A1 - A2)/A1A2 \quad 2.5$$

where S is the specific mass shift constant. In this case also the same A dependence can be found. Therefore mass shift is totally dependent on the atomic structure instead of the nuclear structure.

Field shift

The effect of the finite size of the nuclear charge distribution on the nuclear binding energy leads to the field shift ($\delta\nu_{FS}$). The first order non-relativistic field shift can be expressed as,

$$\delta\nu_{FS} = K * \delta\langle r^2 \rangle^{A1,A2} \quad 2.6$$

where $K = -Ze^2/(6\epsilon_0)A|\psi(0)|^2$, K is the change in electron charge density at nucleus between upper and lower states of the atomic transition. Equation (2.6) is only applicable for light to medium heavy nuclei and holds true for any nuclear shape and thus model independent. For heavier elements relativistic approach should be followed to estimate the field shift. One can see from equation (2.6) that the field shift is proportional to the change in mean square charge radius from one isotope to another and also to the factor K . The direct determination of $\langle r^2 \rangle$ for a nucleus through the measurement of Isotope Shift is not possible as the finite size effect is too small. Thus only a change in $\langle r^2 \rangle$ can be measured for an isotopic series.

2.2 Effect of external magnetic field

The degeneracy in the atomic hyperfine structure can be lifted with the use of external magnetic field [65]. A single hyperfine level is split into $(2F+1)$ magnetic sublevels denoted with the magnetic hyperfine quantum number m_F . This splitting is known as anomalous Zeeman effect under weak magnetic field approximation where the shift due to the magnetic field is small compared to the hyperfine splitting of the atom. In a weak field approximation the magnetic Hamiltonian can be written as,

$$\hat{H}_{mag} = g_J \mu_B \frac{J_z}{\hbar} B \quad 2.7$$

corresponding Zeeman shift is expressed by,

$$\Delta E_{Zeeman} = \mu_B g_F m_F B_z \quad 2.8$$

where $g_F = g_J \frac{F(F+1)+J(J+1)-I(I+1)}{2F(F+1)}$, μ_B is the Bohr magneton, g_F is hyperfine Lande g-factor [65] and B_z is external magnetic field. The direction of the magnetic field serves as the quantization axis. In the strong field limit, the coupling of nuclear angular momentum I and electron angular momentum J breaks down leading to the Paschen-back regime where the external magnetic interaction energy exceeds the hyperfine interaction energy.

2.3 Optical selection rules

Optical selection rules dictate whether an atomic transition between two energy levels is permitted under dipole approximation or not. These selection rules originate from the conservation of atomic and optical angular momentum between the atomic energy levels. They limit the number possible transitions from a particular level when excited with a laser of known electric polarization and allow us to assign resonances to the atomic transitions. When atom absorbs a photon (momentum = $\pm \hbar \vec{k}$), its orbital angular momentum quantum number (L) should change by ± 1 in order to conserve the angular momentum and also to conserve the

overall parity of the atomic wave function. On the other hand total angular momentum quantum number (J) should change by ± 1 or 0. The magnetic quantum numbers change depending on the polarization of the laser light. Following is the list of the general electric dipole selection rules for an atomic transition in terms of different quantum numbers.

$$\Delta l = \pm 1, \Delta L = 0, \pm 1$$

$$\Delta J = 0, \pm 1 \quad (J = 0 \nrightarrow J' = 0)$$

$$\Delta m_J = 0, \pm 1$$

$$\Delta F = 0, \pm 1 \quad 2.9$$

$$\Delta m_F = 0 ; \text{ For linear polarization } (\pi \text{ light})$$

$$\Delta m_F = +1 ; \text{ For left circular polarization } (\sigma^+ \text{ light})$$

$$\Delta m_F = -1 ; \text{ For right circular polarization } (\sigma^- \text{ light})$$

In case of ^{87}Rb $F = 2 \rightarrow F' = 3$ transitions, by applying the above selection rules we can see that it is a closed transition while the other transitions from ^{87}Rb $F = 2$ are 'open' in the sense that they can decay back to other ground hyperfine level (^{87}Rb $F = 1$).

2.4 Laser-atom interaction and line broadening

2.4.1 Einstein's A and B coefficients

Let us consider a two level atomic system which is interacting with a laser field. The probability that a photon is absorbed by the atom per unit time is proportional to the spectral energy density $\rho(\nu)$ of the laser field where $\rho(\nu)$ is given by Plank's radiation law,

$$\rho(\nu) = \frac{8\pi\nu^2}{C^3} \frac{h\nu}{e^{kT} - 1} \quad 2.10$$

and the probability of absorption can be written in terms Einstein's B coefficient,

$$P_{12} = B_{12}\rho(\nu) \quad 2.11$$

Similarly, the probability of stimulated emission by an atom is given by,

$$P_{21} = B_{21}\rho(\nu) \quad 2.12$$

The probability of spontaneous emission is given by Einstein's A coefficient,

$$P_{21} = A_{21} \quad 2.13$$

At steady state, absorption rate must be equal to the rate of emission and we have the following rate equation for the two level system,

$$N_2A_{21} + N_2B_{21}\rho(\nu) = N_1B_{12}\rho(\nu) \quad 2.14$$

where N_2 and N_1 are the number of atoms in state 2 and 1 respectively and they follow the Boltzmann distribution at thermal equilibrium,

$$\frac{N_2}{N_1} = \frac{g_2}{g_1} e^{-\frac{h\nu}{kT}} \quad 2.15$$

g_1, g_2 are the statistical weight factors for the respective energy levels. It can be shown [63] that the Einstein coefficients follow the following relations,

$$B_{12} = \frac{g_2}{g_1}B_{21} \text{ and } A_{21} = \frac{8\pi h\nu^3}{c^3}B_{21} \quad 2.16$$

2.4.2 Line-width and lifetime

Spontaneous emission of a photon by an atom is due to the interaction of the atom with the zero point energy fluctuations and is treated in quantum field theory. Treating the atom as a classical dipole oscillator with damping equal to the decay rate γ , the intensity of spontaneous emission is given by,

$$I(\omega - \omega_0) = I_0 \frac{\gamma/2\pi}{(\omega - \omega_0)^2 + \gamma^2/4} \quad 2.17$$

The corresponding spectral line shape is Lorentzian with a FWHM or natural line-width of γ .

The lifetime associated with the corresponding decay is given by, $\tau = 1/\gamma$.

2.4.3 Line broadening

Generally the natural line-width discussed above is broadened due to many experimental conditions [66]. In the following paragraphs, various types of broadening are discussed which are relevant to our experimental condition.

2.4.3.1. Doppler broadening

The laser spectroscopy experiments were performed on Rb vapour cell at room temperature and the atoms inside follow Maxwell-Boltzmann velocity distribution. As the atoms are in random thermal motion, the absorption lines are Doppler broadened. The mean free path of the atoms inside the vapour cell is given by $\lambda_{mfp} = (\sigma_{coll} n)^{-1}$, where n is the number density of atoms and σ_{coll} is the collision cross section. At room temperature, the mean free path of the Rb atoms is ~ 60 m which is much greater than the cell dimension. Therefore the vapour temperature is determined by the collision of the atoms with the cell wall. In the reference frame of an atom moving with velocity \vec{v} , the resonance frequency (ν_0) is Doppler shifted to $\nu_L = \nu_0 + \vec{k} \cdot \vec{v}/2\pi$, where \vec{k} is the wave vector of the laser. At thermal equilibrium the velocity distribution of the atoms in one dimension is given by,

$$n(v_x)dv_x \propto e^{-(v_x/v_{th})^2} dv_x \quad 2.18$$

where $v_{th} = (2kT/m)^{1/2}$ is the most probable velocity. By changing the variable from velocity to frequency in equation (2.18) we can get the Doppler broadened spectral line profile [63,66] which is given by,

$$I(\omega) = I_0 e^{-\left(\frac{c(\omega-\omega_0)}{\omega v_{th}}\right)^2} \quad 2.19$$

which is Gaussian and its line-width (FWHM) is given by,

$$\Delta\omega_D = \frac{\omega_0}{c} (8kT \ln 2/m)^{1/2} \quad 2.20$$

where k is the Boltzmann constant, m is the mass of atom and T is the vapour temperature.

2.4.3.2. *Transit time broadening*

In many spectroscopic situations interaction time of the atoms with the laser beam is small compared to the spontaneous lifetimes of the atomic transition. In such cases, the line-width of a Doppler-free transition is limited by the time of flight through laser beam which ultimately determines the interaction time. This kind of line broadening is termed as transit time broadening. This can be understood by considering the example of an oscillator which oscillates with constant amplitude during a time interval and then suddenly stops. The frequency spectrum of such oscillator will reveal the corresponding broadening of the line-width. For rectangular laser profile, the FWHM of the absorption line is given by $\delta\nu \cong v/d$ where d is the laser diameter and v is the atom velocity. In practice, for a laser of Gaussian beam profile the transit time broadening is given by, $\delta\nu \cong 0.4 v/w$ where w is the beam waist of the Gaussian beam profile. In a more accurate calculation of the transit time broadening one also has to consider the curvature of the laser wave front.

2.4.3.3. *Collisional broadening*

When two atoms approach one another the energy levels of the atoms shifts because of the interaction between the atoms. This shift depends on the electronic configurations of the atoms and the distance between them. Depending on the nature of the interaction between the atoms the shift in the atomic energy levels may be positive as well as negative. During the collision if one atom undergoes a radiative transition, the transition frequency becomes dependent on the distance between the atoms. The mutual distance between two atoms is also dependent on the pressure and temperature of the gas. Therefore this collision induced line broadening becomes dependent upon temperature as well as pressure. The pressure induced

line broadening is sometimes also referred as *pressure broadening*. In the infrared and microwave region, collision may sometimes cause a narrowing of the line-width instead of a broadening which is known as *Dicke narrowing* [66].

2.5 Dipole matrix element

In the semi-classical picture of laser-atom interaction, the total system Hamiltonian can be written as, $H = H_0 + H_{int}$, where $H_{int} = \hat{d} \cdot \vec{E}$ under *dipole approximation* [63,66,67], $\hat{d} = -q r$ is the dipole operator and \vec{E} is the electric field vector at \vec{r} . As the radiation field causes the transition in the atom, the system wave-function becomes time dependent. Under this circumstances the solution of the time dependent Schrodinger equation, $H\Psi = i\hbar \frac{\partial\Psi}{\partial t}$ can be expressed as,

$$|\Psi\rangle = \sum C_k(t) |k\rangle e^{-iE_k t/\hbar} \quad 2.21$$

The spatial parts of the eigen-functions are the solution of the time independent Schrodinger equation $H_0|k\rangle = E_k|k\rangle$. In the case of a two level system the total wavefunction thus can be written as $|\Psi\rangle = C_1(t)|1\rangle e^{\frac{iE_1 t}{\hbar}} + C_2(t)|2\rangle e^{\frac{iE_2 t}{\hbar}}$ where C_1 and C_2 are the probability amplitudes and normalized to unity by $|C_1|^2 + |C_2|^2 = 1$. Substituting $|\Psi\rangle$ into time dependent Schrodinger equation one can get,

$$\dot{C}_2 = -\frac{i}{\hbar} \left(C_2(t)(E_2 - \hbar\omega) + C_1 V_{21} e^{-i(E_1 - E_2)t/\hbar} \right) \quad 2.22$$

where $V_{12} = d_{12} E$, ω is the carrier frequency and $d_{12} = -q \int \psi_1^* r \psi_2 d\tau$ is called the atomic dipole matrix element [66,67]. The dipole matrix element signifies the strength of the interaction between atom and nearly resonant optical radiation. These matrix elements can be written as a product of a reduced matrix element and Clebsch-Gordan coefficient with the

help of Wigner-Eckart theorem [65] by factoring out the angular dependence. For example, the matrix element for two hyperfine sublevels $|Fm_F\rangle$ and $|F'm'_F\rangle$ can be written as

$$\langle Fm_F|qr|F'm'_F\rangle = \langle F||qr||F'\rangle * \langle Fm_F|F'1m'_F p\rangle \quad 2.23$$

In equation (2.23), the first term on the right hand side is the reduced matrix element and the second term is the Clebsch-Gordan coefficient (Appendix A.1). The index p indicates that component of r is in spherical coordinate basis. Clebsch-Gordan coefficients can be written in terms of Wigner 3-j and 6-j symbol [68,69]. Finally the dipole matrix elements can be written in terms of reduced matrix elements $\langle J||qr||J'\rangle$ which in turn can be estimated from lifetime experiments via the following expression

$$\langle J||qr||J'\rangle = \left(\frac{1}{\tau} * \frac{3\pi\epsilon_0\hbar c^3}{\omega_0^3} \frac{2j'+1}{2j+1} \right)^{1/2} \quad 2.24$$

where τ is the lifetime and ω_0 is the resonance frequency for the transition.

2.6 Rabi frequency

In the field of coherent atomic excitations, Rabi frequency (Ω) plays a very fundamental role. Physically it can be understood as a measure of the interaction strength. It is also the frequency of population inversion in a resonant, lossless two-state system. Generalized Rabi frequency [66] can be defined as,

$$\Omega_0 = \sqrt{\Omega^2 + \Delta^2} \quad 2.25$$

where $\Delta = \omega - \omega_0$ is called the detuning of the excitation frequency from the resonance frequency, $\Omega = d_{12}E_0/\hbar$ is the Rabi frequency for resonance excitation and E_0 is the amplitude of the electric field. For a lossless two level system the population of the excited state can be found by solving the equation (2.22) and is proportional to,

$$|C_2|^2 = \frac{\Omega^2}{\Omega_0^2} \sin^2\left(\frac{\Omega_0 t}{2}\right) \quad 2.26$$

One can see from equation (2.26) that the population of the excited state for a two level system at resonance oscillates with Rabi frequency Ω . $\hbar\Omega$ represents the strength of the atom-laser interaction. It should also be noted that carrier frequency $\omega \gg \Omega$ [70]. The values of the Rabi frequency can be estimated from the following formula [67],

$$\Omega = 2.2 * 10^8 \sqrt{I(W/cm^2)} * d(in a. u.) s^{-1} \quad 2.27$$

where d is the dipole moment and I is the intensity in W/cm^2 .

2.7 Optical pumping

Under thermal equilibrium the atomic populations are evenly distributed among the magnetic sublevels. Laser induced excitation causes this population to change according to the particular linkage pattern. In Fig. 2.1 one such linkage pattern and associated optical pumping is illustrated. Initially all the populations were evenly distributed among different magnetic sublevels. Two grey filled sublevels were affected by the circularly polarized laser radiation while the unfilled sublevel is unaffected by it. After many cycles of such optical pumping all the population is placed into the magnetic sublevel $m_F = +1$. This redistribution of population takes place through a combination of coherent and incoherent processes. After excitation from a ground state, the population can decay back to ground sublevels spontaneously by obeying the optical selection rules mentioned in equation (2.9). After such many excitation and de-excitation cycles, population redistribution takes place among the magnetic sublevels. As these magnetic sublevels are identified with respect to a particular quantization axis, the population redistribution looks something different when the levels are linked with a laser of different polarization. Such examples are discussed by W. B. Shore in [67].

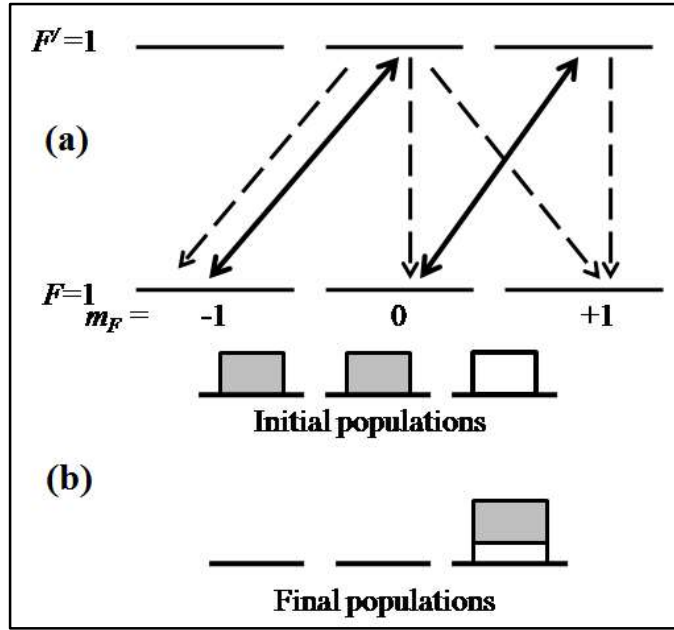


Fig. 2.1 Optical pumping produces complete transfer of population into single quantum state. (a) Linkage pattern for transitions from hyperfine level $F \rightarrow F'$ using circular polarized light. Solid line represents laser linkage while dashed line represents spontaneous emission. (b) Population distribution after many optical pumping cycles of excitations and spontaneous emission.

2.8 Saturation intensity

For a two level atomic system interacting with a laser light, the steady state population density difference between the two levels can be written as [63],

$$N_1 - N_2 = \frac{N}{1 + \frac{I_{pump}}{I_s(\omega)}} \quad 2.28$$

where N_1 and N_2 are the population densities of the lower and upper energy levels respectively. $N = N_1 + N_2$ is the total population density at the steady state. I_{pump} is the pump intensity and I_{sat} is the saturation intensity which is defined as,

$$I_{sat}(\omega_0) = \frac{\pi hc}{3 \lambda^3 \tau} \quad 2.29$$

ω_0 is the resonance frequency. One can see from equation (2.28) that the steady state population density difference at saturation pump intensity is just $N/2$ or the population of upper level is $N_2 = N/4$. The velocity selective minimum of the saturated population density difference is known as *Bennet hole* [71]. Saturation intensity can also be defined in terms of the following equation,

$$\frac{I_{pump}}{I_{sat}} = \frac{2\Omega^2}{\Gamma^2} \quad 2.30$$

For a multilevel system many other decay routes are possible. So the simple expression of saturation is not applicable in such cases. Saturation intensity is also dependent upon the polarization of the light. With pump beam power much higher than the power required to attain saturation, additional line broadening occurs due to laser power. Saturation reduces the absorption near the line centre while the absorption far from the line centre changes due to higher pump power. This gives rise to the broadening of spectral line shape and termed as power broadening. The line-width (FWHM) in such case can be written as a function of saturation intensity and is given by,

$$\Delta\omega_{FWHM} = \Gamma \left(1 + \frac{I_{pump}}{I_{sat}} \right)^{1/2} \quad 2.31$$

2.9 Lamb dip

When pump and probe beams are generated from the same laser beam by reflecting back the incident beam into the absorption cell, the saturated absorption coefficient can be written as,

$$\alpha_s = \alpha^0(\omega) \left[1 - \frac{S_0}{2} \left(1 + \frac{(\gamma_s/2)^2}{(\omega - \omega_0)^2 + (\gamma_s/2)^2} \right) \right] \quad 2.32$$

where S is the saturation parameter, $S_0 = S(\omega_0)$, $\gamma_s = \gamma\sqrt{1 + S_0}$ and γ is the homogeneous line-width of the transition. The absorption profile represented by equation (2.32) shows a Doppler broadened absorption profile $\alpha^0(\omega)$ with a dip at the line center $\omega = \omega_0$ which is known as Lamb dip [71].

2.10 AC stark shift

Apart from changing the atomic population, the perturbing radiation can also change the energy level separation. This change in the energy level separation is known as light shift or ac stark shift. In dressed state picture [72], the energy eigen-values for a two level atom interacting with a monochromatic radiation field can be written as,

$$\lambda = \pm \frac{(\delta^2 + \Omega^2)^{1/2}}{2} \quad 2.33$$

where δ is the laser frequency detuning and can be both positive and negative. Ω is the Rabi frequency or interaction strength. For $\Omega = 0$ the unperturbed eigen-values are separated by δ as shown in Fig. 2.2 and this result resembles the time independent perturbation of two states with an energy separation of δ . These two states are excited states at energies E_2 and $E_1 + \hbar\omega$. For large frequency detuning, the eigen-values can be written as,

$$\lambda = \pm \left(\frac{\delta}{2} + \frac{\Omega^2}{4\delta} \right) \quad 2.34$$

One can see from equation (2.34) that the states are shifted from the unperturbed eigen-values by the light shift $\pm\Omega^2/4\delta$. The effect of ac stark splitting can be seen when an atomic medium is dressed with a strong laser and probed with weak laser. The probe absorption spectrum exhibits doublet structure instead of a single absorption line. This is known as Autler –Townes doublet.

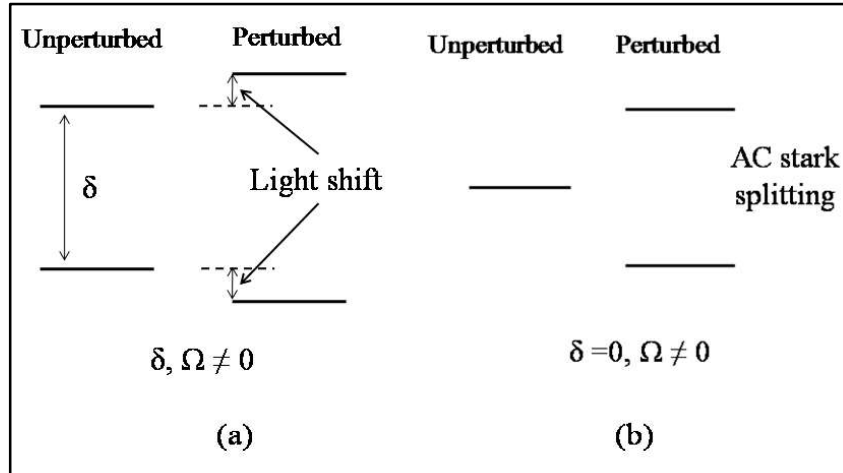


Fig. 2.2 Energy levels show ac stark effect in dressed state picture. (a) Dressed state energy levels when δ and Ω are not equal to zero. (b) Dressed state energy levels for resonant laser ($\delta = 0$).

2.11 Electromagnetically Induced Transparency (EIT)

Quantum interference which is similar to the constructive and destructive interference of classical waves is an interference of alternative pathways of the quantum mechanical processes. Such interference can be observed between the alternative transition pathways when quantum states of atoms or molecules are coupled to one or more laser fields [73]. Radiative transitions to autoionizing states show such quantum interference which is also known as Fano interference [74]. Similar effect is seen in the case of laser control of optical properties of atomic media and is termed as the electromagnetically induced transparency (EIT) [75,76]. Normally, a probe laser tuned to the resonance sees strong absorption. Under EIT, cancellation of such absorption takes place. This is caused by the interference between the atomic coherences induced by the presence of the laser field. EIT also modifies the refractive properties of the system. The application of EIT is seen in lasing without inversion [77,78], coherent population trapping [79] etc.

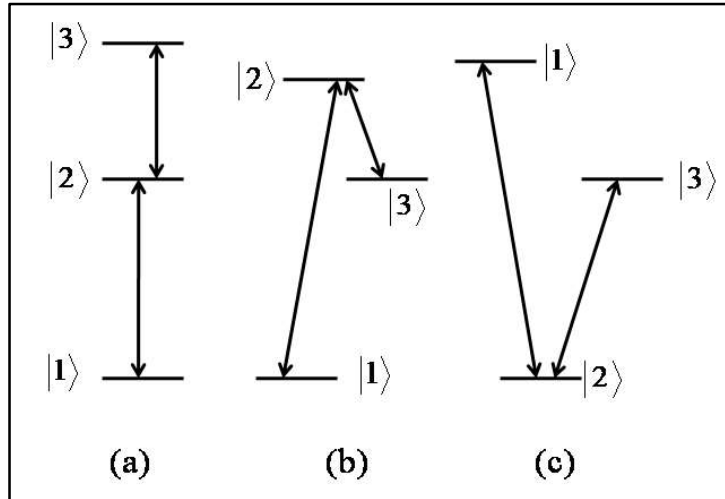


Fig. 2.3 The basic level coupling schemes for three-level atomic system interacting with two near resonant laser fields. (a) Ladder or cascade coupling (b) Lambda (Λ) coupling and (c) V (Vee) coupling scheme. Transition between $|1\rangle - |3\rangle$ energy levels is dipole forbidden.

The physics behind EIT can be understood by considering the example of three-level atomic system. Fig. 2.3 shows the basic coupling schemes of three level systems. The levels are identified as $|1\rangle$, $|2\rangle$ and $|3\rangle$. The transition between $|1\rangle - |3\rangle$ is dipole forbidden. According to the energy levels, these coupling schemes can be categorized into V (Vee), Λ (Lambda) and Ξ (Ladder or cascade) coupling schemes. In order to observe EIT in V system population transfer to level $|1\rangle$ is required whereas for Λ and Ξ system most of the population remains in state $|1\rangle$ as it is the ground state.

When laser fields interact with a three-level atomic system the Hamiltonian of the bare atomic state is modified. The eigenstates of this new Hamiltonian is the linear superposition of the bare atomic states. For exact two-photon resonance condition, two of the eigenstates of the total Hamiltonian are symmetric and anti-symmetric coherent superposition of two lower states (for Λ) of bare atomic basis and can be written as,

$$|C\rangle = \frac{\Omega_1}{\Omega'} |1\rangle + \frac{\Omega_2}{\Omega'} |3\rangle \quad 2.35$$

$$|NC\rangle = \frac{\Omega_2}{\Omega'} |1\rangle - \frac{\Omega_1}{\Omega'} |3\rangle$$

where, Ω_1 and Ω_2 are the Rabi frequencies of the $|1\rangle - |2\rangle$ and $|2\rangle - |3\rangle$ transitions respectively and $\Omega' = (\Omega_1^2 + \Omega_2^2)^{1/2}$. The state $|NC\rangle$ is decoupled from the intermediate state $|2\rangle$ and is termed as the ‘dark state’ which indicates the presence of EIT. This can be readily seen as one tries to construct a dipole moment between $|NC\rangle$ and $|2\rangle$. In the steady state all the population will be in state $|NC\rangle$ through spontaneous decay from state $|2\rangle$.

2.12 Double Resonance Optical Pumping (DROP)

Doppler free spectroscopy of excited state transition is immensely important for many applications. Traditional optical-optical double resonance (OODR) technique [80] in a three-level atomic system utilizes two lasers interacting with the same atom simultaneously and are in resonance with two transitions that share a common intermediate level. The situation is shown in Fig. 2.4. Here one laser (L_1) is used to excite atom from the ground state to the intermediate level ($|2\rangle$) and the other laser (L_2) probes the population of the same level. The main drawback of this technique is the signal-to-noise (S/N) ratio. In a system with high spontaneous emission rate the intermediate level is not easily populated so that it can be probed.

Double resonance optical pumping [81] is very useful in such situations and S/N ratio of the spectrum can be improved significantly by using this technique. However, this effect is only dominant in five-level systems with two ground states ($|1\rangle, |2\rangle$) and two intermediate states ($|3\rangle, |4\rangle$). The idea is to detect the population of the ground state with a probe laser (L_1) instead of the population of the intermediate state. This technique is very useful in alkali atoms as they have high spontaneous emission rate. The population of the coupled ground

state $|2\rangle$) may decrease when the atoms are in simultaneous resonance with both the laser fields (L_1 and L_2). This happens because the atoms excited to level $|5\rangle$ are optically pumped to the uncoupled ground state $|1\rangle$ via the intermediate levels $|3\rangle, |4\rangle$). The extra pumping channel introduced through the state $|3\rangle$ can cause rapid decrease in population of the state $|2\rangle$. In this situation the probe laser (L_1) can detect the excited state transitions with high S/N ratio by detecting the population of state $|2\rangle$.

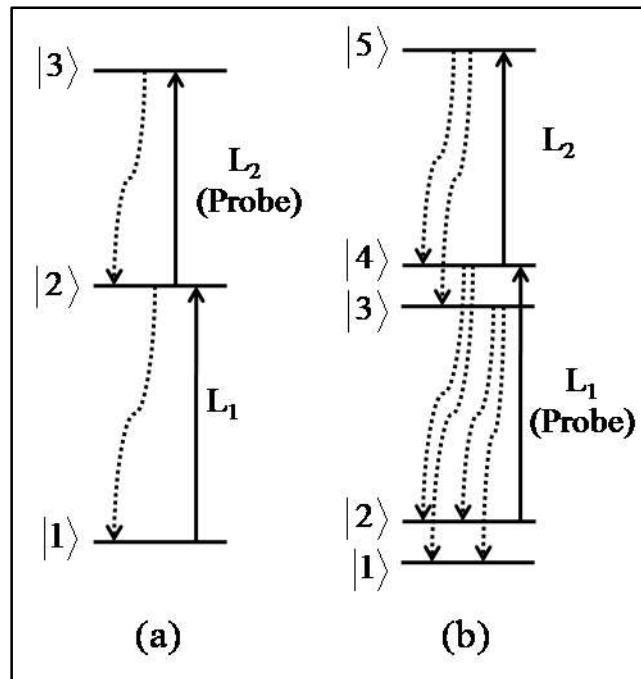


Fig. 2.4 Ladder level coupling scheme showing OODR and DROP (a) OODR in three-level ladder system (b) DROP in five-level system.

Chapter 3

Experimental techniques: A brief introduction

3.1 Saturation absorption spectroscopy

Saturation absorption spectroscopy (SAS) [71] is based upon the velocity selective saturation of the Doppler broadened atomic transitions. The resolution in SAS is no longer limited by the Doppler width but only by the much narrower Lamb dip. The Lamb dips [71] of two transitions can clearly be separated from each other even when the Doppler profiles of the two transitions completely overlap as long as $\Delta\omega = \omega_1 - \omega_2 > 2\gamma_s$ (where γ_s is the width of the Bennett hole) is satisfied. SAS helps to resolve the hyperfine structure for a Doppler broadened medium such as atomic vapour cell.

3.1.1 Experimental schemes

A simple SAS set up is depicted in Fig. 3.1(a). The output laser beam from a tunable laser is splitted into two beams of different intensity. The beam with strong intensity (I_1) is referred as pump beam and the beam with weak intensity (I_2) is referred as the probe beam. The pump and probe beam pass through the vapour cell in counter-propagating configuration and overlap each other. The transmitted probe beam intensity is measured in a detector as a function of the laser frequency ω . The measured signal shows Lamb dips at the centres of the Doppler broadened absorption lines. Fig. 3.1(b) shows one such typical SAS spectra for ^{87}Rb $F=2 \rightarrow F'$ transitions. Absorption peaks identified with 1, 4, 6 are the absorption lines while the peaks 2, 3, 5 are cross-over signals (Section 3.1.2). Often two probe beams are used to enhance the sensitivity. In that case one beam passes through the saturated zone and other through the unsaturated zone. The difference between these two intensities helps to extract the saturation signal.

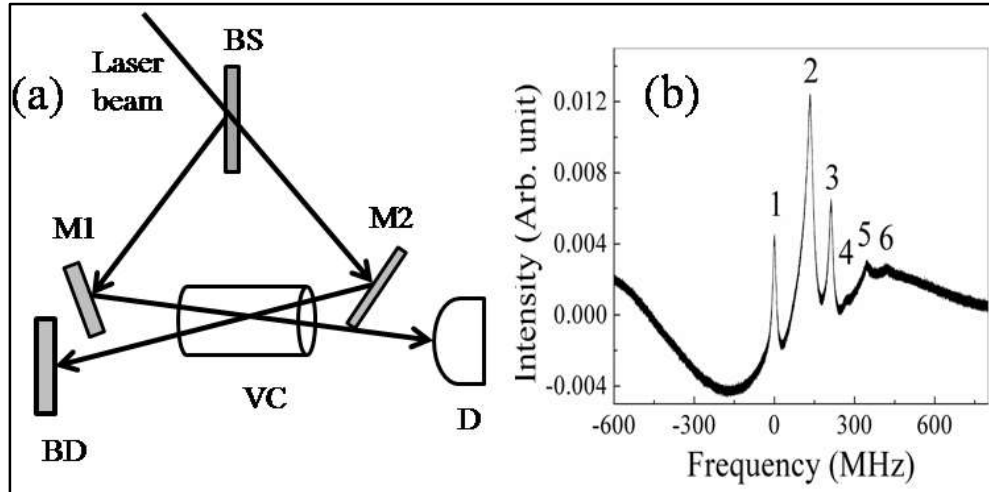


Fig. 3.1 Saturation absorption spectroscopy set up (a) Ray tracing for the arrangement. BS: Beam Splitter, M1, M2: Mirrors, BD: Beam dump, VC: Vapour cell, D: Detector (b) Typical SAS spectra for ^{87}Rb .

The crossing angles of the two beams results in a small Doppler width $\Delta\omega = \Delta\omega_D * \theta$. For very small angles or perfectly anti-collinear situation the probe beam may couple back to the laser resulting in laser instability. Precautions like optical isolators must be placed in front of the laser to get rid of such instability.

3.1.2 Cross-over signals

For a pair of transitions with a common energy level and a frequency separation less than the Doppler width of the transitions, absorption peak appears at average frequency of the pair in a SAS setup [63]. Examples of such peaks are shown in Fig. 3.1(b). For a typical SAS set up, the pump beam burns two holes in the atomic velocity distribution while the probe beam also does the same but in the other side of the velocity distribution. When these holes created by pump and probe beam meet at the maximum of the velocity distribution or when the laser frequencies are at exact resonance with the atomic transitions, we see SAS signals. However cross-over signals appear when the hole burnt by one transition reduces the absorption of the

other transition. These situations occur at exactly the midway between the two saturated absorption peaks.

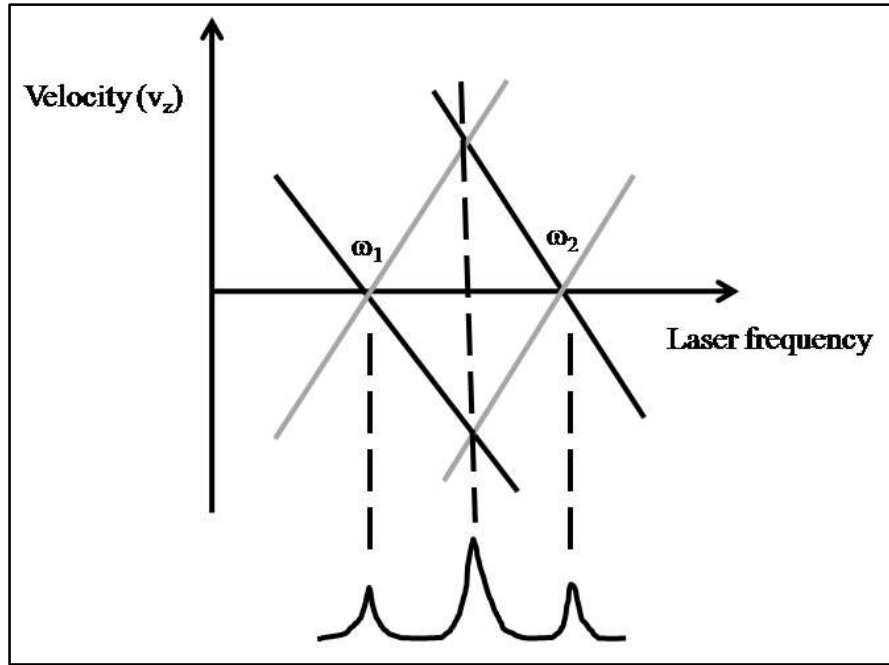


Fig. 3.2. Cross-over signals. The solid black lines represent Doppler shifting with respect to the pump beam while the solid grey lines represent the same for probe beam. At the intersection of these lines we get the absorption peaks. Cross-over signals appear at the midway between the lines at ω_1 and ω_2 .

To elaborate the points let us assume that the two absorption peaks are at ω_1 and ω_2 (Fig. 3.2) and $|\omega_1 - \omega_2| < \Delta\omega_D$ holds valid. At the mid-frequency (i.e. $\omega = (\omega_1 + \omega_2)/2$) between the two absorption line centers, the incident laser beam is shifted against ω_1 by $\Delta\omega = (\omega - \omega_1) = (\omega_1 - \omega_2)/2$. At this condition, the atomic transition at ω_1 can be saturated by the velocity group $v_z \pm dv_z = (\omega_1 - \omega_2)/2k \pm \gamma k$. It is then stated that this velocity groups are in resonance with the incident laser. As the reflected laser experiences opposite Doppler shift, the atomic transition at ω_2 is also saturated by the same velocity group of atoms. Therefore apart from the absorption at ω_1 and ω_2 (corresponding velocity

group $v_z = 0$), we also have absorption at $\omega = (\omega_1 + \omega_2)/2$. The relative sign of this cross-over signal is positive for a common upper level and negative for common lower level. Therefore for a common lower level one can see cross-over peaks at the midway between a pair of transitions with the same sign as of the other absorption peaks [71].

3.2 Polarization spectroscopy

This is a very sensitive Doppler-free spectroscopic technique and different from SAS discussed in the previous section. The technique was first demonstrated by Wieman and Hänsch [82]. In *polarization spectroscopy*, the polarization state of a probe laser is changed by a polarized pump laser which causes both the absorption coefficient and refractive index of the medium to change for the probe laser. In the next subsection the basic principle of polarization spectroscopy is discussed.

3.2.1 Basic working principle

A tunable, monochromatic laser beam is split into a weak probe beam with intensity I_{probe} and a strong pump beam of intensity I_{pump} . The probe beam is passed through a plane polarizer, a vapour cell and another plane polarizer which is in crossed position from the earlier one. The situation is shown in Fig. 3.3. When the pump beam is absent the detector placed behind the second polarizer receives very small signal caused by the residual transmission of the crossed polarizers. A circularly polarized pump beam is sent through the vapour cell from opposite direction. This can be done after allowing a plane polarized pump beam to pass through a $\lambda/4$ plate.

Considering an atomic hyperfine transition from a lower state $|F, m_F\rangle$ to an upper state $|F', m'_F\rangle$, the atoms in the lower state can absorb the pump beam on resonance according to the selection rules described by equation (2.9). Depending on the pump intensity, relaxation processes and absorption cross section, the lower level may get depleted completely or

partially. Also because of the selection rules all the lower levels are not pumped or/and all the upper states are not populated. So in summary it can be said that the pumping process produces an unequal saturation and a non-uniform population of magnetic sublevels.

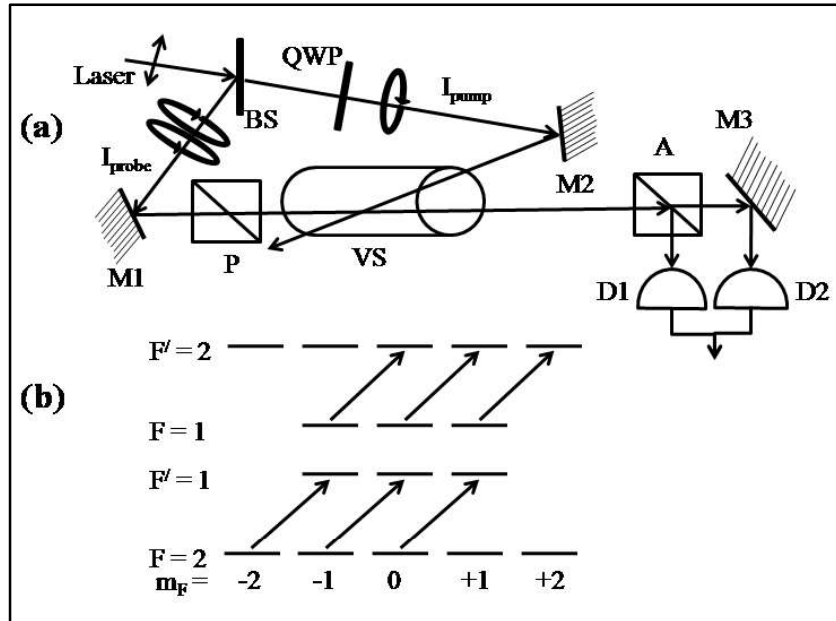


Fig. 3.3 Polarization spectroscopy set up (a) Schematic of set up. BS: Beam splitter, QWP : Quarter wave plate, VS: Vapor cell sample, P: Polarizer, A: Analyzer, M1, M2, M3: Mirror, D1, D2: detector (b) Optical pumping with σ^+ polarization pump beam for two different lower and upper levels. Not all the levels are connected by the pump which leads to birefringence for probe beam and the signal detected at D1 and D2 can produce error signal when act as balanced detector. To observe the absorption spectra one photo-detector is sufficient.

Such an anisotropic distribution of population causes the sample to become birefringent for the incident plane polarized probe laser. The plane of polarization of the probe laser is rotated after traversing through the sample and signal can be seen in the detector. This effect is similar to the *Faraday Effect* but no external magnetic field is needed to create it. Optical

pumping process does not affect all the atoms. Only the subgroup of atoms with the velocity component,

$$v_x \pm \Delta v_x = \frac{(\omega_0 - \omega)}{k} \pm \gamma/k \quad 3.1$$

is affected by the pumping process. For $\omega \neq \omega_0$, the probe beam interacts with a different velocity group of atoms which are not affected by pumping processes. The situation changes when the probe beam frequency coincides with the absorption line center frequency (ω_0) within the homogeneous line-width γ/k and it experiences a birefringence.

3.3 Stabilization of External cavity diode lasers

Stabilization of laser is an important aspect for any laser spectroscopy set up. To study the various effects in a Rubidium vapour cell, as will be discussed in the following chapters, one or more lasers were locked to some external frequency references like, atomic transition or FPI signal. One of the experiments carried out for the present thesis was devoted to study the atomic frequency offset locking scheme in Rubidium ladder system. To perform the spectroscopy on Rubidium we have used external cavity diode lasers (ECDL). The present chapter discusses the properties of diode lasers, locking techniques and associated electronics in subsequent sections.

3.3.1 Diode lasers

Diode lasers are extremely useful tools for a number of research fields such as atomic physics, spectroscopy, metrology, quantum optics etc. They are available in wide range of wavelength. Higher tunability, single mode operation, small beam waist, relatively low power, compactness, low cost and high efficiency make them ideal for this kind of job. However, the spectrum of a free running laser diode is broad (~ 100 MHz). The lasing wavelength is also not well defined and can shift over many MHz over few minutes of

operation. Diodes designed for single mode of operation also shows mode hopping on variations in temperature and drive current. Therefore special care should be taken to use such a system for experiments. Apart from narrow emission line-width and precise wavelength selection, precise control of diode temperature and drive current are absolutely essential. Further details on diode lasers can be found in literature, for example in references [66,83,84,85,86,87]. Fig. 3.4 illustrates the typical band diagram of a $p-n$ junction diode.

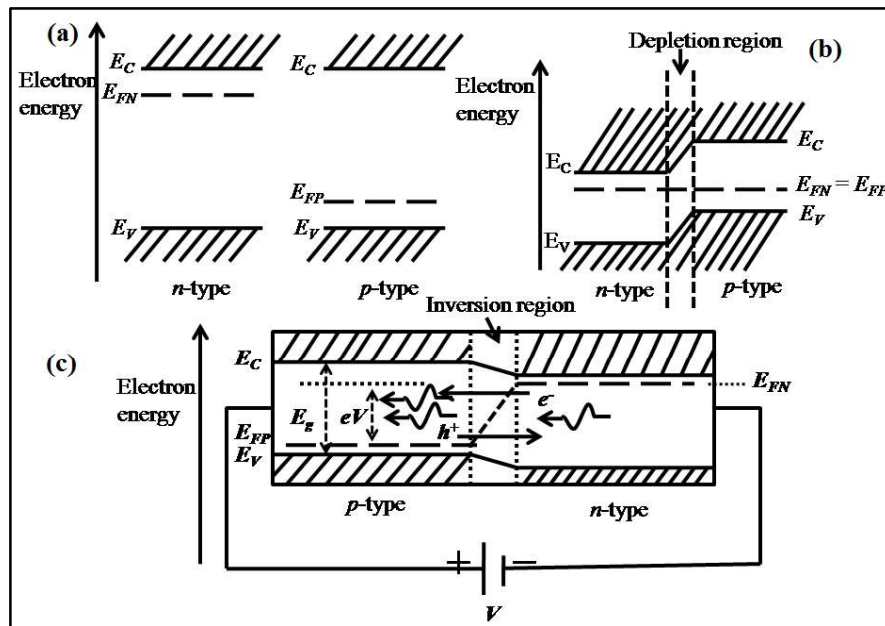


Fig. 3.4 p-n diode band diagram (a) Band diagram for separated p-type and n-type semiconductor (b) p-n diode junction diagram after depletion region is formed (c) p-n junction after forward bias is applied.

3.3.1.1. External cavity diode laser (ECDL)

In practical applications, output beam from laser diode needs to be well collimated using some lens. One way to achieve this is to use a lens and to place the laser source exactly at the focal point of the lens. This helps in creating a parallel output beam. This collimating lens also helps to focus optical feedback exactly on to the diode. The mechanism is shown in Fig. 3.5 . Cavity size of a diode laser is very small and it results in larger bandwidth. In order to

narrow down the bandwidth one needs to increase the effective cavity length. This is achieved by constructing an external cavity. In this type of cavity, the optical feedback is derived from an external mirror placed after the collimating lens. As the feedback from the mirror is higher compared to the feedback from the front facet of the laser diode, the rear facet and the mirror together forms a laser resonator. This new resonator length is $\sim cm$ and it reduces the free spectral range of the system. Finally the laser line-width is reduced to $\sim 1 MHz$ whereas a free running laser diode has line-width $\sim 100 MHz$.

The various advantages of ECDL over traditional diode laser include lower phase noise, reduced line-width, wavelength tuning, mode locking. For a tunable ECDL, a diffraction grating is used as the wavelength selective component. Two different geometries can be used for tunable external cavity diode laser (Fig. 3.5). In the *Littrow* configuration a reflection grating is used as the end mirror after the collimating lens. The first diffraction order of the grating is reflected back into the diode after passing through the collimating lens and zeroth order beam is used as the output. In this configuration the wavelength can be tuned by rotating the diffraction grating.

However, this configuration has the drawback that the output beam direction changes with the laser wavelength tuning. Littrow configuration has a special geometry in which the diffraction angle becomes equal to the incidence angle and the angle is given by,

$$\theta_B = \sin^{-1} \frac{m\lambda}{2d} \quad 3.2$$

where m = diffraction order, λ = wavelength of light, d = line spacing of grating. The other type of configuration is called *Littman-Metcalf* configuration [88]. In this type of configuration the first order diffracted beam is reflected back with the help of an additional mirror whereas the orientation of the grating is fixed. Wavelength can be tuned by rotating the mirror. The fixed direction of the output beam, higher wavelength selectivity and smaller

line-width are the main advantages of this configuration. The disadvantage is the comparatively lower output power than the *Littrow* configuration as the zeroth order beam is lost. Presently, VECC-ISOL laser hut houses three ECDL (Toptica DL100 and Sacher laser Technik Lynx) and all of them are in *Littrow* configuration. For more information on *ECDLs* one can read references [89,90,91,92,93].

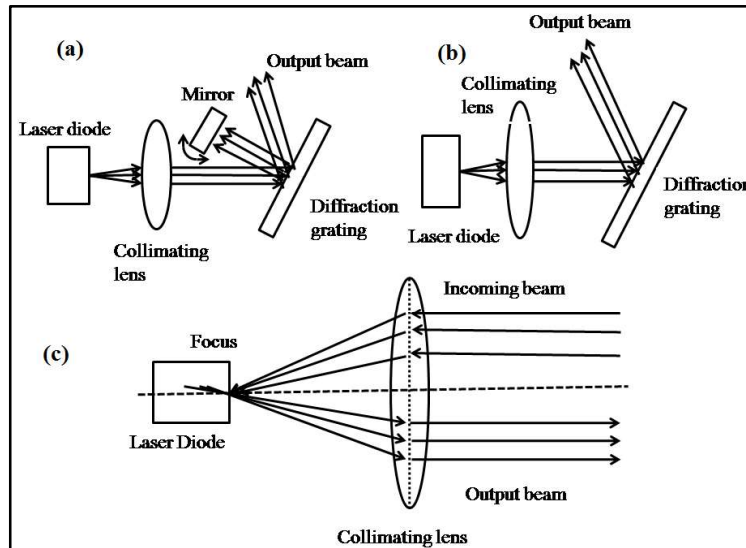


Fig. 3.5 ECDL configurations. (a) *Littman-Metcalf* configuration (b) *Littrow* configuration. (c) Action of a collimating lens. Incoming beam represents feedback and outgoing beam represents the collimated laser output beam.

3.3.1.2. *Ultimate line-width and Noise*

One of the most important properties of laser light is to produce light of high coherence. The finite line-width of the laser light is caused from two primary sources. One of them is the external factor which tends to perturb the cavity. Another factor is the more fundamental mechanism which ensures the ultimate spectral width of the laser arises from the random spontaneous emission in the laser cavity. Since spontaneous emission is incoherent, it leads to a finite width of the laser frequency. This ultimate line-width of an oscillating laser is given by,

$$\delta\nu_{SP} = \frac{2\pi(\Delta\nu_p)^2 h\nu_0}{P_{out}} \quad 3.3$$

This is known as Schawlow-Townes formula [94]. This comes around $\sim 1\text{MHz}$ for $P_{out} = 2\text{mW}$, $\lambda \sim 780\text{nm}$ and $\Delta\nu_p \sim 40\text{GHz}$. As P_{out} increases, stimulated emission dominates over spontaneous emission and ultimate line-width also decreases.

Though equation (3.3) represents the fundamental line-width and matches well for some lasers, significantly higher values are seen for diode lasers. It was later discovered by Charles Henry [95] that the increased line-width results from coupling between intensity and phase noise and introduced an enhancement factor α , known as *Henry factor* to incorporate the effect into the line-width. The final fundamental line-width is written as,

$$\delta\nu_{SP} = \frac{2\pi(\Delta\nu_p)^2 h\nu_0}{P_{out}} * (1 + \alpha^2) \quad 3.4$$

Although it is possible to calculate α for certain semiconductors but it is not an easy task. Typical values of α range from 2 to 6.

Because of the various noise sources in the laboratory and imperfections in the construction of diode lasers, the line-width of the lasers are much higher than the fundamental line-width predicted by equation (3.4). The wavelength of diode laser is mainly affected by temperature and current. Change of temperature can physically alter the cavity length. Temperature also has some effect on threshold current. These variations in the temperature and current depend upon the source. Mechanical disturbances also affect the optical feedback and give rise to additional noise. Some of the noises are termed as fundamental noises. Shot noise, Johnson noise etc fall into this category. This is also known as the quantum noise and is responsible for the fundamental line-width. The spectral distribution of this noise is white. Other sources of noise include environmental noise. They cause mode-hopping in lasers. Power line ripple, mechanical vibrations, air flow etc are few

to name. Usually small noises get amplified through optical feedback. Frequency response of these kind of noise sources is f^{-2} . For these reason they are also named as random walk. Majority of these type of noises are low frequency ($<1 \text{ KHz}$). To control laser output sometimes noises are also added to it intentionally. One very common practice is to dither laser output directly by modulating the laser signal. Therefore these types of noises can also be regarded as artificial noise. They follow f^{-1} power law and also known as flicker noise or pink noise. In depth treatment of noises in semiconductor diode laser can be found in [96].

3.3.2 Basics of frequency stabilization

The free running diode lasers have a frequency stability of several MHz over few seconds. This kind of stability is not suitable for many spectroscopic situations. Additional measures must be taken to achieve the stability required for the particular experiment. Frequency stabilized lasers find its application in the field of high resolution laser spectroscopy [97,98,99,100], quantum optics [101,102], optical frequency standards [103,104,105] etc. Different stabilization techniques have been developed to perform different tasks particularly suiting the requirement. The frequency of any laser is determined within a bandwidth set by the optical resonator. Different types of lasers have different noise characteristics. In most cases the noise can be controlled by electronic servo system. In the following sections basic principles of frequency stabilization are discussed. Different laser types and specific requirements of these lasers have led to the development of a variety of stabilization techniques. Broadly these techniques can be classified into *active* and *passive* stabilization technique.

3.3.2.1. Active stabilization

Active stabilization utilizes electronic feedback which can convert fluctuations of some parameters into an electronic signal. The feedback signal is used to correct fluctuation in the

laser parameter. The efficiency of the stabilization depends upon factors such as detector noise, bandwidth of the control element, design of the feedback system and stability of the reference signal.

3.3.2.2. *Passive stabilization*

Passive stabilization does not include any kind of electronics and based purely on optical effects. For example, laser frequency can be stabilized via optical feedback from a stable reference cavity. In such cases the whole system works as a composite cavity. Such passive stabilization techniques have been used in [106,107,108].

In *active frequency stabilization* schemes, laser frequency is controlled with an electronic servo loop to a reference frequency. The reference may be a *Fabry-Perot* signal, a suitable atomic or molecular transition etc. Locking on *Fabry-Perot (FP)* signal has the advantage of higher signal to noise ratio but the length of the FP cavity can change over time depending on temperature and atmospheric pressure. This shifts the ‘lock point’ itself. Atomic or molecular absorption lines are free from such disturbances and thus are more preferable.

The servo loop acts as a feedback system which continually monitors the laser output and adjusts the wavelength accordingly. Basically the servo loop converts the frequency deviation $\delta\nu = \nu - \nu_r$ between the laser frequency ν and the reference frequency ν_r into an error signal which is proportional to $\delta\nu$. This error signal is amplified by the servo loop and is used to control the laser. In the perfectly ‘locked’ state the error signal vanishes. Fig. 3.6(a) shows the basic scheme of laser frequency stabilization

The error signal does not necessarily have to be a linear function of frequency deviation from the reference value. Practically any monotonous function with a zero crossing at the resonance will serve well as error signal. Fig. 3.6(b) shows several such functions. The change in sign of the error signal at the resonance enables the servo system to determine

whether the laser have higher or lower frequency compared to the reference value and counteract accordingly. Higher slope near the zero crossing means higher sensitivity of the feedback system towards frequency deviation. Slope increases with decreasing line-width of absorption. Following subsections introduces two basic methods of generating error signal.

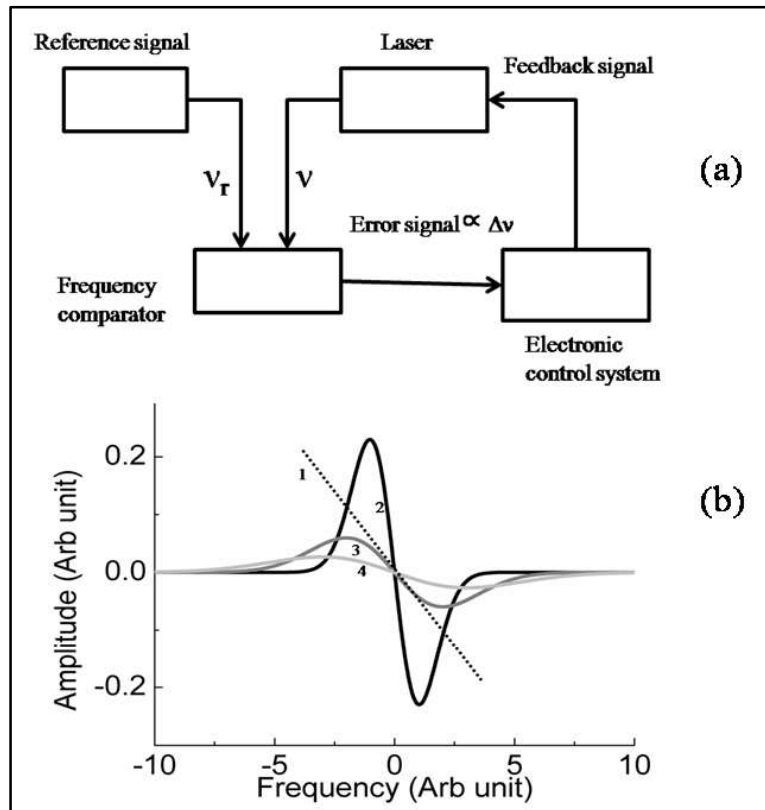


Fig. 3.6 Laser stabilization scheme and error signal (a) laser frequency stabilization scheme. (b) Error signal with different slopes. Highest slope is represented by the signal indicated with 2. Dashed signal (represented by 1) represents a simple linear error signal.

3.3.2.3. Side of the fringe stabilization

This is a very simple and easy to use locking scheme. The reference point is chosen at one side of resonance line between the maximum and minimum values of the resonance line. The scheme is represented schematically in Fig. 3.7. In this side-lock scheme power of the laser to

be stabilized is divided into two equal parts. One part is sent through a dispersive system which produces a signal similar to an atomic absorption line and is captured in a photo detector. Let's say the output of this detector is A . The other part is passed through a variable attenuator and is detected by another detector. The output of this detector may be termed as B which serves as the reference signal. Subtracting B from A (in a differential amplifier) we get the desired error signal (Fig. 3.7). The reference signal may be adjusted by varying the attenuation. In this case we get two lock points for each resonance lines. Near the lock points the error signal has monotonous behaviour and also changes sign at the lock points. The speed of the servo control is ultimately limited by the response times of the reference system.

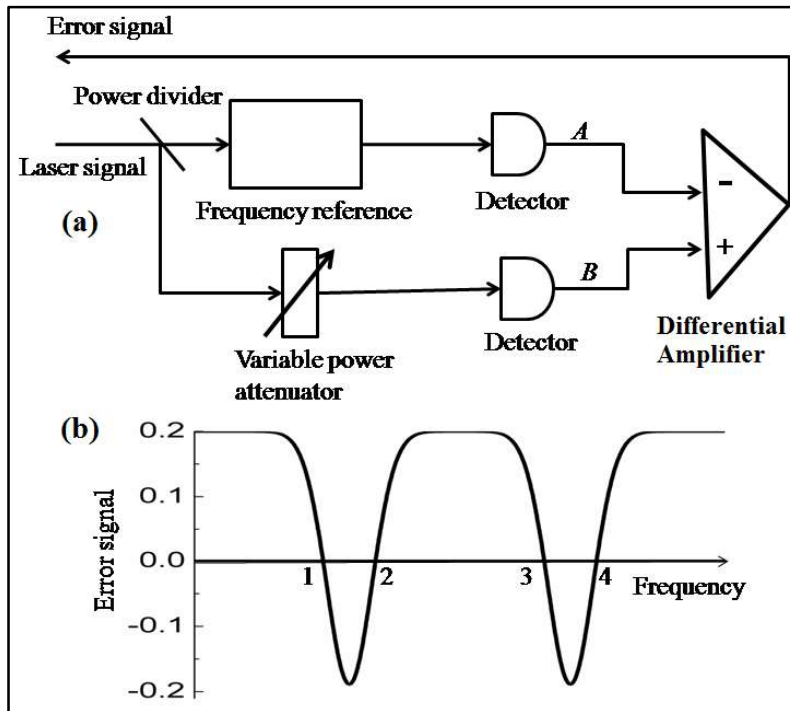


Fig. 3.7 Side of the fringe lock (a) Schematic scheme of a side of the fringe lock (b) Error signal obtained from $A-B$. Four lock points are shown with 1, 2, 3, 4 numbering.

This technique is very easy to implement but offers limited tuning range. Tuning is done by changing the offset B . It is also mostly independent of laser power fluctuations. The

disadvantage is that it can't be locked at the resonance centre. Therefore stability of the lock point is an issue. Lock immunity to power fluctuations is ensured only when both the detectors show same variation in the signal (not often the case when using *Fabry-Perot* cavity as the reference system). Capture range is very asymmetric and can shift the frequency from the lock point for higher positive frequency perturbation.

3.3.2.4. *Top of the fringe stabilization*

In contrast to earlier case, top of the fringe stabilization uses modulation techniques and phase sensitive detection method. Many shortcomings of the side locking scheme can be avoided by locking the laser to the centre of the symmetric resonance lines. This can be achieved by modulating the frequency difference $(\nu - \nu_r)$, which can be done either by modulating the laser or the reference frequency. For non-tunable reference frequency, the laser itself has to be modulated. This can be achieved either by directly modulating laser frequency or by applying some external modulator. Generally square wave or a sine-wave are used to modulate the laser frequency (ν) periodically between $(\nu + \delta\nu)$ and $(\nu - \delta\nu)$ within a half time period $\tau/2$ of the modulation.

Power transmitted through an absorber or the reference system is a function of the laser frequency near the resonance line. If the transmitted power is measured using a detector and integrated for both half periods of modulation, the difference of the two integrated signal $\Delta I(\nu) = I(\nu + \delta\nu) - I(\nu - \delta\nu)$ shows behaviour of an error signal as a function of frequency deviation $(\nu - \nu_r)$ as shown in Fig. 3.8. The error signal is positive when the laser frequency is lower than the reference center frequency and vice versa. Amplitude modulated signal is detected as a function of a frequency modulation either of the laser itself or of the resonance reference. Square wave modulation is avoided because of high frequency components. Generally a simple sine wave is used to create the amplitude modulation. The

integrated difference signal is detected using lock-in-amplifier and phase sensitive detection techniques [109].

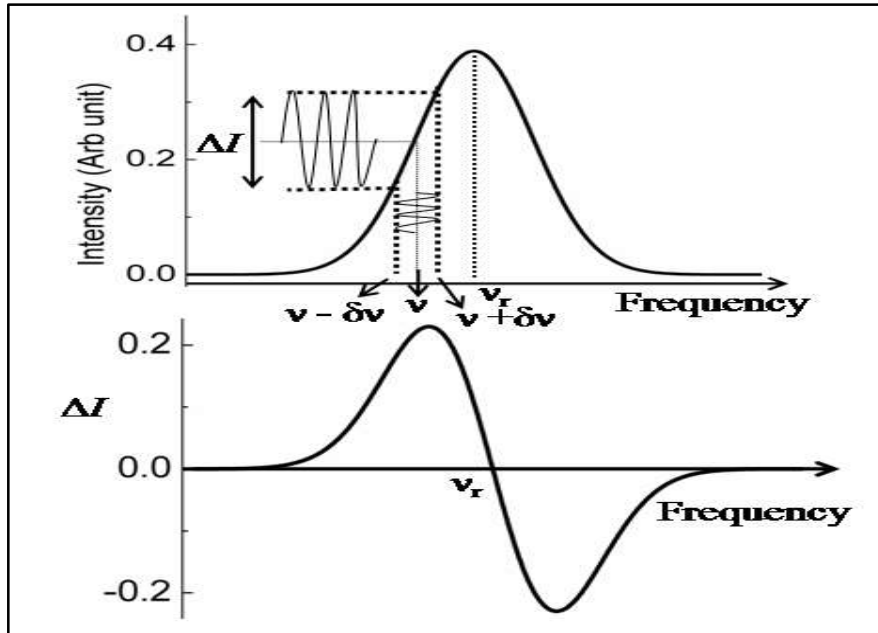


Fig. 3.8 Frequency modulation of laser beam. The frequency modulation is converted into amplitude modulation by the line shape of the absorption signal. The integrated difference signal shows error signal type behaviour.

3.3.3 Locking schemes in vapour cell spectroscopy

In the studies carried out for the present thesis, we are mainly concerned with pump-probe laser spectroscopy while studying the ladder system in rubidium vapour cell and its different aspects. Practically there are numerous methods available for laser locking in vapour cell spectroscopy [110,111,112,113,114,115,116,117,118,119]. In this subsection we will only briefly review a few of them. It may be mentioned that ultimately conventional wavelength modulation spectroscopy was chosen by us as the tool for laser locking in the experiments discussed in the later chapters. Still it is worthwhile to review the available options for a pump probe spectroscopy set up.

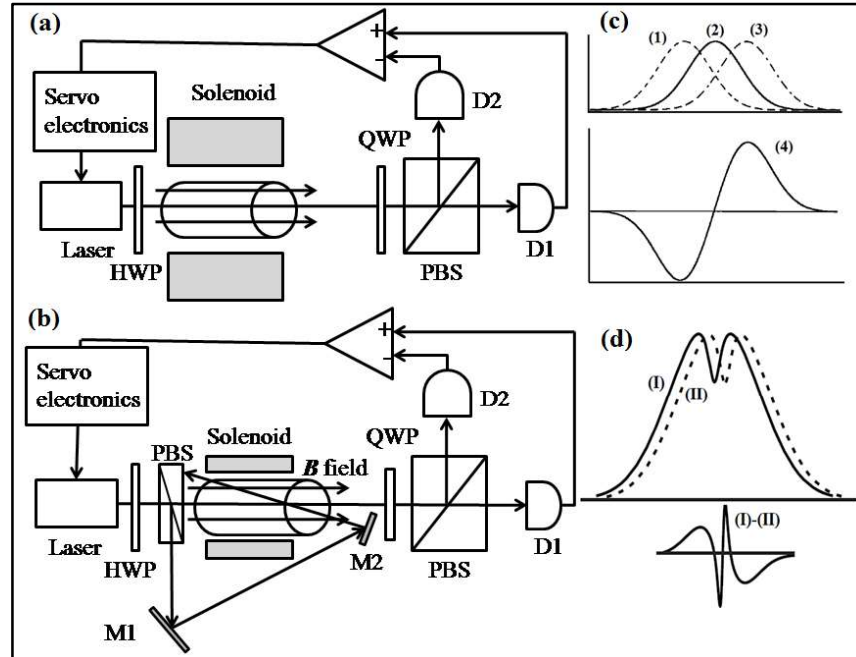


Fig. 3.9 Schematic of DAVLL set up (a) DAVLL for a Doppler broadened atomic transition (b) DAVLL for a Doppler free atomic transition. (c) Absorption spectrum and generated error signal in case of Doppler broadened atomic transition. Error signal is generated from the subtraction of two absorption spectrums corresponding to the absorption of σ^+ and σ^- part of the plane polarized laser beam (d) Similar absorption spectrum and the corresponding error signal in case of Doppler free atomic transition.

3.3.3.1. Dichroic-atomic vapour laser lock

Dichroic atomic vapour laser lock (DAVLL) is a robust method to lock diode lasers on atomic transition. The technique employs a weak magnetic field to Zeeman split the degenerate magnetic sublevels. The technique can be applied for both Doppler broadened [110] and Doppler free [111,114] atomic transition. For a Doppler broadened atomic transition the capture range of the lock is pretty large whereas for a Doppler free transition, the precision of the lock point can be high at the cost of a smaller capture range. Fig. 3.9(a) and Fig. 3.9(b) describe the setup used for Doppler broadened atomic transition and Doppler

free atomic transition respectively while Fig. 3.9(c) Fig. 3.9(d) describes the absorption spectrum and the generated error signal for these two cases.

In both cases, a small DC magnetic field is applied to lift the magnetic sublevel degeneracy. The plane polarized probe beam can be thought of as a combination of σ^+ and σ^- circular polarized beam. Therefore the single atomic resonance is now split into two because of the different selection rules regarding σ^+ and σ^- polarization. The separation between the resonances can be changed by varying the magnetic field strength. As the probe beam passes through the absorbing medium, the σ^+ and σ^- components can be separated using beam splitter and can be detected in two different detectors. Difference between the detected signals reveals the error signal. The Doppler free situation uses only one extra pump beam to get a SAS signal. This enhances the precision of the lock point but diminishes the capture range.

3.3.3.2. Laser lock based on polarization spectroscopy

As discussed in section 3.2, the birefringence induced by the σ^+ circularly polarized pump beam allows the σ^+ component of the probe beam to be absorbed more by the ground state populations compared to the σ^- component. This changes the polarization of probe beam from elliptical at near resonance to plane polarization at resonance. Therefore a dispersion shaped signal can be detected at the balanced detector. The scheme is shown in Fig. 3.3. The superiority of this error signal over others is that it is free of modulation electronics and associated complexity. It is also free of noise due to laser intensity fluctuation. Though the technique is related to saturated absorption technique, it offers much better signal to noise (S/N) ratio and it led to the development of many similar techniques [112,117,118,120,121] based on polarization spectroscopy.

Though the above two techniques are very popular for stabilizing lasers in situations like magneto-optical trap (MOT), another technique called Frequency Modulation Spectroscopy (FMS) is often used in laser locking. FMS uses laser modulation to produce the desired error signal. This is the locking technique which we have used for locking our lasers. Following sub-sections outline the technique.

3.3.3.3. *Frequency modulation spectroscopy*

Frequency modulation spectroscopy in connection with tunable diode lasers is a powerful technique to achieve high spectroscopic sensitivity. This technique falls into two categories depending on the modulation frequency and width of the spectral feature of interest. For modulation frequencies higher than the width of the spectral line shape, it is called frequency modulation spectroscopy and for frequencies lower than the width of the spectral feature, it is called wavelength modulation spectroscopy (WMS) [122]. Among these, WMS is easier to implement. On the other hand we can measure the absorption or dispersion line shape directly from FMS. Theoretically it can be shown that FMS is only limited by shot noise [123]. The use of sidebands in spectroscopy was already demonstrated much earlier for microwave region [124] and NMR technologies [125]. For optical heterodyne spectroscopy, the method was pioneered by Bjorklund [126]. The same was also independently suggested by Drever for high finesse optical cavity [127].

3.3.3.4. *FMS theory*

The spectrum of modulated laser beam can be expressed as a sum of the carrier frequency ω_c and harmonics of modulation frequency ω_m with their amplitudes weighted by *Bessel function* [126]. For modulation index much smaller than unity, the spectrum can be approximated with contributions from only three frequencies, the carrier frequency (ω_c) and

two sidebands at $\pm\omega_m$. Therefore in such case the field amplitude after passing through a vapour cell of length L can be written as,

$$E(t) = \frac{E_0}{2} \{ T_0 J_0(m) e^{i\omega_c t} + T_1 J_1(m) e^{i(\omega_c + \omega_m)t} + T_{-1} J_{-1}(m) e^{i(\omega_c - \omega_m)t} \} \quad 3.5$$

where,

$$T_n = \text{Exp} \left[-L \left(\frac{\alpha_n}{2} + i \eta_n (\omega_c + n \omega_m) / c \right) \right] = \text{Exp} [-\beta_n - i \xi_n] \quad 3.6$$

and $n = 0, -1, 1$, $m =$ modulation index. α_n and η_n are the absorption and refractive index of each frequency component. The β_n describes amplitude attenuation of the beam and ξ_n describes phase shift experienced by each frequency component. For small differences in the attenuation and phase shift among the frequency components or if $|\beta_0 - \beta_1|, |\beta_0 - \beta_{-1}|, |\xi_0 - \xi_1|, |\xi_0 - \xi_{-1}|$ are all small compared to 1, the measured intensity $I_M = \frac{1}{2} \epsilon_0 c |E(t)|^2$, can be written as,

$$I(t) = \frac{1}{2} \epsilon_0 c E_0^2 e^{-2\beta_0} [1 + (\beta_{-1} - \beta_1) J_1(\beta) \cos \omega_m t + (\xi_{-1} + \xi_1 - 2\xi_0) J_1(\beta) \sin \omega_m t] \quad 3.7$$

From equation (3.7) it is evident that the in-phase component ($\cos \omega_m t$) is proportional to the difference in loss experienced by the sidebands. Similarly the quadrature component ($\sin \omega_m t$) is proportional to the difference in phase shift experience by the carrier and the average phase shift experienced by the sidebands. If we further assume that the modulation frequency ω_m is small compared to the width of the spectral feature of interest, the in-phase component becomes proportional to the derivative of the absorption whereas the quadrature component becomes proportional to the second derivative of the dispersion. Typically these conditions are met in conventional wavelength modulation spectroscopy (WMS) which is discussed in the next sub-section. Most of the works presented in this thesis make use of

WMS. Fig. 3.8 shows an absorption line and its corresponding derivative signal which is also proportional to the in-phase component.

3.3.3.5. WMS theory

The result obtained for *WMS* in the previous section can also be obtained considering the heuristic argument presented in [122]. The instantaneous laser frequency (ω_i) is modulated at a modulation frequency ω_m ($\omega_m \ll \Delta\omega$) and can be written as,

$$\omega_j = \omega_c + \Delta m \cos \omega_m t \quad 3.8$$

where $\Delta\omega$ = width of the spectral feature of interest, Δm = maximum deviation from carrier frequency ω_c . The dispersion effect can be neglected as maximum deviation from carrier is considered to be very small. Therefore the light intensity transmitted through the sample can be expressed as,

$$I_t = I_0 e^{-\alpha(\omega)} \quad 3.9$$

Considering the absorption to be weak, we can write $I_t(\omega) = I_0[1 - \alpha(\omega)]$. Expanding the attenuation coefficient $\alpha(\omega)$ into Taylor series around the central carrier frequency ω_c , we can write the transmitted intensity as,

$$I_t(\omega_j) = I_0 \left[1 - \alpha(\omega_c) - \left. \frac{d\alpha}{d\omega} \right|_{\omega_c} \Delta m \cos \omega_m t + \text{higher order terms} \right] \quad 3.10$$

The higher order terms can be neglected for small deviation ($\Delta m \ll \Delta\omega$). Therefore the *WMS* signal detected with a lock-in-amplifier tuned to the modulation frequency ω_m is proportional to the first derivative of the sample absorption. Such a spectrum is shown in Fig. 3.8.

3.3.3.6. Atomic frequency offset locking

In spectroscopic situation when the difference in frequencies between two lasers can be controlled to a fixed value, that property can be used to design a laser locking scheme. *Atomic*

frequency offset locking (AFOL) scheme is based upon this principle. Suppose one of the lasers is locked to some reference signal ω_0 (atomic or molecular transition, FPI signal etc). If any feedback system can compare the frequency of the other laser ω with the frequency of the reference laser (ω_0) and adjusts the frequency of the other laser such that ($\omega_{offset} = \omega - \omega_0$) is held constant at all times, we can say that the other laser is locked to the frequency ($\omega_{offset} + \omega_0$). A pump-probe spectroscopic system, exhibiting EIT phenomenon, is an ideal candidate for AFOL. In such circumstances, the pump laser is locked to some reference signal whereas the probe laser is locked to the EIT signal. As a result the probe laser remains locked to the EIT signal till the pump laser remains locked to the reference signal.

3.3.4 Laser locking at VECC laser hut

Laser locking at VECC is performed using the integrated system *LaseLock 3.0 (TEM Messtechnik)*. This system is a compact user friendly device and consists of an input amplifier, sine wave generator, lock-in-amplifier with adjustable phase and low pass filter, PID regulator, scan generator, output amplifier etc. The job of the PID section is to regulate the laser frequency such that it becomes equal to the reference frequency. It can calculate the difference between an input value and a set value. PID consists of three amplifiers. The proportional amplifier (P) generates output which is proportional to error signal. The output of integrating amplifier (I) is the integral of error signal over time and differentiating amplifier (D) is the derivative of the error signal with respect to time. The output of the regulator is the weighted sum of the three amplifier outputs. PID optimization is just the optimization of the different weights of the amplifiers so that the error becomes as small as possible. Sometimes the whole servo loop consisting of the PID regulator, the actuator (laser) and the sensor (reference frequency) forms stable oscillation of the signal which should be avoided. For more practical purposes one can refer to the user manual provided with *LaseLock3.0*.

We have used conventional wavelength modulation spectroscopy to perform laser locking. With the availability of required electronics and modulation techniques, the main task of laser locking is to find out a suitable line shape e.g. narrow absorption line, for laser locking. Once a suitable line shape is available it can be converted into a dispersion shaped error signal using techniques discussed in section 3.3.3.

3.3.5 Analysis of laser locking

For a frequency stabilized laser, stability and noise are the most important parameters to consider. Because of the change in air pressure, acoustics, fluctuations in the laser medium itself or by any other factors, laser frequency fluctuates. In principle laser frequency fluctuates about a mean value which can drift randomly. The variation in laser frequency can be analyzed by measuring the beat frequency ($\nu_b = \nu_1 - \nu_2$) between two identical lasers which are independently stabilized. When the combined power of such lasers is monitored with a photo-detector, the beat frequency manifests itself as the oscillation in the combined power. These power fluctuations can be converted into photocurrent. The frequency and time domain analysis of the resultant signal reveals the higher frequency fluctuation as well as the slower drift.

3.3.5.1. Spectral density of noise

Fluctuations at frequency f can be detected by a frequency discriminator which converts the frequency fluctuation into a proportional voltage. Assuming the noise components are uncorrelated, the fluctuation is described by $\langle \delta\nu^2 \rangle$, where $\delta\nu$ is the frequency fluctuation at f . This is equivalent to the spectral noise power at frequency f . The power spectral density then can be defined as,

$$S_f = \langle \delta\nu^2 \rangle / BW \quad 3.11$$

where, BW = bandwidth of the noise fluctuation. Similarly the relative power spectral density can be expressed as,

$$S_y = \langle (\delta\nu/\nu)^2 \rangle / BW \quad 3.12$$

Frequency noise of any oscillator can be written in terms of a power series of different Fourier frequency with good approximation [109],

$$S_y = \sum_{\beta=-2}^2 C_\beta f^\beta \quad 3.13$$

Different types of noise have different β values. For random frequency walk $\beta = -2$, flicker noise has $\beta = -1$ and white noise is represented by $\beta = 0$. Usually different noise components show up at different Fourier frequency. Hence the identification of different noise components allows us to eliminate the cause of the noise. Apart from the above mentioned noises environmental sources e.g. mechanical, room temp, optical feedback etc, can also produce some noise.

3.3.5.2. Allan variation

Slow frequency variation can be measured conveniently by measuring the frequency within a time interval. Such measurements are generally advantageous in the time scales of seconds or hours. The relative frequency instability in the time domain is described by *Allan Variance* [128,129]. Considering a statistical process under the presence of correlation, *Allan Variance* best describes the fluctuation as a N -sample variance which is defined as,

$$\sigma_y(N, T, \tau) = \frac{1}{\nu} \left[\frac{1}{2(N-1)} \sum_{n=1}^{N-1} (\nu_{n+1} - \nu_n)^2 \right]^{1/2} \quad 3.14$$

Allan Variance describes the root mean square of difference between two consecutive frequency measurements. The frequency values in equation (3.14) are given by,

$$v_{n+1} = \frac{1}{\tau} \int_{i=n\tau}^{(n+1)\tau} v_i(t) dt \quad 3.15$$

where $T =$ time between two consecutive measurements, $\tau =$ measuring time of a single sample and N is the total number of measurements. As the direct measurement of optical frequency is difficult, it is down converted in the radio frequency range by generating beat signal with respect to another laser radiation. *Allan Variance* can also be calculated from *relative noise power spectral density* [130,131] using the following equation,

$$\sigma_y^2(\tau) = \int_0^{\infty} S_y(f) \frac{(\sin \pi f \tau)^4}{(\pi f \tau)^2} df \quad 3.16$$

Values of two sample *Allan Variance* for different noise types have simple form in terms of τ . For example, in case of random frequency $\sigma_y^2(2, \tau) \propto \tau$ and for other noise type generally it goes down with τ . In the Fourier frequency domain, phase and frequency can be characterized by respective one sided spectral densities, $S_\phi(f)$ and $S_{\Delta\nu}(f)$ and the spectral density $S_y(f) = \frac{1}{v_0^2} S_{\Delta\nu}(f)$. Therefore equation (3.16) can be written in terms of one sided frequency spectral density as a two sample and zero dead time variance as,

$$\sigma_y^2(2, \tau) = \frac{2}{v_0^2} \int_0^{\infty} S_{\Delta\nu}(f) \frac{(\sin \pi f \tau)^4}{(\pi f \tau)^2} df \quad 3.17$$

3.4 Collinear laser spectroscopy (CLS) on accelerated stable ion beam

The VEC-RIB facility [132,133,134,135,136,137,138,139,140,141] which is being built around the K130 cyclotron, will produce ions in the energy range of 1 keV/u to 1 MeV/u. At low energy of about 1 keV/u, a program to study hfs and isotopic shift of unstable and stable nuclei using CLS has been taken. For this program, a CLS setup is being developed around

an existing ISOL facility. The first phase of this development forms a part of the thesis and described in detail in Chapter 10.

Collinear (anti-collinear) laser spectroscopy on accelerated ion beam is performed by shining laser beam, co-propagating (counter-propagating) with the accelerated ion/atom beam. The laser beam probes the accelerated ion beam (energy \sim few keV to tens of keV). Mostly, the ion beam is charge converted in a charge exchange cell and the resultant atoms (still in the form of beam) are probed with lasers. The ions or atoms in the beam get excited by the resonant laser and emit fluorescence photons which are then detected with photomultiplier tube perpendicularly to the flight direction. Due to the acceleration of the atoms the longitudinal velocity spread of the beam gets compressed. The velocity compression appears as the effect of acceleration to a well defined energy E while preserving the initial energy spread δE [47]. The longitudinal velocity spread under acceleration is given by,

$$\delta v = \frac{1}{\sqrt{2mE}} \delta E \quad 3.18$$

From equation (3.18) it is obvious that the longitudinal velocity spread reduces as the energy of the beam increases. This effect is known as ‘acceleration cooling’ and it helps in reducing the Doppler width of any optical transition. This is the main advantage of CLS over conventional vapour cell spectroscopy in which the atoms are in random thermal motion. The typical Doppler width of several GHz in vapour cell spectroscopy reduces to a few tens of MHz in the case of CLS, allowing hyperfine transitions to get resolved. Considering a temperature of ~ 1600 K for the surface ion source at VECC-ISOL setup and Rubidium ion beam energy of $8.0 keV$, the reduction factor is ~ 241 .

3.4.1 Doppler tuning

The accelerated ion beam sees a Doppler shifted laser frequency in its rest frame. In conventional CLS setup this fact is utilized for Doppler tuning. The ion velocity is changed by applying additional voltage gradient before the detection unit. At VECC-ISOL CLS setup, laser frequency is scanned instead of the ion velocity. This eliminates the requirement of additional voltage gradient for Doppler tuning at the expense of repeatability of successive frequency scans. The Doppler shifted laser frequency in the rest frame of the atom is given by,

$$\nu_{rest} = \nu_{laser} \frac{(E + mc^2)}{mc^2} \left(1 \pm \sqrt{1 - \left(\frac{mc^2}{E + mc^2} \right)^2} \right) \quad 3.19$$

where ν_{rest} is the laser frequency in the rest frame of the ion or atom, ν_{laser} is the laser frequency in laboratory frame, m is the rest mass of the ion and $E = eV$ is its kinetic energy, where V is the extraction potential and e is the electronic charge. The '+' sign is for anti-collinear geometry of the laser-ion interaction and '-' sign is for collinear geometry.

3.4.2 New developments in collinear laser spectroscopy

Various nuclear species have already been studied by collinear laser spectroscopy (CLS) since its inception. Many modifications have been made over the traditional approach of CLS over the years to improve the signal to noise ratio, thereby allowing spectroscopic studies on atom beams of very low intensity. Also, the availability of different types of lasers has presented the opportunity to study wide range of atomic species over the nuclear chart. A brief overview of different techniques used to improve the capabilities of the traditional CLS setup is discussed in the following sections.

3.4.2.1. Photon ion coincidence detection

This kind of scheme is used in situations where yield of the radioactive species is low. The stray laser light produces a good amount of background in conventional CLS setup which limits its sensitivity. This situation is overcome with a coincidence detection setup where only those photon events are counted that produce a particle signal at the end detector. The photomultiplier tube is gated with respect to particle signal. The sensitivity of the setup is limited by the spectrometers ability to determine the position origin of the emitted photon and also by the isobaric contamination which can trigger false coincidence.

3.4.2.2. Bunched beam spectroscopy

Gas filled quadrupole ion traps (known as RFQ cooler and buncher) have become an effective tool to cool and bunch ionic ensembles on-line and is already in use with the CLS setup. With this setup, random background can be reduced by $\sim 10^4$ by gating the photon detectors with respect to the bunched beam. The background reduction allows laser spectroscopic studies on short-lived nuclei (exotic nuclei) produced with intensity 1000 ions/s or even less.

3.4.2.3. Detection with optical pumping

Optical pumping is used to resonantly move population from one atomic state to another. This fact is utilized to induce nuclear orientation in radioactive nuclei and subsequent detection of resonant pumping process by measuring the anisotropy in β decay using nuclear spectroscopy. Optical pumping is also used to selectively enhance population of the states which are better suited for CLS. It can also be used in connection with ionization and related spectroscopic techniques. Optical pumping can be used to successfully enhance the detection efficiency of the traditional collinear laser spectroscopy. A detailed discussion on recent techniques can be found in [44].

Part I. Study of ladder system in Rubidium

Chapter 4

Study of optical switching in Rubidium Ladder system

4.1 Introduction

Present chapter discusses the experimental investigation of optical switching through pump laser induced atomic coherence in a Doppler broadened Rubidium (Rb) atomic system. We have chosen the $5S_{1/2} \rightarrow 5P_{3/2} \rightarrow 5D_{5/2}$ cascade or ladder level coupling scheme of ^{87}Rb atom to investigate the optical switching. Pump-probe spectroscopy, using a higher intensity laser as the pump and a lower (below saturation) intensity laser as the probe, on this ladder coupling scheme reveals a combination of double resonance optical pumping (DROP) and electromagnetically induced transparency (EIT) signals on the Doppler broadened one photon absorption background. The media under DROP condition behaves differently than the media under EIT condition in the modulation frequency range of 10 Hz to 10 MHz of the applied intensity modulation. The media is found to be more agile towards faster optical switching under EIT condition than under DROP condition. This fact may be attributed to the different origins of the DROP and EIT signals. Following sections explain the conducted experiment and its outcome in detail.

4.2 Motivation

Different aspects of atomic coherence in alkali vapour media can be studied with the help of pump probe spectroscopy. The phenomena such as, coherence population trapping (CPT), electromagnetically induced absorption (EIA), EIT [1,2,3,142] etc. are the outcome of the existing atomic coherence in the medium. Slowing down of light [4], ultrasensitive magnetometry [5], miniaturized atomic clock [6], frequency offset locking [7,8,9], optical switching [10,11,12,13,14], etc. are the few examples of the several technical applications

which are based on atomic coherence. This makes the field of coherent photon atom interaction interesting to the whole research community.

Coherent pump probe spectroscopy is performed with the use of two or more lasers connecting the atomic hyperfine levels. The lasers are arranged according to the geometry of the level coupling scheme (V, Λ, Ξ, N etc). The otherwise independent lasers become correlated once the atomic coherence is developed in the medium. This aspect of coherence is well explored in atomic frequency offset locking for Λ system [7,8,9] where the applied external frequency modulation on one laser is transferred to the other through coherence assisted modulation transfer. The same coherence assisted modulation transfer was used by Moon et al [15] for frequency stabilization in ladder (Ξ) system. Apart from the transfer of frequency modulation, atomic coherence can also be used to transfer intensity modulation from one laser to the other and this has already been used in coherence assisted optical switching. Demonstration of optical switching in Ξ system has already been done by [13,14]. However, the spectroscopy of ^{87}Rb , $5S_{1/2} \rightarrow 5P_{3/2} \rightarrow 5D_{5/2}$ ladder system exhibits hyperfine structure of the excited state in terms of DROP signal [18,19,20,21] along with the EIT structure. The DROP is a result of population transfer to the uncoupled $F = 1$ ground state due to two-photon excitation of atoms from $F = 2$ level whereas EIT results from quantum destructive interference of excitation pathways. Though both DROP and EIT originate from the same two-photon coherence, there is a subtle difference between them. Therefore it was necessary to study the coherence assisted transfer of intensity modulation in the medium under DROP and EIT conditions and to investigate for any difference in their behaviour.

The present work compares the coherence assisted optical switching phenomenon under DROP and EIT condition. The coupling laser intensity was modulated for this purpose. It is found that under dominant EIT condition, the medium shows prominent switching over a wide frequency range (10 Hz to more than 1 MHz). However the same medium under DROP

condition is found to favour switching only up to 100 *KHz*. Therefore one can obtain a variable switching bandwidth just by manipulating coupling laser parameters in Ξ configuration.

4.3 Intensity switching under EIT

In the steady state picture the susceptibility of an inhomogeneously broadened ladder system is given by [143],

$$\chi(v)dv = \frac{id_{21}^2/(\hbar\epsilon_0)}{\gamma_{21}-i\Delta_p - i\frac{\omega_p}{c}v + \frac{\Omega_c^2}{4} \left[\frac{1}{\gamma_{31}-i(\Delta_p+\Delta_c) - i(\omega_p-\omega_c)\frac{v}{c}} \right]} N(v)dv \quad 4.1$$

where $\Delta_p = \omega_p - \omega_{21}$ ($\Delta_c = \omega_c - \omega_{32}$) is the detuning of the probe (pump) laser beam and Ω_c is the Rabi frequency of the pump laser beam. $\gamma_{ij} \approx (\Gamma_i + \Gamma_j)/2$ is the coherence decay rate for $|i\rangle \rightarrow |j\rangle$ transition. d_{21} is the dipole matrix element between state $|2\rangle$ and $|1\rangle$. For a vapour cell containing Rubidium atom at thermal equilibrium, $N(v)$ is the Maxwell-Boltzmann velocity distribution. Weak probe field approximation is considered while deriving equation (4.1) and also the contribution from upper levels is neglected due to negligible population in the upper states. The imaginary part of the susceptibility (χ) is proportional to the probe laser absorption coefficient. In this case ω_p and ω_c are very close to each other and therefore the Doppler broadening of the two-photon transition is neglected. For observation of EIT, $\Omega_c^2/4\gamma_{21}\gamma_{31} \gg 1$ needs to be satisfied [143] along with the two-photon resonance condition $\Delta_p + \Delta_c \approx 0$.

The transient response of a medium under EIT is already investigated by Li et al [144] under the condition $\Omega_c \gg \gamma_{21} \gg \gamma_{31}$. It is also possible to demonstrate the effect of intensity modulation in a simplistic manner by substituting $\Omega_c^2 \rightarrow \Omega_0^2(C_1 + C_2 \cos \omega_m t)$ into the equation (4.1). Ω_0 is the nominal value of the pump Rabi frequency and C_1, C_2 are so adjusted that the bare minimum value of $\Omega_c^2 \sim 4\gamma_{21}\gamma_{31}$ is maintained. To set transparency into

the system, only this bare minimum value of pump field is required according to the AC stark shift. The result of the simulation is shown in Fig. 4.7 where Imaginary part of the susceptibility (χ) which also represents the absorption by the medium is plotted as a function of the probe detuning.

4.4 Experimental scheme, results and discussion

The level scheme for the present experiment is shown in Fig. 4.1. The probe laser ($\lambda_p \sim 780 \text{ nm}$) Rabi frequency was $\Omega_p \sim 2\pi \times 9 \text{ MHz}$ and it was resonant with $5S_{1/2}(F = 2) \rightarrow 5P_{3/2}(F' = 3, 2, 1)$ transition. The pump laser addresses the $5P_{3/2}(F') \rightarrow 5D_{5/2}(F'')$ transition and has a Rabi frequency $\Omega_c \sim 2\pi \times 70 \text{ MHz}$. In this way the $5S_{1/2} \rightarrow 5P_{3/2} \rightarrow 5D_{5/2}$ transition forms ladder level coupling. The states are identified with the quantum states as, $5S_{1/2} \equiv |1\rangle, 5P_{3/2} \equiv |2\rangle, 5D_{5/2} \equiv |3\rangle$ for easier nomenclature. Corresponding decay rates for the states are, $\Gamma_2 = 2\pi \times 6.066 \text{ MHz}$ and $\Gamma_3 = 2\pi \times 0.97 \text{ MHz}$. The coherent dephasing rate between $|i\rangle$ and $|j\rangle$ states is $\gamma_{ij} \approx (\Gamma_i + \Gamma_j)/2$. $\gamma_{g,1 \rightarrow 2}$ is the coherent dephasing rate between ground hyperfine states $F = 1$ and $F = 2$ and is governed by the transit time broadening.

The experimental arrangement is shown in Fig. 4.2. Linearly polarized pump and probe lasers are depicted with ECDL1 and ECDL2 respectively. A small part of the probe beam was used for SAS set up to reveal the $^{87}\text{Rb } 5S_{1/2}(F = 2) \rightarrow 5P_{3/2}(F' = 3, 2, 1)$ hyperfine transitions and the same was used for frequency calibration. Typical line-width for the $F = 2 \rightarrow F' = 3$ transition is $\sim 12 \text{ MHz}$. The pump and probe lasers were used in counter propagating configuration as this helps to reduce first order Doppler broadening as $\omega_p \approx \omega_c$. The dipole matrix elements were estimated from [145]. Pump laser frequency was monitored with a wavemeter and a Fabry-Perot Interferometer (FPI) cavity. For intensity switching of the pump (coupling) laser, an Electro-optic Amplitude Modulator (Thorlabs EO-AM-NR-C1,

broadband) was placed in the beam path of pump laser. The experiment was conducted in three parts as described in the following sub-sections.

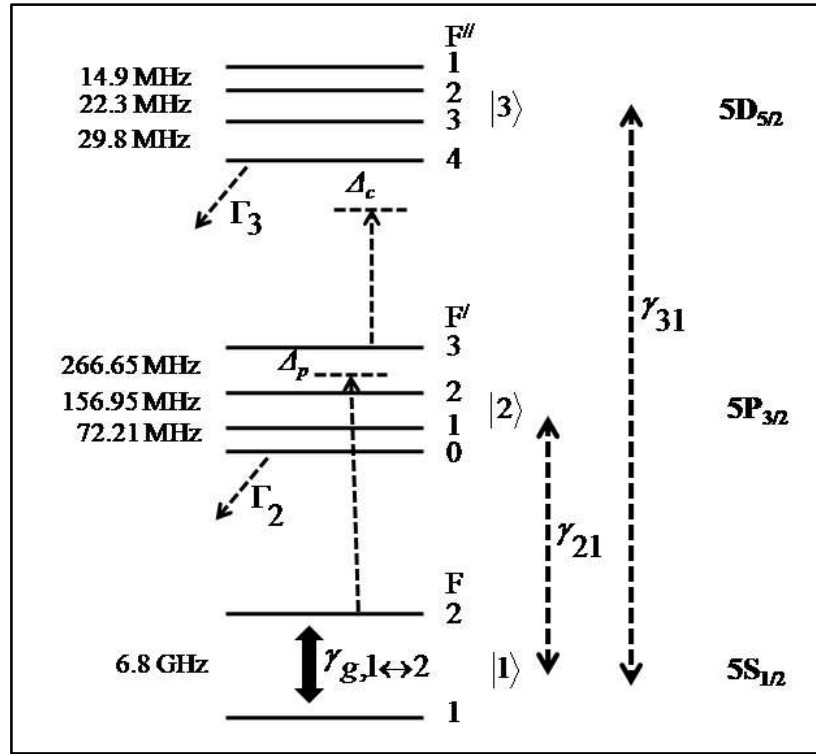


Fig. 4.1 Ladder level scheme for optical switching in ^{87}Rb . Δ_p and Δ_c are the probe and pump laser detuning. Dephasing between ground state hyperfine levels is shown as $\gamma_{g,1\rightarrow 2}$. Spontaneous decay rates are $\Gamma_2 = 2\pi \times 6.066 \text{ MHz}$ and $\Gamma_3 = 2\pi \times 0.97 \text{ MHz}$. More details can be found in the text.

4.4.1 First part of the experiment

In the first part of the experiment, probe absorption spectra were recorded. For this purpose, the probe laser was directly locked on the sides of the (a) $5S_{1/2}(F=2) \rightarrow 5P_{3/2}(F'=3)$ transition (\mathbf{v}_a), (b) $5S_{1/2}(F=2) \rightarrow 5P_{3/2}(F'=3,1)$ cross-over transition (\mathbf{v}_b) and (c) $5S_{1/2}(F=2) \rightarrow 5P_{3/2}(F'=2,1)$ cross-over transition (\mathbf{v}_c). We have avoided FMS for the locking purpose to avoid any modulation induced fluctuation of the laser frequency. The pump laser was scanned over the $5P_{3/2}(F') \rightarrow 5D_{5/2}(F'')$ transition

manifold. Similarly the probe absorption spectra were also recorded as function of probe frequency scan while the pump laser was free running at different frequency settings. Since the data recordings were done within ~ 1 s time scale, the spectra are only limited by the short term laser line-width ($\Delta\nu_{laser} \sim 1$ MHz).

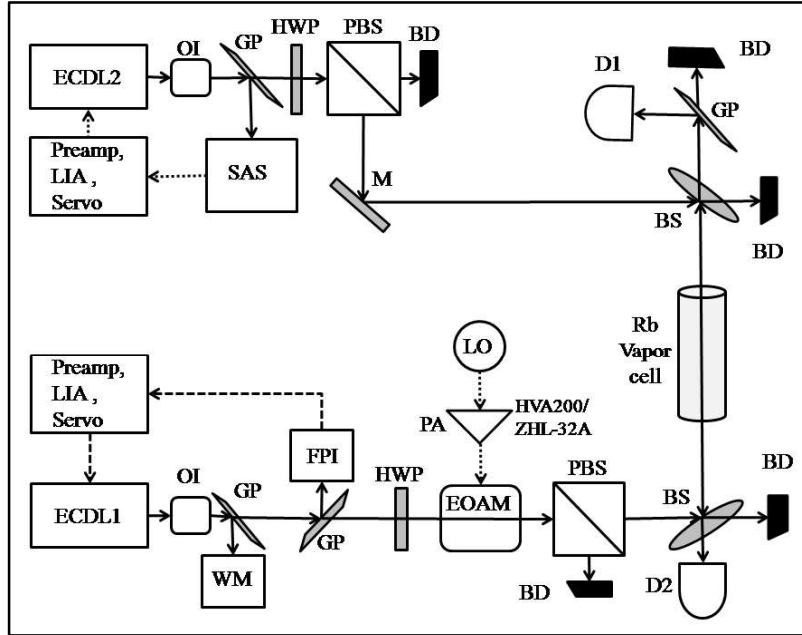


Fig. 4.2 Schematic of the experimental arrangement for optical switching in ladder. ECDL1,2: External cavity diode laser, M: Mirror, PBS: Polarizing cubic beam splitter, BS: Beam splitter, OI: Optical isolator, BD: Beam dump, D1,D2: Photodetectors, HWP: Half wave plate, FPI: Fabry-Perot interferometer, WM: Wavemeter, LO: Local Oscillator, PA: Power amplifier, EOAM: Electro-optic amplitude modulator, GP: Glass plate, SAS: Saturation absorption spectroscopy setup, The readings from D1, D2 and FPI were simultaneously observed on same oscilloscope. For intensity modulation in the frequency range 10 Hz to 1 MHz, HVA 200 unit was used and above 1 MHz we have used ZHL-32A RF power amplifier.

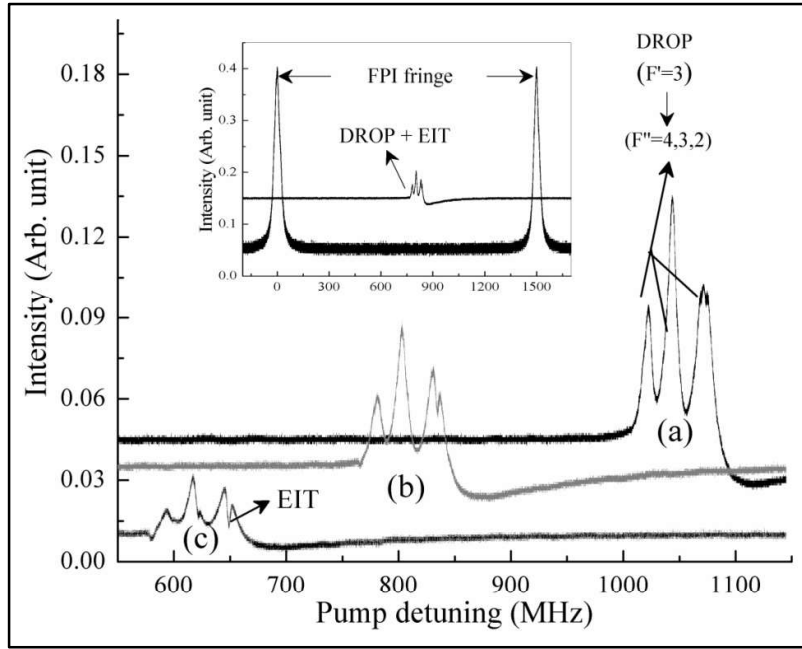


Fig. 4.3 Experimental recording of probe absorption for pump laser frequency scan. Probe laser was locked at frequency (a) ν_a , (b) ν_b and (c) ν_c . Plot (a) shows Strong DROP and weak EIT whereas DROP is reduced and EIT is increased gradually in plot (c) through plot (b). The inset shows simultaneous recording of FPI fringes with probe absorption spectrum. Probe absorption spectrum was calibrated with the help of simultaneous recording of FPI fringes.

The result of the first part of the experiment is shown in Fig. 4.3 and Fig. 4.4. Fig. 4.3 shows the probe absorption spectra for pump scanning. DROP and DROP-EIT feature can be seen on flat background for a frequency locked probe laser. The probe laser addresses small velocity groups of atoms corresponding to the laser line-width and one-photon detuning. These atoms are further excited to the $|3\rangle$ by the pump laser. As $\lambda_c \approx \lambda_p$, no resultant Doppler background is seen on the two photon absorption spectrum of the probe laser. In Fig. 4.3(a), one can see that the two-photon probe absorption spectrum is composed of prominent DROP signal with extremely weak EIT feature on the $F' = 3 \rightarrow F'' = 4$ transition. Probe laser was locked on ν_a for Fig. 4.3(a). One can see that the effect of DROP is gradually

decreased as the probe laser is locked on ν_b and ν_c and the EIT is getting stronger with it (Fig. 4.3b and Fig. 4.3c).

The near absence of EIT even under perfect two-photon resonance condition (Fig. 4.3a) ($\Delta_p \approx \Delta_c \approx 0$) is explained by considering that the $F = 2 \rightarrow F' = 3 \rightarrow F'' = 4$ absorption route is a pseudo-closed absorption-emission channel. Therefore decay of atoms through DROP mechanism to $F = 1$ state is relatively less for this channel compared to the other two-photon absorption channels, viz $F = 2 \rightarrow F' = 3 \rightarrow F'' = 3, 2$. On the other hand EIT originates from the cancellation of the probability amplitudes of the excitation pathways and can be explained using “dressed state” picture [22]. This mechanism of EIT demands no loss of atoms to the $F = 1$ state. Therefore $F = 2 \rightarrow F' = 3 \rightarrow F'' = 4$ absorption channel is the most favourable for observation of EIT but even under that condition the DROP effect is still strong and almost suppresses the EIT feature and only a very weak signature of EIT can be seen on the $F' = 3 \rightarrow F'' = 4$ two-photon absorption feature. For other transitions ($F' = 3 \rightarrow F'' = 3, 2$), relatively larger number of atoms can leak through the DROP mechanism to the $F = 1$ state. Thus DROP being the dominant mechanism, helps to obscure the signature of EIT from other peaks. Since DROP is proportional to the two-photon absorption probability [19], it is maximum for the perfect two-photon resonance ($F = 2 \rightarrow F' = 3 \rightarrow F'' = 4$) case and we call it ‘strong DROP’ condition of the medium. However this condition is also the strong condition for EIT and weak EIT is seen on $F' = 3 \rightarrow F'' = 4$.

In case of Fig. 4.3(b) and Fig. 4.3(c), the presence of EIT is clearly seen. In these cases, the probe laser populates $F' = 2, 1$ levels more compared to the $F' = 3$ level through the detuned one-photon absorption. In return, the average population of atoms to the $F'' = 3, 2$ level increases considerably and this results in more loss of atoms into the $F = 1$ state through decay from $F'' = 3, 2$ levels. In the off-resonant cases, the overall supply of atoms

to the $F'' = 4$ level is reduced compared to the perfect two-photon resonance case. Therefore DROP gets weaker and EIT becomes prominent which is evident from Fig. 4.3(b) and Fig. 4.3(c) as compared to Fig. 4.3(a). This situation is called the ‘weak DROP’ and ‘strong EIT’ condition of the medium. One must note here that the probe coupling also favours single resonance optical pumping (SROP). SROP results into decay of atoms to the $F = 1$ level thereby reducing absorption. For off-resonant condition of the probe laser, this effect (SROP) also contributes to the reduction of the absorption. The atoms which reach to the $F = 1$ state can only be transferred to the $F = 2$ state via the dephasing $\gamma_{g,1\rightarrow 2}$. For room temperature vapour cell without buffer gas, this is mainly dominated by transit time broadening (<50 kHz) which is very slow compared to the other processes (optical pumping and decay). Therefore the system can be considered in equilibrium in the time scale of $\gamma_{g,1\rightarrow 2}$.

The same probe absorption is observed under probe scanning as shown in Fig. 4.4. The probe laser was scanned over the $F = 2 \rightarrow F'$ hyperfine transitions and the pump laser is kept stationary at a nominal frequency, $\nu_0 \sim 776$ nm. Under this situation, probe laser satisfies both one photon and two photon absorption condition. Therefore we can see the two-photon transmission spectra on top of the one photon absorption background. The probe absorption spectra show the evolution of DROP-EIT feature with different pump frequency. By observing the probe absorption spectra and SAS signal on the same oscilloscope we chose the pump frequency. By adjusting the piezo offset voltage, we can select the pump frequency for perfect two-photon resonance condition. In that case the two-photon absorption signal is matched with the $F = 2 \rightarrow F' = 3$ transition peak on the SAS signal. Fig. 4.4 (c) shows such spectrum and is identical to the Fig. 4.3(a) apart from the Doppler background. As we shift pump frequency from the $F = 2 \rightarrow F' = 3 \rightarrow F'' = 4$ condition, EIT becomes prominent and can be seen in other picture of Fig. 4.4. The shapes of EIT signals on the TPA spectra suggest the strong influence of the AT splitting [146].

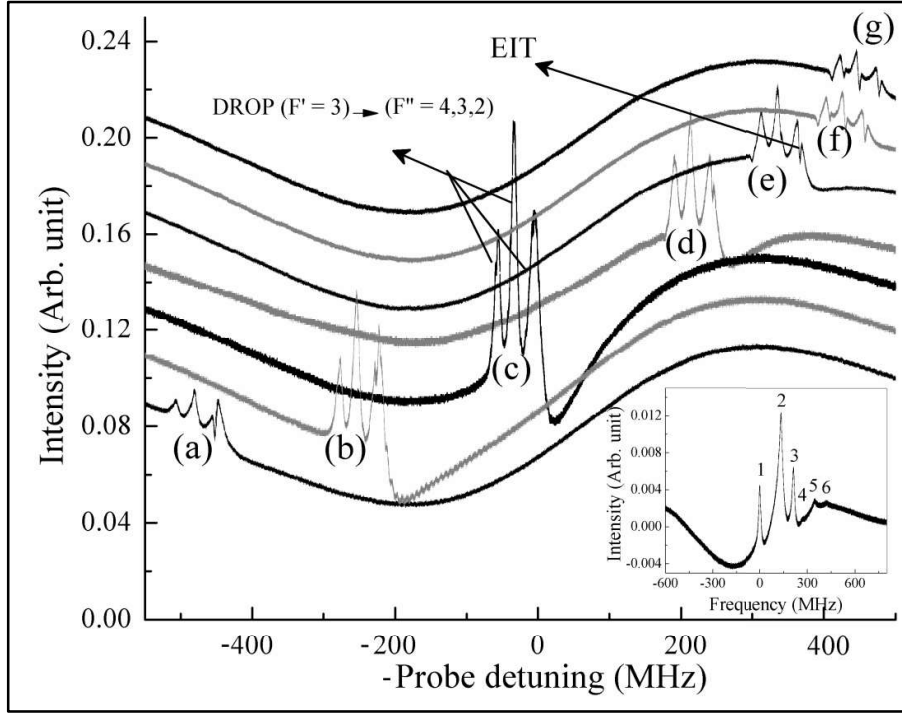


Fig. 4.4 Recording of the probe absorption spectra for probe laser frequency scan. The pump laser frequency was kept fixed at different positions. Simultaneous recording of probe SAS spectra was done initially on the same oscilloscope. The piezo offset voltage of the pump laser was adjusted to bring the TPA spectrum exactly in the position of the closed transition. For other positions pump laser frequency was adjusted by seeing the readings on the wavemeter. (plots a, b, d-g). For plot (g), EIT appears on all DROP signals. Inset shows the simultaneous recording of the SAS spectrum where 2, 3, 5 are the cross-over transitions and 1, 4, 6 are the one-photon absorptions for $5S_{1/2}(F = 2) \rightarrow 5P_{3/2}$ transitions.

4.4.2 Second part of the experiment

In the second part of the experiment, systematic study of coherence induced optical switching was made. For this purpose the probe laser locked on (a) $5S_{1/2}(F = 2) \rightarrow 5P_{3/2}(F' = 3)$ transition (ν_a) and (b) $5S_{1/2}(F = 2) \rightarrow 5P_{3/2}(F' = 3, 1)$ cross-over transition (ν_b). Initially, the pump laser was scanned to monitor the probe absorption spectra and the

FPI fringe simultaneously on the oscilloscope. The FPI fringe was tuned to the desired position which matches with two-photon probe absorption spectra. The pump laser was then locked on the side of the FPI fringe directly. At this condition the intensity modulation of the pump beam was introduced through EOAM.

The result of the second part of the experiment is shown in Fig. 4.5 and Fig. 4.6. The switching for the probe beam is normalized with respect to the switching of the coupling beam to eliminate the contributions from other factors such as, fluctuation in vapour pressure, fluctuation in laser intensity etc. The frequency of the switching was varied from 10 *Hz* to 10 *MHz*. The probe laser was locked on ν_a and ν_b for two cases. Initially the pump laser was scanned to reproduce the two-photon absorption spectra as presented in Fig. 4.3(a) and Fig. 4.3(b). Simultaneously the FPI fringe was observed on the same oscilloscope. By adjusting the DC offset voltage of the FPI cavity mirror, we matched the FPI fringe on the respective two-photon absorption feature. Pump laser is now locked on the FPI fringe in this condition. FWHM of the FPI fringe is ~ 5 MHz which is much less compared to the overall frequency spacing of the $5D_{5/2}$ state (~ 50 MHz) and also less than the line-width of the DROP signal (~ 6.5 MHz for the $F' = 3 \rightarrow F'' = 3$ transition). Hence the selection of the FPI fringe as the reference signal for pump laser locking serves the purpose. Active stabilization of the cavity [147] was avoided and only passive stabilization measure such as isolation of cavity environment was followed. However this did not affect the experiment as we took the readings within the time scale of ~ 1 minute and no visible shift is observed on the FPI fringe within this time scale under test run.

Fig. 4.5(a) and Fig. 4.5(b) show two examples of intensity switching under strong DROP and strong EIT conditions respectively. Plots show the transmitted probe and pump beam signal with respect to time. For Fig. 4.5(a), the probe beam was locked on ν_a and for Fig.

4.5(b) it was locked on ν_b . The pump beam was locked on FPI fringe satisfying the two photon resonance condition in both cases.

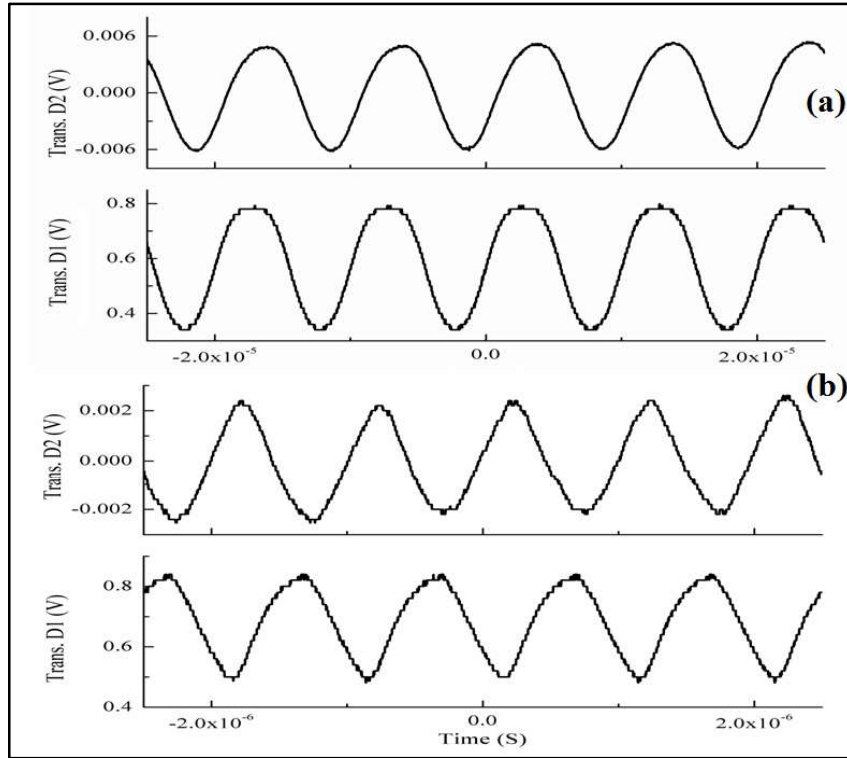


Fig. 4.5 Intensity switching in pump and probe laser under (a) strong DROP and (b) strong EIT. Trans D1, D2 indicates the recording of transmitted intensity from respective detectors. Plot (a) shows modulation at 100 kHz frequency and plot (b) shows the same modulation at frequency 1 MHz. The phase difference between the waveforms are due to the different time constants involved in this process.

Fig. 4.6 shows the bimodal operation of optical switching under DROP and EIT configuration of the medium. The dominant DROP condition shows a sharp cut-off starting from 100 kHz frequency of intensity modulation whereas the dominant EIT condition shows a cut-off at 1 MHz switching frequency. This difference in bandwidth for the two cases originates from the involved processes of optical pumping and relaxation. The involved optical pumping process in ladder system is far more complex [148] compared to an isolated

A system in which case the optical pumping is simply expressed by Ω_c^2/Γ where Ω_c is the pump Rabi frequency and Γ is the decay rate of $|2\rangle$. Intuitively one can conclude that these pumping processes are faster enough to compensate for the decay so that the two photon effects are realized in practice. Therefore under external perturbation the dynamic evolution of the system is only limited by the decay processes (slower than optical pumping). For DROP the main limiting factor is a combination of $\Gamma_2 = 2\pi \times 6.066 \text{ MHz}$ and $\Gamma_3 = 2\pi \times 0.97 \text{ MHz}$ whereas for EIT it is a combination of coherent dephasing $\gamma_{31} \approx 2\pi \times 0.5 \text{ MHz}$ and $\gamma_{21} \approx 2\pi \times 3.0 \text{ MHz}$. The intensity modulation directly competes with the rate of population transfer from $|1\rangle \rightarrow |3\rangle$ for DROP. Therefore only a slower intensity modulation ($\sim 100 \text{ kHz}$) can be accommodated in the system for strong DROP condition without disturbing the system equilibrium. In case of EIT, though the evolution of the system in the time scale of γ_{21} requires transient analysis [144], it may be inferred that the highest speed of switching in an EIT medium is related to the onset of the AC stark shift ($\Omega_c^2 \sim 4\gamma_{21}\gamma_{31}$). Therefore intensity switching faster than $\sim 1 \text{ MHz}$ can still be transported through the system under strong EIT condition.

Fig. 4.7 shows the plot of simulation of equation (4.1). Fig. 4.7(a) shows the plot of $Im(\chi)$ vs the probe laser frequency detuning Δ_p . $Im(\chi)$ is also equivalent to the probe absorption. A transparency window can be seen in the plot at $\Delta_p = 0$. Fig. 4.7(b) and Fig. 4.7(c) show the dynamic evolution of the system in the time scale of optical switching. The plot clearly shows the sinusoidal variation in intensity at the EIT window. In this simulation, the time scale of the physical processes involved is in the order of $(\Omega_c^2/\gamma_{21})^{-1} < \omega_m^{-1} < \gamma_{31}^{-1}$. It is evident from these figures that the effect of high speed switching is observable even at the time scale $\sim 3/\gamma_{21}$. As the time scale of the coherent dephasing between $|1\rangle$ and $|3\rangle$ (γ_{31}^{-1}) is slower compared to the switching speed, the system settles into equilibrium and in such case the system dynamics can be explained in the time scale of ω_m^{-1} . Therefore with the help of

equation (4.1) the system dynamics under EIT condition can be explained phenomenologically.

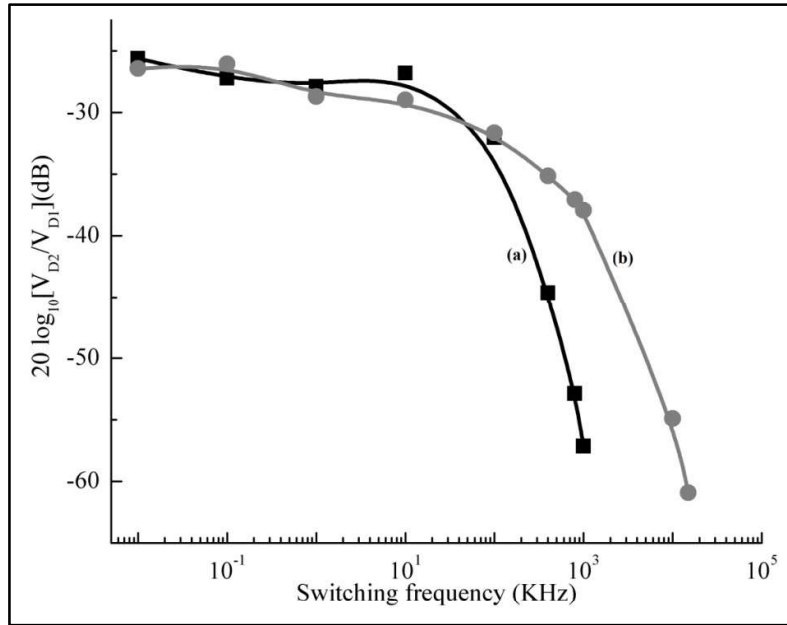


Fig. 4.6 Comparison of intensity switching under (a) strong DROP and (b) dominant EIT conditions. Signal (V_{D2}) obtained through the detector D2 is weighted by the signal (V_{D1}) obtained through D1 and is plotted in a gain-bandwidth like plot.

To drive the EOAM we have used a high voltage driver (Thorlabs HVA 200). A reference sinusoidal voltage was applied on the EOAM through the driver. The driver has a sharp cut-off at 1 MHz. Above 1 MHz we had used a ZHL-32-A (Minicircuits) amplifier for intensity modulation. The pump beam intensity modulation was monitored with the help of a photo-detector placed on the exit side of the Rb vapour cell. The coherence assisted transfer of intensity modulation to the probe beam was monitored using another photo-detector on the other side of the vapour cell.

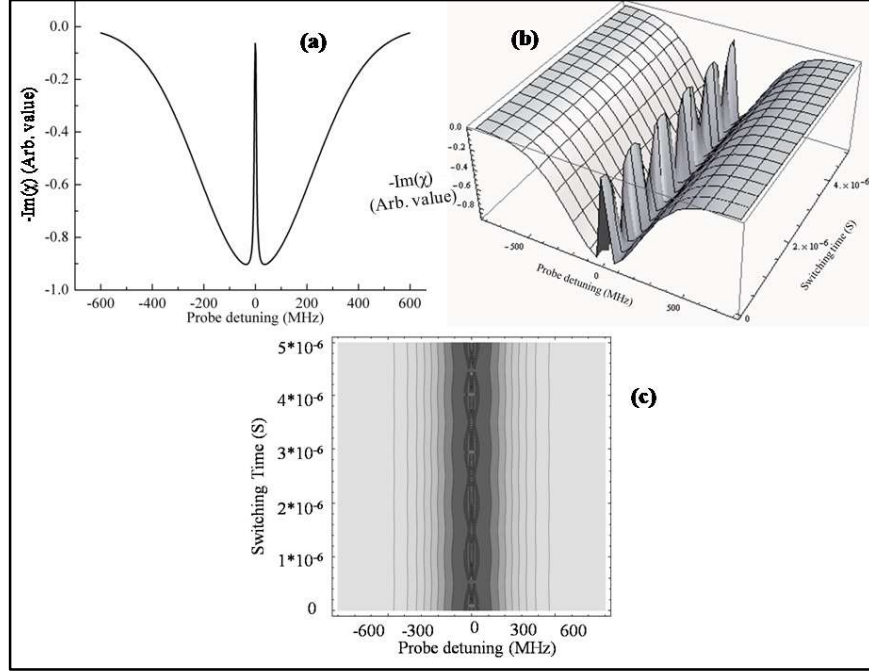


Fig. 4.7 Theoretical simulation of intensity switching in EIT system. (a) Doppler averaged plot of $Im(\chi)$ with the appearance of EIT at zero probe detuning. (b) Doppler averaged plot of $Im(\chi)$ under intensity switching. Sinusoidal intensity switching can be seen on the EIT window. (c) Contour plot of optical switching vs probe detuning. Chosen parameters for the simulations are $C_1 = 0.51, C_2 = 0.50, \Omega_c \sim 2\pi * 100 \text{ MHz}$.

4.4.3 Final part of the experiment

In the last part of the experiment, the effect of power variation of the probe laser on the probe absorption spectra was studied. This part of the experiment was aimed at finding any possible demarcation feature for the transition of the media from prominent EIT condition to strong DROP condition. In this regard, the probe laser was locked on the $5S_{1/2}(F = 2) \rightarrow 5P_{3/2}(F' = 3, 1)$ cross-over transition and the probe absorption spectrum for pump scanning was monitored for different probe laser power. As the media has different switching bandwidth under DROP and EIT condition, the demarcation feature will also act as a

boundary for the different zones of optical switching speed. We are interested to see whether by varying the probe laser power itself one can change between different zones of optical switching.

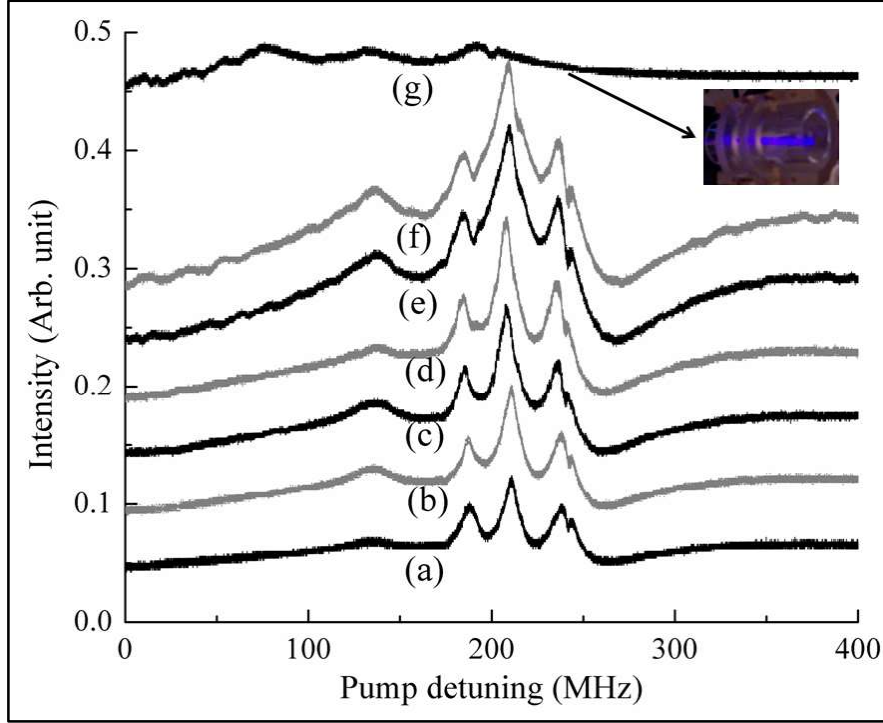


Fig. 4.8 Recording of the probe absorption spectra for different probe laser power. The probe laser Rabi frequency was varied and the values are $2\pi \times (9, 13, 15, 18, 29, 37, 43)$ MHz for plots (a) to (g). At very high power detector D2 is near saturation and is shown in plot (g).

Fig. 4.8 shows the results of the last part of the experiment. Pump laser was scanning while the probe laser was fixed on $F = 2 \rightarrow F' = 3, 1$ cross-over transition (same as Fig. 4.3b). With increase in probe laser power the contrast in EIT feature deteriorates and ultimately smears out from the probe absorption spectrum. The smearing of EIT and subsequent dominance of DROP is marked by appearance of a faint blue radiation in the vapour cell. The blue light appears from the decay route $5D_{5/2} \rightarrow 6P_{3/2} \rightarrow 5S_{1/2}$. At the

strong probe regime, the analytic expression for probe absorption contains higher powers of Ω_p and Ω_c [149]. These multi-photon processes start interfering with the EIT condition and thus EIT smears out from the probe absorption spectrum even though the two-photon condition is still valid.

4.5 Conclusion

The application of EIT in optical switching is an important research topic as it has application in communication network in the role of routing, buffering etc. Though there exists many reports on switching application of EIT, only Lee et al [12] pointed out the typical role of laser frequency detuning for optimization of switching performance. Therefore a systematic experimental investigation was required for the optimization of switching performance.

In this chapter we discussed different aspects of the dual nature of intensity switching in a ladder (Ξ) system. The coupling laser intensity was modulated for this purpose. We found that two phenomenon, DROP and EIT, dominate the probe absorption spectrum. The effect of laser detuning on DROP and EIT has been studied in details. It has been found that the system under EIT condition can exhibit rapid switching even at frequencies >1 MHz speed. The same system can only exhibit a switching speed up to 100 kHz under DROP condition. This difference in performance is due to the fast coherent dephasing for EIT and a combination of slower decay processes for DROP. In the last part of the experiment we have studied the influence of the probe laser intensity on DROP-EIT spectrum. It has been found that the appearance of a faint blue light indicates the elimination of EIT from the medium and other multi-photon processes start dominating. However the DROP spectrum remains intact even under strong probe regime. Therefore this acts as the demarcation feature for the

bimodal character of the optical switching in ^{87}Rb , $5S_{1/2} \rightarrow 5P_{3/2} \rightarrow 5D_{5/2}$ ladder system.

Finally this study will be helpful for the optimization of an all-optical switch based on EIT.

Chapter 5

Study on the application of repump laser in optical switching

5.1 Introduction

The application of EIT in high speed optical switching is a hot research topic. Chapter 4 dealt with such coherence assisted optical switching in a ladder (Ξ) system and has shown that the simultaneous presence of DROP-EIT signal in the probe absorption spectra can be exploited to construct a dual mode (slow-fast) optical switch. However the phenomenon of coherence assisted optical switching is heavily dependent upon the transfer of the intensity modulation from one laser to the other laser. In this chapter we discuss about the experiment conducted to investigate the role of a third laser (repump laser; acronym borrowed from laser cooling experiment) in enhancing the modulation transfer phenomenon from one laser to the other. In this direction we have chosen the same $5S_{1/2} \rightarrow 5P_{3/2} \rightarrow 5D_{5/2}$ ladder level coupling scheme of ^{87}Rb atom to demonstrate the effect of the third laser. Following subsections discuss the experiment in details.

5.2 Motivation

The pump-probe spectroscopy in the $5S_{1/2}(F = 2) \rightarrow 5P_{3/2}(F' = 3, 2, 1) \rightarrow 5D_{5/2}(F'' = 4, 3, 2)$ ^{87}Rb ladder system reveals DROP and EIT signature [19,42]. This fact has already been utilized in one of our works to demonstrate a bi-modal optical switch [150]. In one mode of switching, dominated by DROP mechanism, the switching frequency is limited up to a frequency of 100 kHz. On the other hand the EIT dominated switching can go beyond 1 MHz. The appearance of blue light ($\sim 420 \text{ nm}$) can be used as the marker between strong EIT and strong DROP domain of operation. The DROP appears from the decay of atoms to the uncoupled ground hyperfine state $F = 1$ whereas EIT demands no loss of population from

the $F = 2 \rightarrow F' = 3 \rightarrow F''$ ladder coupling scheme. These counter requirements of DROP and EIT opens up a possibility of introducing a third laser which can retrieve back (repump) the radiation trapped atoms from the uncoupled $F = 1$ state. This has the potential to strengthen the EIT in a ladder level coupling. Such observation compels us to look for the effect of repump laser on the coherence assisted optical switching.

The transfer of intensity modulation from pump laser to probe laser is a coherence assisted phenomenon. Application of a third laser helps in strengthening the effect of coherence assisted modulation transfer. This beneficial aspect of repump laser is based on the manipulation of population in the ladder level coupling scheme. In this regard, we have found that the selectivity of the repumping associated with the σ^+ polarized repump laser is much better compared to the normal hyperfine level repumping with a linearly polarized repump laser and the same comparison is addressed in Chapter 6 with minute details. The introduction of a repump laser enhances the gain of intensity modulation transfer throughout the entire switching frequency domain.

5.3 Experimental scheme

The basic level coupling scheme for the present experiment is shown in Fig. 5.1. Three external cavity diode lasers are used in pump-probe-repump configuration in a Rb vapour cell (without buffer gas) at room temperature. The repump-pump lasers counter propagate the probe laser. The experimental arrangement is shown in Fig. 5.2. The pump laser is in resonance with the $F' = 3 \rightarrow F'' = 4, 3, 2$ transition while the probe laser scans over the $F = 2 \rightarrow F'$ hyperfine domain. The intensity modulation is introduced to the pump frequency by using an electro-optic amplitude modulator. The coherence assisted transfer of modulation from pump laser to probe laser is monitored with photodiodes. The probe laser is stabilized on the SAS reference and pump laser is slowly scanned to two-photon resonance conditions.

An additional σ^+ polarized repump laser connects the $5S_{1/2}(F = 1) \rightarrow 5P_{3/2}(F' = 2)$ transition to restore the ‘lost’ population from $F = 1$ level. The gain-bandwidth response of the switch is determined at different modulation frequency. Similar gain-bandwidth response of the system without the repumping laser is also obtained.

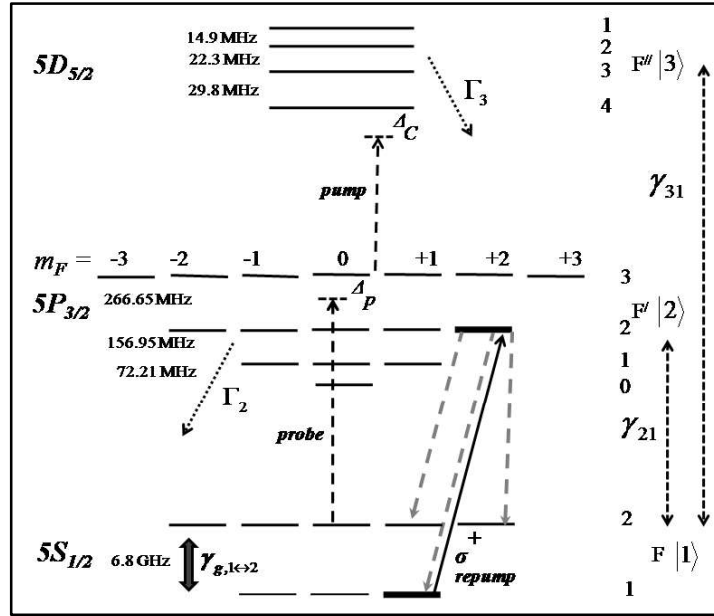


Fig. 5.1 Level coupling scheme for optical switching with repump laser. Black solid arrow shows the σ^+ repump laser connection. Associated gray dashed arrows represent the possible decay routes. Γ_3 and Γ_2 are the spontaneous decay rates from the corresponding levels. γ_{31} , γ_{21} and $\gamma_{g,1 \rightarrow 2}$ are the coherence dephasing rates.

The intensity switching in a ladder system can also be described phenomenologically with the help of equation (4.1) by merely substituting $\Omega_c^2 \rightarrow \Omega_0^2(C_1 + C_2 \cos \omega_m t)$ into the equation (4.1). Ω_0 is the nominal value of the pump Rabi frequency and C_1 , C_2 are so adjusted that the bare minimum value of $\Omega_c^2 \sim 4\gamma_{21}\gamma_{31}$ is maintained. To set transparency into the system, only this bare minimum value of pump field is required according to the AC stark shift. A sinusoidal variation in the pump intensity over the bare minimum pump Rabi frequency brings out the intensity switching without disturbing the steady state assumption.

The results of the simulation are already shown in Fig. 4.7. In the following section we discuss the experimental results.

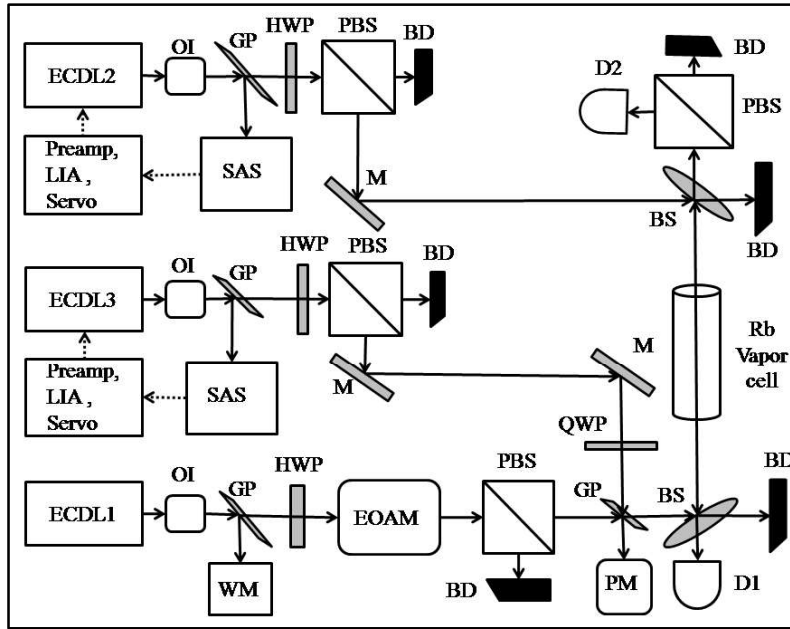


Fig. 5.2 Schematic of the experimental arrangement to study effect of repump laser in optical switching. ECDLs: External cavity diode laser, ECDL1: Pump laser, ECDL2: Probe laser, ECDL3: repump laser, M: Mirror, PBS: Polarizing beam splitter, OI: Optical isolator, BD: Beam dump, D1, D2: Photodetector, BS: Beam splitter, HWP: Half wave plate, QWP: Quarter wave plate, PM: Power meter, WM: Wave meter, GP: Glass plate, SAS: Saturation absorption spectroscopy, LIA: Lock-in-amplifier.

5.4 Results & discussion

The Rabi frequencies of the pump and probe lasers are $\Omega_p \sim 2\pi \times 9 \text{ MHz}$ and $\Omega_c = 2\pi \times 70 \text{ MHz}$ respectively. The repump laser power was chosen to be $\sim 1.5 \text{ mW}$ for the present experiment. The counter-propagating geometry of probe and pump laser beam eliminates the effect of residual Doppler broadening whereas the same for the probe and

repump lasers ensures that the EIT due to Λ connection does not appear in this experiment.

The issue of double dark resonance is treated in Chapter 7.

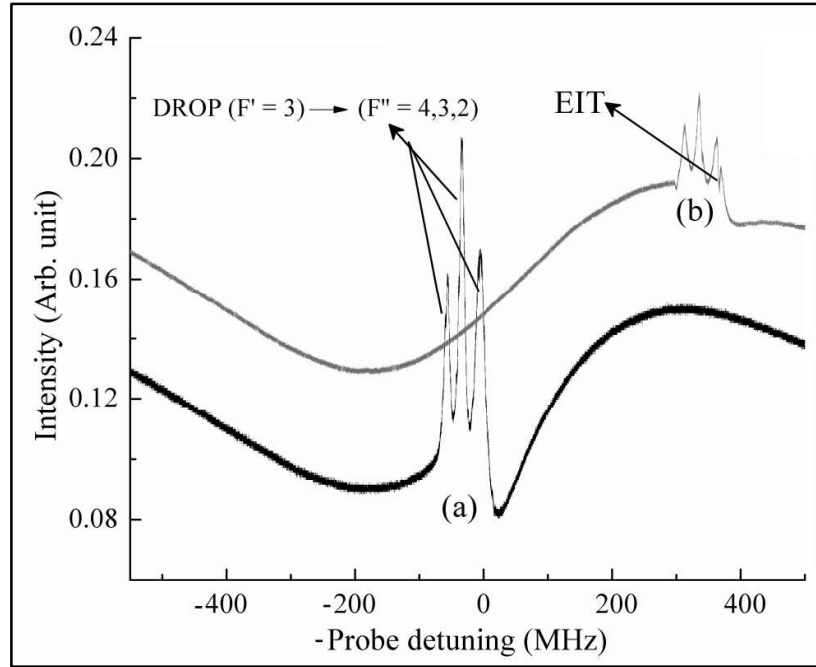


Fig. 5.3 probe absorption spectrum showing DROP-EIT feature without repump laser. (a) Spectrum for resonant ladder coupling addressing the $F = 2 \rightarrow F' = 3 \rightarrow F'' = 4, 3, 2$ transition manifold. (b) The same spectrum under off-resonant coupling addressing the $F = 2 \rightarrow F' = 3, 1$ cross-over $\rightarrow F''$ transition manifold. For on-resonant spectra very small EIT feature can be seen on $F = 2 \rightarrow F'' = 4$ transition whereas EIT is very prominent on the off-resonant coupling.

Fig. 5.3 shows the DROP-EIT spectrum under probe frequency scan. Fig. 5.3(a) shows the spectrum under perfect two-photon resonance condition i.e. the pump-probe combination address the $5S_{1/2}(F = 2) \rightarrow 5P_{3/2}(F' = 3) \rightarrow 5D_{5/2}(F'' = 4)$ transition manifold. In this condition the DROP is dominant and EIT is obscured. Fig. 5.3(b) shows the spectrum under $5S_{1/2}(F = 2) \rightarrow 5P_{3/2}(F' = 3, 1$ cross-over) $\rightarrow 5D_{5/2}(F'' = 4)$ coupling condition i.e. the pump laser is blue detuned compared to Fig. 5.3(a). In Fig. 5.3(b), appearance of EIT can be

clearly seen in the DROP background. Under perfect two-photon resonance condition ($\Delta_p = \Delta_c \approx 0$) the EIT is expected to be strongest but the loss of atoms to $F = 1$ level is still very dominant and we can only see the DROP signals. However under off-resonant coupling two-photon resonance condition is $\Delta_p + \Delta_c \approx 0$; $\Delta_p \neq 0, \Delta_c \neq 0$ and EIT is expected to be weak. In practice, DROP signal also becomes weak under off-resonant coupling as less numbers of atoms are pumped to the excited state. Therefore the EIT signal becomes prominent on the DROP profile for this condition.

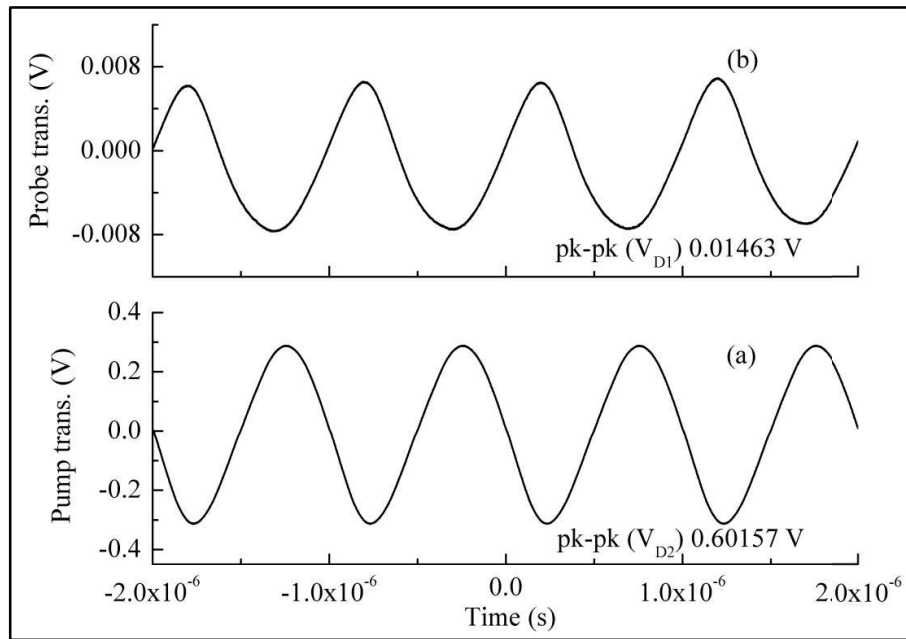


Fig. 5.4 Intensity switching of pump laser and its effect on probe laser. (a) Shows the intensity variation in the pump laser transmission signal (b) Shows the same intensity variation in the probe laser. The intensity switching is obtained in the presence of σ^+ repump laser.

Fig. 5.4 shows the transfer of intensity modulation from pump laser to the probe laser under the presence of repump laser at 1 MHz. The σ^+ repump laser connects $F = 1, m_F = +1 \rightarrow F' = 2, m_F' = +2$ transition. The intensity modulation detected in the form of transmission signal by the photo-detectors D1 and D2 is plotted with respect to time in this

plot. The average peak to peak voltage (V_{D1} and V_{D2}) is determined from the plot and is used to estimate the gain $\sim 20 \log(V_{D1}/V_{D2})$.

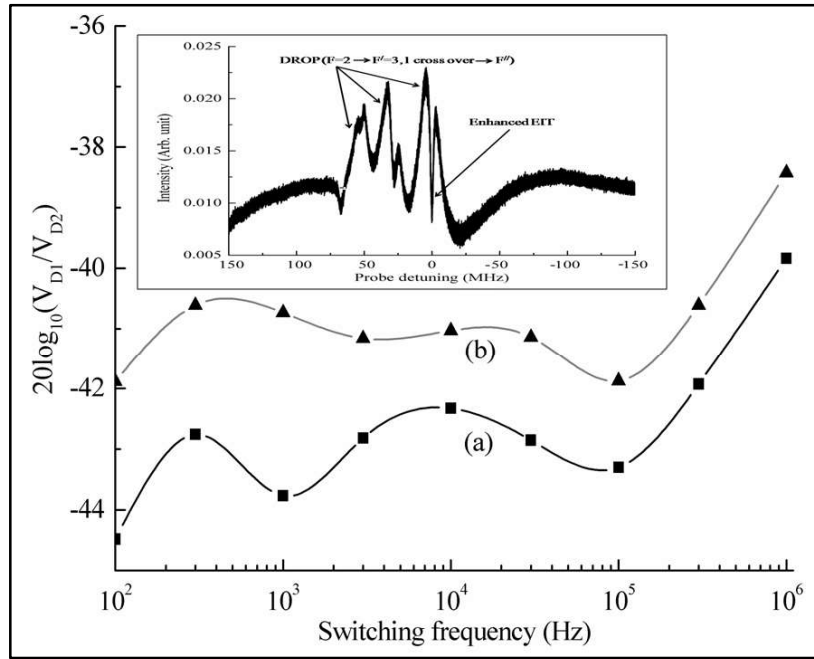


Fig. 5.5 Gain-bandwidth response of the optical switch in ladder system (a) without repump laser and (b) in presence of σ^+ repump laser. An overall increment of ~ 3 dB in the gain is observed after using the repump laser. B-spline curve is fitted to the data for better visualization. The inset shows an enhanced EIT (reduced DROP) in the probe absorption spectra in presence repump laser.

Fig. 5.5 shows the effect of repump laser on the gain-bandwidth curve of the intensity switching under off-resonant coupling. Fig. 5.5(a) shows the situation with repump laser and Fig. 5.5(b) shows the same action without the repump laser. One can see an increase in the gain of about ~ 3 dB over a bandwidth of 100 Hz to 1 MHz due to the presence of repump laser. The repumping process is more selective [151] under σ^+ repumping as the number of decay route gets limited because of the atomic selection rules. This is evident from Fig. 5.5(a) and Fig. 5.5(b). Inset of Fig. 5.5 shows that the strength of EIT is strongly enhanced under

off-resonant coupling. This happens due to the restoration of radiation trapped atom from $F = 1$ level to the respective Ξ level coupling scheme.

In this regard it should also be noted that the chosen level coupling scheme has similarity with an inverted Y or tripod linkage [26,67] but the generation of the double dark state in such system is dependent upon the geometrical configuration of the pump-probe-repump laser propagation direction. It should also be noted that the repump laser connects the $F = 1, m_F = +1 \rightarrow F' = 2, m'_F = +2$ level whereas the probe laser address the $F = 2 \rightarrow F' = 3$ transition. Therefore the resulting Λ or ladder connection is not resonant. Therefore the enhancement of the EIT in the inset of Fig. 5.5 is only due to the recirculation of ‘lost’ atoms to the Ξ excitation channel formed by the probe and pump laser.

5.5 Conclusion

In this chapter we have discussed the effect of repump laser on optical switching in ^{87}Rb ladder system. The repump laser effectively re-circulates the ‘lost’ atoms to the ladder coupling channel which benefits the EIT. Strengthening of the EIT is manifested through the enhancement of switching gain under the presence of repump laser. This study might be helpful in obtaining a better gain-bandwidth product of the switch. This study may also find its application in routing, data storage, buffering etc.

Chapter 6

Controlling coherence in ladder system

6.1 Introduction

In Chapter 5 we have shown the effect of a σ^+ repump laser on optical switching. In this chapter we present the experimental study about the role of repump laser in controlling the existing coherence in $5S_{1/2}(F = 2) \rightarrow 5P_{3/2}(F') \rightarrow 5D_{5/2}(F'')$ ladder system in ^{87}Rb . Application of the repump laser shows a substantial increment in EIT signal strength along with a reduction in DROP signal throughout the entire Doppler width. The repump laser helps to reduce the effect of incoherent pumping and related radiation trapping in this system. It is found that the repump laser intensity and detuning has a profound effect on EIT line-width and strength. Both normal hyperfine level repumping and Zeeman sublevel repumping has been introduced in the system to see its effect on the concerned spectrum. Following subsections discuss the experiment and its outcome in detail.

6.2 Motivation

The ladder system finds its application in the field of optical switching [13], metrology [16], frequency conversion [17], atomic line filter [39] etc. EIT in such a system [143,2,76,152] has helped in exploring the excited state hyperfine structure using atomic coherence [153]. Systematic studies of EIT in both closed and open ladder system in ^{87}Rb have been conducted by Moon et al [18,154]. These articles investigate the complicated interplay among different mechanisms of absorption, decay, coherence etc. In literature, many experimental studies are available on controlling the coherence in atomic system. For example, Jiang et al [155] worked on a ' N ' type system [23,24] and Akulshin et al [25] investigated blue light generation in a ladder linkage. The effect of repump laser on Atomic

line filter and optical switching was already investigated by us [156,157] but the issue of controlling coherence in ladder system with the help of a repump laser was still unexplored. In that direction this experiment is the first investigation on coherence control in a ladder type atomic system exhibiting DROP and EIT feature.

In a typical ladder system as shown in Fig. 6.1, pump laser connects the states $|2\rangle$ and $|3\rangle$ while the probe laser scans over the $|1\rangle \rightarrow |2\rangle$ transition. The counter propagating pump-probe configuration helps to eliminate the first order Doppler broadening [143]. Under two-photon resonance condition probe absorption almost vanishes resulting in a ‘transparency’ in the probe absorption spectrum. This transparency may be due to AT splitting [158] as well as coherence excitation of ‘dark state’. Level dressing in the system is responsible for the AT splitting whereas destructive interference among the excitation amplitudes leads to EIT in the system [22]. Both of these phenomenon depends upon the dephasing (γ_{31}) between $|1\rangle$ and $|3\rangle$. For zero coherence dephasing, both AT and EIT occurs at the same probe detuning.

In ^{87}Rb $5S_{1/2}(F = 2) \rightarrow 5P_{3/2}(F') \rightarrow 5D_{5/2}(F'')$ ladder system, both DROP and EIT features can be seen in a pump-probe spectroscopy [18]. A perfect EIT condition demands no population loss to the uncoupled states whereas the condition for strong DROP is just the opposite. This non-trivial behaviour of DROP and EIT is the basis of this investigation. We have introduced a third laser connecting $F = 1 \rightarrow F' = 2$ transition in order to retrieve the radiation trapped atoms from the $F = 1$ state to $F = 2$ ground hyperfine state. In order to optimize the repump process both Zeeman sublevel repumping and hyperfine repumping was studied. In this connection $F = 1 \rightarrow F' = 2 \rightarrow F''$ open ladder system was also studied and the effect of repump (connecting $F = 2 \rightarrow F' = 2$ transition) on the open ladder system was investigated.

6.3 Repumping in ladder system

The level coupling scheme for the current experiment is shown in Fig. 6.1. A weak probe laser is resonant with the $|1\rangle \rightarrow |2\rangle$ transition and a strong pump laser connects the $|2\rangle \rightarrow |3\rangle$ transition. The pump laser can be considered as always on resonance [150] while the probe laser scans the whole Doppler width of the $|1\rangle \rightarrow |2\rangle$ transition. For perfect two-photon resonance i.e. $\Delta_c = \Delta_p = 0$, probe absorption spectra shows transparency at the line centre of the transition. For $\gamma_{31} \rightarrow 0$, perfect EIT can be observed [143,159]. For the present case the separation between the pump and probe laser frequency is much smaller than the nominal laser frequency i.e. $\omega_c - \omega_p \ll \omega_0$ also $\gamma_{31} < \gamma_{21}$.

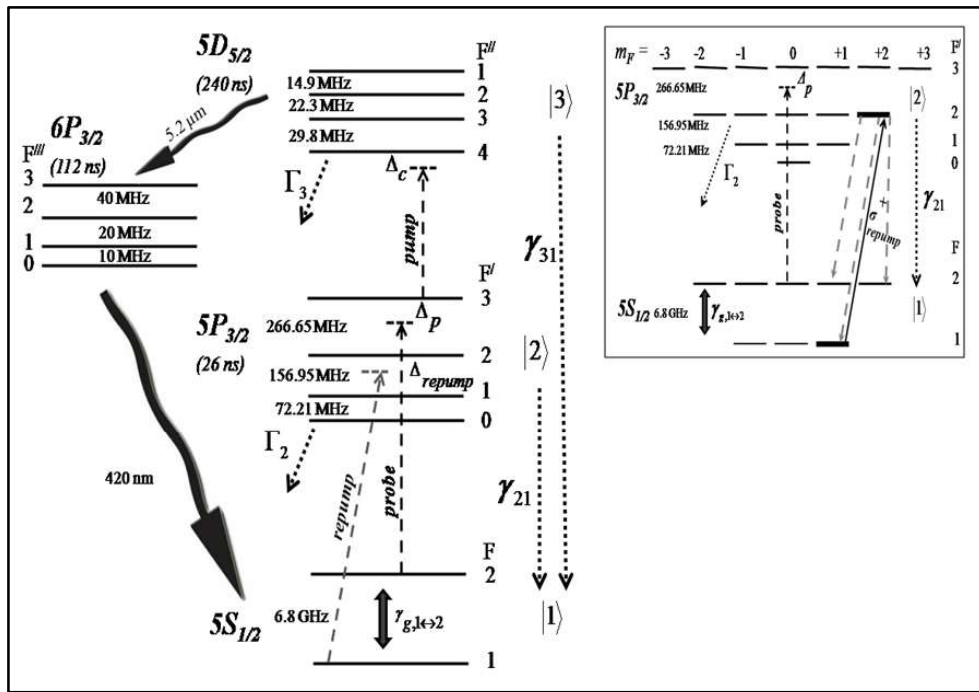


Fig. 6.1 Level scheme of ^{87}Rb $5S_{1/2} \rightarrow 5P_{3/2} \rightarrow 5D_{5/2}$ transition for current experiment. $\Gamma_3 = 2\pi \times 0.97 \text{ MHz}$, $\Gamma_2 = 2\pi \times 6.066 \text{ MHz}$, $\gamma_{ij} = (\Gamma_i + \Gamma_j)/2$, lifetimes of the levels are marked with the respective levels. In the inset Zeeman sublevel repumping is shown explicitly.

The condition for EIT in ladder system is $\Omega_c^2/\gamma_{21} \gg \gamma_{31}$. This is similar to the Λ linkage except for the higher dephasing rate. Generally for alkali vapour cell without buffer gas at room temperature one may expect the EIT line-width (Γ_{EIT}) [160] to hold $\gamma_{31} \ll \Gamma_{EIT} \ll \Omega_c^2/\Delta\omega_D$ true. Apart From the presence of EIT, state $|3\rangle$ gets populated via the two-photon absorption (TPA) which has a probability [161],

$$R_{1\rightarrow 3} = \frac{2\pi}{\hbar} \left| \left(\frac{\langle 3|\vec{d}\cdot\vec{E}_c|+\rangle\langle +|\vec{d}\cdot\vec{E}_c|1\rangle}{\left(\omega_{21} + \frac{\Omega_c}{2}\right) - \omega_p} \right) + \left(\frac{\langle 3|\vec{d}\cdot\vec{E}_c|-\rangle\langle -|\vec{d}\cdot\vec{E}_p|1\rangle}{\left(\omega_{21} - \frac{\Omega_c}{2}\right) - \omega_p} \right) \right|^2 \times \delta(\omega_{31} - \omega_p - \omega_p) \quad 6.1$$

where, $|\pm\rangle$ are the dressed states and arises due to the AC stark splitting of state $|2\rangle$. For two-photon resonance condition i.e. $\Delta_p + \Delta_c = 0$, TPA or transparency appears on the probe absorption spectrum at three different frequencies corresponding to $F' \rightarrow F'' = 4, 3, 2$ transitions [162]. The EIT in ladder system is comparatively less robust than the Λ system EIT. Practically the description of EIT in ladder system is incomplete without the consideration of the incoherent pumping present. This can arise from spontaneous emission and re-absorption cycle of both $|1\rangle \rightarrow |2\rangle$ and $|2\rangle \rightarrow |3\rangle$ transitions. In effect the incoherent pumping depletes the upper atomic level and the atomic population gets ‘radiation trapped’ or ‘lost’ to the uncoupled ground hyperfine state. This hinders the optical pumping required to produce EIT.

Atomic population from the excited states $|3\rangle$ and $|2\rangle$ can decay via different decay route. Finally it comes down to the ground hyperfine state $F = 1$ or $F = 2$. When the population is ‘lost’ to the uncoupled ground hyperfine state from the two photon absorption channel, we get DROP signal in the probe absorption spectra as is the case for close ladder system ($F = 2 \rightarrow F' = 3 \rightarrow F''$) [19,162]. Similarly when the ground hyperfine state receives more atoms from the excited state decay, we have the two-photon absorption (TPA) feature on the

probe absorption spectra and can be seen for spectroscopy in open ladder system ($F = 1 \rightarrow F' = 2 \rightarrow F''$) [154].

In this particular case, the method of controlling the coherence relies on the velocity selective recirculation of radiation trapped population from the uncoupled ground hyperfine state $F = 1$ to the $F = 2 \rightarrow F' = 3 \rightarrow F''$ ladder linkage. For this purpose we introduce a repump laser counter propagating to the probe laser connecting the $F = 1 \rightarrow F' = 2$ transition. Frequency of the repump laser satisfies the velocity selective Raman coupling condition [63], $2\vec{k} \cdot \vec{v} = \omega_{F=2} - \omega_{F=1} - (\omega_{repump} - \omega_p)$. However for large Ω_{repump} , one may expect the contribution from the other velocity groups of atoms which populates levels other than $F' = 2$ and this opens up additional decay channels which is detrimental to the repump mechanism. Therefore for effective repumping, Ω_{repump} should be around saturation intensity, ω_{repump} should be resonant with the strongest hyperfine transition and the mechanism has to be highly selective. The first two requirements are easily met by adjusting the repump laser intensity and frequency. To make the repump process highly selective, we consider degenerate Zeeman sublevel repumping ($|F = 1, m_F = +1\rangle \rightarrow |F' = 2, m'_F = +2\rangle$) [157] instead of general hyperfine repumping ($F = 1 \rightarrow F' = 2$, where all the magnetic sublevels get to share the population).

6.4 Experimental schemes

Experimental layout for this experiment is shown Fig. 6.2. The experiment can be divided into two parts. In the first part, we investigate the response of the closed ladder system under different repump conditions. In the second part of the experiment, we show the complexity in controlling the coherence in open ladder system. During the experiment, the frequency of the probe and repump laser was monitored using respective SAS set up. The pump laser frequency was monitored using a wavemeter as state $|3\rangle$ has a small Einstein 'A' coefficient.

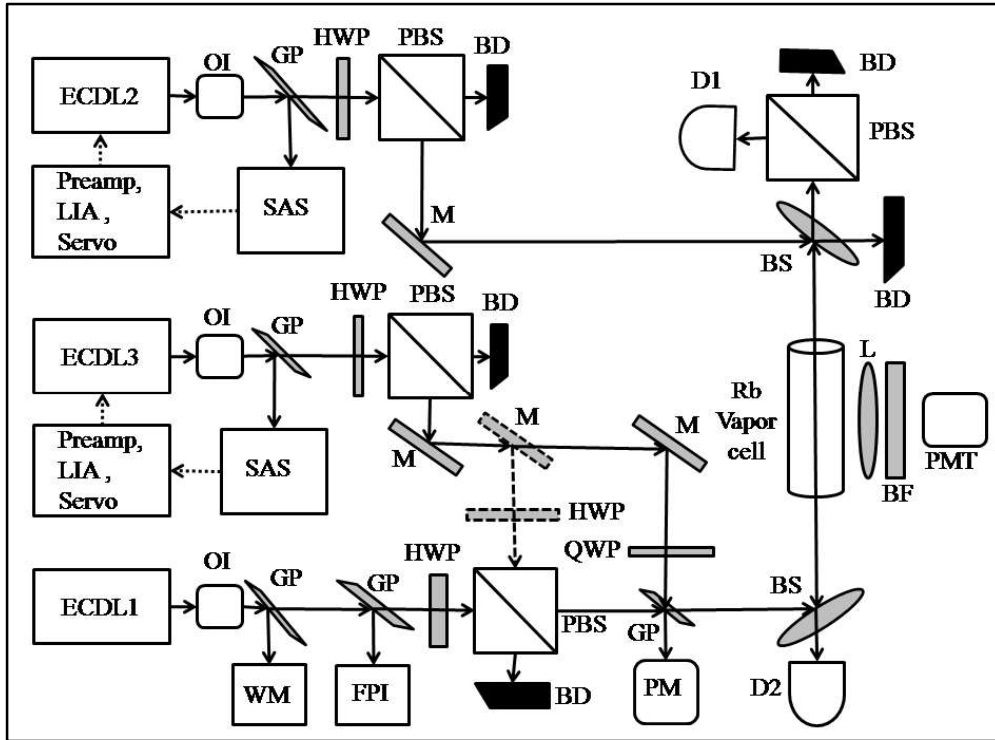


Fig. 6.2 Schematic of experimental arrangement for coherence control in ladder system. ECDLs: External cavity diode laser, M: Mirror, PBS: Polarizing beam splitter, OI: Optical isolator, BD: Beam dump, D1, D2: Photodetector, BS: Beam splitter, HWP: Half wave plate, QWP: Quarter wave plate, FPI: Fabry-Perot interferometer, PM: Power meter, WM: Wave meter, GP: Glass plate, L: Lens, BF: Blue filter, PMT: Photomultiplier tube, SAS: Saturation absorption spectroscopy

The pump and repump beam was counter propagating to the probe beam. During the experiment, the polarization of the repump beam was changed accordingly to address the normal hyperfine repumping (linear polarization) and Zeeman sublevel repumping (σ^+ polarization). Using PMT (Hamamatsu R5611 Photomultiplier tube) blue fluorescence was also detected.

In the first part of the experiment, probe laser was scanned while the pump laser was free running. As the data were taken within ~ 1 s time scale, the spectrum is only limited by the

laser line-width ($\sim 1\text{MHz}$). Repump laser was locked on $F = 1 \rightarrow F' = 2$ transition using current modulation and SAS set up. Similarly probe laser was locked and data recorded for pump scanning. The pump frequency scan was calibrated using Fabry Perot Interferometer (FPI).

The simple observations of DROP and EIT are not sufficient to emphasize the efficiency of coherence control as these are weighted by complex processes involving optical pumping, decay, etc. Simultaneous measurement of blue fluorescence ($\lambda = 420\text{ nm}$, originating from the decay channel $5D_{5/2} \rightarrow 6P_{3/2} \rightarrow 5S_{1/2}$) as a function of pump frequency provides a direct monitoring of atomic population at the $5D_{5/2}$ state [163]. This blue fluorescence is primarily limited by $2\pi \times 1.3\text{ MHz}$ due to the natural line-width of $6P_{3/2} \rightarrow 5S_{1/2}$ transition [164]. The major contributions to the total line-width of the blue fluorescence are residual Doppler broadening ($\sim 3\text{MHz}$), laserline-width ($\sim 1\text{MHz}$), transit time broadening ($\sim 0.05\text{ MHz}$) and contribution from optical misalignment. Contribution from power broadening is absent as laser power is below blue saturation intensity. Similarly the effect of atomic collision in the vapour cell is absent for room temperature Rb vapour cell without any buffer gas.

In the second part of the experiment, $F = 1 \rightarrow F' = 2 \rightarrow F''$ transition was chosen as the open ladder system and the repump laser was locked on $F = 2 \rightarrow F' = 2$ transition. The system was also studied for detuned two-photon resonance condition i.e. $\Delta_c + \Delta_p = 0, \Delta_c \neq \Delta_p \neq 0$.

6.5 Results and discussion

The saturation intensity for linearly polarized repump laser is $\sim 6.0\text{ mW/cm}^2$ whereas for σ^+ polarized repump it is $\sim 3.33\text{ mW/cm}^2$. The Rabi frequency corresponding to the saturation intensity of repump laser is $\sim 2\pi \times 4\text{ MHz}$. For the excited states we have considered data from [145]. For both types of repumping we have used 1.5 mW laser power

and corresponding Rabi frequency is $\sim 2\pi \times 10 \text{ MHz}$ for linear repump and $2\pi \times 13 \text{ MHz}$ for σ^+ repumping. The experimentally obtained line-width for DROP and EIT is $\sim 9.01 \text{ MHz}$ and $\sim 3.5 \text{ MHz}$ respectively [165].

The probe absorption signal without repump is shown in Fig. 6.3. DROP and EIT feature can be seen in it clearly. Fig. 6.3(a) and Fig. 6.3(b) represent the probe absorption spectra for probe scanning while the pump laser was free running. For detuned two-photon resonance condition, probe laser frequency was locked on cross-over resonance ($F = 2 \rightarrow F' = 2,1$). Similarly Fig. 6.3(c) and Fig. 6.3(d) is the probe absorption spectra for pump frequency scan while the probe frequency locked on respective SAS signal.

In Fig. 6.3(c) and Fig. 6.3(d) there is no Doppler background present while in Fig. 6.3(a) and Fig. 6.3(b) one can see its presence. This is due to the fact that the pump frequency scan was addressing a very small velocity group of atoms whereas for probe frequency scan, it can address very large velocity groups of atoms. From the figures one can also see that the EIT becomes prominent as we go further away from the perfect two-photon resonance condition which is contrary to the belief that EIT is strongest for perfect two-photon resonance condition. The reason is the relative competition between the two-photon phenomenon DROP and EIT. For the perfect two-photon resonance condition ($F = 2 \rightarrow F' = 3 \rightarrow F'' = 4$), the decay route forms a pseudo-closed absorption-emission cycle. However the population transfer to the $F = 1$ state is still very significant and thus giving rise to a DROP signal which can mask the EIT signal. For detuned two-photon resonance condition, optical pumping includes many more levels for the $F = 2 \rightarrow F' = 3,2,1 \rightarrow F''$ transition. Therefore the no. of decay channels leading to $F = 2,1$ are also more. At the same time the overall supply of atoms to F'' levels decreases due to off-resonant coupling of the probe laser. Interplay among these allowed absorption-decay routes complicates the level coupling picture. The result in Fig. 6.3 indicates that the overall decay of atoms to $F = 1$ state

decreases. This in turn weakens DROP and EIT and it is clearly visible on the spectrum. Similar observation was made by Moon et al [19].

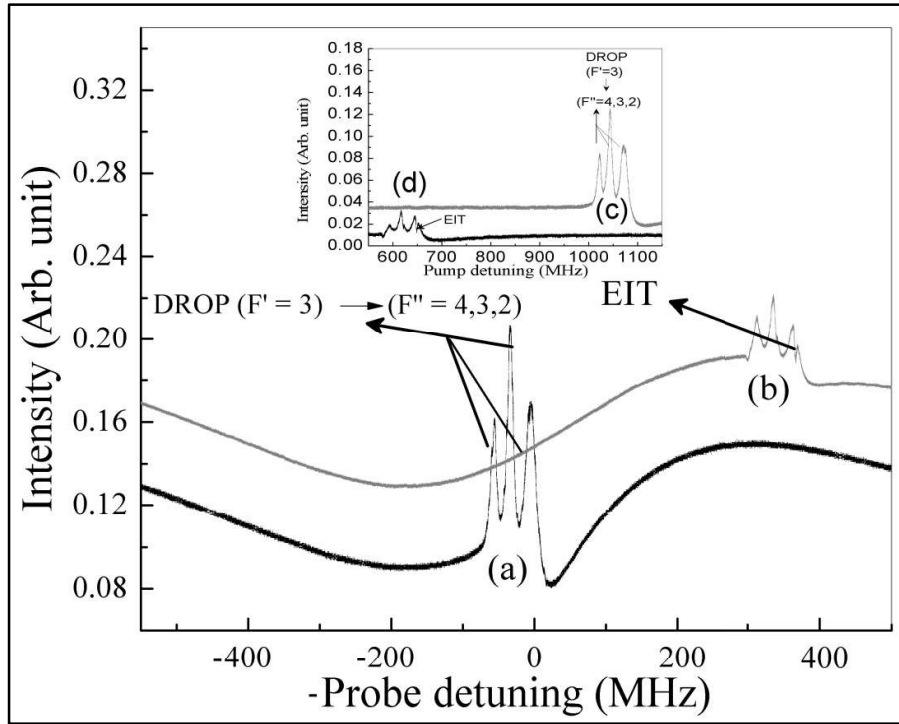


Fig. 6.3 Probe absorption spectra as a function of probe detuning. $\Omega_c = 2\pi \times 70$ MHz and $\Omega_p = 2\pi \times 9$ MHz. Spectrum was calibrated using SAS spectra. During experiment ω_c was adjusted to bring the system into (a) perfect two-photon resonance and (b) red detuned by ~ 345 MHz with respect to $F = 2 \rightarrow F' = 3$ transition. Inset shows the same spectra for pump scanning. ω_p was stabilized on (c) $F = 2 \rightarrow F' = 3$ transition and (d) $F = 2 \rightarrow F' = 2, 1$ transition.

Fig. 6.4 shows the blue fluorescence spectra obtained for normal hyperfine repump and Zeeman sublevel repump action. The spectra clearly show the presence of two-photon transition resulting from $5S_{1/2} \rightarrow 5D_{5/2}$ transition. The presence of repump enhances the population at $5D_{5/2}$ level due to strong TPA and weakening of DROP and can be clearly seen from the area under respective two-photon absorption signal (Table 6.1).

Table 6.1 Fitted fluorescence line intensities corresponding to $5S_{1/2}(F = 2) \rightarrow 5D_{5/2}(F'' = 4, 3, 2, 1)$ two-photon transition.

Normalized to A_1 under no repump situation	A_1	A_2	A_3
No repump	1	0.402	0.358
σ^+ polarized pump	1.544	0.641	0.529
Linearly polarized pump	1.507	0.798	0.708

Table 6.2 Fitted fluorescence line-widths corresponding to $5S_{1/2}(F = 2) \rightarrow 5D_{5/2}(F'' = 4, 3, 2, 1)$ two-photon transition.

Fluorescence line-width (MHz)	Γ_1	Γ_2	Γ_3
No repump	10.3	7.4	7.7
σ^+ polarized pump	9.1	7.1	6.7
Linearly polarized pump	9.4	7.1	7.7

The relative line strengths (A_i) and line-widths (Γ_i) are estimated from multi-peak fitting of the fluorescence spectra (Table 6.1 and Table 6.2). Around 50% enhancement in line-strengths clearly shows that it is possible to accumulate larger excited state population through repump action. Therefore the effect of incoherent pumping has been reduced through the velocity selective recovery of radiation trapped atoms. The effect of σ^+ repump is seen more on $F = 2 \rightarrow F'' = 4$ two-photon transition. This shows the effectiveness of Zeeman sublevel repumping compared to the normal hyperfine level repumping. For other transitions

($F = 2 \rightarrow F'' = 3, 2$) the effect of σ^+ repump is comparable with the normal hyperfine level repumping. This may be due to the higher dipole moment for $F = 2 \rightarrow F'' = 4$ transition. However $F = 2 \rightarrow F'' = 1$ transition is not observed on fluorescence spectra and the same can be said for the observation of hyperfine structure in $6P_{3/2}$ state. Low population density in the vapour cell may be the reason for this. It may also be noted that the usual proportionality of DROP and TPA strength may not remain valid when we are using repump.

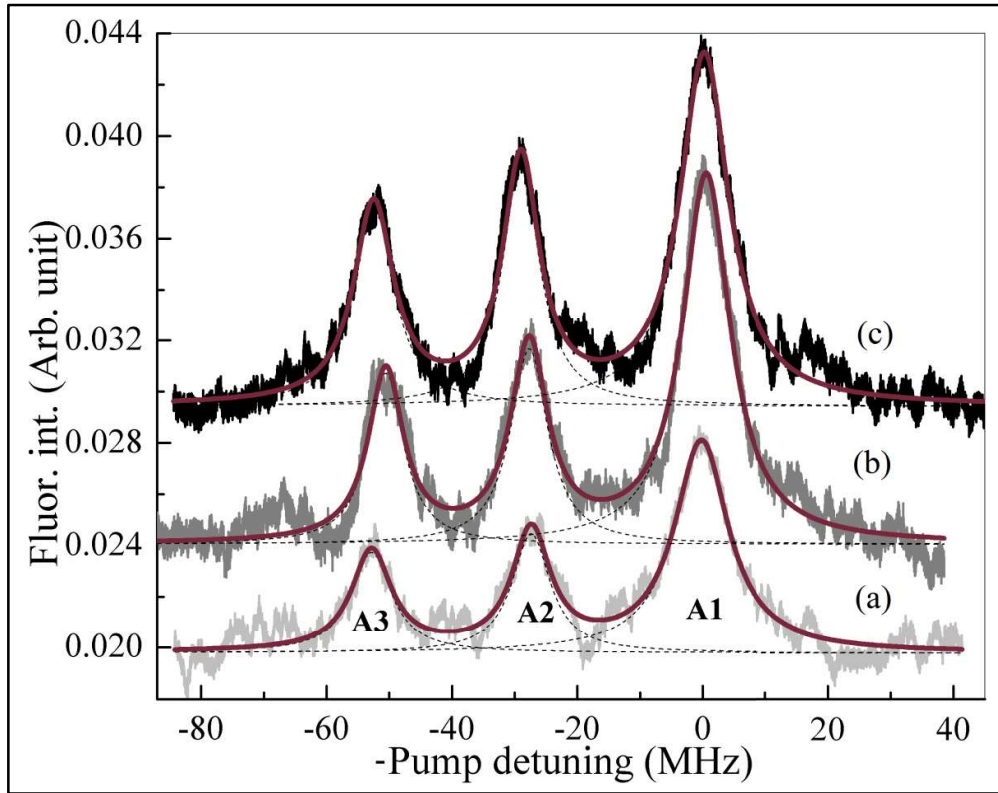


Fig. 6.4 Blue fluorescence spectra recording as a function of pump detuning from $6P_{3/2} \rightarrow 5S_{1/2}$ transition. Spectrum was calibrated using FPI. A1, A2 and A3 are the fitted area under the TPA peaks for (a) No repump, (b) σ^+ polarized repump and (c) linearly polarized repump. The profiles were fitted with Lorentzian multi-peak profiles. Extracted parameters are listed in Table 6.1.

Fig. 6.5 shows the effect of repump on probe absorption spectra for pump scanning. Effect of σ^+ polarized repump is shown in Fig. 6.5(a) whereas the same for linearly polarized

repump is shown in Fig. 6.5(b). The insets in the Fig. 6.5 show the multi-peak fitting on the highlighted portion of the spectrum. Lorentz line shape is considered for multi-peak fitting of the curve as the contribution from Doppler broadening is negligible for pump scanning. Relative line strength for EIT (ζ) is determined from the ratio of the area under EIT and total area under the DROP-EIT combination. Therefore, $\zeta = A_{k(EIT)} / \sum_{k=1 \rightarrow 3} A_k$ where k stands for all peaks including split DROP and EIT. ζ represents the ratio of the line strength of EIT and that of the two-photon absorption background. EIT line-width (Γ_{EIT}) was also extracted from the same fitting.

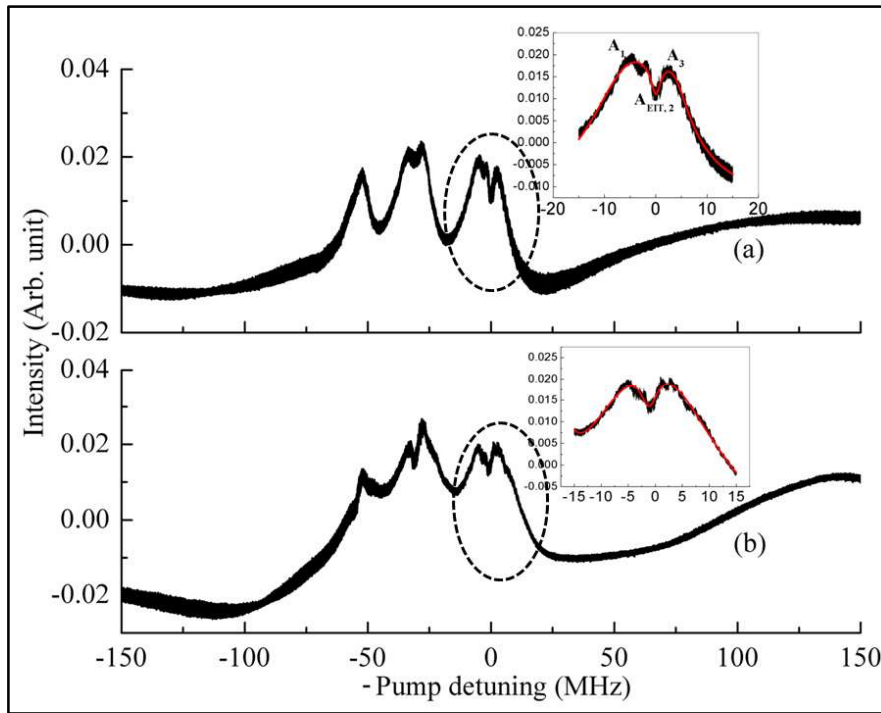


Fig. 6.5 Coherence control of DROP-EIT medium under $F = 2 \rightarrow F' = 3 \rightarrow F' = 4$ resonant coupling. (a) σ^+ repump of $\Omega_{repump} = 2\pi \times 13$ MHz. (b) Linear repump of $\Omega_{repump} = 2\pi \times 10$ MHz. Insets show snapshots of the highlighted part of the spectra. Fitted line profiles are Lorentzian (Red line in colour). A_k indicates k -th peak of DROP-EIT profile.

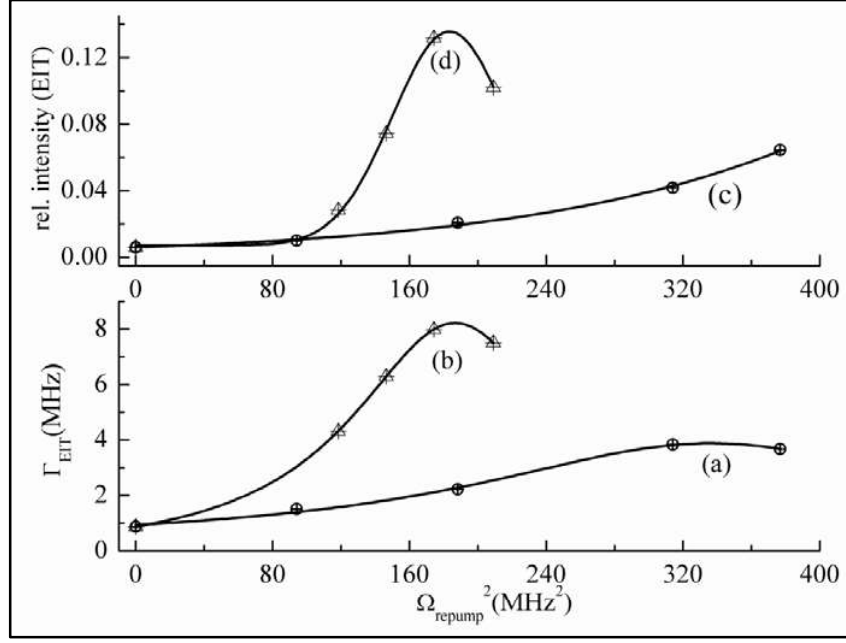


Fig. 6.6 Comparison of relative intensity (ζ) and line-width (Γ_{EIT}) of EIT vs repump intensity (a) for σ^+ repumping and (b) for linear repumping. Both (a) and (b) are fitted with Lorentzian function. (c) for σ^+ repumping and (d) for linear repumping. Both (c) and (d) are fitted with gaussian function. Details are in the text.

Fig. 6.6 shows the plots of ζ and Γ_{EIT} vs Ω_{repump}^2 data for different repump types. Fig. 6.6(a) and Fig. 6.6(b) show the plots of Γ_{EIT} vs Ω_{repump}^2 data and it fits well with Lorentz model for both types of repumping. This indicates homogeneous broadening character of EIT. For linear polarized repumping, Fig. 6.6(b) shows that Γ_{EIT} exceeds Γ_2 at a very moderate value of Ω_{repump}^2 compared to the σ^+ polarized repumping. For linear repump, increasing repump power may introduce additional dephasing which in turn broadens the EIT peak. Therefore one can conclude that EIT under linear repump is more prone to repump power broadening. Fig. 6.6(c) and Fig. 6.6(d) show the plots of ζ vs Ω_{repump}^2 data for linear and σ^+ polarized repump laser respectively. Both graphs fit well with Gaussian function indicating the velocity selective optical pumping enforced by repump action. The higher strength of EIT under linear repumping (Fig. 6.6d) indicates poor velocity selection compared

to σ^+ polarized repumping which adds additional degree of selectivity through Zeeman sublevel repumping.

It should be noted that repumping of atoms into ladder linkage adds clarity to EIT by reducing the DROP background but it also adds to the Γ_{EIT} . Hence the optimized condition depends upon a trade-off between Γ_{EIT} and ζ . One should choose a situation in which Γ_{EIT} remains sub-natural but a moderate increment in line intensity (ζ) compared to the case of no repump is obtained. This choice makes σ^+ repumping best candidate for coherence control in such a case.

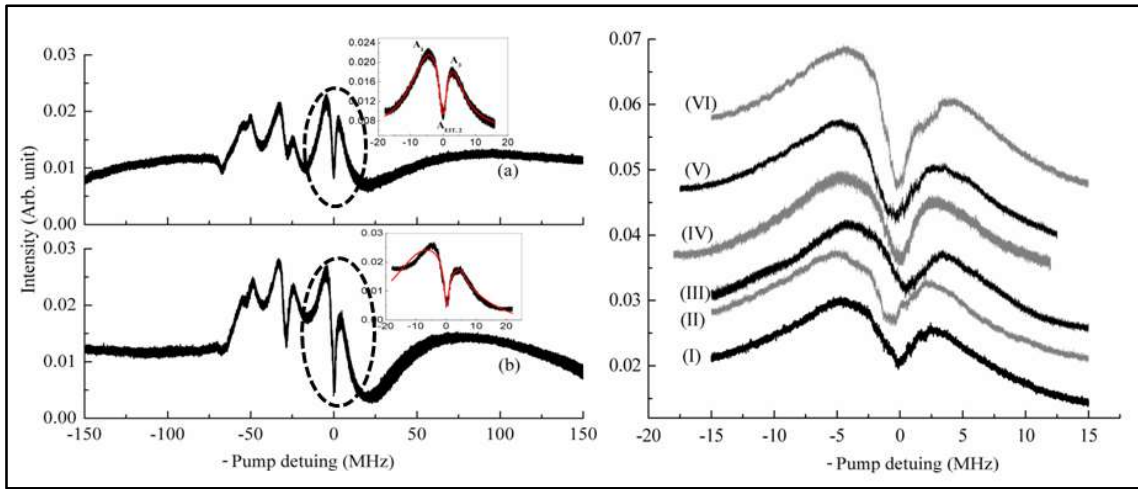


Fig. 6.7 Coherence control of DROP-EIT medium under detuned two-photon resonance where probe laser was locked on $F = 2 \rightarrow F' = 3,1$ crossover transition for (a) σ^+ repump and (b) linear repump. Repump power ~ 1.5 mW. Insets show the snapshot of the highlighted portion of the probe absorption spectra under pump scanning. Fitted line profiles are Lorentzian (Red lines in colour). (c) Evolution of the highlighted DROP-EIT part under varying repump power from 0.5 mW (I) to 3 mW (VI) with a increment of 0.5 mW each step. Pump and probe Rabi were fixed at $\Omega_c = 2\pi \times 80$ MHz and $\Omega_p = 2\pi \times 9$ MHz respectively.

Fig. 6.7 shows probe absorption spectra for pump scanning under detuned condition. The probe laser was detuned by ~ 212 MHz from resonance coupling and was locked on cross-over originating from the $F = 2 \rightarrow F' = 3$ and 1 transitions. Fig. 6.7(a) and Fig. 6.7(b) show the results for σ^+ and linear repumping respectively. Fig. 6.7(c) shows the change in the highlighted DROP-EIT portion of Fig. 6.7(a) over a range of Ω_{repump} values. For detuned two-photon resonance, probe addresses a wide range of excited states. As a result the number of permissible decay routes also increases and the corresponding branching ratios dominate the resultant spectrum.

Fig. 6.8 shows the plot of ζ and Γ_{EIT} vs Ω_{repump}^2 data for different repump types under detuned resonance condition. It can be seen from Fig. 6.8(a) and Fig. 6.8(c) that the behaviour of the ζ and Γ_{EIT} for σ^+ repumping under detuned resonance condition is similar to the behaviour for the perfect two-photon condition. For σ^+ repumping, Γ_{EIT} vs Ω_{repump}^2 plot (Fig. 6.8a) shows good fit to Lorentzian. Similarly, ζ vs Ω_{repump}^2 plot (Fig. 6.8c) shows good fit to Gaussian function indicating the preservation of velocity selective optical pumping feature even under detuned two-photon resonance condition for σ^+ repumping. The same can't be said for linear repumping. Fig. 6.8(b) and Fig. 6.8(d) show that the behaviour of the ζ and Γ_{EIT} for linear repumping under detuned resonance condition. The usual fitting of Gaussian and Lorentzian function does not work in the case of linear repumping and the dependence is far more complex than the earlier resonance case. Therefore from the previous observations one can conclude that σ^+ repumping offers better control over velocity selection in both cases (resonance and detuned) and it helps in precise control of the transparency window.

One must note here that a ladder system with one additional repump laser under detuned two-photon resonance condition simultaneously satisfies a tripod [67] or inverted Y [26] level

coupling. In these types of systems two ‘dark’ resonances can be observed which arises from respective ladder and Λ coupling schemes. Its practical manifestation is the convolution of two different EITs which exhibits high degree of asymmetry. However in the present experimental arrangement, repump laser is counter propagating to the probe laser and thus two-photon resonance condition for EIT in Λ system can’t be met. Therefore the arrangement simply favours the velocity selective Raman process. In effect the role of repump laser as a means for population recirculation is still valid for detuned resonance condition. For the perfect two-photon resonance condition, the tripod linkage breaks down as the repump laser can’t address $F = 1 \rightarrow F' = 3$ transition. Therefore the EIT in such condition is arising purely out of the ladder linkage.

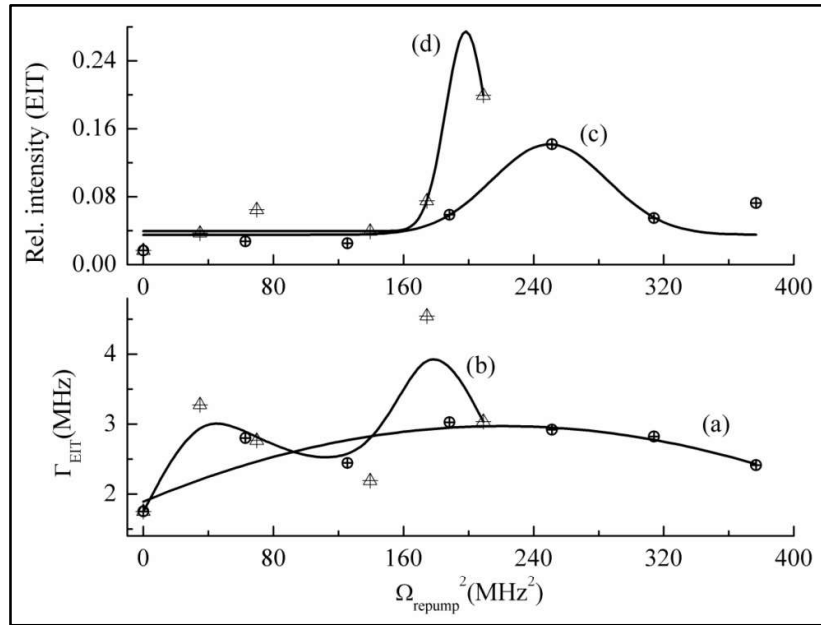


Fig. 6.8 Comparison of relative intensity (ζ) and line-width (Γ_{EIT}) of EIT vs repump intensity (a) for σ^+ repumping and (b) for linear repumping. Only (a) can be fitted with Lorentzian function and B-spline curve is added to the (b) data. (c) for σ^+ repumping and (d) for linear repumping. Only (c) shows good fit to Gaussian function. For (d) B-spline curve is added to the data. Details are in the text.

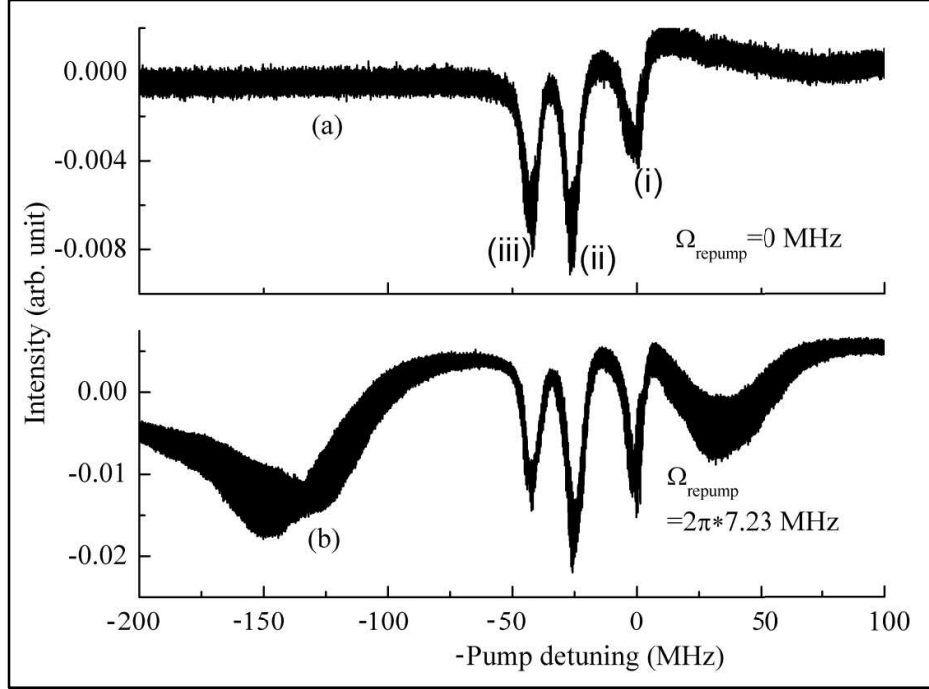


Fig. 6.9 Example of open system TPA. under linearly polarized repump for (a) zero repump Rabi and (b) $\Omega_{repump} = 2\pi \times 7.23 \text{ MHz}$. Here pump and probe Rabi were $\Omega_c = 2\pi \times 80 \text{ MHz}$ and $\Omega_p = 2\pi \times 2.5 \text{ MHz}$ respectively. TPA peaks correspond to $F = 1 \rightarrow F'' = 3, 2, 1$ transitions and are marked with (i), (ii) and (iii) respectively. Under repump TPA becomes stronger but no EIT can be seen.

Finally we considered $F = 1 \rightarrow F' = 2 \rightarrow F''$ level coupling as the open ladder system for investigation. The repump laser was chosen between $F = 2$ and $F' = 2$ state. Relevant Rabi frequencies were $\Omega_c = 2\pi \times 80 \text{ MHz}$ and $\Omega_p = 2\pi \times 2.5 \text{ MHz}$. Fig. 6.9(a) shows the probe absorption spectra without any repump for pump scanning and probe laser fixed on $F = 1 \rightarrow F' = 2$ transition. Three TPA signals can be clearly seen on one photon probe absorption profile and unlike the earlier case (closed ladder system) TPAs appear as the absorption signal on the probe absorption spectra. Fig. 6.9(b) shows the same spectra when a repump laser of $\Omega_{repump} = 2\pi \times 7 \text{ MHz}$ is used. Though no EIT is observed in this case still the repump laser enhances the TPA signal. From Fig. 6.9 it is evident that the influence of

repump laser under open ladder system is much weaker than the closed ladder system. This is due to the fact that in the open ladder system, the one photon transition $F = 1 \rightarrow F' = 2$ is an open one while in the close ladder system it is a closed transition ($F = 2 \rightarrow F' = 3$). In order to observe EIT in open ladder system one needs to make $I_c:I_p \sim 1350:1$, which is much larger than the present ratio of pump and probe laser intensity.

6.6 Conclusion

Present investigation establishes the repump control of existing coherence in the close ladder system of $^{87}\text{Rb } 5S_{1/2}(F = 2) \rightarrow 5P_{3/2}(F') \rightarrow 5D_{5/2}(F'')$ transition. The counter propagating configuration of repump and probe laser beam paves the way for velocity selective Raman transitions. Such transition helps in restoring the radiation trapped population from the uncoupled $F = 1$ state. This restoration in turn improves the effective optical pumping required for EIT. This is justified through the control of EIT line-width (Γ_{EIT}) and line strength (ζ) as a function repump laser intensity for a fixed set of pump-probe combination. It is shown that in controlling the coherence, σ^+ repump offers much more optimized solution compared to the linear repump for both perfect two-photon resonance and detuned two-photon resonance condition. We have also observed the effect of linear repump laser in resonant, open ladder coupling. Repump laser only strengthens the TPA but no EIT can be seen in such system. More study on this system is required especially to understand the influence of laser power on coherence control.

Chapter 7

Double dark resonance in inverted Y system and its effect on optical switching

7.1 Introduction

The application of electromagnetically induced transparency (EIT) as a novel type of memory has got enough attention in the field of optical communication. Light pulses also get slow and spatially compressed in this type of transparency. Therefore, newer means of controlling and manipulating the transparency window in a multilevel atomic system will open unknown avenues of research. In this chapter we will discuss the relevant works in the ^{87}Rb ($5S_{1/2} \rightarrow 5P_{3/2} \rightarrow 5D_{5/2}$) inverted Y system. The appearance of double dark resonance is a typical signature of this system. This kind of system is an extension of the ladder system with one additional laser coupling. The formation of matched double dark resonance and its application in the field of optical switching was investigated by us and we have found that the double dark resonance plays important role in attenuating the optical switching action. It has also been found that the overall system works as a combination logic gate. In the following sections we will discuss the motivations and the results of the conducted experiment.

7.2 Motivation

Dark resonances appearing from the atom-photon interaction manifests itself in the detection of EIT [2,76] and CPT [152]. They have important applications in the field of atomic clock [6], ultra-sensitive magnetometer [5], optical switch [13], frequency conversion [17], slowing down of light [4], detection of high lying Rydberg states [166] etc. These coherence associated phenomena in three-level linkage pattern was already studied in atomic vapours [167,168], quantum-dot materials [169], photonic micro-circuits, nano-photonic

device etc [170] and in many other applications. In the modern optical communication network, optical switching plays a very important role.

Currently considerable efforts have been put to study the multiple dark resonances appearing in different systems such as N type [23], tripod or inverted Y type [26,27,28,29] etc. Anton et al [30] have explored the application of optical switching in N -tripod type system. On the other hand Min Yan et al [31] have found a way to suppress the two-photon absorption in an inverted Y system using quantum interference.

Pump-probe spectroscopy on $5S_{1/2} \rightarrow 5P_{3/2} \rightarrow 5D_{5/2}$, rubidium (^{87}Rb) ladder (Ξ) system reveals double resonance optical pumping (DROP) and EIT because of the two-photon absorption (TPA) occurring in the system. In this type of system EIT manifest itself as a narrow transparency window within the DROP/TPA spectrum [19,154]. Previous studies on the same ladder system have shown that a bi-modal slow-fast switching could be implemented in the same system [150]. It was also shown that the intensity modulation depth can be increased and the coherence of such a system can be controlled with the help of additional repump laser [157,171]. In all these previous works counter propagating probe-repump configuration was used. In the present work we have used a third laser co-propagating with the probe laser and is termed as the ‘control’ laser for the present experiment. This co-propagating configuration introduces additional ‘dark resonance’ in the system from the interplay between control and probe laser. Present work aims at exploring the interplay among these dark resonances in an inverted Y system and its application in optical switching. As it will be shown in the latter sections that the appearance of ‘double dark resonance’ (DDR) results in attenuation of the usual three-level pump-probe switching action.

7.3 Optical switching in an inverted Y level scheme

The level scheme for the present experiment is shown in Fig. 7.1. The chosen manifold is the $5S_{1/2}(F = 2, 1) \rightarrow 5P_{3/2}(F' = 3, 2, 1) \rightarrow 5D_{5/2}(F'' = 4, 3, 2)$ level coupling of ^{87}Rb atom. The external control field is applied between $F = 1$ and $F' = 2$ hyperfine levels. In this type of inverted Y coupling, two different EITs originate from the respective ladder linkage ($F = 2 \rightarrow F' = 2 \rightarrow F'' = 3, 2, 1$) and the Λ linkage ($F = 2 \rightarrow F' = 2 \leftarrow F = 2$). When the control and the probe laser does not address the same middle level ($|2\rangle$), the overall system almost acts as two independent ladder linkages ($F = 2 \rightarrow F' \rightarrow F''$ and $F = 1 \rightarrow F' \rightarrow F''$). Inverted Y connection forms only when the middle levels addressed by the probe and the control laser are the same.

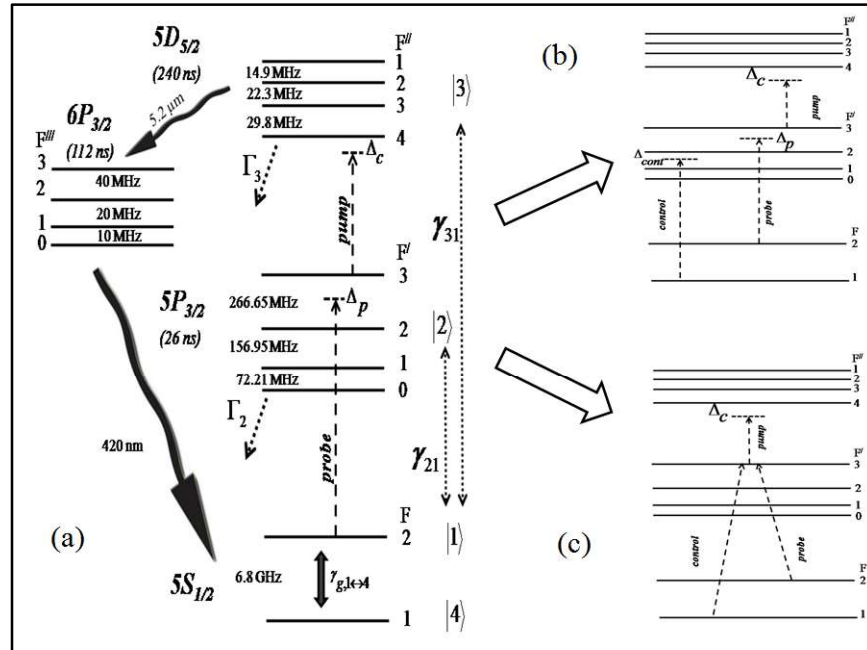


Fig. 7.1 Level coupling scheme for inverted Y system. (a) ^{87}Rb $5S_{1/2} \rightarrow 5P_{3/2} \rightarrow 5D_{5/2}$ isolated ladder connection. (b) Two simultaneous ladder system due to probe and control laser. (c) Resonant inverted Y connection. Lifetimes of the levels are mentioned alongside the level marking.

EIT in a Λ system appears only when the probe and the control laser is in the co-propagating configuration whereas for a ladder system, pump and probe laser have to be in counter propagating configuration for EIT to appear. In an inverted Y system, EIT is the mixture of these two types of EITs. Under such circumstance, the solution of the system Hamiltonian provides a set of three eigenvalues out of which two are null [26]. The corresponding eigenstates are the linear combination of F and F'' states. This situation generates a scope of constructing matched double dark state by carefully choosing the field parameters. In a matched DDR, the usual three-level pump-probe coherence converts into a four level coherence. Experimental demonstration of the creation of a matched double dark state can be done by monitoring the DROP spectra and simultaneous recording of the blue fluorescence originating from the $5D_{5/2} \rightarrow 6P_{3/2} \rightarrow 5S_{1/2}$ decay route.

Fast optical switching can be achieved using EIT. Sometimes one requires selective switching for greater control over the switching action. In this regard the on-off control over the three-level EIT using DDR may act as an extra handle. It is found that the transfer of intensity switching from pump to probe beam in a three-level coherence assisted switching can almost be attenuated with the help of DDR. The situation may also be linked to the response of a combination logic gate.

To clarify the above mentioned points, let us consider the coupling scheme as depicted in Fig. 7.1. The whole coupling scheme can be thought of as a combination of two ladder (Ξ) scheme (originating from $F = 1$ and $F = 2$) and a Λ coupling scheme. When $\Omega_{cont} \gg \Omega_p$ and $\Omega_{cont} < \Omega_c$, the so called ‘dark states’ of the system can be written as,

$$|NC1\rangle \approx |1\rangle - \frac{\Omega_p}{\Omega_c} |3\rangle \tag{7.1}$$

$$|NC2\rangle = \frac{\Omega_c}{\sqrt{\Omega_c^2 + \Omega_{cont}^2}} |4\rangle - \frac{\Omega_{cont}}{\sqrt{\Omega_c^2 + \Omega_{cont}^2}} |3\rangle$$

$$|NC3\rangle \approx |1\rangle - \frac{\Omega_p}{\Omega_{cont}} |4\rangle$$

where the states $|NC1\rangle$ and $|NC2\rangle$ appears from the ladder connection whereas $|NC3\rangle$ appears due to the Λ connection. The dark states are constructed following the convention of Marangos [22]. The eigenvalues of the inverted Y system are $0, 0, \sqrt{\Omega_p^2 + \Omega_{cont}^2 + \Omega_c^2}$ which is similar to that of a tripod system except that the inverted Y system has more decoherence effect. Here the '0' eigenvalues correspond to the dark states $|NC1\rangle$ and $|NC3\rangle$. Therefore two distinct EIT can be seen in the probe absorption spectrum (Fig. 7.2). Under favourable condition these two dark states superimpose with each other and form a matched double dark state [27]. As a result the medium becomes completely transparent to the probe laser. Practicality of such a situation is justified as the separation between ^{87}Rb hyperfine ground states $F = 2$ and $F = 1$ is $\sim 6.8 \text{ GHz}$ which is much greater than the pump laser Rabi frequency.

The transfer of intensity switching from the pump laser to the probe laser can be seen in an isolated ladder (Ξ) system. This is unlikely in an inverted Y system when the condition of double dark resonance is satisfied as the influence of the Λ system also comes into picture. In principle, the intensity switching of the pump laser should be mapped onto the probe laser through coherence. The effect of intensity switching in a Doppler broadened inverted Y system can be described in terms of susceptibility [26,143,28] which can be written as,

$$\chi(v)dv = \frac{id_{21}^2/(\hbar\epsilon_0)}{\gamma_{21} - i\Delta_p - i\frac{\omega_p}{c}v + \frac{\Omega_{cont}^2}{4} \left[\frac{1}{\gamma_{g,1\rightarrow 4} - i(\Delta_p - \Delta_{cont}) - i(\omega_p - \omega_{cont})\frac{v}{c}} \right] + \frac{\Omega_c^2}{4} \left[\frac{1}{\gamma_{31} - i(\Delta_p - \Delta_c) - i(\omega_p - \omega_c)\frac{v}{c}} \right]} N(v)dv \quad 7.2$$

where $\Delta_p = \omega_p - \omega_{21}$ ($\Delta_c = \omega_c - \omega_{32}$) is the detuning of the probe (pump) laser beam and Ω_p (Ω_c) is the Rabi frequency of the probe (pump) laser beam. $\Delta_{cont} = \omega_{cont} - \omega_{24}$ and Ω_{cont} is the detuning and the Rabi frequency of the control laser beam. $\gamma_{g,1\rightarrow4}$ is the coherent dephasing between state $|4\rangle$ and $|1\rangle$ and is determined by the transit time broadening in this case. $\gamma_{ij} \approx (\Gamma_i + \Gamma_j)/2$ is the coherence decay rate for $|i\rangle \rightarrow |j\rangle$ transition. d_{21} is the dipole matrix element between state $|2\rangle$ and $|1\rangle$. Γ_i is the spontaneous decay rate from state $|i\rangle$. For a vapour cell containing Rubidium atom at thermal equilibrium, $N(v)$ is the Maxwell-Boltzmann velocity distribution. Weak probe field approximation is considered while deriving equation (7.2) and also the contribution from upper levels is neglected due to negligible population in the upper states. The imaginary part of the susceptibility (χ) is proportional to the probe laser absorption coefficient. In this case ω_p and ω_c are very close to each other and therefore Doppler broadening of the two-photon transition is neglected in the simulation. Intensity switching can be incorporated phenomenologically in equation (7.2) by substituting $\Omega_c^2 \rightarrow \Omega_0^2(C_1 + C_2 \cos \omega_m t)$. The constants C_1 and C_2 should be adjusted in a way so that the bare minimum value for optical pumping is maintained. This bare minimum value can be obtained from $\Omega_c^2 \gg 4\gamma_{21}\gamma_{31}$ for ladder EIT and $\Omega_{cont}^2 \gg 2\gamma_{21}\gamma_{g,1\rightarrow4}$ for Λ EIT. One can see that the minimum necessary optical pumping for Λ EIT is far less compared to the ladder EIT as the coherent dephasing between the dipole forbidden states ($\gamma_{g,1\rightarrow4}$ and γ_{31}) is different for the two cases.

Fig. 7.2 shows the results of the simulation of equation (7.2). The imaginary part of the complex susceptibility, $Im(\chi)$, is plotted as function of probe detuning (Δ_p) under two different conditions. In Fig. 7.2(a) two different EITs are observed with different line-widths for $\Delta_c = 0$ and $\Delta_{cont} = 2\pi * 40 \text{ MHz}$. The narrower EIT appears from the Λ connection while the other one appears from the ladder connection.

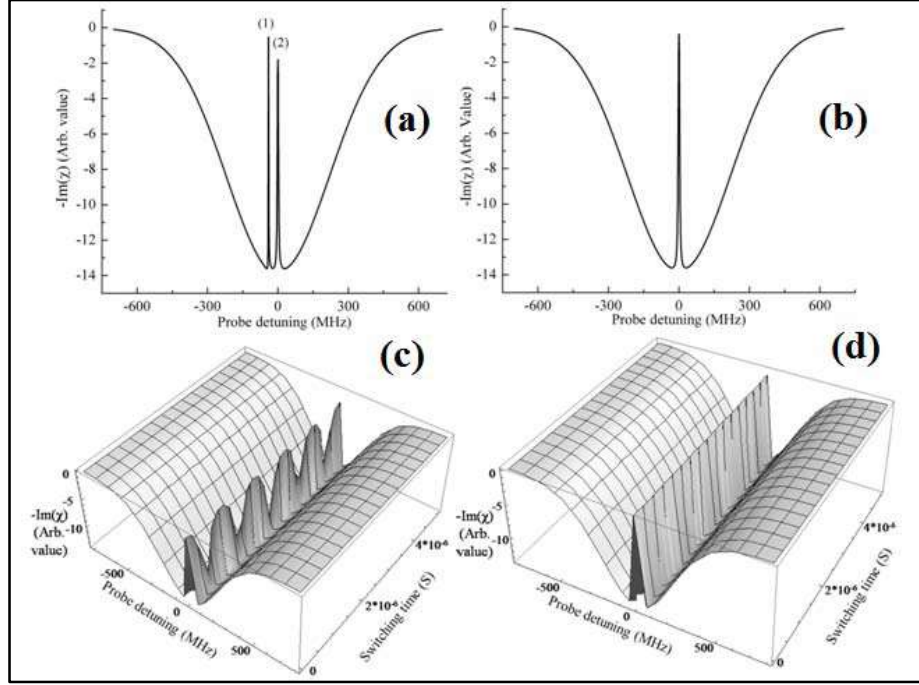


Fig. 7.2 Simulation of optical switching in inverted Y system. (a) shows $-\text{Im}(\chi)$ vs probe detuning (Δ_p) when ladder (peak 2) and Λ (peak 1) systems are separate. (b) shows $-\text{Im}(\chi)$ vs Δ_p when the two subsystems are resonant and forms a resonant inverted Y system. (c) and (d) depict the intensity switching under condition (a) and (b) respectively. Vanished switching in (d) represents the on resonant inverted Y system. Chosen values are $C_1 = 0.54, C_2 = 0.54, \Omega_c = 2\pi * 50, \Omega_{cont} = 2\pi * 30, \omega = 2\pi \text{ MHz}, \Delta_c = 0 \text{ MHz}$.

The line-widths of the EITs are dominated by the coherent dephasing between the dipole forbidden states. For Λ connection it is γ_{14} ($\sim 2\pi * 0.05 \text{ MHz}$) and for ladder connection it is γ_{13} ($\sim 2\pi * 0.5 \text{ MHz}$). In Fig. 7.2(b) both of them merge ($\Delta_c = 0$ and $\Delta_{cont} = 0 \text{ MHz}$) and open up the possibility of prospective controlling the ladder EIT by the Λ EIT. For the simulations the constants C_1, C_2 are so adjusted that the bare minimum value of optical pumping is maintained. This minimum value of optical pumping required for Λ EIT much less compared to the ladder EIT. Fig. 7.2(c) and Fig. 7.2(d) show the effect of pump intensity

switching at frequency $\sim 1\text{MHz}$. For the matched DDR condition no transfer of switching to the probe laser can be seen (Fig. 7.2d).

7.4 Experimental arrangement

The experimental layout for the present experiment is shown in Fig. 7.3. The linearly polarized lasers (pump, probe, control) address the ^{87}Rb hyperfine manifold as described in previous section. The coarse wavelength readouts are taken from a wavemeter (WaveMaster, Coherent Inc). SAS set ups (prepared using retro-reflection as well as polarization spectroscopy technique) are used for probe and control lasers for scanning and locking purpose.

The control laser is frequency modulated and locked on the derivative signal of $F = 1 \rightarrow F' = 2$ transition. One part of the co-propagating probe and control laser combination is sent through a separate vapour cell to satisfy the Λ configuration. The probe laser was locked on the Λ EIT signal using atomic frequency offset locking technique [41]. The pump laser is scanned over the $F' \rightarrow F''$ manifold.

The probe beam is double passed through an acousto-optic modulator (AOM1) [172]. This double pass arrangement does not change the beam path while using the AOM for scanning the laser frequency by changing the rf modulation frequency. Another acousto-optic modulator (AOM2) is used in the latter stage as the frequency shifter with a final frequency offset of $(\delta\omega_{AOM2} - 2\delta\omega_{AOM1})$. This arrangement helps us to scan probe laser frequency with finer steps (highest precision $\sim 3\text{MHz}$). The main part of the probe-control laser combination is sent through another Rb vapour cell (room temperature and without buffer gas) counter propagating to the pump laser beam to form the inverted Y system. In order to monitor the pump laser frequency, we have used a FPI cavity (FSR 1500MHz). An electro-optic

amplitude modulator (EOAM) is used for pump laser intensity switching. Both pump and probe laser intensity is monitored using respective photo-detectors.

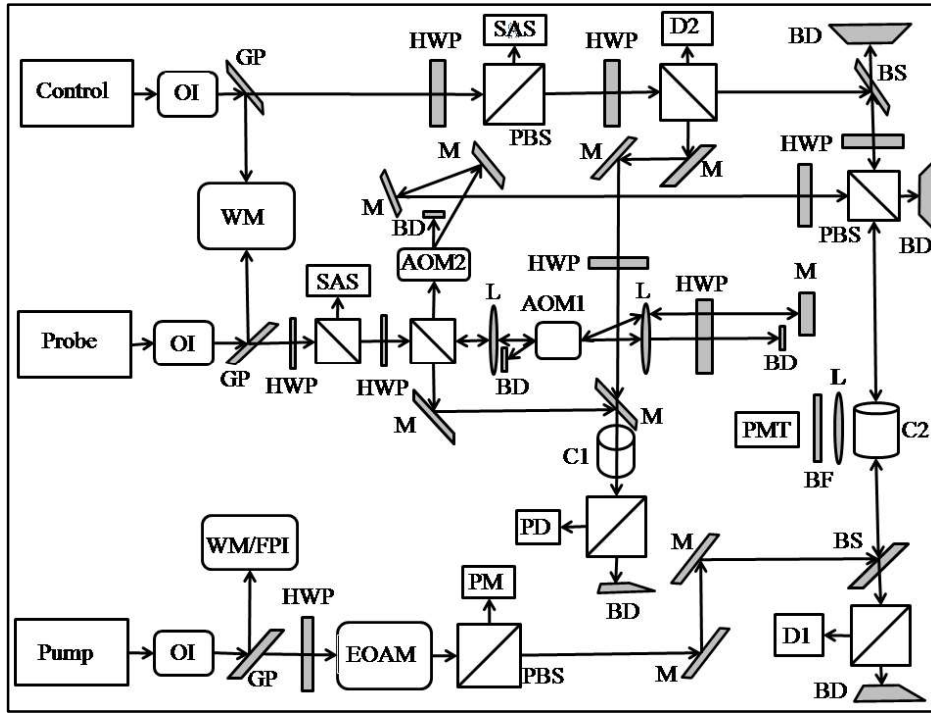


Fig. 7.3 Schematic of experimental arrangement for DDR in inverted Y system. Control, probe and pump are the ECDL lasers, M: Mirror, L: Lens, HWP: Half wave plate, D1, D2, PD: Photo-detectors, BS: Beam splitter, WM: Wavelength meter, FPI: Fabry-Perot interferometer, PM: Power meter, BD: Beam dump, EOAM: Electro-optic amplitude monitor, PBS: Polarizing cubic beam splitter, SAS: saturation absorption spectroscopy set-up, OI: Optical isolator, GP: Glass plate, C2, C1: Rubidium vapour cell, BF: Blue light filter, PMT: Photomultiplier tube, AOM1, 2: Acousto-optic modulator.

7.5 Results and discussion

The line-width of an EIT [173] under ladder coupling scheme is given by Ω_c^2/γ , where the homogeneous line-width γ consists of all the possible decay rates from the uppermost level

($5D_{5/2}$) to the other levels. The life-time of $6P_{3/2}$ level (112 ns) is much longer compared to the $5P_{3/2}$ level (26 ns). Therefore several optical pumping and decay cycles centred on $5P_{3/2}$ level can be integrated over a single lifetime of $6P_{3/2}$ level. On the other hand the lifetime of $5D_{5/2}$ level (240 ns) is roughly twice that of the $6P_{3/2}$ level. Hence one can say that the spontaneous decay through the $5D_{5/2} \rightarrow 6P_{3/2} \rightarrow 5S_{1/2}$ channel will replicate the hyperfine structure of the $5D_{5/2}$ level. Therefore the blue fluorescence can act as an effective monitor for the whole excitation decay process. The blue fluorescence was recorded simultaneously with the probe absorption spectrum during the experiment and the results are discussed in the following subsections.

7.5.1 First part of the experiment

The experiment was conducted in three parts. In the first part of the experiment, we tried to investigate the behaviour of the system (inverted Y) while the sub-systems (Ξ and Λ) behave independently. The results are presented in Fig. 7.4 and Fig. 7.5. Λ linkage is formed by the $F = 2 \rightarrow F' = 2 \leftarrow F = 2$ transition and $F = 2 \rightarrow F' = 3 \rightarrow F''$ forms the ladder linkage. Pump frequency is detuned from the $F' = 3 \rightarrow F'' = 4, 3, 2$ transition. Fig. 7.4(a) shows the resulting EIT in the reference Rb vapour cell C2 (Fig. 7.3) where all the three laser beams interact. Fig. 7.4(b) shows the spectrum for another reference cell C1 where only probe and control lasers interact. Both the spectrum appears to be same as the sub-systems work independently even under the presence of all the lasers. Line-width of the Λ EIT ($\Gamma_{\Lambda EIT}$) is plotted as a function of the experimental Rabi frequency (Ω_{cont}) of the control laser and is shown in the inset of Fig. 7.4. It is clearly seen that $\Gamma_{\Lambda EIT} \propto \Omega_{cont}$. In general, line-width of the EIT for this isolated Λ system is given by [174],

$$\Gamma_{EIT} = \sqrt{\frac{2\gamma_{14}}{\Gamma/2}} \Omega_{cont} \sqrt{1 + \left(\frac{\Omega_{cont}}{\Omega_{sat}}\right)^2} \quad 7.3$$

where $\Omega_{sat} = \Delta\omega_D * \sqrt{\gamma_{14}/\Gamma}$ is the saturation intensity and $\Delta\omega_D$ is the FWHM of the Doppler width. One can see from equation (7.3) that $\Gamma_{EIT} \propto \Omega_{cont}$ for $\Omega_{cont} \ll \Omega_{sat}$ and the very condition for the bare minimum optical pumping is also maintained under the same condition.

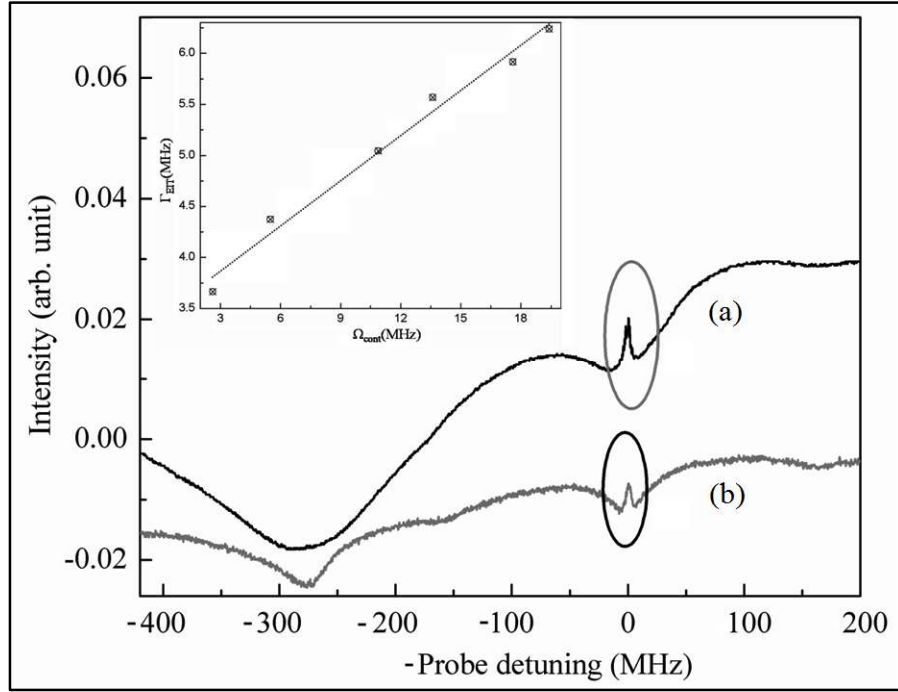


Fig. 7.4 Probe absorption spectra for Λ connection in inverted Y system. (a) The pump-probe-control lasers interact in the main ^{87}Rb vapour cell C2 with probe (control) addressing $F = 2 \rightarrow F' = 2$ ($F = 1 \rightarrow F' = 2$) transition. The pump is detuned from $F' \rightarrow F''$ transition domain. (b) The probe-control interacts in the reference cell C1 with no pump present. The highlighted signals show the corresponding EIT feature. Inset shows the Γ_{EIT} vs Ω_{cont} plot for $\Omega_p = 2\pi * 2 \text{ MHz}$ and it can be seen that $\Gamma_{EIT} \propto \Omega_{cont}$.

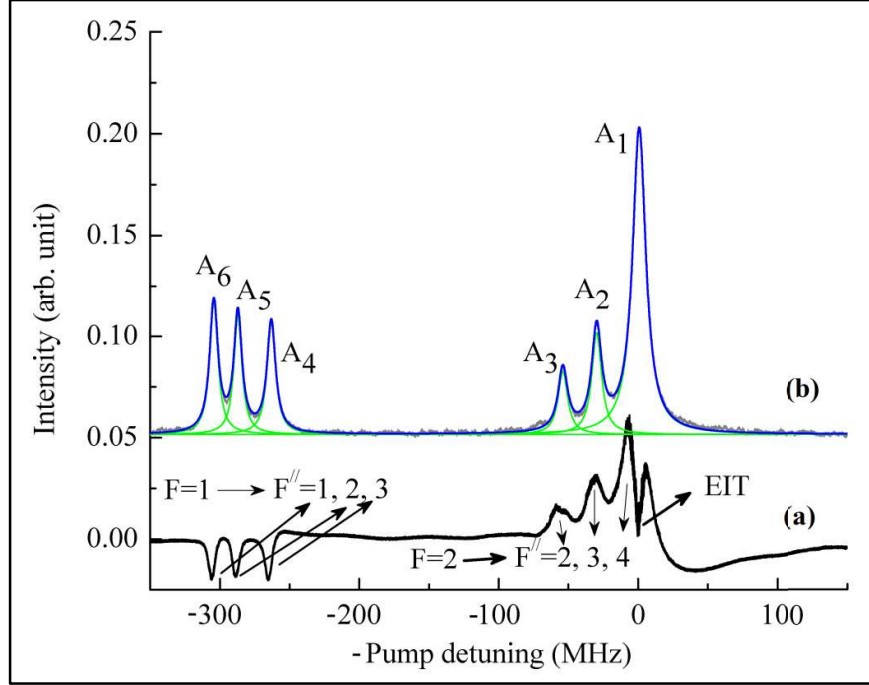


Fig. 7.5 Probe transmission and blue fluorescence spectra in inverted Y system. (a) probe transmission under pump scanning. (b) Corresponding blue fluorescence peaks. Fluorescence peaks are marked according to the associated linkages. Corresponding Rabi frequencies are $\Omega_p = 2\pi * 2 \text{ MHz}$, $\Omega_{cont} = 2\pi * 6 \text{ MHz}$, $\Omega_c = 2\pi * 80 \text{ MHz}$. Clear EIT signal can be seen on $F = 2 \rightarrow F'' = 4$ peak. Blue fluorescence peaks are fitted with multi-peak Lorentzian function and the results are listed in Table 7.1.

This situation is much more clarified in Fig. 7.5. The pump laser is scanned over the $F' \rightarrow F''$ domain while the probe (control) laser frequency is fixed on $F = 2 \rightarrow F' = 3$ ($F = 1 \rightarrow F' = 2$) transition. The results clearly show the existence of two ladder systems ($F = 2 \rightarrow F' = 3 \rightarrow F''$ and $F = 1 \rightarrow F' = 2 \rightarrow F''$). Under this condition, the population from $5D_{5/2}$ can decay via all the permissible decay routes and it leads to two situations. In one situation, population may be 'lost' to the uncoupled ground hyperfine level ($F = 1$) from the closed transition $F = 2 \rightarrow F' = 3 \rightarrow F''$ ($F = 2 \rightarrow F' = 3$ is closed transition) and it

gives rise to the DROP spectra [19]. In another situation, $F = 1$ state may receive more atoms than usual (from the $F = 1 \rightarrow F' = 2 \rightarrow F''$ transition, $F = 1 \rightarrow F' = 2$ is open transition) and gives rise to the TPA spectra [154]. Fig. 7.5(a) shows the DROP and TPA spectra under pump laser frequency scanning. The DROP spectra clearly show the presence of EIT. Fig. 7.5(b) shows the simultaneous presence of the blue fluorescence spectra with one to one correspondence to Fig. 7.5(a). The fluorescence peaks are designated ($A_k, k = 1$ to 6) into two groups. The FWHM of the blue light [164] is limited by the natural broadening $2\pi \times 1.3$ MHz. Lorentzian multi-peak fitting was performed on the blue fluorescence peaks to extract the respective line intensities and line-widths. The population history of the $F'' = 3, 2$ hyperfine levels can be found from the peak area sums ($A_2 + A_4$) and ($A_3 + A_5$). This is possible because the two sub-systems are nearly independent of each other. The results of the fitting are shown in Table 7.1.

7.5.2 Second part of the experiment

In the second part of the experiment, the interaction of the sub-systems under exact resonance was explored. The results are presented in Fig. 7.6. The observed spectrum changes when the probe-pump (probe-control) laser combination is tuned to the $F = 2 \rightarrow F' = 2 \rightarrow F''$ ($F = 2 \rightarrow F' = 2 \rightarrow F = 1$) transition i.e. the system transforms into an inverted Y system. The transition is performed into following steps. In the first step, the control laser frequency is locked to the derivative signal of the $F = 1 \rightarrow F' = 2$ SAS set up. In the second step, the DROP signals are coarsely matched on the Λ EIT positions by changing the piezo offset voltage of the pump laser and observing the probe absorption spectrum for probe frequency scanning. In the third step, the probe laser frequency was locked on the derivative of the Λ EIT signal obtained from the other reference cell (C1, Fig. 7.3). The probe laser frequency is now scanned with the help of the AOM1 over a very small frequency interval. The pump laser frequency was adjusted for exact matching of DROP and

Λ EIT. Finally the probe laser frequency scan was stopped and probe laser absorption spectrum was obtained by scanning the pump laser frequency. When the probe laser frequency is locked on the $F = 2 \rightarrow F' = 2$ transition, the character of the DROP signal is already changed from that of the $F = 2 \rightarrow F' = 3$ probe laser coupling case. Fig. 7.6(a)-(c) shows the probe absorption signals of different strengths as the DROP signal strength is proportional to the strength of the actual TPA [19]. In these figures, we superpose different DROP signals ($F = 2 \rightarrow F''$) on the Λ EIT successively. The blue fluorescence spectrum was also recorded simultaneously. In Fig. 7.6(a) the Λ EIT was superposed on the $F = 2 \rightarrow F'' = 4$ transition. It shows that the DROP feature corresponding to $F = 2 \rightarrow F'' = 3, 2$ transition is almost reduced to the background except for the DROP corresponding to the $F = 2 \rightarrow F'' = 4$ transition. This indicates that the medium is nearly transparent for the probe light. In Fig. 7.6(b) Λ EIT was superposed on the $F = 2 \rightarrow F'' = 3$ transition. It is seen that except for the DROP corresponding to the $F = 2 \rightarrow F'' = 4$ transition, all the other spectral features are completely wiped out. In Fig. 7.6(c) all the DROP signals are largely reduced and enhanced EIT can be seen on the spectrum. Λ EIT was superposed on the $F = 2 \rightarrow F'' = 2$ transition in this case. The striking feature of Fig. 7.6(a)-(c) is that the DROP signal corresponding to the $F = 2 \rightarrow F'' = 4$ transition remains prominent in all the three cases and appears even stronger than the independent ladder system (Fig. 7.5). In all cases four blue fluorescence peaks are clearly visible. The peak fittings of the blue fluorescence signals are done in the similar fashion as that in Fig. 7.5 and the results are listed in Table 7.2.

The pump laser acts on the population of the $F' = 3, 2, 1$ levels for further excitations to F'' levels. When the probe and control lasers are resonant ($\Delta_p = \Delta_c = 0$) with the $F' = 2$ level, the population of the $F' = 3, 1$ ($F' = 1$) levels are arising from the off-resonant coupling of the probe laser (control laser). Only the excitations from the $F' = 2$ to $F'' = 3, 2$ levels can satisfy the exact double dark resonance condition. This explains the near absence

of the $F = 2 \rightarrow F'' = 3, 2$ DROP signals as described in the previous paragraph. The increased intensity of DROP-EIT spectrum corresponding to $F = 2 \rightarrow F'' = 4$ transition results from the effective repumping by the control laser. Under DDR condition, the medium becomes fully transparent to the probe light. The appearance of the blue fluorescence corresponding to the states $F'' = 3, 2$ even under DDR is due to the presence of $F = 1 \rightarrow F' = 2 \rightarrow F''$ ladder coupling. From Table 7.2 one can see that the strengths of the $F'' = 2, 3$ blue peaks together is almost $\sim 65\%$, 67% and 62% of the total population for Fig. 7.6(a), Fig. 7.6(b) and Fig. 7.6(c) respectively. By comparing these results with the same from Table 7.1, one can conclude that the highest share of the population is transferred from $F'' = 4$ blue peak to $F'' = 3, 2$.

In principle it is also possible to construct another matched DDR system by detuning the control laser frequency to the $F' = 3$ hyperfine state and by coupling the probe-pump lasers to the $F = 2 \rightarrow F' = 3 \rightarrow F''$ transition. Fig. 7.6(d)-(f) show the results for such system when the detuned Λ EIT was successively matched with the resonant DROPs originating from $F = 2 \rightarrow F'' = 4, 3, 2$ transitions. The simultaneously recorded blue fluorescence signals are fitted and the results are shown in Table 7.3. It is found that the values of the relative intensity and the line-width vary according to the order of transition strengths for $F = 2 \rightarrow F''$ transitions. The main difference with the earlier observations (Fig. 7.6a-c) is that the highest share of the population is with the blue fluorescence peak corresponding to the $F'' = 4$ DROP signal. The reason behind this is the weakening of the off-resonant Λ EIT with the increase in control laser frequency detuning (Δ_{cont}). This becomes more prominent in Fig. 7.6(f), where the blue fluorescence becomes very weak and multi-peak fitting fails to converge. The population of the F'' level decreases considerably as more and more atoms are 'lost' in the $F = 1$ level because of the inefficient excitation from $F = 1$ level.

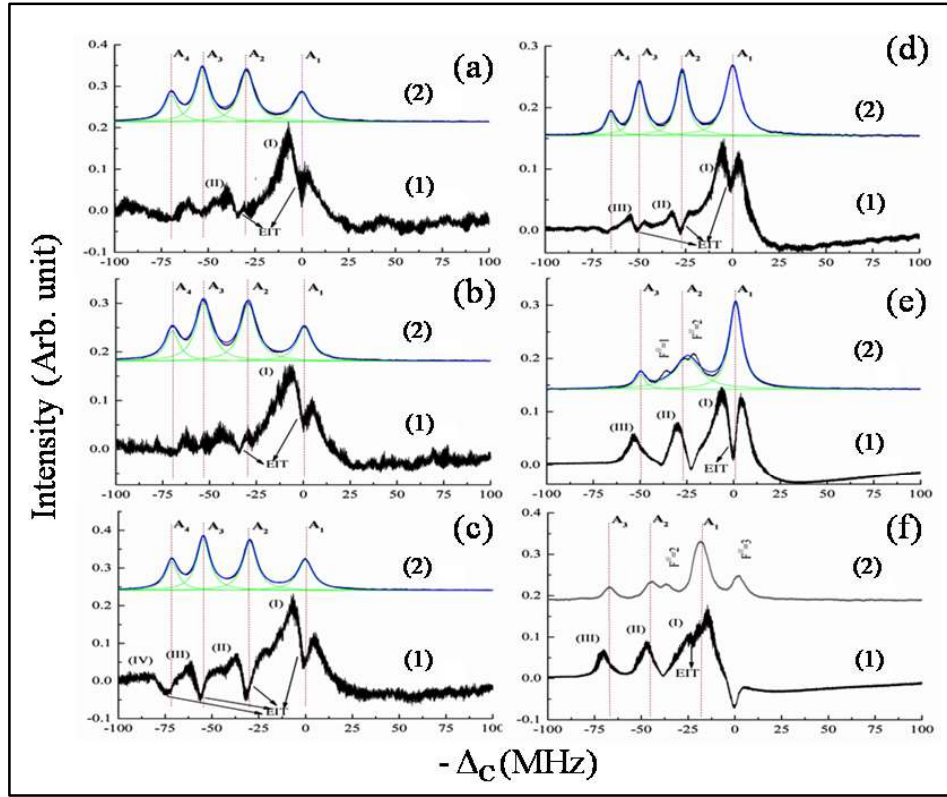


Fig. 7.6 Probe transmission and blue fluorescence spectra for pump scanning. The Rabi frequencies are $\Omega_p = 2\pi \times 2 \text{ MHz}$, $\Omega_{cont} = 2\pi \times 10 \text{ MHz}$, $\Omega_c = 2\pi \times 80 \text{ MHz}$. Different plot represents different central frequencies of the pump laser scan for resonant (plots a to c) and off-resonant (Plots d to f) Λ connection. The pump laser frequency is adjusted to values corresponding to the matching of the DROP signals with the Λ EIT signal as observed on probe absorption spectra for probe laser scanning condition. More details are given in the text.

Table 7.1 Blue fluorescence statistics when two independent Ξ systems act in parallel.

Two-photon excitation channel	Fitted blue light peak	Relative intensity (ξ_i)	FWHM (MHz)
$F = 2 \rightarrow F' = 3 \rightarrow F''$	$A_1(F'' = 4)$	0.469	11.5
	$A_2(F'' = 3)$	0.114	8.4
	$A_3(F'' = 2)$	0.069	8.2
$F = 1 \rightarrow F' = 2 \rightarrow F''$	$A_4(F'' = 3)$	0.110	7.4
	$A_5(F'' = 2)$	0.109	6.9
	$A_6(F'' = 1)$	0.126	7.1

Remark: $A_2 + A_4 = 0.2252$ is the relative population strength at $F'' = 3$ and $A_3 + A_5 = 0.1792$ is the relative population strength at $F'' = 2$

Table 7.2 Blue fluorescence statistics under on resonance matched DDR mode (Λ and Ξ connections both address the same $F' = 2$ intermediate level).

Matching condition to select appropriate pump laser frequency	Results of the blue fluorescence fitting							
	$A_1 (F'' = 4)$		$A_2 (F'' = 3)$		$A_3 (F'' = 2)$		$A_4 (F'' = 3)$	
	Relative intensity (ξ_i)	FWHM (MHz)	Relative intensity (ξ_i)	FWHM (MHz)	Relative intensity (ξ_i)	FWHM (MHz)	Relative intensity (ξ_i)	FWHM (MHz)
$F'' = 4$ peak matches with Λ EIT peak	0.19	10.0	0.33	9.7	0.31	8.8	0.15	8.4
$F'' = 3$ peak matches with Λ EIT peak	0.18	9.7	0.32	10.1	0.33	10.2	0.14	8.7
$F'' = 2$ peak matches with Λ EIT peak	0.21	9.9	0.31	8.9	0.31	8.6	0.16	8.0

Remark: Population at the upper level is localized at $F'' = 3, 2$ levels at the cost of the population at $F'' = 4$ level. Highest population at $F'' = 2$ level when $F'' = 3$ peak matches with Λ EIT peak signifies the exact matched DDR mode. Rest of the connections are in the near exact DDR match mode.

Table 7.3 Blue fluorescence statistics under off-resonant DDR mode. (Ξ connection address the $F' = 3$ intermediate level and intermediate level of Λ connection is detuned accordingly).

Condition for matching to select appropriate pump laser frequency	Results of the blue fluorescence fitting							
	$A_1 (F'' = 4)$		$A_2 (F'' = 3)$		$A_3 (F'' = 2)$		$A_4 (F'' = 3)$	
	Relative intensity (ξ_i)	FWHM (MHz)	Relative intensity (ξ_i)	FWHM (MHz)	Relative intensity (ξ_i)	FWHM (MHz)	Relative intensity (ξ_i)	FWHM (MHz)
$F'' = 4$ peak matches with Λ EIT peak	0.41	9.8	0.28	7.4	0.22	7.0	0.07	6.0
$F'' = 3$ peak matches with Λ EIT peak	0.53	8.3	0.39	16.8	0.06	6.1	Nearly obscured	
$F'' = 2$ peak matches with Λ EIT peak	No fitting data available as fit did not converge							
Remark: Population at the upper level is localized according to the $F' = 3 \rightarrow F''$ transition strengths. The matched DDR mode is weak and can't alter the population distribution as observed in earlier results.								

From the above discussions it is now well evident that there is considerable difference in response of the four-level system under different control laser beam conditions. Compared to our other works [157,171], the new alignment geometry of the lasers (probe-control laser

counter propagating to pump laser) introduces additional dynamics into the system. Two cases are discussed. In one the inverted Y system was addressing the $F' = 3$ intermediate hyperfine level and in another it was the $F' = 2$ hyperfine level. In the second case the effect of the Λ EIT was found to be weak.

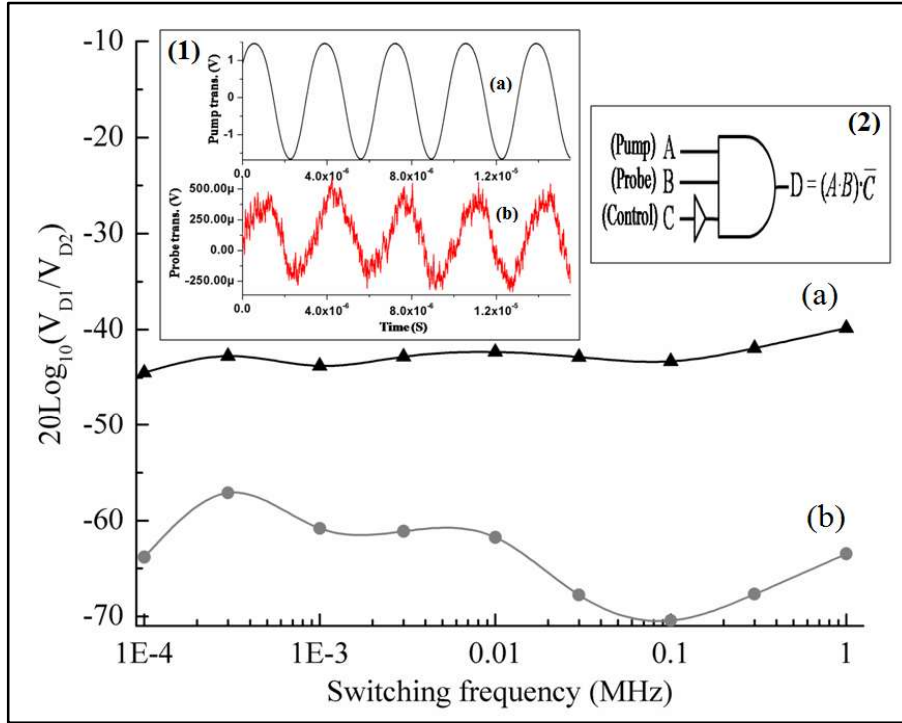


Fig. 7.7 Gain bandwidth response of the switch in inverted Y system. Plot (a) represents response of isolated ladder system and plot (b) represents the response for matched DDR inverted Y system. An overall ~ 20 dB decrease in the gain can be seen in plot (ii). Graphs data are simply connected with BSpline curve. The gain parameters are obtained by normalizing the peak to peak voltage of the probe response signal to that of the pump switching signal as recorded in the photo-detectors D1 and D2 respectively. Inset (1) shows the signals recorded in D1 and D2 for 300 kHz switching frequency. Inset (2) shows the logic gate representation of the switching action.

7.5.3 Final part of the experiment

In the last part of the experimental investigation, the effect of DDR on the optical switching was studied. The probe-pump (probe-control) combination satisfies the matched DDR coupling configuration $F = 2 \rightarrow F' = 2 \rightarrow F''$ ($F = 2 \rightarrow F' = 2 \rightarrow F = 1$). The pump laser intensity was modulated using an EOM within the frequency range 100 Hz to 1 MHz. Individual probe response at different frequencies was normalized with respect to the pump laser response as detected by the photo-detectors D1 and D2 and the same is plotted in Fig. 7.7. The result from our other work [157] is plotted on the same graph for comparison. It can be seen that the probe response is suppressed by ~ 20 dB over the whole switching frequency zone. This indicates that the degree of coherence assisted switching can be attenuated by altering the geometry of the control laser. The matched DDR condition is highly efficient in doing so. Therefore it is evident that the ladder EIT is highly influenced by the presence of the Λ EIT. The inset of Fig. 7.7 shows the behaviour of the pump and probe laser under optical switching at 0.3 MHz switching frequency. The combination logic representation of such an attenuator is shown in the inset (2) of Fig. 7.7. The system behaviour replicates the action of a composite AND and NOT gate.

This type of attenuation is highly sensitive to the respective detunings of the individual lasers. Since the probe and the control lasers are locked, the pump laser frequency can be varied at will to the desired value. The susceptibility of the composite system exhibits steeper rise and fall with respect to probe detuning for a fixed set of other parameters as it has two resonance frequencies [170]. A small offset in the ($> \gamma_{21} + \gamma_{24}$) between the probe-control combination frequency is enough to destroy the existing coherence and makes the sub-systems independent. The three level ladder EIT is strictly dependent upon the Ω_c^2 whereas the response of the inverted Y system can be tuned by only adjusting the ratio of the pump and control laser intensities. However, the action of the attenuator is limited within the

matched DDR mode of operation. Hence it needs to be put through a control loop for stable operation. The blue fluorescence peaks (Fig. 7.6) can be used as the desired discriminator for the stabilization of the pump laser. We can also use sidebands in phase locking mode of a single laser system for generation of locked probe-control pair which might improve the performance.

7.6 Conclusion

The present chapter discussed ^{87}Rb inverted Y system and its application in optical switching. In order to introduce DDR in the system, the probe-control laser combination counter propagates the pump laser. The role of control laser is dual. It helps to create match DDR for resonant inverted Y system and also repumps atoms back into the main ladder system for off-resonant connections. This is established through the simultaneous observation of probe absorption spectra and blue fluorescence light. It is found that the system can be made completely transparent from partial transparency by simply changing the system to on-resonant inverted Y from an off-resonant one. As shown in previous sections, such transition to the on-resonant inverted Y system introduces many new features, for example, the population can be selectively localized to higher excited state, coherence between pump-probe is altered and a new coherence is set with the formation of DDR, attenuation of optical switching action etc. The present experiment may find its application in photonic device for the implementation optical switching attenuator and will also be useful for quantum information processing in the form of logic gate.

Chapter 8

Effect of repump laser on Atomic line filter

8.1 Introduction

Present chapter deals with the experimental study conducted on atomic line filter (ALF) to improve its performance using an additional repump laser. The line filter action is exhibited by the pump-probe laser configuration on the $5S_{1/2}(F = 2) \rightarrow 5P_{3/2}(F' = 3) \rightarrow 5D_{3/2}(F'' = 3)$ transition of ^{87}Rb atom. The additional repump laser couples the $5S_{1/2}(F = 1)$ state to the intermediate $5P_{3/2}(F' = 2, 1, 0)$ hyperfine states. The performance of the ALF was optimized by carefully choosing the detuning and intensity of the repump laser. This was done after conducting a detail study on the dependence of ALF on the intensity and detuning of repump laser. It is observed in this experiment that the selective repumping of atoms can increase the transmittance of ALF by $\sim 30\%$. The calibration of the signal was performed using the DROP signals unlike the earlier reports where it was done using the FPI cavity fringes of larger free spectral range. ALF finds its application in free space optical communication, laser spectroscopy etc fields and this study might help in improving the performance of a narrow bandwidth ALF. Following subsections discuss the motivation behind the experiment, experimental scheme, observation, explanation and conclusion from the conducted experiment in detail.

8.2 Motivation

Pump-probe spectroscopy in coherently prepared alkali vapour media exhibits many novel phenomenon such as coherent population trapping [1], electromagnetically induced transparency [2], electromagnetically induced absorption [3], etc. This fascinating area of physics find its application in the field of ultrasensitive magnetometry [5], miniaturized

atomic clock [6], slowing down of light [4], etc. One such important application of pump-probe spectroscopy is in the field of narrowband optical filter which have applications in the field of laser imaging detection and ranging [35,36,37], generation of narrowband quantum light [33,34], free space laser communication [32], etc.

Over the years several different types of optical filters have been developed. Faraday anomalous dispersion optical filter (FADOF) [175,176,177], induced dichroism excited atomic line filter (IDEALF) [38,39,40] etc are a few to name. Using atomic hyperfine manifold or velocity selective optical pumping signal to execute atomic filter has also been attempted [178,179]. The main focus of these developments has always been to improve the transmittance, width, out of band rejection ratio, etc of the filter. In line of these developments, the effect of an additional repump laser on the characteristic properties of an atomic line filter was still unexplored. The present experiment was conducted to fill that gap. To demonstrate the power of a repump laser, we choose an IDEALF realized in the excited states of $5S_{1/2} \rightarrow 5P_{3/2} \rightarrow 5D_{3/2}$ ladder level coupling scheme in ^{87}Rb .

A left circularly polarized (σ^+) pump beam was used to dress the Rb D_2 transition ($5S_{1/2}(F=2) \rightarrow 5P_{3/2}(F'=3)$) whereas a scanning (around $5P_{3/2}(F'=3) \rightarrow 5D_{3/2}(F''=3)$ hyperfine transition) linearly polarized probe beam was used to sense the pump induced dichroism. The resulting spectrum shows the existence of an atomic line filter with peak transmittance of $\sim 17\%$ and a FWHM of ~ 174 MHz. In the realization of IDEALF, atoms can decay to the $5S_{1/2}(F=1)$ level from the excited states and are considered 'lost' from the pump-probe cycle as the hyperfine level $5S_{1/2}(F=1)$ is not connected with any laser. In this situation, the repump laser connects the hyperfine level $5S_{1/2}(F=1)$ to $5P_{3/2}(F')$ level and it helps to bring the 'lost' atoms back in the ALF coupling scheme. Experimental observation shows that, the transmittance of the ALF can be

increased by more than 30% with the help of the repump laser. It also helps to increase the width of the ALF by ~ 20 MHz.

To calibrate the ALF we have used the signature DROP signal from the same level coupling scheme. Line-width of these signals are of the order of natural line-width of the $5S \rightarrow 5P$ transition and the frequency spacing between two DROP signal is considerably lower than the FWHM of ALF signal. Hence they can be used for calibration of the filter.

8.3 Controlling IDEALF using repump laser

In this section the physical origin of ALF is discussed. The σ^+ pump laser enables a net population transfer from $F = 2, m_F = +2$ to $F' = 3, m'_F = +3$ state. The linearly polarized probe beam allows population transfer from $5P_{3/2}(F' = 3)$ state to $5D_{3/2}(F'')$ state. The probe beam can be considered as a combination of σ^+ and σ^- components. Because of the selection rule only the σ^- component gets absorbed ($F' = 3, m'_F = +3 \rightarrow F'' = 3, m''_F = +3, +2$) whereas the σ^+ component passes un-attenuated. Therefore an optical anisotropy is created within the system by the pump-probe beam configuration. The effect is more pronounced at higher atomic number density. This can be achieved by heating the vapour cell. The figure of merit of the filter depends upon the population transfer from $5S_{1/2}$ state to $5P_{3/2}$ state through the $5S_{1/2} \rightarrow 5P_{3/2} \rightarrow 5D_{3/2}$ ladder chain. As a result of decay from the excited states, population may get trapped in the $5S_{1/2}(F = 1)$ state which lies outside the $5S_{1/2}(F = 2) \leftrightarrow 5P_{3/2}(F' = 3) \leftrightarrow 5D_{3/2}(F'' = 3)$ absorption emission cycle. This population trapping may limit the performance of the ALF. The same decay phenomenon also gives rise to DROP signal. Therefore simultaneous recording of DROP signal in another arm of the spectrometer acts as a marker for the radiation trapping of atoms. Under normal condition, the dephasing ($\gamma_{g,1 \leftrightarrow 2}$) between $F = 1$ and $F = 2$ ground hyperfine state is determined by the transit time factor, which is ~ 50 KHz in the present case. Therefore many

cycles of optical pumping get averaged within this slow time scale of ground state dephasing and the whole system settles into equilibrium. For the vapour cell without buffer gas and at elevated temperature ($\sim 100^{\circ}\text{C}$), the mean free path is much larger than the resonance wavelength. Therefore only phase changing collision can occur which has a very limited role in ALF.

Following the density matrix analysis of Liu et al [180,181] one can estimate the susceptibility (χ_+ , χ_-) of the vapour medium for the components (σ^+ , σ^- respectively) of the probe light. The ALF comes into existence because of the induced circular dichroism which is proportional to $Im(\chi_+ - \chi_-)$. If the radiation trapped atoms are pumped back into the ALF channel, more atoms will be pumped to the $F' = 3$ state. This will allow for more absorption of the σ^- component of the probe laser whereas the same will have no effect on the σ^+ component. Hence the repump laser will have prominent effect on ALF.

The presence of a linearly polarized repump laser allows atoms to be coupled to states other than $F' = 2$ hyperfine state through off-resonant coupling. This may affect the beneficial aspect of the repump laser as the atoms can still decay back to $F = 1$ state via additional decay routes. In this situation the introduction of Zeeman sublevel repumping ($F = 3, m_F = +1 \rightarrow F' = 2, m'_F = +2$) can limit the possible decay routes (only to $m_F = +2, +1$) and thus is more beneficial for ALF.

8.4 Experimental arrangement

Fig. 8.1 shows ^{87}Rb atomic hyperfine levels, decay rates [20] and the relevant coupling schemes for the present experiment. The external cavity diode laser (ECDL1) is resonant with the $5P_{3/2} \rightarrow 5D_{3/2}$ transition ($\lambda_p \sim 775.94 \text{ nm}$) whereas another external cavity diode laser (ECDL2) which is resonant with the $5S_{1/2} \rightarrow 5P_{3/2}$ transition ($\lambda_c \sim 780 \text{ nm}$). For both the lasers short term line-width ($\Delta\nu_{laser}$) is less than 1 MHz. Wavelength of the probe laser is

monitored using a wavemeter and a FPI cavity as the transition between the excited states can't produce any fluorescence. Schematic of the experimental arrangement is shown in Fig. 8.2. An acousto-optic frequency shifter (AOFS) splits the probe beam from ECDL1 into zeroth and first order paths with a frequency difference of 80 MHz between the two. The laser beam intensities of the both paths can be controlled at will using the variable attenuators placed in the beam path. The pump beam was also split into two paths using a beam splitter and used in the two arms of the spectrometer. A small part of the pump beam was used for SAS on ^{87}Rb $5S_{1/2} \rightarrow 5P_{3/2}$ transition and subsequent frequency stabilization of the pump laser.

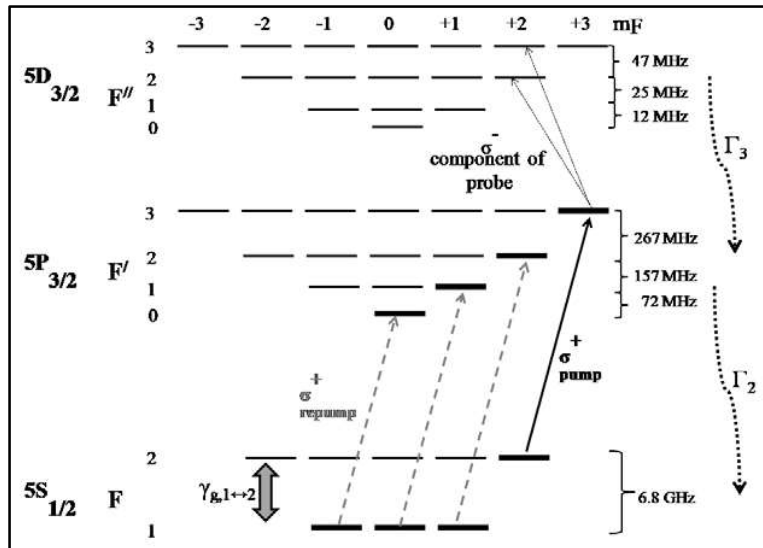


Fig. 8.1 Level scheme of $5S_{1/2} \rightarrow 5P_{3/2} \rightarrow 5D_{3/2}$ transition of ^{87}Rb atom with degenerate Zeeman sublevels relevant to ALF experiment. Spontaneous decay rate from $|j\rangle$ is represented by Γ_j . $\Gamma_2 = 2\pi \times 6.066$ MHz, $\Gamma_3 = 2\pi \times 0.97$ MHz. Relevant repump transitions are represented in gray scale.

In order to avoid first order Doppler broadening, the pump and the probe laser were used in counter propagating configuration in both arms of the spectrometer. In one arm of the spectrometer, the zeroth order part of ECDL1 acts as the pump beam (pump1) whereas the

weak part of ECDL2 acts as the probe (probe1). In the other arm, the first order part from AOFS acts as the probe beam (probe2) whereas the strong part from the ECDL2 acts as the pump (pump2) beam. The first arm is used to detect the DROP signal resulting from the current ladder coupling scheme. In the other arm we have a linearly polarized probe beam (first order part from AOFS) and a left circularly polarized (σ^+) pump beam to detect the ALF. This nontrivial arrangement lets us monitor the DROP and ALF spectra simultaneously.

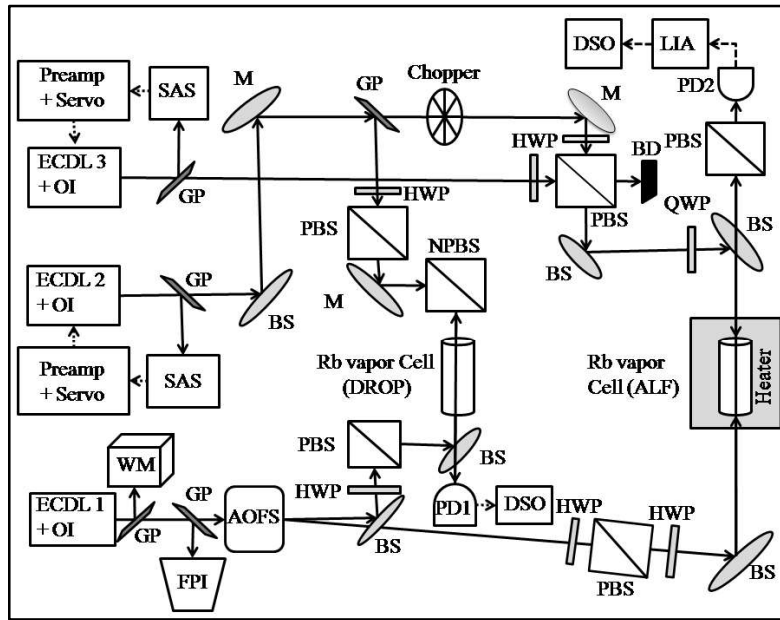


Fig. 8.2 Schematic of experimental arrangement for ALF. ECDL: External cavity diode laser, M: Mirror, DSO: Digital storage oscilloscope, PBS: Polarizing cubic beam splitter, NPBS: Non-polarizing cubic beam splitter, HWP: Half wave plate, QWP: Quarter wave plate, FPI: Fabry perot interferometer, AOFS: Acousto optic frequency shifter, BS: Beam splitter, LIA: Lock-in-amplifier, GP: Glass plate, WM: Wavemeter, PD1, PD2: Photo detector, SAS: Saturation absorption spectroscopy set up.

Before inserting the Rb vapour cell in the path of the second arm, the $\lambda/2$ plate and the PBS cube were put into crossed polarized configuration. This assembly has an extinction of

$\sim 10^{-3}$ of the probe laser intensity. The Rb vapour cell in the second arm was also heated in close loop to $\sim 100^{\circ}C$ to increase the atom density. A mechanical chopper in the path of the pump2 allows for lock-in detection of ALF.

Another laser ECDL3 ($\Delta\nu_{laser} \sim 1$ MHz) is used in the second arm of the spectrometer as the repumping laser. A small part of it is used in a SAS set up which helps in stabilizing the repump laser using frequency modulation. The repump laser is collinear with pump2 but the chopper was only used on pump2.

8.5 Results and discussion

The Rabi frequency of pump2 (Ω_{c2}) and probe2 (Ω_{p2}) is $\sim 2\pi \times 53$ MHz and $2\pi \times 2$ MHz respectively [67]. The values of the Rabi frequencies are estimated using equation (2.27) where the values for the dipole moment was taken from [65,145]. The saturation intensity for the pump2 is $\sim 2\pi \times 4.3$ MHz.

The Doppler width for the filter transition is ~ 570 MHz and can be estimated using equation (2.20). This is much smaller than the ground state hyperfine level energy separation between $F = 1$ and $F = 2$ state. Further the energy spacing of $F \rightarrow F'$ transition much larger than the $F' \rightarrow F''$ transition. Therefore for pump2 stabilized at $5S_{1/2}(F = 2) \rightarrow 5P_{3/2}(F' = 3)$ transition, the probe2 laser connecting the $F' = 3 \rightarrow F''$ transition is almost on resonance. The oscillator strength for the $5P_{3/2} \rightarrow 5D_{3/2}$ transition is ~ 0.06 .

In the case of resonant laser coupling i.e. when the pump2 is in resonance with $F = 2, m_F = +2 \rightarrow F' = 3, m_{F'} = +3$ transition and probe2 connects $F' = 3 \rightarrow F''$ transition, the transmittance of the ALF is $\sim 16\%$ and is comparable with reference [38]. This situation changes when a repump laser ($\Omega_{repump} \sim 2\pi \times 14$ MHz) is introduced to replenish the ‘loss’ of atoms to $F = 1$ state. Fig. 8.3(a) shows the ALF spectrum when a σ^+ repump laser is

introduced to connect $F = 1, m_F = +1$ with $F' = 2, m_F' = +2$ Zeeman sublevels. More than 30% improvement in transmittance and ~ 20 MHz additional broadening in FWHM is observed compared to the case without repump laser (shown in Fig. 8.3(b)). Fig. 8.3(a) also exhibits a side lobe with peak transmittance $\leq 3\%$.

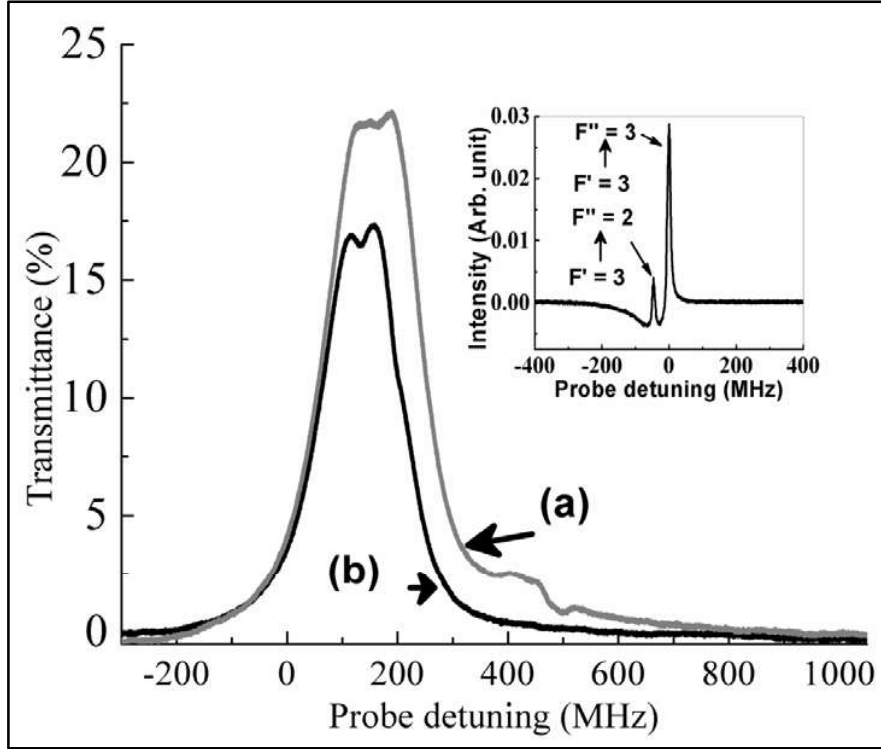


Fig. 8.3 Experimental recording of ALF signal vs probe2 detuning for resonant pump2. Inset shows the relevant DROP signal arising from pump1-probe1 configuration. This DROP signal is used to calibrate ALF signal. (a) ALF with repump laser (b) ALF without repump laser. The transmittance is estimated with respect to the cross polarizer configuration. For DROP no repump was used.

The increase in the ALF parameters is due to the recirculation of the ‘lost’ atom into the ALF channel which increases the population in the intermediate level ($F' = 3, m_F' = +3$). In effect the σ^- component of probe2 ‘sees’ more number of atoms which can be excited to F'' state. In this recirculation process, the contribution from another velocity group of atoms

gives rise to the side lobe seen in Fig. 8.3(a). The double peak structure seen on the ALF signal is due to the AT splitting of the transition. AT splitting appears because of a relatively stronger pump2 beam ($\Omega_{c2} \gg \Omega_{sat}$). The neighbouring levels as well as the repump laser will also contribute to the overall dressing of the system. The overall ALF spectrum is shifted from zero of the frequency axis which is calibrated using DROP signal. The 80 MHz downshifted pump2 frequency and the dressing of the system is responsible for this shifting.

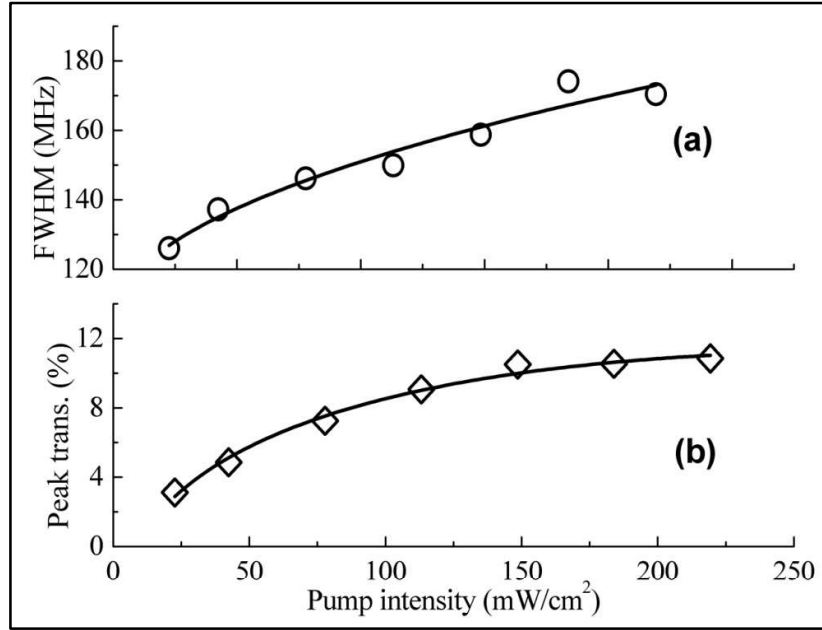


Fig. 8.4 ALF characteristic parameter vs pump intensity. (a) FWHM of ALF vs pump2 intensity. Plot shows \sqrt{I} dependence. (b) Peak transmittance vs pump2 intensity. Plot shows a $(c_0 + c_1 I + c_2 \sqrt{I})$ dependence.

The dependence of the peak transmittance (Tr_{ALF}) and FWHM of the ALF (Δw_{ALF}) on the pump2 laser intensity is shown in Fig. 8.4. The Tr_{ALF} vs pump intensity data shows a good fit to the $(c_0 + c_1 I + c_2 \sqrt{I})$ curve. The linear portion of the graph represents the below saturation threshold whereas above saturation limit, \sqrt{I} behaviour is exhibited. The Δw_{ALF} also shows the \sqrt{I} behaviour which indicates the onset of broadening after saturation. These results are consistent with the earlier observations reported in [39,38].

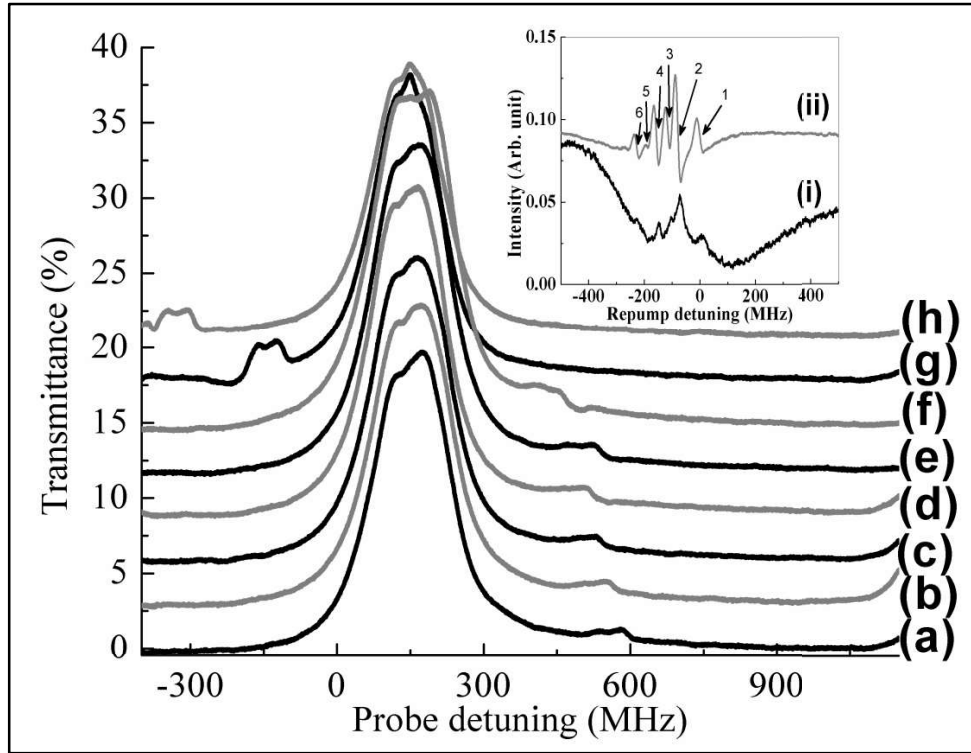


Fig. 8.5 Effect of repump detuning on ALF spectrum. Repump laser laser frequency positions were fixed at (a) $F = 1 \rightarrow F' = 0$ transition, (b) $F = 1 \rightarrow F' = 0,1$ cross-over transition, (c) $F = 1 \rightarrow F' = 1$ transition, (d) $F = 1 \rightarrow F' = 2,0$ cross-over transition, (e) $F = 1 \rightarrow F' = 2,1$ cross-over transition, (f) $F = 1 \rightarrow F' = 2$ transition, (g) Blue detuned by 209 MHz from $F = 1 \rightarrow F' = 2$ transition, (h) Blue detuned by 580 MHz from $F = 1 \rightarrow F' = 2$ transition. Inset shows SAS signal and its first derivative.

For resonant pump2 laser, the effect of the repump laser detuning on the ALF has been studied and is shown in Fig. 8.5. The repump laser was selectively red detuned with respect to the $5S_{1/2}(F = 1) \rightarrow 5P_{3/2}(F' = 2)$ transition and was locked on available first derivative discriminators of the SAS spectrum of $5S_{1/2}(F = 1) \rightarrow 5P_{3/2}(F' = 2, 1, 0)$ hyperfine transition manifold. However the blue detuned frequency positions were selected by zooming in on the desired position on the SAS spectra. The laser was kept free running during the

recording of the spectrum as there was no suitable I_f discriminator available for the laser to lock for the blue detuned positions. As the recording of the spectrum takes only ~ 1 s, laser frequency fluctuation does not affect the spectrum.

In Fig. 8.5, both the red and blue detuned positions of the repump laser frequency show the presence of second velocity group of atoms. However for the red detuned positions, the contribution from the second velocity group of atoms is low ($\sim <5\%$ of respective transmittance) compared to the substantial contribution ($\sim \geq 20\%$ of the respective peak transmittance) from them for the blue detuned positions. For repump frequency positions marked by $F = 1 \rightarrow F' = 2, 1$ transition and in between, the contribution from the second velocity group of atoms are almost same. For repump laser resonant with $F = 1 \rightarrow F' = 0$ transition, ΔW_{ALF} and Tr_{ALF} has the same values as if there is no repump laser acting.

The relative strengths of different σ^+ repump transition are different and can be found in [65]. The ratio of the dipole matrix elements $| \langle J = 1/2 || er || J' = 3/2 \rangle |$ for the three σ^+ repump transitions ($F = 1 \rightarrow F' = 2, 1, 0$) is $\sqrt{1/4} : \sqrt{5/24} : \sqrt{1/6}$. Probability of atom recirculation is more for transitions with higher strength. For a far blue detuned repump laser, the contribution from the off-resonant coupling of atoms to $F' = 2$ state is only significant whereas the effect of velocity selective optical pumping of secondary groups of atoms are stronger at and around the blue detuned side of the $F = 1 \rightarrow F' = 2$ transition. For the red detuned side of σ^+ repump laser, the contribution from the $F = 1 \rightarrow F' = 2, 1$ and in between have the similar strengths. The situation changes when the repump laser addresses the $F = 1 \rightarrow F' = 0$ transition as the atoms are forbidden to decay to $F = 2$ hyperfine state or the ALF channel. So the situation is similar to the no repump case. The small difference between them arises due to the contribution from the off-resonant coupling of atoms to the neighbouring hyperfine levels.

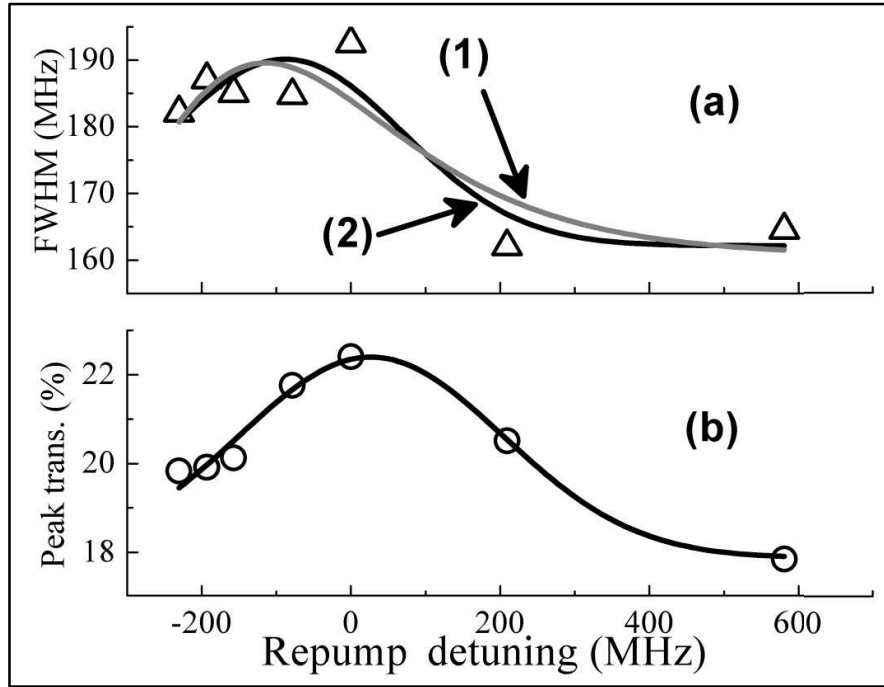


Fig. 8.6 Peak transmittance and FWHM of ALF vs repump laser detuning. (a) Δw_{ALF} vs repump detuning data. Data fits well with (1) 'Extreme function' and (2) Gaussian. (b) Tr_{ALF} vs repump detuning data and fits well with a Gaussian function indicating velocity selective nature of repump.

Fig. 8.6 shows the behaviour of the Δw_{ALF} and Tr_{ALF} with the variation of the repump laser detuning (Δ_{repump}) and it fits well with a Gaussian. This is due to the velocity selective nature of the repump based population transfer. Apart from that the spontaneous decay, branching ratio, intensity and detuning of repump laser etc also comes into play. The effect of the repump is maximum for $F = 1 \rightarrow F' = 2$ repump transition and minimum for $F = 1 \rightarrow F' = 0$ transition. The continuous evolution of the ALF line shape vs Δ_{repump} over the Doppler width of the repump transition suggest that the function describing the behaviour must be continuous and bounded within the presented interval. To this end, the Δw_{ALF} vs Δ_{repump} also shows a good fit to the 'extreme function' of the form $y = y_0 + A \exp\left\{-\exp\left(\frac{x-x_0}{w}\right) - \frac{x-x_0}{w} - 1\right\}$ along with the Gaussian fitting. However these

explanations must be considered as just a qualitative approach and explicit density matrix calculation is required to explain the observed behaviour.

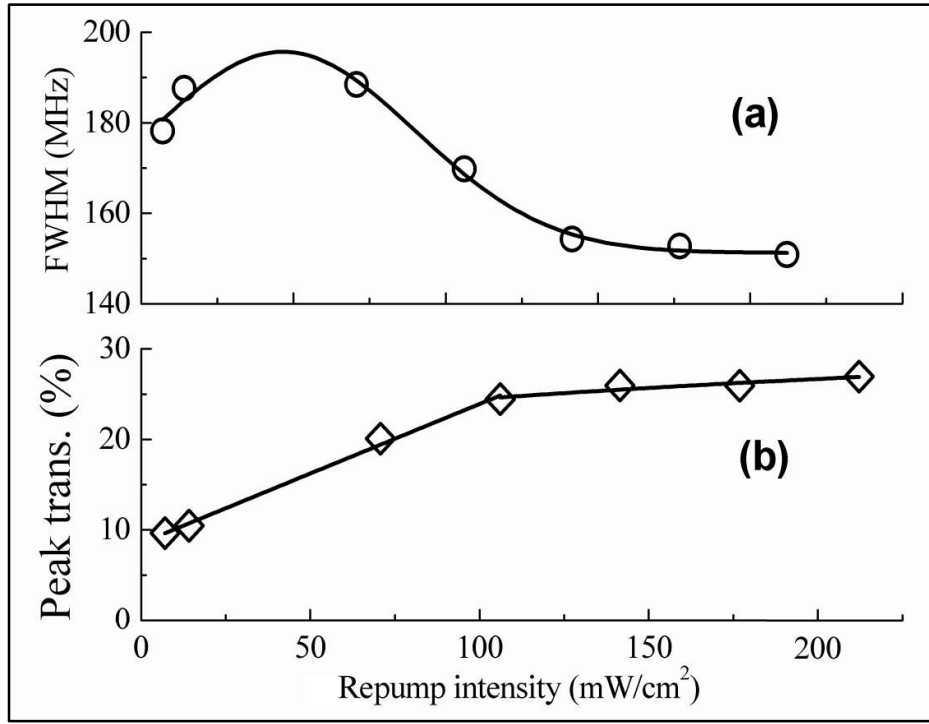


Fig. 8.7 Peak transmittance and FWHM of ALF vs repump laser intensity. Pump and repump are in resonance with respective transitions. (a) Δw_{ALF} vs repump intensity data and it shows a good fit to Gaussian function. (b) Tr_{ALF} vs repump intensity (I_{repump}) data. Below saturation intensity Tr_{ALF} is $\propto I_{repump}$ whereas above saturation it is $\propto \sqrt{I_{repump}}$.

The effect of the repump laser intensity (I_{repump}) on Δw_{ALF} and Tr_{ALF} is shown in Fig. 8.7. The peak transmittance (Tr_{ALF}) data shows power law regression with the variation in I_{repump} . Below saturation intensity peak transmittance $\propto I_{repump}$ and above saturation intensity it is $\propto \sqrt{I_{repump}}$. Therefore the presence of the saturation limit on repump transition is profound for a pump-probe configuration. However the Δw_{ALF} vs I_{repump} data shows a Gaussian dependence. The initial increase in filter width I_{repump} may be due to the increase

in atom number in $F = 2$ state with I_{repump} but at larger intensities the probability of population transfer to levels other than $F = 2$ state increases. This can open new decay channels which may be detrimental to ALF. Therefore one can control the ALF parameters with repump intensity alone.

8.6 Conclusion

In the present work, the role of one additional repump laser in ALF, especially for IDEALF, has been investigated. As the realization of IDEALF is easier, several groups have made attempt to theoretically as well as experimentally investigate it. Still the issue of the application of repump laser was not addressed before. The present study deals with this problem in detail.

We have studied experimentally the effect of a σ^+ polarized repump laser on atomic line filter realized in $^{87}\text{Rb } 5S_{1/2} \rightarrow 5P_{3/2} \rightarrow 5D_{3/2}$ transition. The use of repump considerably increases the peak transmittance by $\sim 30\%$ and FWHM by ~ 20 MHz. This repumping action also gives rise to side lobe for detuned repump frequency and can be eliminated by carefully choosing the repump frequency. It is found that the ALF peak transmittance at different repump detuning is a function of atom velocity distribution but the FWHM of ALF is a complex function of repump action. The dependence of the ALF on repump intensity is also studied and it is shown that the peak transmittance follows a power law regression whereas the FWHM resembles a Gaussian shape. Therefore by changing the repump intensity alone one can change the peak transmittance and FWHM of the ALF. This study may help in realizing a better IDEALF.

Chapter 9

Tunable Atomic frequency offset locking in ladder system

9.1 Introduction

Current chapter deals with the experimental study on Atomic Frequency Offset Locking (AFOL) scheme for a laser. The concerned laser (probe laser) is used to couple the $5S_{1/2} \rightarrow 5P_{3/2}$ transition in Rubidium in association with another laser (pump laser) which couples the $5P_{3/2} \rightarrow 5D_{5/2}$ transition. These particular two photon transition manifold ($5S_{1/2} \rightarrow 5P_{3/2} \rightarrow 5D_{5/2}$) was chosen to demonstrate the capability of AFOL in terms of its frequency stability and tunability. The coherent pump-probe spectroscopy on this manifold reveals a two photon absorption (TPA) signal along with an electromagnetically induced transparency (EIT) signal on top it. The probe laser beam was locked on to the EIT and TPA spectra whereas the pump beam was locked on to the fringe produced by a scanning Fabry-Perot Interferometer. The advantage of the present locking scheme is its large tunability. The lock point can be chosen anywhere on the Doppler width of ($5S_{1/2} \rightarrow 5P_{3/2}$) transition without any compromise on the frequency stability. Such tunable offset locking scheme (TAFOL) finds its application in the field of metrology, high precision coherent spectroscopy etc. The scheme can also be used for laser locking in multistep processes like laser ionization. Following subsections discuss the theory, motivation behind the experiment, results of the experiment and the conclusion in detail.

9.2 Motivation

It is known that AFOL is very much suitable for a system exhibiting EIT phenomenon. The Λ level coupling scheme in a three level atomic system has already been exploited to achieve AFOL on lasers [7,8,41] because of its high degree of coherence [42]. However the

tunability of such system is limited by the unavailability of ultra-narrow EIT signal throughout the scanning range of the probe laser. The issue of tunability can be addressed by locking the probe laser on the Autler-Townes (AT) doublet signal [9]. In that case the precision of locking is degraded as the line-width of the AT doublet is often higher compared to the EIT signal and also difficult to obtain sometimes. Therefore there always remains a trade-off between the tuning range of the lock point and its precision.

The next best candidate to investigate AFOL is the three level ladder or cascade (Ξ) system. The coherent pump probe spectroscopy on the ladder system reveals two photon absorption (TPA) signal along with the EIT signal depending upon the Rabi frequency of the pump laser. In case of Λ scheme, the EIT appears on top of the one photon absorption background whereas the same for ladder appears on top of the two photon absorption background [41,18,19]. The line-width of these TPA or EIT signal is only limited by the decay rates in the absence of any collisional dephasing [143]. Furthermore the TPA or EIT signal shows profound dependence on the detuning of the pump beam. Therefore they can be considered for tunable laser frequency reference.

Earlier works on frequency stabilization in ladder (Ξ) system through coherent pump-probe spectroscopy used SAS signal to lock the probe laser whereas the pump laser was locked on TPA or EIT signal [43,15,182,81]. Since the probe laser can only be locked at discrete points on the SAS signal, the tuning range of such a lock is limited and discontinuous. Therefore the current experimental study was undertaken to investigate the issue of frequency tunability in a ladder system and also to explore the level of coherence assisted modulation transfer in a particular ladder coupling scheme where the ground state laser (probe laser) Rabi frequency is much smaller than the pump laser Rabi frequency.

In this regard the pump laser frequency was locked on a FPI cavity reference to make it free from any discrete spectroscopic references. The probe laser on the other hand is offset locked on TPA/EIT signal at different frequencies. The pump beam was frequency modulated and the corresponding coherence assisted modulation transfer allowed to lock the probe laser frequency. As the pump laser was locked on FPI reference, it can be tuned easily and continuously. This in turn also tunes the probe laser frequency. The resulting locking scheme is a tunable AFOL.

9.3 Transfer of frequency modulation in a coherently driven Ξ system

The chosen $5S_{1/2} \rightarrow 5P_{3/2} \rightarrow 5D_{5/2}$ level coupling scheme was already investigated by Jin et al [153]. The level coupling scheme for the current experiment (on ^{87}Rb) is shown in Fig. 9.1. Following the derivation of Banacloche et al [143] for the EIT in a ladder type inhomogeneously broadened media, the pump-probe response of a realistic ladder (Ξ) system can be understood qualitatively from the theoretical susceptibility (χ) of the system. Considering the number of atoms per unit volume with velocity v is $N(v)dv$, their contribution to the total susceptibility of a multilevel atomic system is give by,

$$\chi(v)dv = \frac{id_{21}^2/(\hbar\epsilon_0)}{\gamma_{21} - i\Delta_p - i\frac{\omega_p}{c}v + \frac{\Omega_c^2}{4(\sum_{k=1}^3 A_k)}} \left[\frac{A_1}{\gamma_{31} - i(\Delta_p + \Delta_c + \delta_1)} + \frac{A_2}{\gamma_{31} - i(\Delta_p + \Delta_c + \delta_2)} + \frac{A_3}{\gamma_{31} - i(\Delta_p + \Delta_c + \delta_3)} \right] N(v)dv \quad 9.1$$

where $\Delta_p = \omega_p - \omega_{21}$ ($\Delta_c = \omega_c - \omega_{32}$) and Ω_p (Ω_c) are the detuning and Rabi frequency of the probe (pump) laser beam. $\gamma_{ij} \approx (\Gamma_i + \Gamma_j)/2$ is the coherence decay rate for $|i\rangle \rightarrow |j\rangle$ transition. d_{21} is the dipole matrix element between state $|2\rangle$ and $|1\rangle$. For a vapour cell containing Rubidium atom at thermal equilibrium, $N(v)$ is the Maxwell-Boltzmann velocity distribution. Weak probe field approximation is applied to derive the equation (9.1) and also the contribution from upper levels is neglected due to negligible population in the upper states. A_k is the line strength of the $F' \rightarrow F'' = k$ transition and is experimentally determined.

δ 's are the hyperfine energy gap as measured from $F'' = 4$ level. The contribution from the hyperfine transitions added phenomenologically to the equation (4.1) to arrive at the new equation (9.1). The imaginary part of the susceptibility is proportional to the probe laser absorption coefficient. In this case ω_p and ω_c are very close to each other and therefore the contribution from the two-photon Doppler width is neglected. Fig. 9.2(a) shows one such plot of $Im(\chi)$ vs Δ_p .

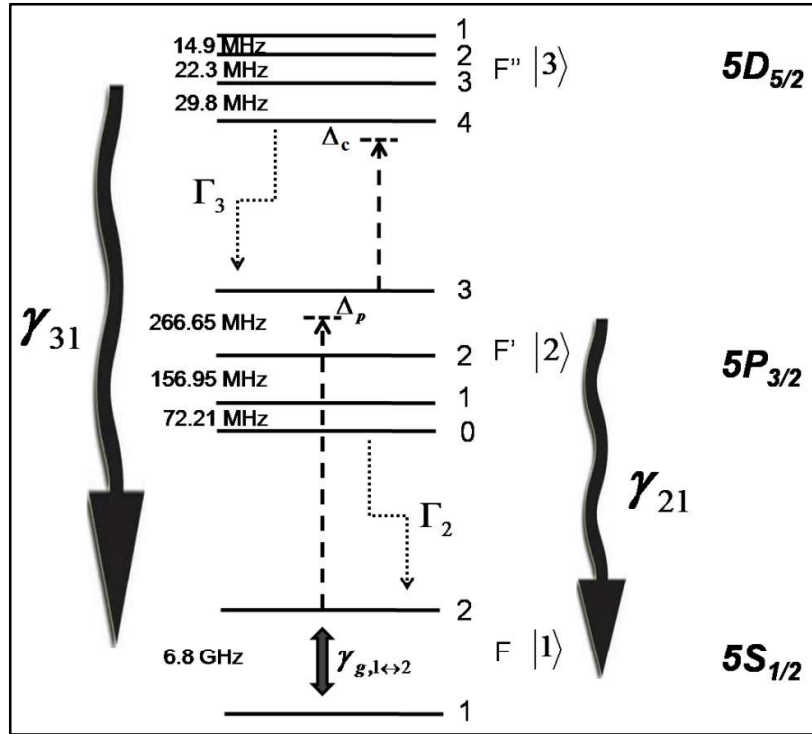


Fig. 9.1 Ladder level coupling scheme in Rubidium-87. γ_{ij} is the coherence decay rate between state $|i\rangle$ and $|j\rangle$. $\gamma_{g,1\leftrightarrow 2}$ represents coherence dephasing between the ground states $F = 1$ and $F = 2$. Spontaneous decay from state $|i\rangle$ is represented by Γ_i . $\Gamma_3 = 0.97$ MHz, $\Gamma_2 = 6.066$ MHz, $\Gamma_1 = 0.0$ MHz.

As shown in the level scheme in Fig. 9.1, the hyperfine levels identified with the F ($5S_{1/2}$), F' ($5P_{3/2}$) and F'' ($5D_{5/2}$) are denoted as $|1\rangle$, $|2\rangle$ and $|3\rangle$ respectively. For a resonant pump-probe coupling, the zero velocity groups of atoms are simultaneously at resonance with

pump and probe laser. These atoms are then transferred to the state $|3\rangle$ through the resonant coupling ($F = 2 \rightarrow F' = 3 \rightarrow F'' = 4,3,2$). In all these cases TPAs appear as the sharp and discrete transparency windows imprinted on the one-photon Doppler broadened absorption background as the pump laser (sometimes also referred as coupling laser) detuning Δ_c is much smaller than the Doppler width $\Delta\omega_D$. Fig. 9.2(a) shows such transparency windows on one photon absorption background. The pump laser frequency ω_c may be considered at near resonance or exact resonance for all the values of probe laser frequency ω_p while it was scanning the whole Doppler broadened $F = 2 \rightarrow F'$ transitions. For near resonant cases, the generalized Rabi frequency [146] $\Omega = \sqrt{\Omega_c^2 + \Delta_c^2(\nu)}$ comes into play. However equation (9.1) is not enough to explain the appearance of EIT as it is always accompanied by strong TPA.

The appearance of EIT within the TPA signal can be explained following the work of Zhu and Wasserlauf [183] on Λ system. The appearance of both EIT and TPA satisfies the two photon resonance condition $\Delta_p + \Delta_c = 0$ in a ladder system. Under this condition velocity averaged single absorption window splits into two absorption windows known as Autler-Townes' doublet with a transparency window in between [158,184]. For $\Delta_p = \Delta_c = 0$ and $\gamma_{31} \rightarrow 0$, the maximum transparency is observed at the line centre of the original absorption window and it coincides with the position of EIT. For finite value of γ_{31} , EIT becomes weaker and also the transparency within the AT doublet becomes wider [185]. The EIT itself appears as the consequence of so called "Dark state" due to the dressing of bare atomic levels [22]. As a result the absorbing medium becomes transparent to the probe laser with EIT appearing on the background of the TPA. In order to observe the EIT for a Λ system, $\Omega_c^2 / \Gamma \gg \gamma_{dipole\text{-forbidden}}$ must be maintained [186]. Similarly for a ladder system $\Omega_c^2 / 4\gamma_{21} \gg \gamma_{31}$ must be maintained [143] to observe the EIT.

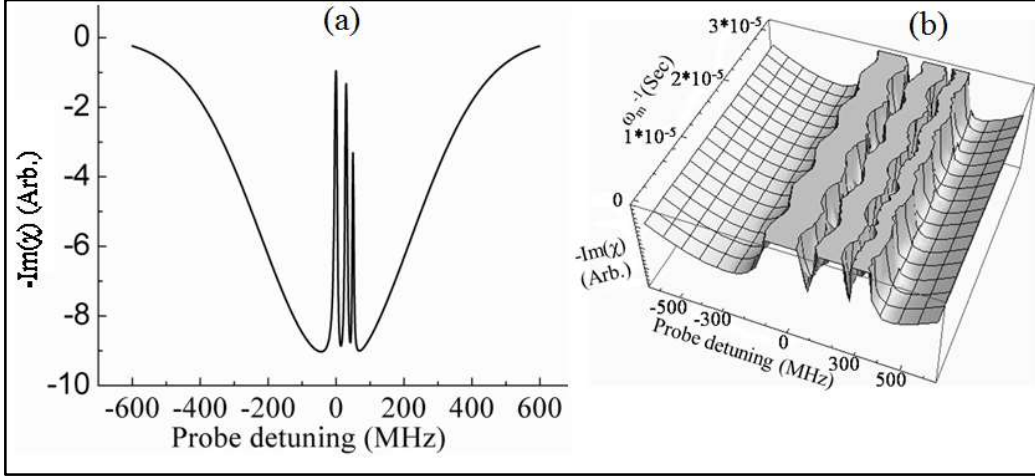


Fig. 9.2 Probe absorption and modulation transfer in a three level ladder system in the presence of strong pump beam. (a) Plot of $-Im(\chi)$ vs Δ_p (Doppler averaged) for $F \rightarrow F' \rightarrow F''$ ladder transition. Three F'' levels are separated by $\delta_2 = 30$ MHz and $\delta_3 = 50$ MHz, assuming $\delta_1 = 0$ MHz. $A_1:A_2:A_3 \approx 1:0.82:0.36$ from experiment. $\gamma_{12} = 3.033$ MHz, $\gamma_{13} = 0.485$ MHz. (b) Results of the theoretical simulation of modulation transfer is shown as zoomed 3D plot of the $-Im(\chi)$ vs Δ_p with time as a third variable in the time scale of ω_m^{-1} . The plot clearly reveals the transfer of pump modulation in the probe spectrum ($\omega_m = 100$ kHz).

Physically these conditions can be understood in terms of optical pumping in the time scales of $(\Omega_c^2/4\gamma_{12})^{-1}$ and γ_{31}^{-1} . Another time scale is the time scale of frequency modulation (ω_m^{-1}). Frequency modulation is introduced through the pump frequency. Theoretically this is incorporated in equation (9.1) by changing $\Delta_c \rightarrow \Delta_0 + A \sin \omega_m t$. Δ_0 is the DC pump detuning whereas A represents the amplitude of the frequency modulation. Additive inclusion in the pump detuning is justified as $\omega_m^{-1} \gg (\Omega_c^2/4\gamma_{12})^{-1}$ or γ_{31}^{-1} . In other words one can say that the slow duty cycle of the modulation enables the coherence processes to build. Therefore this simple substitution can easily explain the process of modulation transfer. In two photon resonance condition, the probe frequency also follows the

pump frequency. Fig. 9.2(b) shows how the pump modulation is transferred into the probe modulation for a modulation frequency of $\omega_m = 100 \text{ kHz}$, $\Delta_0 = 0$.

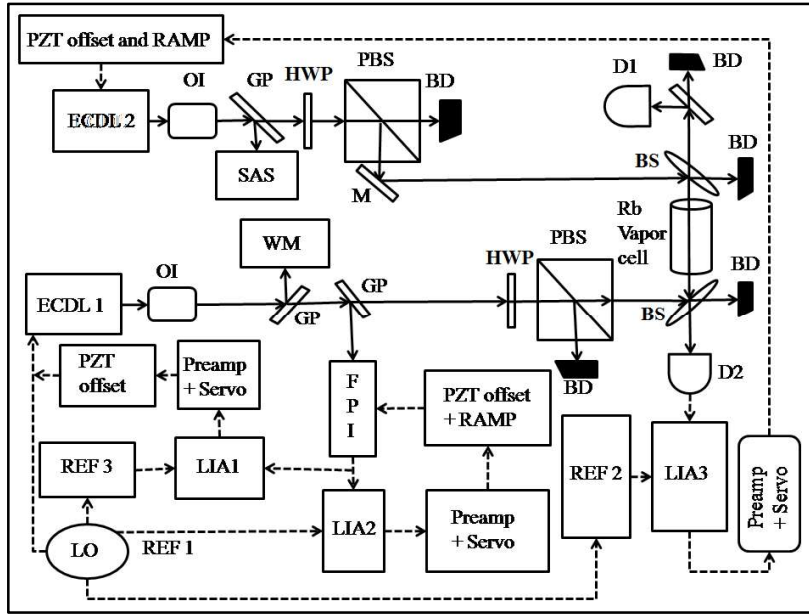


Fig. 9.3 Schematic of the experimental arrangement for TAFOL. ECDL1, 2: External cavity diode laser, M: Mirror, PBS: Polarizing cubic beam splitter, BS: Beam splitter, OI: Optical isolator, BD: Beam dump, D1, D2: Photodetectors, HWP: Half wave plate, FPI: Fabry-Perot interferometer, WM: Wavemeter, LO: Local Oscillator, Ref: Reference oscillator, GP: Glass plate, SAS: Saturation absorption spectroscopy, Preamplifier with servo control unit is used for frequency stabilization of the laser. All the reference oscillators were synchronized with the ‘mother’ oscillator.

9.4 Experiment, result and discussion

Experimental arrangement for the present experiment is shown in Fig. 9.3. Two external cavity diode lasers ECDL1 and ECDL2 are used as the pump and probe beams respectively. A small SAS arrangement on the probe laser reveals the $F = 2 \rightarrow F' = 3, 2, 1$ hyperfine transition of ^{87}Rb D_2 transition. This will help to calibrate the experimental data. Lasers are

used in perpendicular linearly polarized configuration with Rabi frequencies of $\Omega_p \sim 9$ MHz and $\Omega_c \sim 70$ MHz.

Pump and probe lasers are used in counter propagating configuration. This particular configuration helps to eliminate first order residual Doppler broadening as $\omega_p \approx \omega_c$. The experiment was conducted into several parts. Following few paragraphs provide the explanations along with the observations for each part of the experiment.

9.4.1 First part of the experiment

The probe laser was side locked on $5S_{1/2}(F = 2) \rightarrow 5P_{3/2}(F' = 3)$ transition of SAS signal. The pump laser was scanned across the $5P_{3/2} \rightarrow 5D_{5/2}$ transitions. Part of the pump laser beam was fed into FPI to monitor the fringes. The resulting spectra is shown in Fig. 9.4.

For a frequency locked probe laser, the resulting TPA and TPA with EIT signals appear without any Doppler background. As the probe laser is locked on respective SAS signal, the probe laser resonates only with small velocity groups of atoms. These atoms reach upper state $|3\rangle$ due to the presence of pump laser. As a result the usual presence of Doppler background is missing while we are scanning the pump laser. Extremely weak EIT feature can be seen within the $F' = 3 \rightarrow F'' = 4$ transition profile while the probe laser is side locked on $F = 2 \rightarrow F' = 3$ closed transition and is shown in Fig. 9.4(c). The same can't be seen on the $F' = 3 \rightarrow F'' = 3, 2$ transitions. By changing the lock positions of the probe laser to the cross-over transitions ($F = 2 \rightarrow F' = 3, 1$ and $F = 2 \rightarrow F' = 2, 1$ cross-overs) one can see that the strength of the TPA is gradually reduced and EIT signals are now clearly visible which is depicted in Fig. 9.4(b) and Fig. 9.4(a).

For the current experimental scheme $\Delta E_{F' \rightarrow F''} \ll \Delta E_{F \rightarrow F'}$, therefore $F = 2 \rightarrow F' = 3 \rightarrow F''$ transition indicates almost resonant coupling of atoms between $5S_{1/2} \rightarrow 5D_{5/2}$ transition.

The atoms which are coupled to $5D_{5/2}$ state via other excitation routes ($F' = 3 \rightarrow F'' = 3, 2$), can decay back to $F = 1$ level or leave from the present ladder coupling scheme. This is known as the double resonance optical pumping (DROP) [19,18] and is always present with the TPA spectra. The decay route $F'' = 4 \rightarrow F' = 3 \rightarrow F = 2$ forms a pseudo closed absorption-emission cycle [164] and the probability of losing atoms to $F = 1$ state due to DROP is minimum. This is why the EIT is noticeable on the $F' = 3 \rightarrow F'' = 4$ transition profile while it is absent on the other peaks.

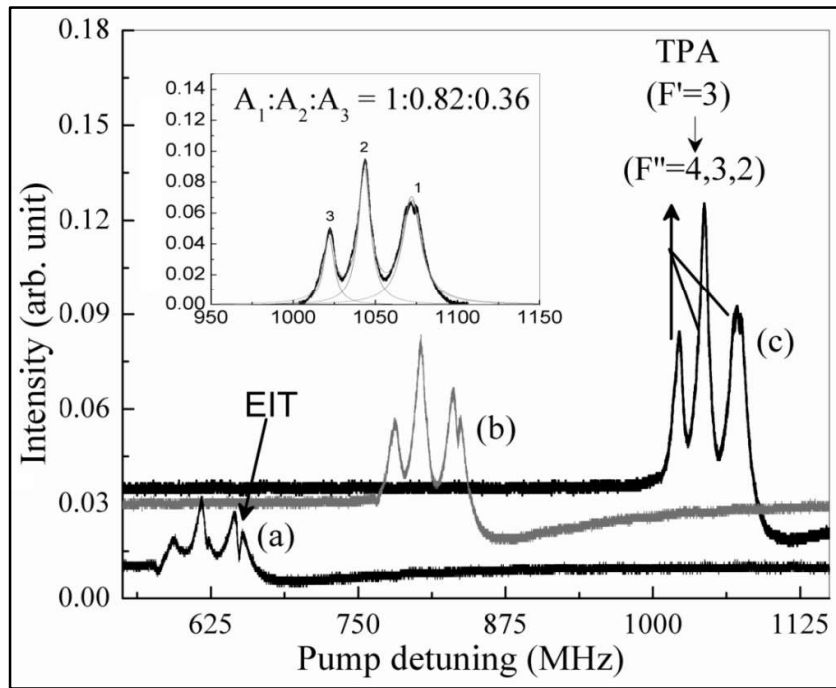


Fig. 9.4 Probe absorption spectrum vs pump detuning. Probe laser is side locked on SAS signal. (a) Shows prominent EIT and reduced DROP feature (b) Intermediate position (c) Strong TPA with very weak EIT feature. X-axis is calibrated with FPI fringe recordings. The inset shows fitting of TPA spectrum. Relative line strengths of the TPAs are determined from the fitting.

For Fig. 9.4(b) and Fig. 9.4(a) the probe laser was locked on the cross-over SAS signals. Therefore the transitions are non-resonant two photon transition. These transitions address

more velocity group of atoms than the pseudo closed resonant transition which in turn increases the population of the excited states and also the probability of atom loss to $F = 1$ state through DROP. Ultimately the TPA signal becomes weaker and can be seen on Fig. 9.4(b) and Fig. 9.4(a). In this situation EIT becomes prominent as it is always present in the system.

Since the $\Omega_p \ll \Omega_c$ and $\Delta_p \approx 0$, the number of atoms pumped to $5P$ level is very small. The relative line strengths of the $F' = 3 \rightarrow F''$ transitions are estimated from the area under the recorded TPA spectra as shown in Fig. 9.4(c) and the fitting is shown in the inset of Fig. 9.4. This comes out to be $A_1:A_2:A_3 \approx 1:0.82:0.36$ and is used in the simulation of equation (9.1). Since the experiment was done without FMS, line broadening due to modulation does not appear in the estimation. This estimate includes the laser line-width of the respective lasers. The ratios of line strengths are not exact as there is a small probability of atom leakage from the pseudo closed absorption-emission cycle. In the case of a room temperature vapour cell without buffer gas, the dephasing mechanism (represented by $\gamma_{g,1 \rightarrow 2}$.) between $F = 2$ and $F = 1$ is governed by the transit time effect which is very slow compared to the other decay and pumping processes. Therefore the ground state dephasing doesn't come within the scope of the present discussion.

9.4.2 Second part of the experiment

Demonstration of offset locking is performed in the second part of the experiment. This is achieved by locking the pump laser at a frequency matching the $5P_{3/2} \rightarrow 5D_{5/2}$ transitions. To select the desired pump frequency for locking, probe laser is scanned across the $5S_{1/2}(F = 2) \rightarrow 5P_{3/2}(F')$ transition. Once the TPA signals are visible on probe scan spectrum, pump frequency is adjusted using the correct piezo offset voltage so that the TPA signals are at desired position on the probe absorption spectrum. In the next step FPI cavity is

scanned with a ramp signal so that the fringes are observed on another oscilloscope. A small current modulation ($\Delta v_m < 1 \text{ MHz}$) is applied on the pump laser for FMS at this stage. Using two separate but phase locked phase sensitive detection (PSD) modules, $1f$ and $3f$ spectrums of the fringe discriminator is extracted. The $1f$ signal is used to provide the electrical feedback to the piezo transducer (PZT) of the FPI cavity for stabilization. Once the FPI cavity is stabilized on $1f$ discriminator signal, the error signal obtained at the $3f$ discriminator output of the lock-in amplifier LIA1 detects the consequent pump laser fluctuation from the FPI lock point. Therefore the closed loop containing the $3f$ discriminator signal and LIA1 (Fig. 9.3) can stabilize the pump laser frequency on FPI cavity fringes. Fig. 9.5 shows the obtained $1f$ and $3f$ signal along with the FPI fringes.

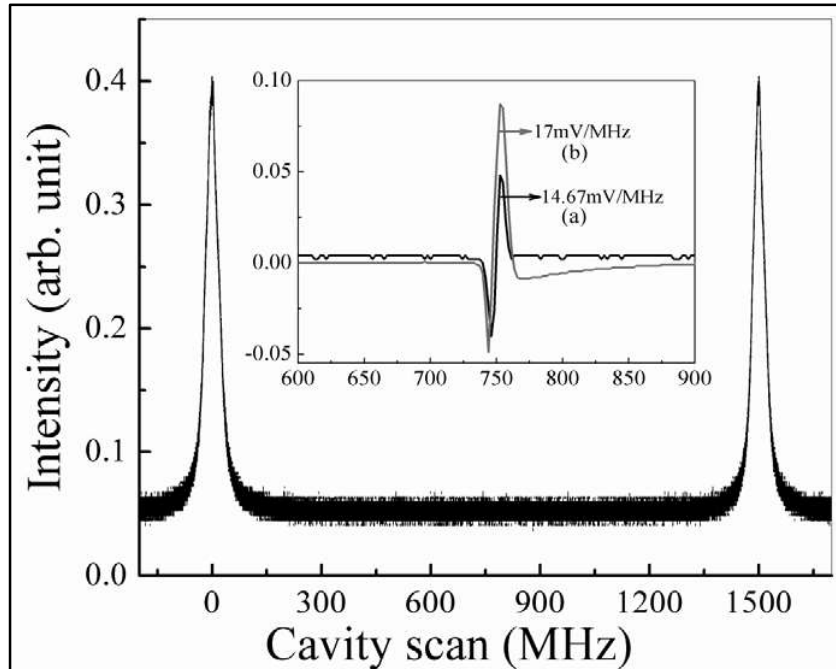


Fig. 9.5 Recorded fringes from a scanning FPI. FSR of the FPI (Thorlabs SA-200-5B) is 1500 MHz and FWHM of the fringes ~ 5.3 MHz. One particular fringe is chosen using the piezo offset voltage and RAMP generator to lock the pump laser at desired frequency. (a) $1f$ output from LIA2. (b) $3f$ output from LIA1 after the pump frequency modulation is switched ON.

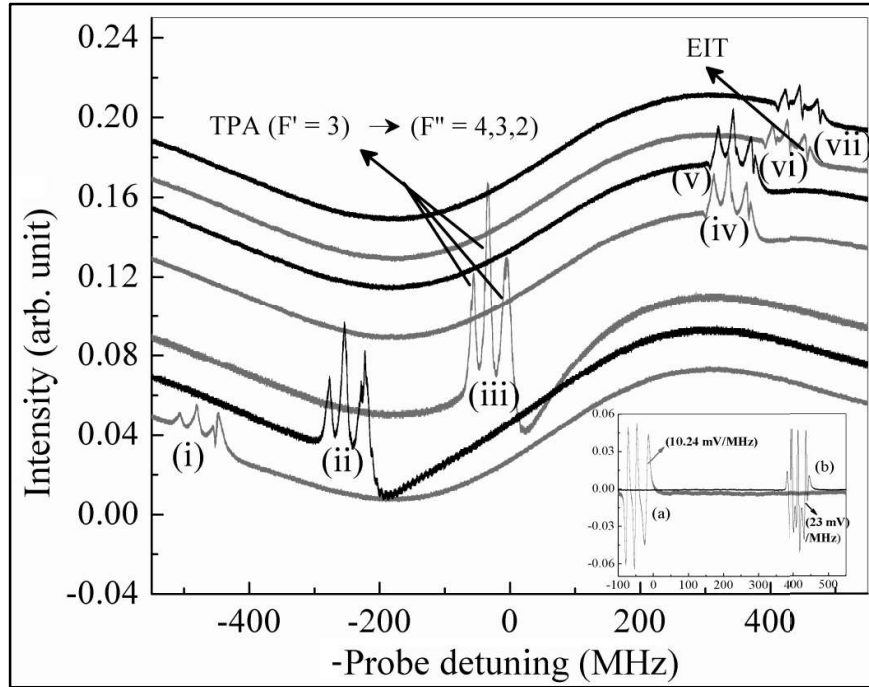


Fig. 9.6 Probe absorption spectra for different pump frequency settings. Rabi frequencies are kept unchanged with previous readings. Pump laser is static in free running condition. Simultaneous monitoring of SAS spectra and probe absorption spectra are required for calibration. The piezo offset voltage of the pump laser is adjusted to change pump laser frequency. Plot (iii) shows the position of pseudo-closed two photon transition. Plot (i) to (ii) and (iv) to (vii) represent different pump frequency positions on both sides of the resonant two photon excitation respectively. Inset shows (a) If signal of TPA when TPA originates from pseudo-closed transition and corresponds to plot (iii). (b) If signal for EIT when $|\Delta_c| = 450$ MHz from $F' = 3 \rightarrow F'' = 4$ transition and corresponds to plot (vi).

As the frequency modulation is transferred to the probe laser, one can extract the If discriminator signal from the probe laser absorption spectra. Another phase locked PSD is used to extract the If discriminator signal from the respective TPA/EIT signal which helps to stabilize the probe laser frequency on the TPA/EIT reference. Once all the components viz.

FPI cavity, pump laser and probe laser are stabilized, the corresponding error signals are recorded.

Since the recording are done within ~ 1 s time scale window, the long term drift of ω_c does not affect the spectrum. The probe SAS spectrum is used for calibration purpose. Fig. 9.6(iii) and Fig. 9.4(c) are identical apart from the Doppler background present in the probe absorption spectrum. TPA and EIT signal can be seen throughout the entire Doppler width. From Fig. 9.6 it is clear that DROP feature weakens and the optical pumping to $F = 1$ level become stronger as we go further away from the resonant TPA coupling. The asymmetry in the EIT signal on the TPA background can be attributed to the AT splitting for off resonant condition [183].

In order to stabilize the pump laser at ~ 776 nm, one should have a spectroscopic reference with good S/N at this wavelength. But the atomic population in the $5P$ state is not significant which makes it hard to get any spectroscopic reference at this wavelength. Again in order to achieve a tunable offset locking, the lock point of the pump laser frequency must be tunable over a wide range. This large tunability of the pump laser results in frequency tunability of the probe laser. Therefore we are bound to use a FPI signal to lock the pump laser. The FPI cavity fringe which has a FWHM of 5 MHz which is much smaller than the overall frequency spacing of $5D_{5/2}$ (~ 50 MHz) and Γ_{TPA} . Therefore FPI cavity can serve as a suitable reference to fix the pump laser frequency. As the FPI fringes are easy to find at any wavelength within the pass band of the cavity, the locking is easy to implement and the lock point can be tuned over a wide range. For example the tuning range can cover the whole $5S_{1/2}(F = 2) \rightarrow 5P_{3/2}(F')$ transition region. Fig. 9.6 shows the probe absorption spectra for different pump frequencies. This shows about $\Delta_p \sim 1$ GHz wide tuning range of the frequency offset reference. The EIT feature in case of ladder (Ξ) system is sub-natural ($< \Gamma_2$) throughout the

$F = 2 \rightarrow F'$ absorption profile. Therefore one can obtain sub-natural atomic offset reference over a wide range and at will. This is much different than the Λ scheme where the option is limited to only few points.

In order to stabilize the FPI cavity and pump laser frequency we have used proportional-integrator (PI) control loop which has a corner frequency (3dB) of 500 Hz. The piezo actuator for the ECDL is more sensitive than the same for FPI cavity. For this reason we have used a $3f$ signal with relatively higher slope for pump laser stabilization. The transferred FM in the probe frequency helps to generate I_f discriminator signal from the TPA and EIT spectra. The probe laser is locked at two different frequencies. (a) on the TPA originating from the $F = 2 \rightarrow F' = 3 \rightarrow F'' = 4$ coupling and (b) on the EIT originating due to pump at $|\Delta_c| = 450 \text{ MHz}$ from the $F' = 3 \rightarrow F'' = 4$ resonance condition. Corresponding I_f discriminate signals can be seen in the inset of Fig. 9.6 which also corresponds to the I_f derivative of Fig. 9.6(iii) and Fig. 9.6(vi). The obtained discriminator slopes for EIT, FPI and TPA are $\sim 23.00 \text{ mV/MHz}$, 17.00 mV/MHz , 10.24 mV/MHz respectively.

The line-width of TPA (Γ_{TPA}) is limited by the spontaneous decay whereas the same for EIT (Γ_{EIT}) is limited by the coherence decay rate and the line-widths of the lasers itself [15]. Experimentally obtained values $\Gamma_{TPA} = 9.01 \text{ MHz}$ and $\Gamma_{EIT} = 3.5 \text{ MHz}$ are very close to the theoretical values ($\Gamma_{TPA} = 8.5 \text{ MHz}$ and $\Gamma_{EIT} = 2.1 \text{ MHz}$). The measured line-width also contains the effect of modulation. It should be noted that $\Gamma_{TPA} \sim \Gamma_2$ which can be achieved at best for SAS of alkali atoms [187]. Therefore it can be said that the TAFOL scheme does not pose any serious trade-off between the wide tunability and the discriminator line-width. This has been possible due to the mutual competition between the DROP and EIT mechanism throughout the Doppler width ($\Delta\omega_D$) and in the end it customary to say that the Ξ scheme is more competitive towards TAFOL compared to Λ coupling scheme.

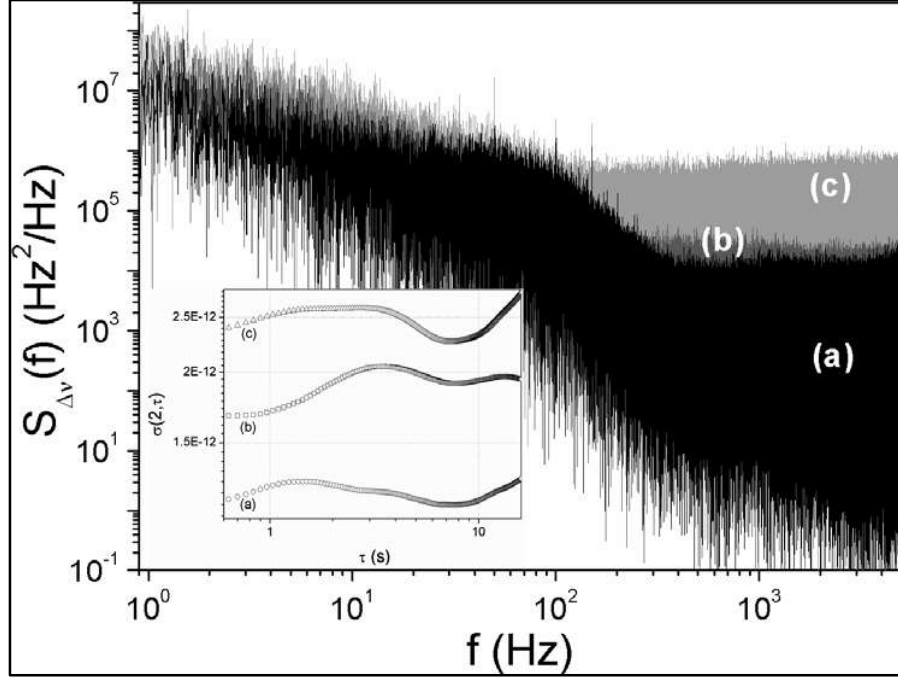


Fig. 9.7 Frequency noise spectral density ($S_{\Delta\nu}$) vs Fourier frequency (f) plot. for (a) probe lock on EIT (b) pump lock on FPI cavity fringe (c) probe lock on TPA. $S_{\Delta\nu}$ is estimated in close-loop condition using FFT analysis. Plot (a) shows the control bandwidth of 100 Hz of the PI control. Inset shows the Allan variance $\sigma(2, \tau)$ vs integration time τ for three different locking situations. Details are described in the text.

Fast Fourier transform (FFT) is carried out on the recorded error signal to reveal the frequency noise spectral power density $S_{\Delta\nu}(f)$. Square root of *Allan Variance* $\sigma(2, \tau)$ is estimated from $S_{\Delta\nu}(f)$ to determine the stability of the respective frequency locking using equation (3.17). The nominal frequency $\nu_0 = 3.843 \times 10^{14} \text{ Hz}$ and τ is the integration time in equation (3.17). $S_{\Delta\nu}(f)$ vs Fourier frequency (f) data is obtained from the FFT analysis of the recorded error signal (Fig. 9.7). The behaviour of $\sigma(2, \tau)$ with τ is shown in the inset of Fig. 9.7 for pump and probe lasers. It is observed that at $\tau = 10 \text{ s}$, the locking of probe laser attains a stability of $\sigma \sim 1.2 \times 10^{-12}$ for locking on EIT signal and $\sigma \sim 2.35 \times 10^{-12}$ for

locking on TPA signal. The same for pump laser is $\sigma \sim 2.4 \times 10^{-12}$. This method of frequency stability measurement under closed loop condition does not include the noise of the discriminator still it can effectively determine the relative frequency stability of the laser.

From the inset of Fig. 9.7 it is pretty clear that in the shorter averaging time scale ($\tau \sim 0.5 \text{ s to } 20 \text{ s}$) probe laser lock on EIT has the best behaviour. This is due to the steeper slope of the I/f discriminator signal. The superiority of this EIT lock over the Pump laser lock on FPI fringe can be understood from the fact that the EIT line-width is mainly dominated by γ_{31} and is pretty immune to the effect of pump frequency fluctuation as long as $|\Delta_p + \Delta_c| \sim \gamma_{31}$ is maintained and conditions for optical pumping ($\Omega_c^2/4\gamma_{12} \gg \gamma_{31}$) is satisfied. The different slopes for EIT and TPA resonance indicate different degrees of modulation transfer for each case. The steeper slope of EIT exhibits a higher degree of coherence assisted modulation transfer compared to the TPA resonance [188].

9.5 Conclusion

Present chapter explored the possibility of using $^{87}\text{Rb } 5S_{1/2} \rightarrow 5P_{3/2} \rightarrow 5D_{5/2}$ ladder (Ξ) system for TAFOL. In this endeavour it is found that the probe absorption spectrum is dominated by DROP and EIT. The strength of DROP is proportional to the TPA signal. The effect of probe and pump laser detunings have been studied in great details. External modulation on pump laser is successfully transferred to the probe laser through two-photon coupling. A phenomenological attempt has been taken to explain the stated modulation transfer which is found to be more effective under EIT compared to DROP. The results of the frequency stabilization were presented. It is found that EIT based lock of the prober laser frequency shows better stability ($\sigma \sim 1.2 \times 10^{-12}$) in the shorter time scale (0.5sec to 20 sec). The same for locking on TPA is $\sigma \sim 2.35 \times 10^{-12}$. The pump laser was locked on FPI cavity fringe at $\sim 776 \text{ nm}$ and can be tuned at will.

In summary, this study helped in creating a tunable (over 1GHz) offset reference with a 780 nm laser. The trade-off for large tuning range vs discriminator line-width has been avoided in the present case. The discriminator line-width is within 8.5 MHz to 2.1 MHz and in the worst case it is equivalent to the best case of Γ_{SAS} . This makes the study useful for cases which require continuous tunability and precision frequency stability. We have considered transferring modulation from pump laser to the probe laser contrary to the earlier efforts [43,15] and it results in a better transfer as the Rabi frequency of pump laser $\Omega_c \gg \Omega_p$. Large modulation depth produces better workable discriminator signal but it introduces additional instrumental line-width into the system. Use of external modulation may eliminate this problem.

**Part II. Development of a collinear laser spectroscopy
setup at the ISOL facility at VECC**

Chapter 10

Development of the collinear laser spectroscopy set up at VECC- ISOL facility

10.1 Introduction

The present chapter discusses the development of a collinear laser spectroscopy setup at the ISOL facility at VECC and the corresponding detection of Rubidium absorption lines. The collinear laser spectroscopy (CLS) setup will be used to study the radioactive species produced from the interaction of a primary beam from VEC cyclotron and a suitable target. The program is primarily aimed at measuring the isotopic shift and hyperfine splitting of rare ions/atoms online. The reaction products produced at the target will be transferred to the surface ion source present at the VECC-ISOL facility [189,190] using gas jet recoil transport techniques [191]. The elements produced in the target chamber will be transported to the surface ion source due to differential pumping. The ion source and the whole facility are placed on the high bay above the cyclotron beam line. Currently the ion source is operated in the offline mode to benchmark the CLS setup. The whole ion source is operated at high voltages (up to +30 KV). The ion beam extracted from the ion source is guided by two quadrupole magnets arranged in X-Y focussing mode. A 55° bending magnet is used downstream to mass separate the accelerated ion beam. The beam guiding system was designed for a dispersion of 2.52 m for 100% rigidity change. Ion beam current is monitored using Faraday cups to optimize the beam transmission to the CLS setup. The CLS set up has been installed downstream of the existing ISOL beam line. However, downstream of the dipole magnet there is not enough space to allow installation of high voltage electrodes in the charge exchange cell satisfying safety norms. For Doppler scanning, therefore, we choose the

option of laser frequency scanning rather than the voltage scanning of the ion beam in the present setup.



Fig. 10.1 Current status of collinear laser spectroscopy setup

As the ISOL system up to the focal plane after the dipole magnet was already in place, the beam line comprising of the charge exchange cell (CEC), photon detection unit, and Faraday cup was designed, fabricated and installed. Ion beam transport was revisited using computer code TRANSPORT [192] for the entire beam-line including the new extension to ensure efficient beam transmission and adequate resolution. The beam optics simulations show that the laser spectroscopy setup can be accommodated within the space available at the VECC-ISOL site. The current status of the facility is shown in Fig. 10.1. As a first step towards the detection of rare ion beams, stable ion beam of Rubidium is accelerated in the system. The neutral beam of Rubidium atoms (after charge exchange) emits fluorescence photon after interacting with a Doppler shifted laser and the same is detected in the photon detection unit. The best value for the measured photon detection efficiency in the present setup is $\sim 1/(6 \times$

10^5) (detected signal photon count/atom number) in the presence of a $\leq 10^4$ /sec background photons. The following sections discuss about the development of the experimental setup and the first experimental test with 8.0 keV stable Rubidium beam. The future directions and the scope of further improvements are also discussed in the later portions of the chapter. 3D view of the beam transport system of the ISOL experimental facility is shown in Fig. 10.2.

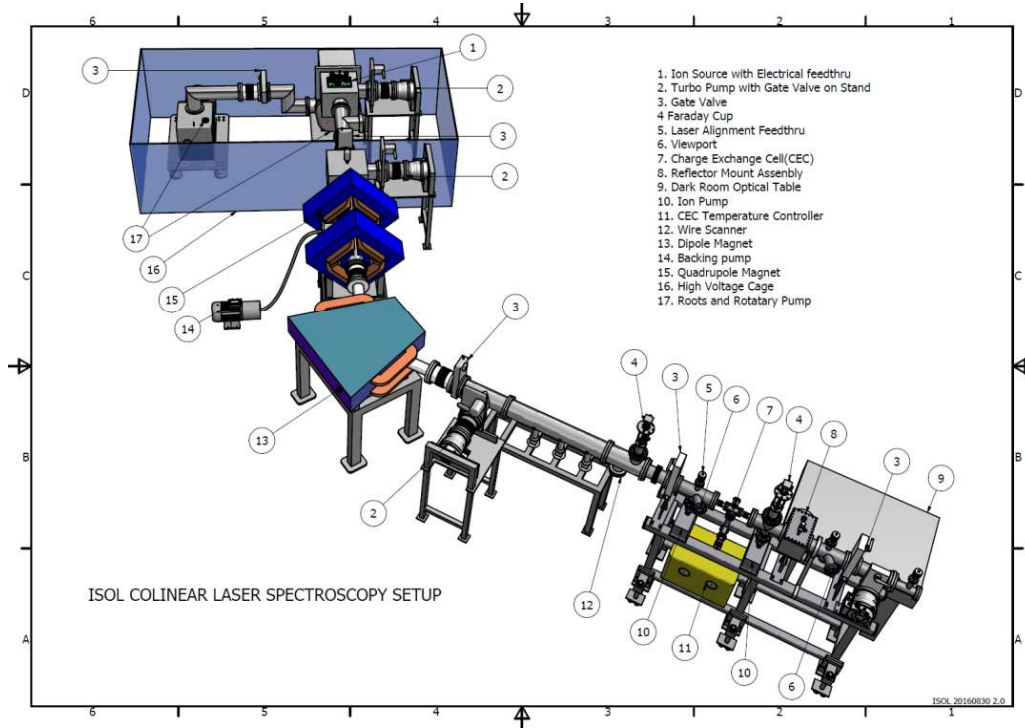


Fig. 10.2 3D view of the ion beam transport system for ISOL-CLS setup.

10.2 Collinear laser spectroscopy setup at the VECC-ISOL facility

The five main components of the ISOL - Collinear Laser Spectroscopy (CLS) set up are: ion source, beam transport system, charge exchange cell, photon detection unit and laser system. The ion beam of a particular atomic species (Rubidium in the first test) and energy (decided by the extractor potential) from the ion source is guided by the beam transport system and transported through the charge exchange cell. A fraction of the ion beam undergoes charge exchange collision in the CEC and is converted into atoms. This atom

beam when illuminated with a resonant laser light emits fluorescence photons which are then collected by the photon detection system.

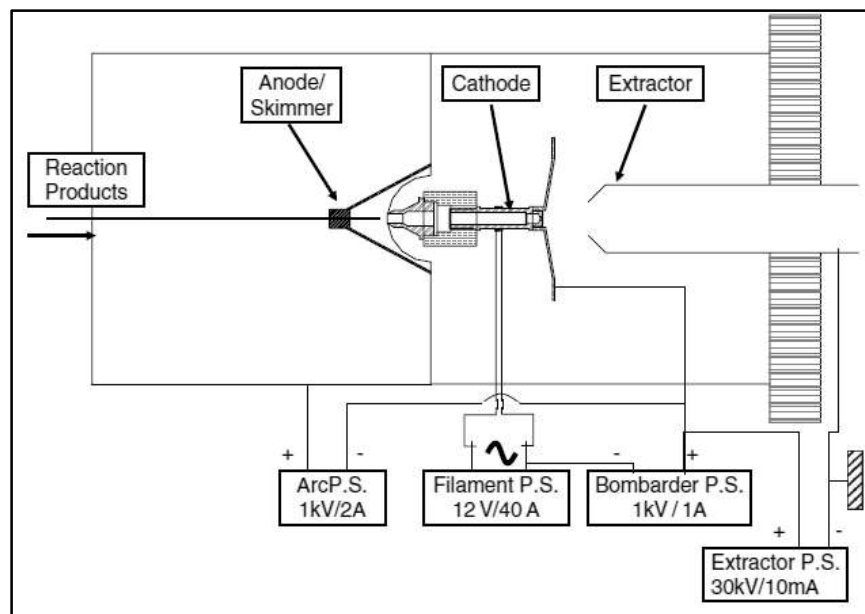


Fig. 10.3 Ion source (schematic) of the ISOL-CLS facility

10.2.1 Offline ion source

The ion source was part of the already existing VECC-ISOL facility [193] and it can be used in both online and offline mode. For online operation the reaction products will be transported to the ion source from the Gas-jet target chamber by differential pumping. The high dynamic gas load due to the use of a carrier gas (He) is taken care of by a roots pump (pumping speed around $1300 \text{ m}^3 \text{ h}^{-1}$). The ion source can be operated in high temperature surface ionization mode (SI) as well as in hollow cathode (HC) type arc discharge mode. For the present work we operated the ion source only in the surface ionization mode. The schematic diagram of the ion source with electrical connections is shown in Fig. 10.3 . The entire ion source can be floated up to $+30 \text{ KV}$ while the extractor is kept at ground potential. For the present work only $+8 \text{ KV}$ is applied for beam extraction from the ion source. The filament is heated using AC power supply to avoid the solenoidal field which might arise

from DC heating. The cathode of the ion source is indirectly heated by electron bombardment as it is kept at positive potential (up to 1kV) compared to the filament. The cathode, anode and filament of the ion source are made of Tantalum. Boron nitride is used as the insulator. As the un-normalized emittance is proportional to the size of the hole on the cathode, smaller hole was made to achieve higher mass resolution from the system. The smaller hole also ensures better vacuum at the extraction side. The cathode hole diameter used by us is either 0.8 mm or 1 mm. The cathode chamber is pumped by (Pumping speed ~ 500 lps) a turbo molecular pump. A vacuum gauge placed on the high voltage platform helps to monitor the operational pressure inside the ion source chamber.

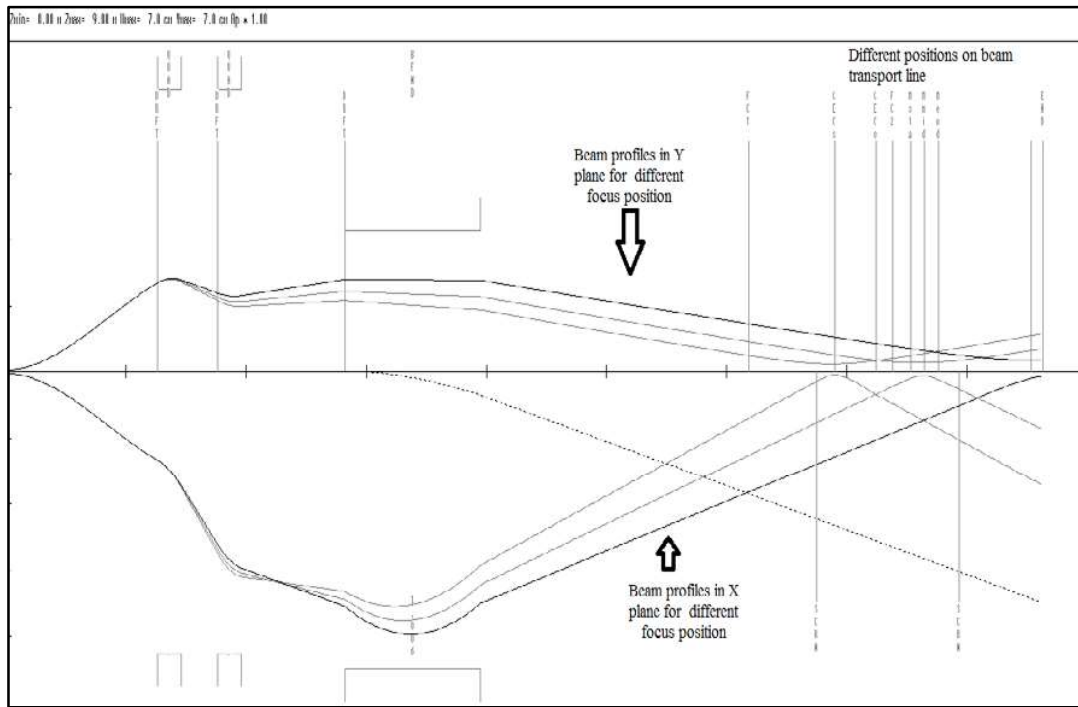


Fig. 10.4 Ion beam profile simulated in TRNASPORT

10.2.2 Beam transport system, diagnostics and beam tuning

The beam optics of the whole system is revisited by incorporating the newly designed laser spectroscopy setup into the already existing VECC-ISOL system. The main goal of the new beam optics design is to transport the ion beam to the optical detection chamber with

minimum loss. The design considers a Rubidium-85 ion beam with beam emittance of about $7.5 \pi \text{ mm mrad}$ and a beam of energy 8.00 keV . The design parameters for the new design are listed in Table 10.1. Simulation shows 100% beam transport is possible with the existing magnets (one dipole magnet and two quadrupole magnets). The simulated beam profile can be seen in Fig. 10.4. The simulation further shows further that by varying the strengths of the quadrupole magnets a double focussing condition ($R_{12} = 0, R_{34} = 0$; $R_{ij} = \text{TRANSPORT parameters}$) can be achieved at different locations in the beam line. The charge converted ion/atom beam finally stops at the glass view port (end flange) after crossing the detection chamber. The apertures on the both sides of the ellipsoidal mirror limit the size of the ion beam reaching the end flange. To measure the beam transport efficiency and also to calibrate the charge exchange cell efficiency two faraday cups were used - one before (FC1) and the other (FC2) after the charge exchange cell. Experimental transport efficiency of the whole system is listed in Table 10.2. The placement of the apertures in the photon collection chamber reduces the beam transport efficiency. Typically we obtain an efficiency of 15%.

During the beam tuning, ion beam current is maximized at the end flange by adjusting the quadrupole and dipole magnet settings. As the mass resolving power of the system is pretty high (~ 719), we had to change the dipole and quadrupole magnet settings in between the experiment to obtain a full spectrum consisting of both ^{85}Rb and ^{87}Rb resonance lines. Simultaneous monitoring of the ion beam profile using a wire scanner placed before the charge exchange cell (CEC) helps in optimizing the ion beam current and beam shape. One such ion beam profile is shown in Fig. 10.5. In order to increase the ion beam current either the filament current or the bombarder voltage of the ion source is adjusted so that the desired beam current can be achieved. Up to $\sim 3 \mu\text{A}$ beam current could be obtained at FC1 for a bombarder voltage of $\sim 700 \text{ V}$ and filament current of $\sim 30 \text{ A}$. Typical ion source operating parameters are listed in Table 10.2.

Table 10.1. Beam optics simulation results for the ISOL-Collinear laser spectroscopy beam line

Focussing position	Quad1 (KGauss)	Quad2 (KGauss)	Beam size at FC1 (cm)		Beam size at CEC start (cm)		Beam size at FC2 (cm)		Beam size at Reflector entry (cm)	
			X-plane	Y-plane	X-plane	Y-plane	X-plane	Y-plane	X-plane	Y-plane
At CEC start	-0.51383	0.35917	2.00	0.72	0.16	0.37	1.34	0.59	2.41	0.88
Reflector middle position	-0.47997	0.32367	3.59	1.30	2.19	0.85	0.66	0.46	0.32	0.42
End flange	-0.43759	0.28390	5.16	2.06	3.96	1.60	2.63	1.12	2.32	1.01

Simulation considers 8.0 keV ^{85}Rb ion beam. The emittance is taken to be $7.5 \pi \text{mm mrad}$ for a beam size of 1 mm in both X and Y plane at ion source. The results are only indicative as no emittance measurement was performed on the system.

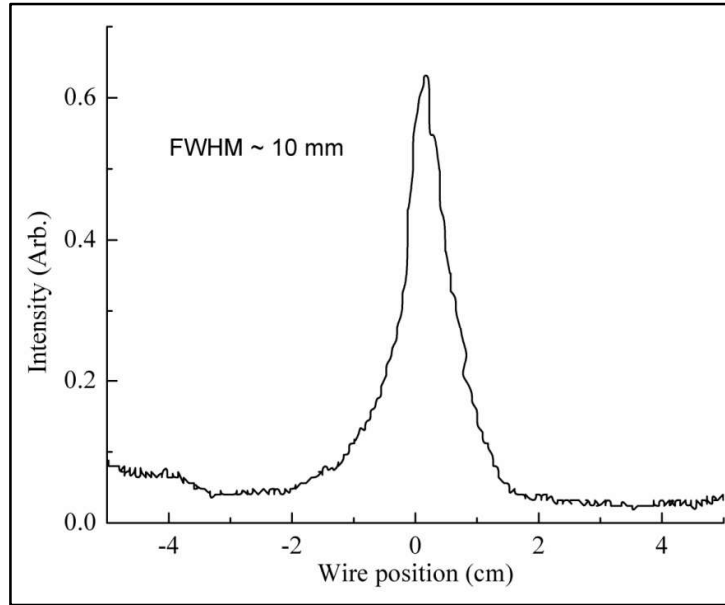


Fig. 10.5. Ion beam profile in X plane as measured using wire scanner

Table 10.2 Ion source parameters and practical beam transport efficiency

Ion source operating parameters			Transport efficiency		
Filament	Bombarder		FC1-FC2	FC2-End flange	FC1-End flange
Current	Current	Voltage	(%)	(%)	(%)
(A)	(mA)	(V)			
28	150	540	30 %	50 %	15%

10.2.3 Design of the charge exchange cell

The present design of the VECC-collinear laser spectroscopy set up is based on laser scanning. Thus as compared to the other type of CEC [194] which incorporates the post-acceleration section of the ion beam, our set up is based on the design of M. Bacal et al [195]. This kind of CEC is suitable for easy access and maintenance. The CEC is placed before the photon detection region and converts a fraction of the ion beam into atom beam. It consists of

a detachable SS flange with the provisions for placing the alkali glass ampoule (5gm, Sigma-Aldrich) inside it (Fig. 10.6). This portion of the chamber can be isolated from the main beam line vacuum using a mini gate valve. In order to refill the CEC, the glass ampoule is placed inside the designated holder in the detachable flange. The whole detachable flange assembly is then attached with the main beam line body. Careful handling is mandatory while refilling the CEC to avoid breaking of the glass ampoule. After the flange is vacuum sealed with the main vacuum chamber, a metal rod inserted through the mechanical feed through into the CEC, is used to break the tip of the ampoule (Fig. 10.6 b). A cracking sound can be heard from the outside of the chamber as the ampoule is broken inside. This, along with the pressure readings on two ion pumps on both sides of the CEC, can be used as the indicators to ensure the breaking of the glass ampoule inside the chamber. The pressure reading on the ion pumps increases momentarily and settles down to its previous values quickly. As the sealed glass ampoule also contains Ar gas, it causes the fluctuation in the pressure readings when it is broken inside the chamber.

The CEC is heated in a thermostat type closed loop using ~7 mica band heaters. These heaters ensure a proper temperature distribution along the CEC for the recycling of the unused metal vapour. The 'T' portion of the CEC is cooled with water. This cooling helps to condense the metal vapour on the mesh welded inside the 'T' portion of CEC. A slight inclination is made on the 'T' portion of the CEC which helps the condensed alkali metal droplets to move near to the main reservoir by the action of the gravity. This way the unused alkali metal can be recycled and used in further experiments. Typically a 5 gm ampoule can be used for 25 hrs or more of continuous operation. The entrance and exit port of the CEC has a smaller diameter (~ 20 mm) compared to the rest of the beam pipe. This ensures minimum leakage of the alkali atom vapour from the CEC zone to the main beam line at the cost of some loss in beam intensity.

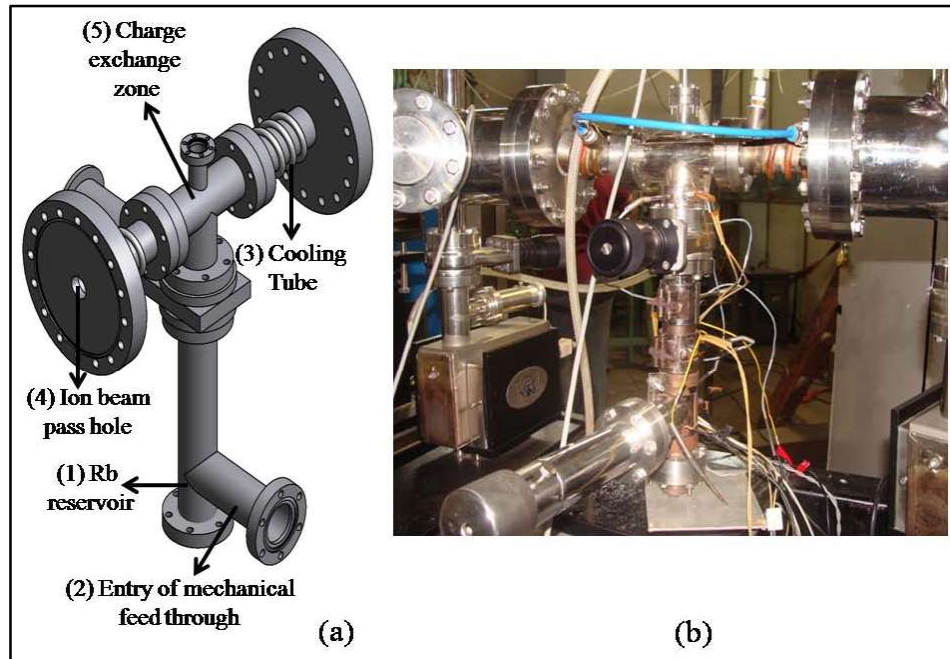


Fig. 10.6 Charge exchange cell for ISOL-CLS setup: (a) 3D design view of the CEC
 (b) Photograph of CEC in the ISOL-CLS setup.

The pressure and ion current readings on the ion pump are the indicators of the health of the alkali metal inside the CEC. Usually the ion current reading holds at $\sim 2 \text{ mA}$ (nearby chamber pressure of $\sim 2 \cdot 10^{-5} \text{ mbar}$) when the CEC contains enough amount of alkali metal for charge exchange. The depletion of the alkali metal is indicated by the reduced ion pump current (down at $\sim 1 \text{ micro amp}$). After the depletion of the metal inside CEC, the chamber is opened for cleaning and refilling with proper precautions. The whole chamber is then cleaned with alcohol for further use. The beam line is regularly filled with Argon (Ar) gas at $\sim 1 \text{ atm}$ pressure after the day's activity is over. This prevents the residual alkali metal from forming oxides.

10.2.4 Photon detection unit and PMT handling

The optical detection unit used is similar to the one presented in the dissertation of Jörg Krämer [196]. The unit consists of a SS box containing an ellipsoidal reflector (REM-144.2-

31.8-21.0, CVI Melles Griot) which provides $\geq 80\%$ reflectance over a wavelength region of 400-900 nm. The reflector collects the fluorescence photons from the primary focus and reflects those to the secondary focus. It is fixed on a mirror holder with mechanical screws. The holder itself can be mounted on one side of the SS box wall. The other side of the wall has a vacuum compatible glass flange fixed on it. The position of the secondary focus is right at the middle of this flange. The exact location of the secondary focus is determined by constructing an image of the primary focus with the help of fluorescence photons from a Rb vapour cell placed on the ellipsoidal reflector (Fig. 10.7). The laser beam (tuned to ^{85}Rb $5S_{1/2} - 5P_{3/2}$ transition) passing through the vapour cell emits fluorescence photons which are then passed through the primary focus and are reflected towards the secondary focus. The construction of the image at the secondary focus also ensures a proper alignment of the laser beam passing through the detection unit. A photomultiplier tube (R-943-02, Hamamatsu) is fixed at the location of the secondary focus using the cage mount assembly (Fig. 10.8) to collect these secondary photons. The corresponding markings on the beam line catcher (Fig. 10.2) helps in laser beam alignment during the experiment. The same exercise was also tried with dry gas like Argon or Nitrogen but we could not achieve enough luminescence at the secondary focus.

In order to reduce the noise from background stray light, the PMT is covered with black paper and is placed inside the makeshift dark room created for the purpose. Any open viewport on the beam-line is also covered with black papers during the experiment. Careful arrangements are made so that no power line noise is present at the output of PMT. Power line noise is very common for an old system like the existing ISOL facility of VECC. A rectangular aperture (9mm \times 9 mm) is placed in front of the PMT to prevent any residual stray noise from entering the PMT. Usually the fluorescence photons are concentrated on the

central region of the secondary focus while the stray lights are focused at the boundary of the same [197].

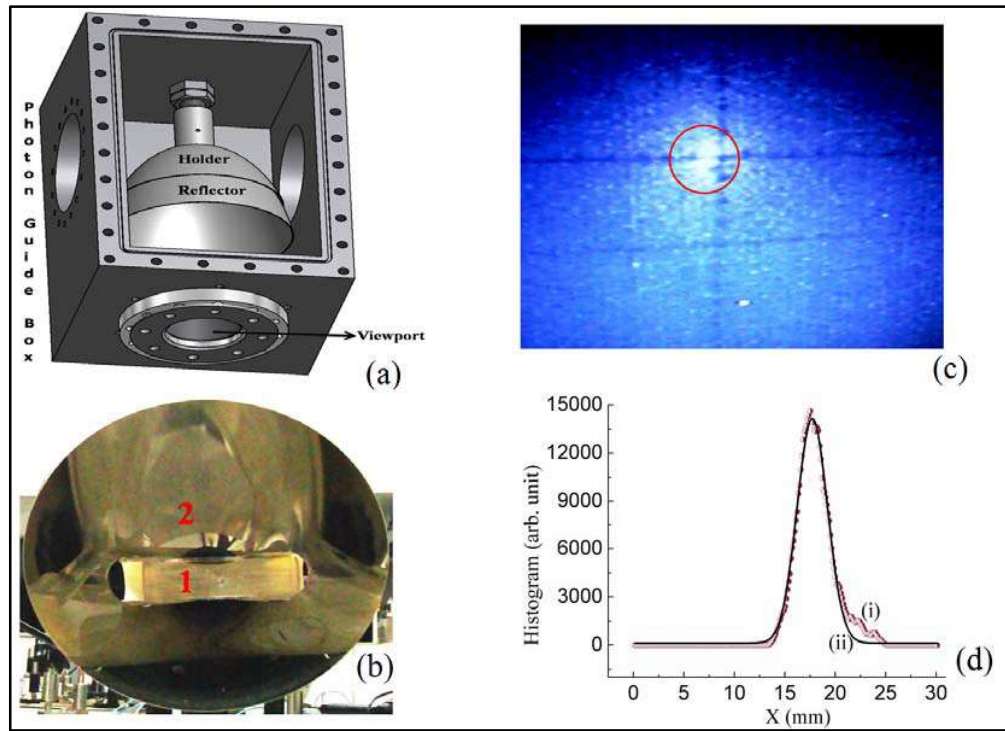


Fig. 10.7 Reflector assembly and detection of second focus (a) 3D view of the reflector assembly inside beam line (b) Rb vapour cell is placed inside the reflector to detect the second focus. The vapour cell is marked with ‘1’ and the holder is marked with ‘2’. (c) Image formed by fluorescence photon at the second focus (d) Histogram plot of (i) the intensity within the highlighted portion at the second focus shown in (c) and (ii) Gauss fit to estimate the fluorescent photon area.

In order to achieve a detectable signal with good S/N ratio, one has to reduce the background noise as much as possible for a given laser power. Several modifications have been made on our original design so that actual noise count reduces to a comprehensive level. The inside portions of the photon detection chamber has been painted black using black Aluminium foil (BKF12, Thorlabs) and vacuum compatible adhesive (Torr seal) as much as possible leaving the areas nearer to the ion beam path. The reflector holder and the sharp

edges on the reflector were also blackened with the same black aluminium foil. Graphite paint has been applied on the portions of the detection chamber which are near to the ion beam path. The holes (diameter ~ 30 mm) on the reflector are blocked with apertures (Fig. 10.9) on both sides. The aperture facing the laser is smaller in diameter (~ 7 mm) compared to the aperture (~ 15 mm) that is facing the ion beam. Instead of using several apertures of increasing diameters [196,198], we restricted ourselves to using a single aperture as a first attempt to achieve the fluorescence signal.

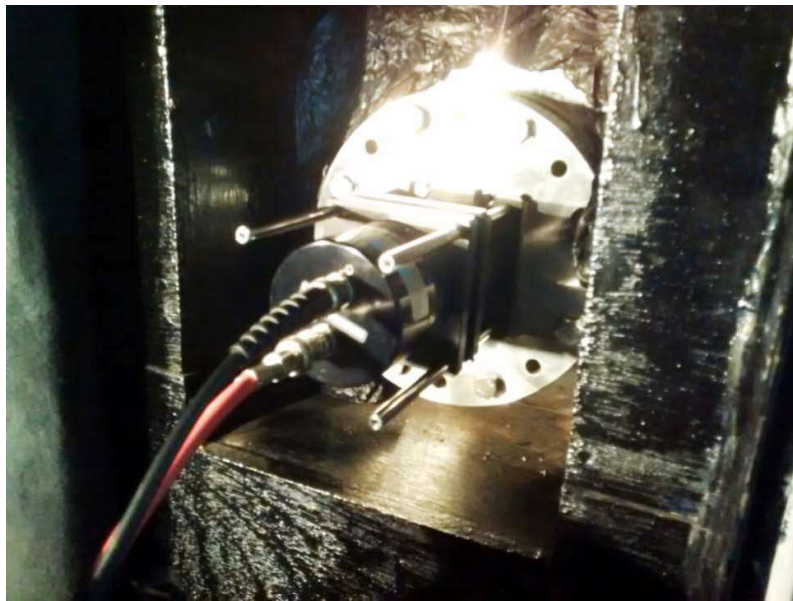


Fig. 10.8 PMT fixed on beam line with the help of cage mount assembly

A good laser beam shape is necessary for testing the apertures otherwise unnecessary noises may enter the PMT even with smaller sized apertures. Raw PMT output (without any preamplifier) was checked while experimenting with the laser facing aperture of different diameters. The PMT showed a continuous dc signal for larger aperture diameter. The PMT dc signal decreased as we kept on decreasing the aperture diameter. Finally discrete photon pulses were seen at the output of the PMT for ~ 7 mm aperture diameter (PMT bias voltage ~ -1900 V). Finally we settled for ~ 7 mm diameter for the laser facing aperture and ~ 15 mm diameter for the ion beam facing aperture.

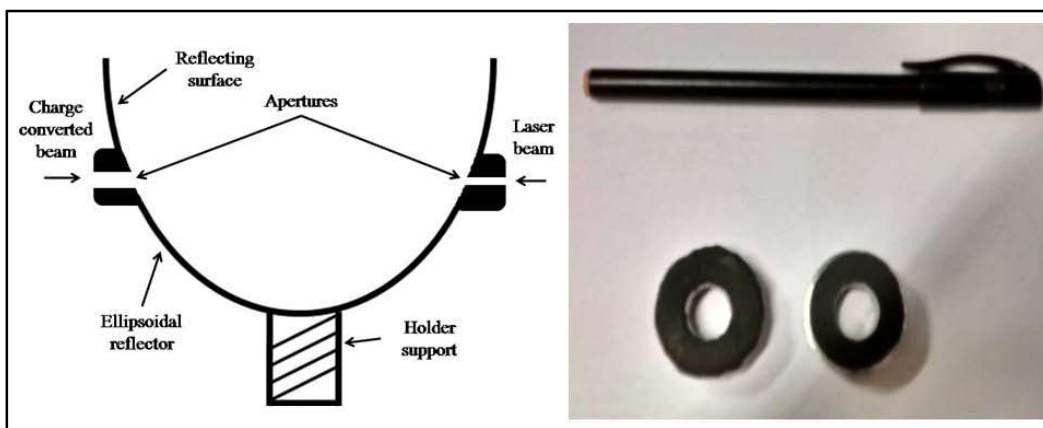


Fig. 10.9. Positioning of apertures on reflector and photograph of apertures

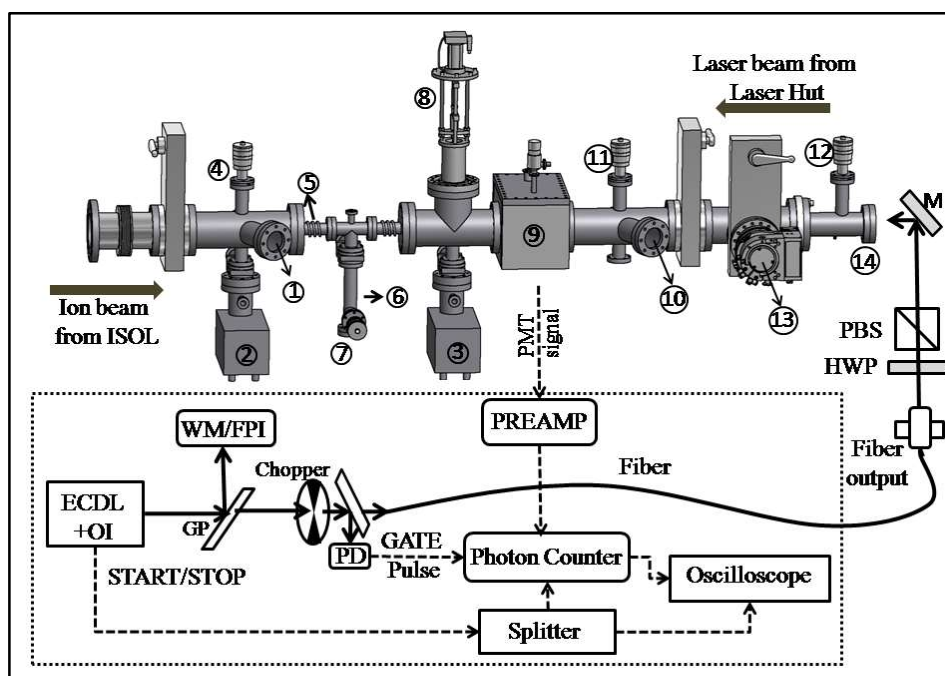


Fig. 10.10 Schematic overview of the laser system layout for ISOL-CLS setup

10.2.5 Laser system

The first detection of fluorescence spectrum was performed using a tunable diode laser (DL100 Pro, Toptica). The schematic layout of the laser system is shown in Fig. 10.10 and photographs of the laser system layout inside the laser hut and the adjacent dark room is shown in Fig. 10.11(a) and Fig. 10.11(b) respectively. The laser light is transported from the

RIB laser hut in to the adjacent dark room using an optical fibre. Laser beam intensity can be controlled from both rooms through the combination of polarizer and analyzer. Proper beam matching at the entry side of the optical fibre is necessary for maximum laser intensity at the other side of the optical fibre. A live feed of the dark room using a CCTV camera (Bosch Dinion D/N camera) is necessary for fibre-laser matching and maximizing the laser power at the fibre output. Final laser power was measured using a power meter (Newport Optical Power meter-1916R). We have achieved $\sim 25\%$ laser beam transmission in the present set up which served our purpose very well.

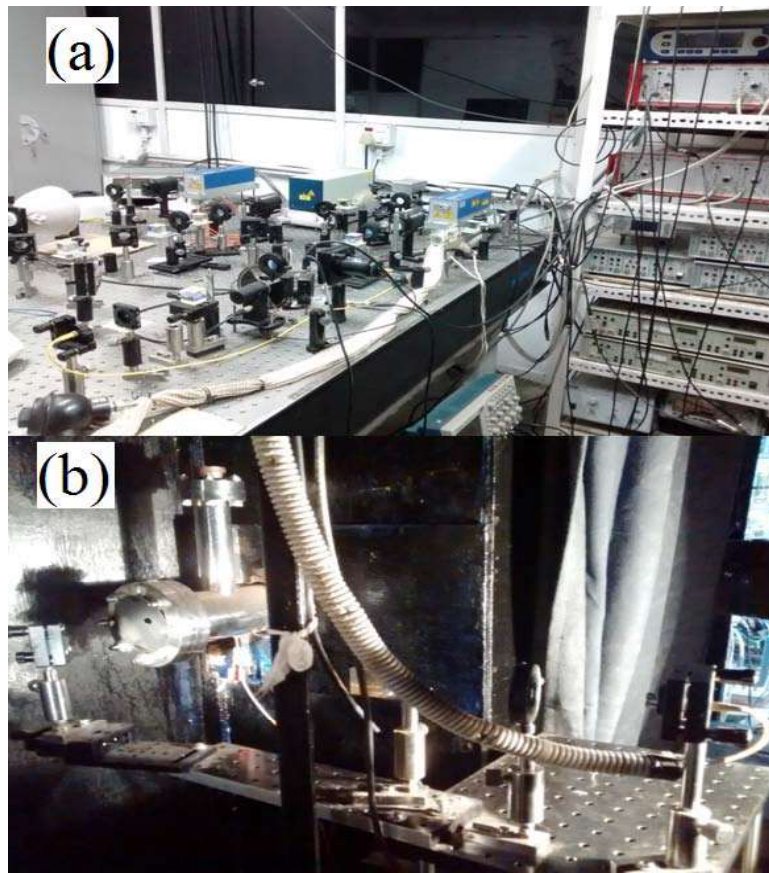


Fig. 10.11 Laser system layout with different optical components (a) inside laser hut
(b) inside adjacent dark-room

Apart from the adjustable fibre mount we have used an additional mirror for laser beam alignment. The markings on the beam line catcher ensure that the laser beam passes through

the first focus of the ellipsoidal reflector. Proper alignment of the laser beam path and the first focus is necessary to optimize the detection efficiency. The diameter of the laser beam can be adjusted with the exit side fibre collimator. Laser beam enters the beam line through the end flange (DN63CF, Fused silica, LewVac). It is important that the end flange is maintained in a clean condition otherwise unnecessary scattering from the window itself may increase the background photon count.

Laser scanning is performed with a function generator (Agilent 33521A) while the laser controller is working in the remote operation mode. Total scan time can be controlled by the laser scan frequency. In the present setup, the fluorescence detection is performed in the synchronous photon counting mode. A small part of the chopped laser output is used as the trigger signal (Fig. 10.12) for the photon counting. Synchronous photon counting mode eliminates the noise due to any residual stray light. A small part of the laser beam is fed into a Fabry-Perot Interferometer (Thorlabs, SA200-5B) for calibration of the laser scan. Another small part of the laser beam is fed into the wavemeter (Wavemaster, Coherent Inc) for wavelength readout and this helps in tuning of the laser wavelength to match the correct Doppler shift. The readout of the wavemeter is also used for isotope shift estimation. The diameter of the laser beam (~ 6 mm) is kept below the aperture size so that the laser beam scattering from the apertures remains nominal.

10.2.6 Data acquisition and experimental control

The main objective of the experiment is to collect fluorescence signal at different laser frequencies. The pre-amplified output of the PMT is transferred from the darkroom to the main laser control room (RIB laser hut) using a long coaxial cable and fed into the input of the gated photon counter (SR400, Stanford Research System). The discriminated PMT signal pulse is counted by the photon counter and the resultant photon count is plotted as a function of time. The time axis is calibrated with the Fabry Perot interferometer (FSR ~ 1500 MHz) to

the laser frequency. Trigger signal, counting gates, discriminated PMT signal etc all are shown Fig. 10.12. Total no. of data points considered for a single scan is 2000 (maximum possible value for SR400) and it takes about 500 sec to complete a single scan with 54 msec gate window. The choice of the discriminator voltage level should be such that the most of the noise pulse falls below it while the signal pulses are larger. The laser scan frequency and the chopper frequency are estimated considering the no. of data points per absorption peak (Appendix A.7).

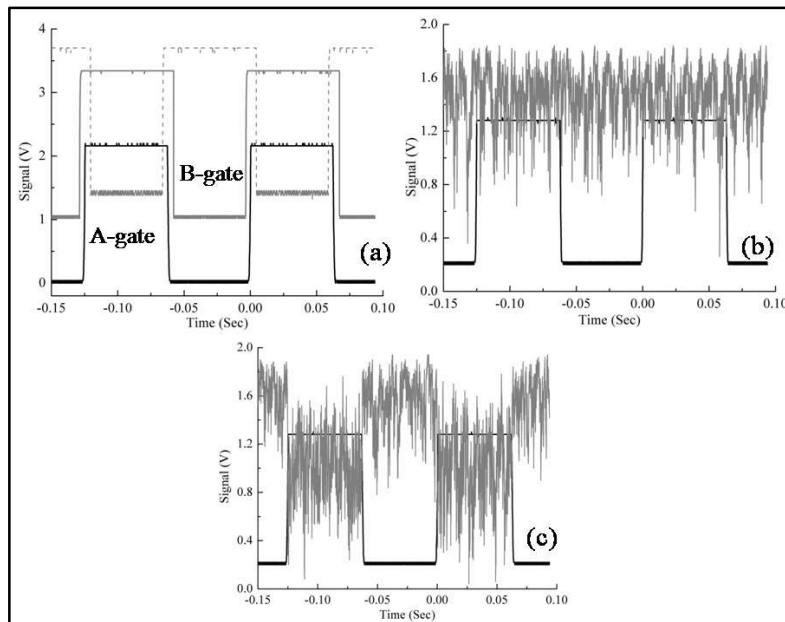


Fig. 10.12 Synchronous-mode photon counting (a) Trigger signal and gate output signals. (b) Discriminated PMT signal output when there is no laser present. ‘A’ and ‘B’ gate both show similar nature for the background photons. (c) Discriminated PMT signal output when laser is present. ‘A’ gate shows the presence of laser induced background count. Readings were taken when there was no ion beam current present.

In order to reduce the noise originating from the environment (apart from the laser induced noise), we used synchronous mode or “chopped” mode photon counting. Two gated photon

counters (A & B) are used for this purpose. ‘A’ gate counts the signal plus background during the chopper open state while the gate ‘B’ counts only the background during the chopper off state. The difference (A-B) between the two counters is the signal (Fig. 10.12). The mechanical chopper is used to modulate the laser intensity at a very slow speed ($\sim 8\text{Hz}$). Up to 2000 data points can be taken within a laser scan period. The external trigger signal which marks the starting of the laser frequency scan also starts the photon counter. Between every single set of (A-B) counts there is a dual period. The D/A output of the counter is monitored on the oscilloscope as the Y signal. For data monitoring in X-Y mode, port1 output (typical to SR400) from the counter is used as the X input to the oscilloscope.

Data collection starts with the laser scan trigger signal and ends after collecting 2000 data points, the limit set by the counter. In order to repeat the data counting the counter was reset and restarted. At the same time monitoring of the ion beam current is also necessary. The faraday cups were controlled remotely from the laser hut and the current in the end flange Faraday Cup was only monitored during the laser scan. Schematic of the data acquisition control and current readout technique is shown in Fig. 10.13 .

The transit time of the atoms in our set up from the end of the CEC to the reflector was $\sim 2\mu\text{sec}$ for the chosen extraction voltage. In such cases, to reduce the effect of hyperfine repumping high frequency (in the timescale of $5P_{3/2}$ level life-time) laser intensity modulation is generally used [199,200]. At present we don’t have the high frequency RF driver for the electro-optic amplitude modulator. Therefore the hyperfine optical pumping was allowed to happen in the present setup.

10.2.7 Beam line vacuum

The vacuum pumps for the existing VECC-ISOL facility were already installed and operational [201]. Ion source vacuum is maintained with a roots pump (pumping speed \sim

1300 m^3h^{-1}) on the skimmer side and a turbo-molecular pump on the ion-source cathode side. As the ion source is also intended to operate under online condition, the roots pump can take care of the high dynamic load of the inert gas (He, Ar etc) appearing from the gas jet transport technique. The vacuum of the rest portion of the beam line is maintained using two turbo-molecular pumps. Manually operated gate valves are placed at different sections of the beam line. The newly designed laser spectroscopic section is supported with one turbo-molecular pump and two sputter ion pumps. The ion pumps are placed on both sides of the CEC. These pumps are intended to take care of the alkali metal atoms leaking from the CEC. One mini gate valve is placed on the vertical column of the CEC so that CEC can be refilled when required. Fig. 10.2 shows ISOL-CLS beam line and associated vacuum pumps.

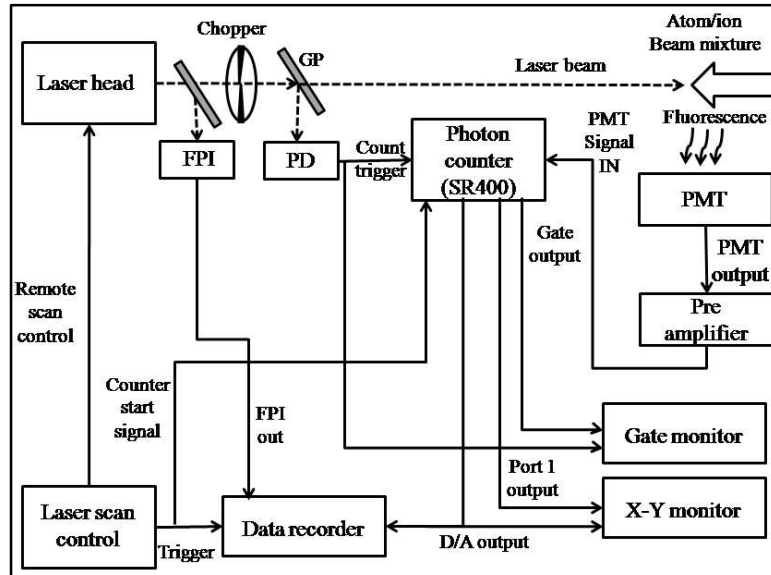


Fig. 10.13 Data acquisition layout for ISOL-CLS setup; PD: Photo detector, GP: Glass plate, FPI: Fabry-Perot Interferometer

10.3 Results and discussion

In the first experimental run, Rubidium ion beam of 8.0 keV energy has been accelerated by the surface ion source. After charge conversion at the CEC, the atom beam passes through

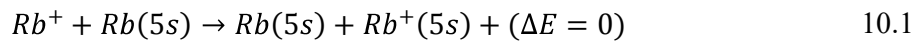
the photon detection system and the fluorescence photons emitted by the atom beam were collected by the ellipsoidal reflector. The ion beam and the laser beam were in counter propagating configuration. The Doppler shifted resonance frequency of the atomic transition corresponding to the particular ion beam energy was estimated using equation (3.19) and the laser frequency was tuned to that value before laser scanning. The whole experiment was conducted in two parts. In the first part, we have calibrated the CEC in terms of the charge exchange efficiency and CEC vapour zone temperature. In the second part of the experiment, we have scanned the laser frequency to obtain the whole Rubidium $5S_{1/2} \rightarrow 5P_{3/2}$ atomic transition lines. The corresponding experimental parameters are listed in Table 10.3.

Table 10.3 Experimental parameters for CLS experiment.

Laser power (mW)	PMT voltage (V)	Ion beam current at FC2 (nA)	CEC reservoir temperature ($^{\circ}$ C)	Ion pump current while CEC is ON (mA)
1.5	-1900	70	140	2

10.3.1 Calibration of CEC

We are mainly concerned with the resonant Rb^+ -Rb charge exchange process for the generation of Rubidium atom beam. The resonant interaction [194,202] is given by,



However there also exist other reaction channels with very small probability where the energy defects are non zero. These interactions might give rise to satellite peaks.

The CEC was filled with neutral Rubidium atom and was heated at different temperatures (T) using several mica band heaters. Beam optical parameters were adjusted to ensure 8.0 keV Rubidium ion beam from the ion source passes through the CEC. The faraday cups placed

just before (FC1) and after (FC2) the CEC monitors the ion beam current at the entry and exit of the CEC. To take care of any fluctuation in the ion beam current, the beam current at FC2 is normalized with respect to the beam current at FC1. The normalized ion beam current at FC2 can be written as,

$$I_2 = (1 - \eta)I_1 \quad 10.2$$

where $I_2 = I_{FC2}/I_{FC1}$, η is charge exchange efficiency. I_2 and η are function of CEC vapour zone temperature. $I_1 = I_{FC2}/I_{FC1}$ is estimated at room temperature before the CEC heaters are on. The charge exchange efficiency is estimated only for 8.0 keV Rubidium ion beam. The uncertainty in the estimation of η is determined by the uncertainty in the current measurement ($\approx 2nA$) and the temperature measurement ($\approx \pm 5^0C$ at higher temperature). The curves for η vs T can be described with a simple model for attenuation when the ion beam is passing through a medium with reaction cross section σ which is given by [196],

$$\eta = 1 - e^{-n\sigma l} \quad 10.3$$

where n is neutral atom density and l is the length of the vapour zone. Atom density (n) is estimated from the vapour pressure of the liquid ^{85}Rb [203], standard pressure (p_0 , in atm), Avogadro's number (N_A) and molar volume (V_{mol}) from the following equation,

$$n = \frac{N_A 10^{4.312 - \frac{4040}{T}}}{V_{mol} p_0} \quad 10.4$$

Fig. 10.14 shows the experimental curve for η vs T . The curve is fitted with equation (10.3). Fig. 10.14(a) shows the charge conversion efficiency with respect to reservoir temperature (Temperature of the lower portion of CEC) and Fig. 10.14(b) shows the same data with respect to the temperature of the zone through which ion beam passes. The value of the charge exchange cross section (σ) obtained from the fitting of Fig. 10.14(a) is $\sim 1.8 \times 10^{-16} \text{ cm}^2$ while the same for Fig. 10.14(b) is $\sim 6.7 \times 10^{-15} \text{ cm}^2$. The fitting of the charge

conversion data with respect to the ‘ion beam pass zone’ temperature or ‘vapour zone’ temperature matches well with the reported values of the charge exchange cross section [204,194]. The calibration with respect to the reservoir temperature yields a little lower value of the charge exchange cross section. The reason behind this is that the whole CEC is heated with ~ 7 heaters and the temperature recorded by the heat sensors placed around the ion beam pass zone represents more accurately the actual temperature of the neutral vapour inside the CEC which is participating in the charge conversion. The length of the vapour zone (l) is about 150 mm . Typical vapour zone temperature is kept around $\sim 75^{\circ}\text{C} - 90^{\circ}\text{C}$ during experiment. The corresponding reservoir temperature was around $\sim 130^{\circ}\text{C} - 150^{\circ}\text{C}$.

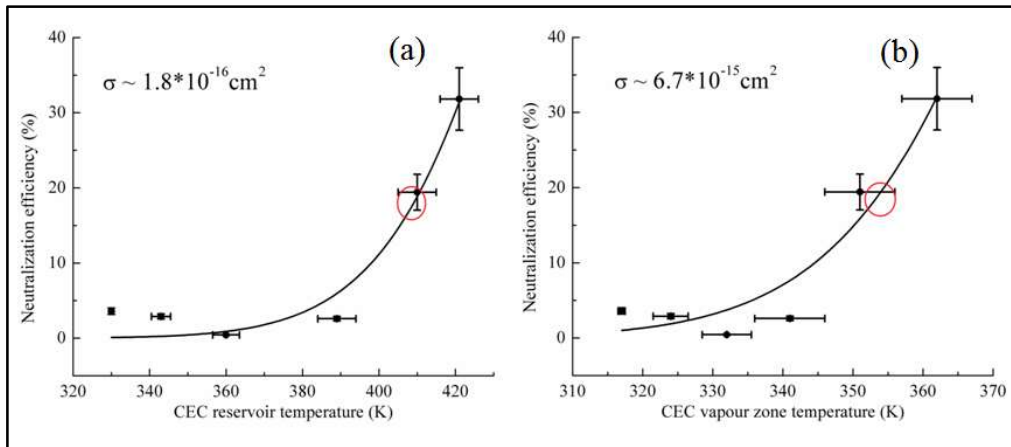


Fig. 10.14 Neutralization efficiency vs temperature plot. (a) Neutralization efficiency plotted with respect to reservoir temperature of CEC (b) Neutralization efficiency plotted with respect to ‘ion beam pass zone’ temperature.

Apart from the temperature calibration, the CEC was investigated for any possible loss of neutral Rubidium vapour from the CEC. We used a 780.241 nm laser beam to pass through the vapour zone of the CEC after turning on the CEC heaters. Inspecting with IR viewers no fluorescence can be seen outside the CEC zone. Absence of any physical evidence of coating of Rb on the nearby elements e.g photon reflector, glass viewport etc also attest the fact that

Rb atoms were recycled efficiently within CEC. The radius to length ratio ($r/l \ll l$) of the CEC ion beam pass zone minimises the direct loss of Rb atoms from the CEC.

10.3.2 Detection of Rb fluorescence spectra

In order to record the fluorescence spectra, laser frequency was scanned in the present setup. Fig. 10.15 and Fig. 10.16 show the first recorded spectrum of the VECC-ISOL collinear laser spectroscopy setup. Only single laser scan is recorded to avoid the problem of repeatability in multiple laser frequency scan. The separation in time between the recorded FPI fringes can also give some indication about the possible nonlinearity in laser frequency scan. D/A output of the photon counter is recorded along with the FPI fringes to calibrate the X-axis in terms of laser frequency detuning. A wavemeter is also used to monitor the Doppler shifted laser frequency. The CEC is put into operation once the ion beam current is available at FC2 and end flange. The quadrupole and dipole magnets were adjusted to transport the 8.0 keV Rb ion beam to the collinear laser spectroscopy setup. The ion beam profile in the X-plane was monitored on the oscilloscope using the wire scanner and a good beam shape was ensured (Fig. 10.5) at the focal plane. Before starting the laser scan, the laser frequency was tuned to the Doppler shifted transition frequency of the Rubidium manifold. Initially the piezo voltage of the ECDL was varied manually to find the peak positions and the respective count in the photon counter was monitored. Any fine tuning of the CEC temperatures, gate width, discriminator voltage etc. were done in the next steps. Finally the laser frequency was put into scanning mode and the corresponding spectra are recorded.

The theoretical Doppler shifted laser frequency in the atomic rest frame for 8.0 keV Rubidium ion beam are 384.056596019 THz ($^{85}\text{Rb } F = 3 \rightarrow F'$), 384.057465116 THz ($^{87}\text{Rb } F = 2 \rightarrow F'$), 384.059509800 THz ($^{85}\text{Rb } F = 2 \rightarrow F'$) and 384.064030229 THz ($^{87}\text{Rb } F = 1 \rightarrow F'$). To record these transitions ~ 7.5 GHz of laser frequency scan is required which

can accommodate around 5 FSR of FPI fringes. In the present setup, ^{85}Rb and ^{87}Rb can be clearly resolved and separated at FC2. In order to record the full spectrum in a single laser scan we had to change the magnet settings during the laser scan. The positions of the observed spectra as seen on the wavemeter are in proximity with the theoretically calculated values.

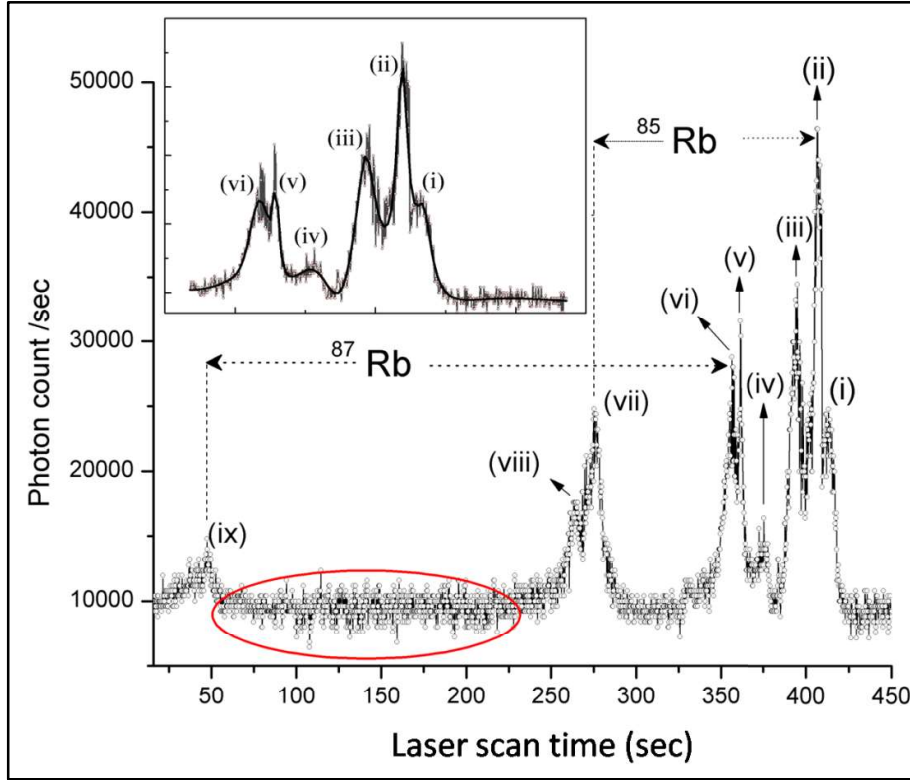


Fig. 10.15 First recorded spectra of 8.0 keV Rb ion beam using ISOL-CLS setup.

Inset shows the hyperfine components of $^{87,85}\text{Rb}$ transition from upper ground hyperfine state. The background photon count is highlighted (by red mark in colour).

The X-axis is calibrated with laser scan time.

Fig. 10.15 shows different atomic hyperfine transitions marked (i) to (ix). The hyperfine components are fitted with multipeak pseudo-Voigt fitting (see inset). Fitting of the peaks (i)-(vi) shows the hyperfine transition manifold of $^{85}\text{Rb } F = 3 \rightarrow F'$ and $^{87}\text{Rb } F = 2 \rightarrow F'$. It is found that the peaks (i)-(ii) and (iv)-(v) are in near agreement with the $^{85}\text{Rb } F = 3 \rightarrow F' =$

3, 4 and $^{87}\text{Rb } F = 2 \rightarrow F' = 2, 3$ hyperfine transitions respectively. However the peaks (iii), (vi) and (viii) are due to the change in the magnet settings during the experiment as it is already mentioned that the change in the magnet settings were necessary to accommodate all the Rb transitions in a single laser scan. In an earlier work [196], change in dipole magnet setting was not necessary as the dipole magnet could not resolve the $^{85,87}\text{Rb}$ beam and a mix beam is probed by the laser. The peaks (vii) and (ix) appear from the $^{85}\text{Rb } F = 2 \rightarrow F'$ and $^{87}\text{Rb } F = 1 \rightarrow F'$ respective transitions. The results of the fitting are shown in Table 10.4.

The X-axis of Fig. 10.15 is calibrated by considering the separation between the first and the last recorded FPI fringes (FSR of 1.5 GHz) of the whole laser frequency scan (range ~ 7.5 GHz) as the marker. The value of the isotope shift extracted from the fitting of the peaks is ~ 139.052 MHz as compared to 78.095(12) MHz reported in [203]. This deviation is due to the fact that the observed hyperfine peak separations do not exactly match with the literature values [65,203] and there is a deviation of about 40 MHz (Table 10.4). However, when the hyperfine spectrum is only recorded for $^{85}\text{Rb } 5S_{1/2} F = 3 \rightarrow 5P_{3/2} F' = 4, 3, 2$ transitions (Fig. 10.16), the observed hyperfine peak separation matches closely with the literature values. In this case, the laser frequency is scanned only over ~ 1.8 GHz which is much smaller compared to the 7.5 GHz scan (Fig. 10.15). The simultaneous recording of the FPI fringes also reveals that the laser frequency scan is not exactly linear over higher frequency scan range. This occurs due to the very slow scan of the laser frequency (2 mHz) using the piezo voltage and the shift in the DC value of the piezo voltage during the scan. It seems therefore that the non-linearity in the laser scan is responsible for the observed differences in the hyperfine peak separations when the laser frequency was scanned over larger range of 7.5 GHz.

Table 10.4 Results of the first recorded spectra on Rb using ISOL-CLS beam line

Transition manifold (Identified from Wavemeter reading)	Peak No.	Peak designation	Fitted peak positions (in MHz scale)	Observed Peak separation (MHz)	Reference data (MHz) from Steck [203]	Remark
^{85}Rb ($5S_{1/2}$ $F = 3 \rightarrow$ $5P_{3/2}F'$)	(i)	$F = 3 \rightarrow F' = 3$	7764(6)	(i)-(ii) 165(6)	120.640	Around 40 MHz difference is observed on peak separation between experimentally observed value and reference value.
	(ii)	$F = 3 \rightarrow F' = 4$	7599(0)			
	(iii)		7324(4)			
^{87}Rb ($5S_{1/2}$ $F = 2 \rightarrow$ $5P_{3/2}F'$)	(iv)	$F = 2 \rightarrow F' = 2$	6955(0)	(iv)-(v) 307(3)	266.650	
	(v)	$F = 2 \rightarrow F' = 3$	6648(3)			
	(vi)		6526(6)			
<p>Peaks (iii) and (vi) do not belong to any hyperfine transition. These peaks appear due to the change in the magnet settings during laser frequency scan. One possible reason behind the observed difference between the experimentally observed hyperfine peak separation and reference value could be the nonlinearity in laser frequency scan.</p>						

As already mentioned, Fig. 10.16 shows $^{85}\text{Rb } 5S_{1/2} F = 3 \rightarrow 5P_{3/2} F' = 4, 3, 2$ transitions recorded in a separate scan. The $F = 3 \rightarrow F' = 4$ transition is the cyclic transition and has the highest strength [203]. The ^{85}Rb atoms excited through the non-cyclic channels may decay back to $F = 2$ state which is out of the optical pumping-decay channel and are ‘lost’ from the main absorption emission cycle. Due to this reason the non cyclic transitions appear much lower in intensity than their cyclic counterpart. The strong asymmetry in the $F = 3 \rightarrow F' = 4$ transition is due to multiple collisions in the CEC which generates a tail of slower ions. The observed peaks are fitted with pseudo-Voigt function and the peak positions are listed in Table 10.5. The peak separation matches well with the values mentioned in [203].

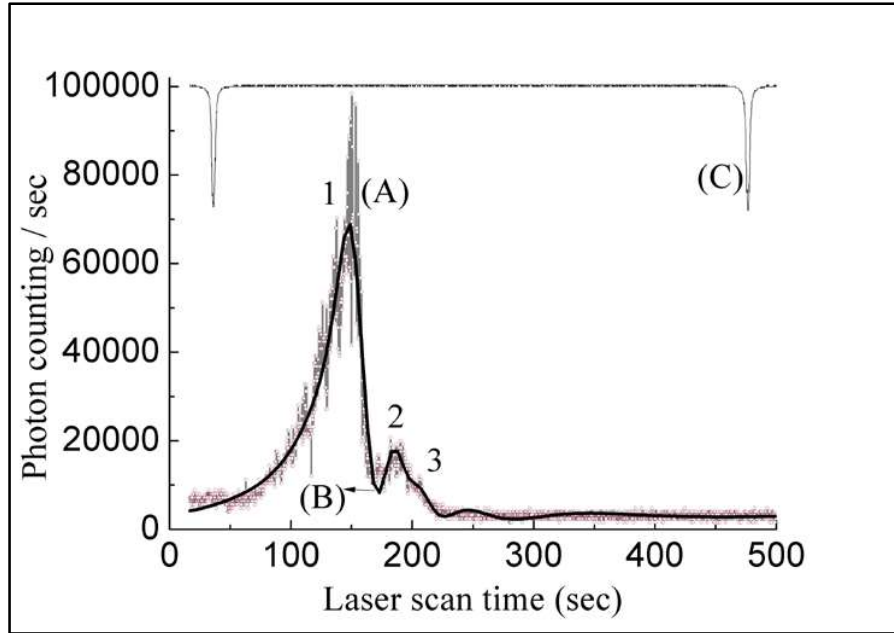


Fig. 10.16 Recording of $^{85}\text{Rb } (F = 3 \rightarrow F')$ hyperfine transition in a single laser scan . X-axis is calibrated with respect to a single FSR of the FPI. (A) Highlights the laser scan data. Peak 1 appears from $F = 3 \rightarrow F' = 4$ transition, peak 2 and peak 3 is due to $F = 3 \rightarrow F' = 3, 2$ transitions respectively. (B) Multi-peak pseudo-Voigt fitting curve and (C) FPI fringes.

Table 10.5 Results of the fitting of ^{85}Rb lines (recorded in a separate scan).

Transition manifold (Identified from Wavemeter reading)	Peak No.	Peak designation	Fitted peak positions (in MHz scale)	Peak separation (MHz)	Reference data (MHz) from Steck [203]
^{85}Rb ($5S_{1/2}F = 3 \rightarrow$ $5P_{3/2}F'$)	(1)	$F = 3 \rightarrow F' = 4$	514(1)	(1)-(2) 112(1)	120.640
	(2)	$F = 3 \rightarrow F' = 3$	626(0)	(2)-(3) 72(1)	63.401
	(3)	$F = 3 \rightarrow F' = 2$	698(1)		
The difference between the experimentally observed hyperfine peak separation and reference value is limited by the FWHM of the etalon fringe which is 6.438 MHz in this case. Under short range scan of the laser frequency the problem of nonlinearity in the laser scan is largely reduced.					

The signal detection efficiency of the spectrometer is evaluated from Fig. 10.16. The average current of ^{85}Rb ion beam at FC2 (I_{FC2}) is ~ 70 nA. The charge conversion factor is taken to be $\sim 20\%$ at 140°C of the reservoir temperature. It should also be considered that only one half of the total atoms are available for excitation from $F = 3$ hyperfine ground state. Hence total number of atoms/sec responsible for the ^{85}Rb $F = 3 \rightarrow F'$ transition is given by,

$$N = \frac{I_{FC2}}{e} * \frac{\eta}{1 - \eta} * 0.5 \quad 10.5$$

The maximum signal photon count (C_{max}) for ^{85}Rb $F = 3 \rightarrow F' = 4$ transition is $\sim 10^5/\text{sec}$.

Therefore the total signal detection efficiency is, $\epsilon_{total} = C_{max}/N \sim 1/(6 \times 10^5)$ which is

the best value we obtained for a single laser scan. The background photon count is $\leq 10^4/sec$. In determining the efficiency we assumed 100% beam transport from FC2 to first focal point of the reflector and a perfect overlap between the atom beam and laser. In order to have better idea about these factors we need to measure beam profiles at various positions.

10.4 Conclusion

The present chapter discussed about the development of collinear laser spectroscopy (CLS) setup at ISOL facility at VECC and the measurement of hfs of stable Rubidium in the same setup. The production and transport of radioactive elements such as $^{42,43}K$ with a rate of $\sim 10^5$ pps in RIB facility at VECC [135,136] has encouraged the development of present CLS setup at ISOL-VECC. The characterization of the present setup is done using 8.0 keV stable Rubidium ion beam from the ISOL ion source. The calibration of the charge exchange cell is done using $Rb^+ - Rb$ charge exchange process and the same is also reported in this chapter. Rubidium $5S_{1/2} \rightarrow 5P_{3/2}$ transition is detected in counter propagating geometry. The best value of the signal detection efficiency in the present setup is $\sim 1\text{photon}/(6 \times 10^5\text{ atoms})$ for a background of $\leq 10^4\text{ photons/sec}$. The detected hyperfine peak separations are more or less in agreement with the standard literature values.

Though first experimental data has come out of the system, significant amount of work is still left. In that direction the first step would be to increase the detection efficiency of the present setup through several modifications in the present design. First and foremost step planned is to install a setup for voltage scan instead of laser frequency scan. This will resolve many issues regarding the repeatability of the laser scan and will also help to improve the S/N ratio. Also, the background photon count in the present setup is mainly due to the laser power itself. Modifications in the present photon detection unit are necessary to get rid of the unwanted laser power induced photon background. Also the present scheme of ‘synchronous

photon counting' should be replaced in order to improve the S/N ratio. In order to incorporate the voltage scan the design of the CEC needs to be changed. The new CEC design should also aim on better utilization of the Rubidium neutralizer. Currently, we are designing the CEC to incorporate voltage scanning and also better ion guide and photon detection unit to improve the performance of the present system in order to make it suitable for laser spectroscopic studies on β^- unstable species for which the beam intensity could be in the range of 10^5 pps or less.

Appendix A. Important formulae used in the thesis

A.1. Clebsch-Gordan Coefficients

Clebsch-Gordan (CG) coefficients are expansion coefficients of total angular momentum quantum numbers and appear in the theory of angular momentum coupling and a very useful quantity for laser spectroscopy. For two angular momentum vectors $|l_1 m_1\rangle$ and $|l_2 m_2\rangle$ that can be coupled to form a total angular momentum vector $|LM\rangle$ we can write,

$$|LM\rangle = \sum_{m_1 m_2} |l_1 m_1\rangle |l_2 m_2\rangle \langle l_1 m_1 l_2 m_2 | LM \rangle \quad \text{A.1.1}$$

where $\langle l_1 m_1 l_2 m_2 | LM \rangle$ is a real number and is known as Clebsch-Gordan (CG) coefficient. It is often represented in terms of Wigner 3- j symbol through the following relation,

$$\langle l_1 m_1 l_2 m_2 | LM \rangle = (-1)^{l_1 - l_2 + M} \sqrt{2L + 1} \begin{pmatrix} l_1 & l_2 & L \\ m_1 & m_2 & -M \end{pmatrix} \quad \text{A.1.2}$$

where $\begin{pmatrix} l_1 & l_2 & L \\ m_1 & m_2 & -M \end{pmatrix}$ is the Wigner 3- j symbol.

A.2. Mean free path

The average distance travelled by the gas molecules between two collisions is termed as the mean free path (mfp). From kinetic theory of gas we get the following expression for mfp ,

$$mfp = \frac{1}{\sqrt{2}\pi d^2 n} \quad \text{A.2.1}$$

where, d is the molecular diameter and n is the molecular number density. In case of Rb vapour cell at room temperature (25°C), and considering $d = 2 * 248 \text{ pm}$, mfp comes around $\sim 67 \text{ m}$.

A.3. Estimation of required laser power

In most of the experiments probe laser intensity is kept below or near about the saturation intensity (I_{sat}) of the particular transition. During experiment laser power (LP) is directly measured with power meters instead of the laser intensity. Conversion between the saturation intensity and laser power is done through the following conversion,

$$LP = I_{sat} * \pi \frac{d^2}{4} \quad \text{A.3.1}$$

where, d is the laser diameter.

A.4. Magnet calibration

ISOL-CLS beam transport system comprises of two quadrupole magnets and one dipole magnet. Magnetic fields produced by these magnets were calibrated using a Hall probe against the magnet power supply settings. The field values of the quadrupole can be directly computed from the following formula,

$$B \text{ (in Gauss)} = 11.4461 * I \text{ (in A)} + 6.9358 \quad \text{A.4.1}$$

where, B is the magnetic induction and I is the magnet current as seen on the power supply parameter display. Similarly the magnetic field produced by the dipole magnet can be estimated from the following equation,

$$B \text{ (in Gauss)} = 6.3473 * 10^{-3} * SET \text{ ADC} + 16.8459 \quad \text{A.4.2}$$

where, B is the magnetic induction and ‘ $SET \text{ ADC}$ ’ is the set values on the magnet power supply reading dial.

A.5. Doppler shift estimation

A particle of rest mass m and velocity $v = \beta c$ moving parallel or anti-parallel to the laser (lab frame frequency ν_{las}) encounters the Doppler shifted laser frequency (ν_{rest}) which is given by,

$$\nu_{rest} = \nu_{las} * \frac{1 \pm \beta}{\sqrt{1 - \beta^2}} \quad A.5.1$$

where '+' sign is for counter-propagating geometry and '-' sign is for co-propagating geometry. Normalized particle velocity (β) can be estimated from the total kinetic energy (eV) of the accelerated ion beam using the following formula,

$$\beta = \sqrt{1 - \left(\frac{mc^2}{eV + mc^2}\right)^2} \quad A.5.2$$

Inserting equation (A.5.2) in equation (A.5.1) we get the following formula for Doppler shifted laser frequency,

$$\nu_{rest} = \nu_{las} * \frac{(eV + mc^2)}{mc^2} \left(1 \pm \sqrt{1 - \left(\frac{mc^2}{eV + mc^2}\right)^2}\right) \quad A.5.3$$

where, V is the extraction potential of the ion source.

A.6. Isotope shift estimation

In VECC-CLS setup we scan the laser frequency instead of the post-acceleration voltage. This makes the estimation of isotope shift rather non-trivial. For two isotopes of mass m_1 and m_2 and the respective resonance positions marked by the laboratory frame laser frequencies ν_{las1} and ν_{las2} , the isotope shift can be estimated from the following formula.

$$\Delta v_{IS} = v_{las1} * \frac{(eV + m_1 c^2)}{m_1 c^2} \left(1 \pm \sqrt{1 - \left(\frac{m_1 c^2}{eV + m_1 c^2} \right)^2} \right) - v_{las2} \quad \text{A.6.1}$$

$$* \frac{(eV + m_2 c^2)}{m_2 c^2} \left(1 \pm \sqrt{1 - \left(\frac{m_2 c^2}{eV + m_2 c^2} \right)^2} \right)$$

Where, '+' sign is applicable in case of counter-propagating geometry and '-' sign is used for co-propagating geometry.

A.7. Photon counting

Let us assume that laser scan frequency is f . Therefore the total time required for a single laser scan is $T = \frac{1}{f}$. In the present set up, it requires 2 chopper periods for a single data acquisition because of the 'dual time' of the counter. Therefore chopper frequency is $2 * \text{no. of data pints} / (\text{scan time})$. Gate time width is set below the half period of the chopper. No. of data points in a scan is 2000.

References

- [1] E. Arimondo, "Coherent population trapping in laser spectroscopy," *Progress in optics*, vol. XXXV, p. 258, 1996.
- [2] K. J. Boller, A. Imamoglu, S. E. Harris, "Observation of Electromagnetically Induced Transparency," *Physical Review Letters*, vol. 66, no. 20, pp. 2593-2596, May 1991.
- [3] A. M. Akulshin, S. Barreiro, A. Lezama, "Electromagnetically induced absorption and transparency due to resonant two-field excitation of quasidegenerate levels in Rb vapor," *Physical Review A*, vol. 57, no. 4, pp. 2996-3002, April 1998.
- [4] Olga Kocharovskaya, Yuri Rostovtsev, Marlan O. Scully, "Stopping Light via Hot Atoms," *Physical Review Letters*, vol. 86, no. 4, pp. 628-631, January 2001.
- [5] M. Stahler, S. Knappe, C. Affolderbach, W. Kemp, R. Wynands, "Picotesla magnetometry with coherent dark states," *Europhysics Letters*, vol. 54, no. 3, pp. 323-328, May 2001.
- [6] Svenja Knappe et al, "A microfabricated atomic clock," *Applied Physics Letters*, vol. 85, no. 9, pp. 1460-1462, August 2004.
- [7] Han Seb Moon, Lim Lee, Kyoungdae Kim, Jung Bog Kim, "Laser frequency stabilization using electromagnetically induced transparency," *Applied Physics Letters*, vol. 84, no. 16, pp. 3001-3003, April 2004.
- [8] S.C. Bell, D.M. Heywood, J.D. White, J.D. Close R.E. Scholten, "Laser frequency offset locking using electromagnetically induced transparency," *Applied Physics Letters*, vol. 90, no. 171120, pp. 1-3, 2007.

- [9] Y.B. Kale, Ayan Ray, Q.V. Lawande, B.N. Jagatap, "Coherent spectroscopy of a Lambda atomic system and its prospective application to tunable frequency offset locking," *Physica Scripta*, vol. 84, no. 035401, pp. 1-9, August 2011.
- [10] H. Schmidt, R. J. Ram, "All-optical wavelength converter and switch based on electromagnetically induced transparency," *Applied Physics Letters*, vol. 76, no. 22, pp. 3173-3175, May 2000.
- [11] Rong Yu, Jiahua Li, Chunling Ding, Xiaoxue Yang, "Dual-channel all-optical switching with tunable frequency in a five-level double-ladder atomic system," *Optics Communications*, vol. 284, pp. 2930-2936, February 2011.
- [12] Meng-Jung Lee, Yi-Hsin Chen, I-Chung Wang, Ite A. Yu, "EIT-based all-optical switching and cross-phase modulation under the influence of four-wave mixing," *Optics Express*, vol. 20, no. 10, pp. 11057-11063, May 2012.
- [13] Jason Clarke, Hongxin Chen, William A. van Wijngaarden, "Electromagnetically induced transparency and optical switching in a rubidium cascade system," *Applied Optics*, vol. 40, no. 12, pp. 2047-2051, April 2001.
- [14] Subramanian Krishnamurthy, Y. Wang, Y. Tu, S. Tseng, M.S. Shahriar, "High efficiency optical modulation at a telecom wavelength using the quantum Zeno effect in a ladder transition in Rb atoms," *Optics Express*, vol. 20, no. 13, pp. 13798-13809, June 2012.
- [15] Han Seb Moon, "Frequency stabilization of a laser diode to hyperfine structure of the $4D_{5/2}$ state of 85Rb atoms," *Optics Communications*, vol. 284, pp. 1327-1330, 2011.
- [16] D. Touahri et al, "Frequency measurement of the $5S_{1/2}(F = 3) - 5D_{5/2}(F = 5)$ two-

- photon transition in rubidium," *Optics Communications*, vol. 133, pp. 471-478, January 1997.
- [17] A. S. Zibrov, M. D. Lukin, L. Hollberg, M. O. Scully, "Efficient frequency up-conversion in resonant coherent media," *Physical Review A*, vol. 65, no. 051801(R), pp. 1-4, April 2002.
- [18] Han Seb Moon, Lim Lee, Jung Bog Kim, "Coupling-intensity effects in ladder-type electromagnetically induced transparency of rubidium atoms," *Journal of Optical Society of America B*, vol. 22, no. 12, pp. 2529-2533, December 2005.
- [19] H.S. Moon, L. Lee, J.B. Kim, "Double resonance optical pumping effects in electromagnetically induced transparency," *Optics Express*, vol. 16, no. 16, pp. 12163-12170, August 2008.
- [20] H.S. Moon, H.R. Noh, "Optical pumping effects in ladder-type electromagnetically induced transparency of $5S_{1/2}$ - $5P_{3/2}$ - $5D_{3/2}$ transition of 87Rb atoms," *Journal of Physics B: Atomic, Molecular and Optical Physics*, vol. 44, no. 055004, pp. 1-6, February 2011.
- [21] Baodong Yang, Jing Gao, Tiancai Zhang, Junmin Wang, "Electromagnetically induced transparency without a Doppler background in a multilevel ladder-type cesium atomic system," *Physical Review A*, vol. 83, no. 013818, pp. 1-5, January 2011.
- [22] J.P. Marangos, "Electromagnetically induced transparency," *Journal of Modern Optics*, vol. 45, no. 3, pp. 471-503, August 1998.
- [23] S. E. Harris, Y. Yamamoto, "Photon Switching by Quantum Interference," *Physical Review Letters*, vol. 81, no. 17, pp. 3611-3614, October 1998.

- [24] V. M. Entin, I. I. Ryabtsev, A. E. Boguslavski, I. M. Beterov, "Experimental Implementation of a Four-Level N-type Scheme for the Observation of Electromagnetically Induced Transparency," *JETP Letters*, vol. 71, no. 5, pp. 175-177, January 2000.
- [25] A.M. Akulshin, A.A. Orel, R.J. McLean, "Collimated blue light enhancement in velocity-selective pumped Rb vapour," *Journal of Physics B: Atomic, Molecular and Optical Physics*, vol. 45, no. 015401, pp. 1-7, November 2012.
- [26] Amitabh Joshi, Min Xiao, "Electromagnetically induced transparency and its dispersion properties in a four-level inverted-Y atomic system," *Physics Letters A*, vol. 317, pp. 370-377, September 2003.
- [27] Jianbing Qi, "Electromagnetically induced transparency in an inverted Y-type four-level system," *Physica Scripta*, vol. 81, no. 015402, pp. 1-8, 2010.
- [28] Jun Kou et al, "Double dark resonances and the dispersion properties in a four-level inverted-Y atomic system," *Optics Communications*, vol. 284, pp. 1603-1607, 2011.
- [29] S. Kumar, T. Laupretre, R. Ghosh, F. Bretenaker, F. Goldfarb, "Interacting double dark resonances in a hot atomic vapor of helium," *Physical Review A*, vol. 84, no. 023811, pp. 1-6, 2011.
- [30] M.A. Anton, F. Carreno, Oscar G. Calderon, S. Melle, I. Gonzalo, "Optical switching by controlling the double-dark resonances in a N-tripod five-level atom," *Optics Communications*, vol. 281, pp. 6040-6048, September 2008.
- [31] Min Yan, Edward G. Rickey, Yifu Zhu, "Suppression of two-photon absorption by quantum interference," *Physical Review A*, vol. 64, no. 043807, September 2001.

- [32] Tang Junxiong et al, "Experimental study of a model digital space optical communication system with new quantum devices," *Applied Optics*, vol. 34, no. 15, pp. 2619-2622, May 1995.
- [33] Xiao-Hui Bao et al, "Generation of Narrow-Band Polarization-Entangled Photon Pairs for atomic quantum memories," *Physical Review Letters*, vol. 101, no. 190501, pp. 1-4, November 2008.
- [34] J. S. Neergaard-Nielsen, B. Melholt Nielsen, H. Takahashi, A.I. Vistnes, E. S. Polzik, "High purity bright single photon source," *Optics Express*, vol. 15, no. 13, pp. 7940-7949, June 2007.
- [35] Josef Hoffner, Cord Fricke-Begemann, "Accurate lidar temperatures with narrowband filters," *Optics Letters*, vol. 30, no. 8, pp. 890-892, April 2005.
- [36] Cord Fricke-Begemann, Matthias Alpers Josef Hoffner, "Daylight rejection with a new receiver for potassium resonance temperature lidars," *Optics Letters*, vol. 27, no. 21, pp. 1932-1934, November 2002.
- [37] H. Chen, M. A. White, David A. Krueger, C. Y. She, "Daytime mesopause temperature measurements with a sodium-vapor dispersive Faraday filter in a lidar receiver," *Optics Letters*, vol. 21, no. 15, pp. 1093-1095, August 1996.
- [38] Zhusong He, Yundong Zhang, Hao Wu, Ping Yuan, Shuangqiang Liu, "Theory and experiment for atomic optical filter based on optical anisotropy in rubidium," *Optics Communications*, vol. 282, pp. 4548-4551, August 2009.
- [39] L. D. Turner, V. Karaganov, P. J. O. Teubner, R.E. Scholten, "Sub-Doppler bandwidth atomic optical filter," *Optics Letters*, vol. 27, no. 7, pp. 500-502, April 2002.

- [40] S. K. Gayen et al, "Induced-dichroism-excited atomic line filter at 532 nm," *Optics Letters*, vol. 20, no. 12, pp. 1427-1429, June 1995.
- [41] Y.B. Kale, A. Ray, R. D'Souza, Q.V. Lawande, B.N. Jagatap, "Atomic frequency offset locking in a Λ type three-level Doppler broadened Cs system," *Applied Physics B: Lasers and Optics*, vol. 100, pp. 505-514, March 2010.
- [42] David J. Fulton, Sara Shepherd, Richard R. Moseley, Bruce D. Sinclair, Malcolm H. Dunn, "Continuous-wave electromagnetically induced transparency: A comparison of V, λ and cascade systems," *Physical Review A*, vol. 52, no. 3, pp. 2302-2311, September 1995.
- [43] R. P. Abel, A. K. Mohapatra, M. G. Bason, J. D. Pritchard, K. J. Weatherill, U. Raitzsch, C.S. Adams, "Laser frequency stabilization to excited state transitions using electromagnetically induced transparency in a cascade system," *Applied Physics letters*, vol. 94, no. 071107, pp. 1-3, February 2009.
- [44] P. Campbell, I. D. Moore M. R. Pearson, "Laser spectroscopy for nuclear structure physics," *Progress in Particle and Nuclear Physics*, vol. 86, pp. 127-180, 2016.
- [45] H. Andra, New York, 1975, vol. 4.
- [46] William H. Wing et al, "Observation of the infrared spectrum of the hydrogen molecular ion HD⁺," *Physical Review Letters*, vol. 36, no. 25, pp. 1488-1491, June 1976.
- [47] S. L. Kaufman, "High resolution laser spectroscopy in fast beams," *Optics communications*, vol. 17, no. 3, pp. 309-312, June 1976.
- [48] K. R. Anton et al, "Collinear laser spectroscopy on fast atomic beams," *Physical*

Review Letters, vol. 40, no. 10, pp. 642-645, March 1978.

- [49] R. Neugart, "Laser spectroscopy on mass separated radioactive beams," *Nuclear Instruments and Methods*, vol. 186, pp. 165-175, 1981.
- [50] R. Neugart, "Collinear laser spectroscopy on unstable isotopes-A tool of nuclear physics," *Hyperfine Interactions*, vol. 24, pp. 159-180, 1985.
- [51] Pierre Jacquinet, Robert Klapisch, "Hyperfine spectroscopy of radioactive atoms," *Reports on Progress in Physics*, vol. 42, pp. 773-832, 1979.
- [52] J Billowes P Campbell, "High-resolution laser spectroscopy for the study of nuclear sizes and shapes," *Journal of Physics G: Nuclear and particle physics*, vol. 21, pp. 707-739, 1995.
- [53] W. Geithner et al, "Measurement of nuclear moments and radii by collinear laser spectroscopy and by beta-NMR spectroscopy," *Hyperfine Interactions*, vol. 129, pp. 271-288, 2000.
- [54] R. Neugart, "Lasers in nuclear physics-A review," *The European Physical Journal A*, vol. 15, pp. 35-39, October 2002.
- [55] H. Jurgen Kluge, Wilfried Nortershauser, "Lasers for nuclear physics," *Spectrochimica Acta Part B*, vol. 58, pp. 1031-1045, 2003.
- [56] R. Neugart, G. Neyens, "Nuclear moments," *Lecture Notes in Physics*, vol. 700, pp. 135-189, 2006.
- [57] H. J. Kluge, "Atomic physics techniques for studying nuclear ground state properties, fundamental interactions and symmetries: status and perspectives," *Hyperfine*

- interactions*, vol. 196, pp. 295-337, 2010.
- [58] B Cheal K. T. Flanagan, "Progress in laser spectroscopy at radioactive ion beam facilities," *Journal of Physics G: Nuclear and Particle Physics*, vol. 37, no. 113101, pp. 1-38, 2010.
- [59] Wilfried Nortershauser, "Recent developments in collinear laser spectroscopy at COLLAPS/ISOLDE," *Hyperfine Interactions*, vol. 198, pp. 73-83, 2010.
- [60] K Blaum et al, "Measurement of ground-state properties for nuclear structure studies by precision mass and laser spectroscopy," *Journal of Physics: Conference series*, vol. 312, no. 092001, pp. 1-10, 2011.
- [61] Klaus Blaum, Jens Dilling Wilfried Nortershauser, "Precision atomic Physics techniques for nuclear physics with radioactive beams," *Physica Scripta*, vol. T152, no. 014017, pp. 1-32, January 2013.
- [62] A. Kramida, Yu. Ralchenko, J. Reader and NIST ASD Team. (2015) NIST Atomic Spectra Database (Version 5.3). Online.
- [63] Christopher J. Foot, *Atomic Physics*.: Oxford University Press, 2005.
- [64] Ernst W. Otten, *Treatise on Heavy-Ion Science, Vol 8 Nuclei far From Stability*, D. Allan Bromley, Ed.
- [65] D. A. Steck. (2001, Sep) Alkali D Line Data. [Online]. <http://www.steck.us/alkalidata>
- [66] Wolfgang Demtroder, *Laser Spectroscopy, Vol 1: Basic Principles*, 4th ed.: Springer, 2008.
- [67] W. Bruce Shore, "Coherent manipulations of atoms using laser light," *Acta Physica*

Slovaca, vol. 58, no. 3, pp. 243-486, June 2008.

- [68] Valerio Magnasco, *Elementary Molecular Quantum Mechanics: Mathematical Methods and Applications*, 2nd ed.: Elsevier, 2013.
- [69] G.R. Satchler D.M. Brink, *Angular Momentum*, 2nd ed.: Clarendon Press, Oxford, 1968.
- [70] Christopher Gerry, Peter Knight, *Introductory Quantum Optics*: Cambridge University Press, 2005.
- [71] Wolfgang Demtroder, *Laser Spectroscopy, Vol 2: Experimental Techniques*, 4th ed.: Springer, 2008.
- [72] Claude N. Cohen-Tannoudji, "Manipulating atom with photons," *Reviews of Modern Physics*, vol. 70, no. 3, pp. 707-719, July 1998.
- [73] U. Fano, "Effects of Configuration Interaction on Intensities and Phase Shifts," *Physical Review*, vol. 124, no. 6, pp. 1866-1878, December 1961.
- [74] R. P. Madden K. Codling, "Two-electron excitation states in Helium," *The Astrophysical Journal*, vol. 141, no. 2, pp. 364-375, September 1964.
- [75] Stephen E. Harris, "Electromagnetically induced transparency," *Physics Today*, vol. 50, no. 7, pp. 36-42, July 1997.
- [76] S. E. Harris, J. E. Field, A. Imamoglu, "Nonlinear Optical Processes Using Electromagnetically Induced Transparency," *Physical Review Letters*, vol. 64, no. 10, pp. 1007-1110, March 1990.
- [77] M. S. Zubairy et al, "Lasing without inversion: interference of radiatively broadened

- resonances in dressed atomic systems," *Optics Communications*, vol. 94, pp. 599-608, April 1992.
- [78] Paul Mandel, "Lasing without inversion: A useful concept?," *Contemporary Physics*, vol. 34, no. 5, pp. 235-246, August 1993.
- [79] B. W. Shore, *Theory of Coherent Atomic Excitation*. New York: Wiley, 1990.
- [80] Marc Breton et al, "Optically pumped Rubidium as a frequency standard at 196 THz," *IEEE Transactions on Instrumentation and Measurement*, vol. 44, no. 2, pp. 162-165, April 1995.
- [81] H. S. Moon, W. K. Lee, L. Lee, J. B. Kim, "Double resonance optical pumping spectrum and its application for frequency stabilization of a laser diode," *Applied Physics Letters*, vol. 85, no. 18, pp. 3965-3967, November 2004.
- [82] C. Wiemang, T. W. Hansch, "Doppler-Free Laser Polarization Spectroscopy," *Physical Review Letters*, vol. 36, no. 20, pp. 1170-1173, May 1976.
- [83] Cunyun Ye, *Tunable external cavity Diode Lasers*.: World scientific, 2004.
- [84] Halina Abramczyk, *Introduction to Laser Spectroscopy*.: Elsevier, 2005.
- [85] D Sands, *Diode Lasers*.: IOP Publishing, 2005.
- [86] Haiyin Sun, *Laser Diode Beam Basics, Manipulations and characterizations*.: Springer, 2012.
- [87] K. Thyagarajan, Ajoy Ghatak, *Lasers: Fundamentals And Applications*, 2nd ed.: Springer, 2010.
- [88] Michael G. Littman, Harold J. Metcalf, "Spectrally narrow pulsed dye laser without

- beam expander," *Applied Optics*, vol. 17, no. 14, pp. 2224-2227, July 1978.
- [89] B. Mroziewicz, "External cavity wavelength tunable semiconductor lasers-a review," *Opto-electronics review*, vol. 16, no. 4, pp. 347-366, 2008.
- [90] K.P. Weber, C.J. Hawthorn, R.E. Scholten, "Littrow configuration tunable external cavity diode laser with fixed direction output beam," *Review scientific Instruments*, vol. 72, no. 12, pp. 4477-4479, December 2001.
- [91] Mark W. Fleming, Aram Mooradian, "Spectral characteristic of external-cavity controlled semiconductro lasers," *IEEE journal of quantum electronics*, vol. QE-17, no. 1, pp. 44-59, January 1981.
- [92] Karen Liu, Michael G. Littman, "Novel geometry for single mode scanning of tunable lasers," *Optics Letters*, vol. 6, no. 3, pp. 117-118, March 1981.
- [93] RP Photonics Encyclopedia. [Online]. <https://www.rp-photonics.com>
- [94] A.L. Schawlow, C.H. Townes, "Infrared and Optical Masers," *Physical review*, vol. 112, no. 6, pp. 1940-1949, December 1958.
- [95] Charles H. Henry, "Theory of linewidth of semiconductor lasers," *IEEE Journal of Quantum Electronics*, vol. QE-18, no. 2, pp. 259-264, February 1982.
- [96] Minoru Yamada, *Theory of semiconductor Lasers.*: Springer, 2014.
- [97] A. Yu. Nevsky et al, "A narrow-line-width external cavity quantum dot laser for high resolution spectroscopy in the near-infrared and yello spectral ranges," *Applied Physics B*, vol. 92, pp. 501-507, 2008.
- [98] Leo Hollberg, V.L. Velichansky, C.S. Weimer, R.W. Fox, "High-accuracy

spectroscopy with semiconductor lasers: Application to laser frequency stabilization," in *Frequency control of semiconductor lasers*, Motoichi Ohtsu, Ed., 1996, ch. 3.

- [99] S Uetake, A. Yamaguchi, D. Hashimoto, Y. Takahashi, "High-resolution laser spectroscopy of ultracold ytterbium atoms using spin-forbidden electric quadrupole transition," *Applied Physics B*, vol. 93, pp. 409-414, 2008.
- [100] A. Hemmerich, D.H. McIntyre, D. Schropp Jr., D. Meschede T.W. Hansch, "Optically stabilized narrow line-width semiconductor laser for high resolution spectroscopy," *Optics communications*, vol. 75, no. 2, pp. 118-122, 1989.
- [101] R. Islam et al, "Beat note stabilization of mode-locked lasers for quantum information processing," *Optics letters*, vol. 39, no. 11, pp. 3238-3241, June 2014.
- [102] J.L. Hall, "Stabilizing lasers for application in quantum optics," in *Quantum optics IV*, J.D. Harvey and D.F. Walls, Ed., 1986, ch. 4, pp. 273-284.
- [103] Fritz Riehle, *Frequency Standards: Basics and Applications.*: WILEY-VCH Verlag GmbH & Co., 2004.
- [104] Th. Udem, R. Holzwarth T.W. Hansch, "Optical frequency metrology," *Nature*, vol. 416, pp. 233-237, 2002.
- [105] S. Y. Zhang et al, "Direct frequency comb optical frequency standard based on two-photon transitions of thermal atoms," *Nature*, vol. 5, no. 15114, pp. 1-8, 2015.
- [106] Liming Qian et al, "Passive frequency stabilization in Nd:YAG pulse laser using reflective volume Bragg grating," *Applied Optics*, vol. 50, no. 32, pp. 6094-6097, November 2011.

- [107] Zhaoshuo Tian, Shiliang Qu, Zhenghe Sun, "Active and passive frequency stabilization for a Q-switched Z-fold radio-frequency-excited waveguide Co₂ laser with two channels," *Applied Optics*, vol. 44, no. 29, pp. 6269-6273, October 2005.
- [108] H. Talvitie, A. Pietilainen, H. Ludvigsen E. Ikonen, "Passive frequency and intensity stabilization of extended-cavity diode lasers," *Review of Scientific Instruments*, vol. 68, pp. 1-7, January 1997.
- [109] Frank Trager, Ed., *Springer Handbook of Lasers and Optics.*, 2007.
- [110] Kristan L. Corwin, Zheng-Tian Lu, Carter F. Hand, Ryan J. Epstein, Carl E. Wieman, "Frequency-stabilized diode laser with the zeeman shift in an atomic vapor," *Applied Optics*, vol. 37, no. 15, pp. 3295-3298, May 1998.
- [111] T. Petelski, M. Fattori, G. Lamporesi, J. Stuhler, G.M. Tino, "Doppler-free spectroscopy using magnetically induced dichroism of atomic vapor: A new scheme for laser frequency locking," *The European Physical Journal D*, vol. 22, pp. 279-283, 2003.
- [112] Yutaka Yoshikawa, Takeshi Umeki, Takuro Mukae, Yoshio Torii, Takahiro Kuga, "Frequency stabilization of a laser diode with use of light-induced birefringence in an atomic vapor," *Applied Optics*, vol. 42, no. 33, pp. 6645-6649, November 2003.
- [113] Y.T. Zhao, J.M. ZHao, T. Huang, L.T. Xiao, S.T. Jia, "Frequency stabilization of an external-cavity diode laser with a thin Cs vapour cell," *Journal of Physics D: Applied Physics*, vol. 37, pp. 1316-1318, April 2004.
- [114] G. Wasik, W. Gawlik, J. Zachorowski, W. Zawadzki, "Laser frequency stabilization by Doppler-free magnetic dichroism," *Applied Physics B: Lasers and Optics*, vol. 75, pp.

613-619, September 2002.

- [115] Valeriy V. Yashchuk, Dmitry Budker, John R. Davis, "Laser frequency stabilization using linear magneto-optics," *Review of Scientific Instruments*, vol. 71, no. 2, pp. 341-346, February 2000.
- [116] D.J. McCarron, S.A. King S.L. Cornish, "Modulation transfer spectroscopy in atomic rubidium," *Measurement Science and Technology*, vol. 19, no. 105601, p. 1, August 2008.
- [117] C.P. Pearman, C.S. Adams, S.G. Cox, P.F. Griffin, D.A. Smith, I.G. Hughes, "Polarization spectroscopy of a closed atomic transition: applications to laser frequency locking," *Journal of Physics B: Atomic, Molecular and Optical Physics*, vol. 35, pp. 5141-5151, December 2002.
- [118] G.P.T. Lancaster, R.S. Conroy, M.A. Clifford, J. Arlt, K. Dholakia, "A polarisation spectrometer locked diode laser for trapping cold atoms," *Optics Communications*, vol. 170, pp. 79-84, October 1999.
- [119] Tsutomu Yabuzaki, Akira Ibaragi, Hirokazu Hori, Masao Kitano, Toru Ogawa, "Frequency-Locking of a GaAlAs Laser to a Doppler-Free Spectrum of the Cs-D2 Line," *Japanese Journal of Applied physics*, vol. 20, no. 6, pp. L451-L454, June 1981.
- [120] T.W. Hansch, B. Couillaud, "Laser frequency Stabilization by Polarization spectroscopy of a reflecting reference cavity," *Optics communications*, vol. 35, no. 3, pp. 441-444, December 1980.
- [121] V.B. Tiwari, S. Singh, S.R. Mishra, H.S. Rawat, S.C. Mehendale, "Laser frequency stabilization using Doppler-free bi-polarization spectroscopy," *Optics Communications*,

vol. 263, pp. 249-255, January 2006.

- [122] James M. Supplee, Edward A. Whittaker, Wilfried Lenth, "Theoretical description of frequency modulation and wavelength modulation spectroscopy," *Applied Optics*, vol. 33, no. 27, pp. 6294-6302, September 1994.
- [123] G. C. Bjorklund, M. D. Levenson, W. Lenth, C. Ortiz, "Frequency Modulation (FM) Spectroscopy," *Applied Physics B*, vol. 32, pp. 145-152, July 1983.
- [124] R. V. Pound, "Electronic Frequency Stabilization of Microwave Oscillators," *The Review of Scientific Instruments*, vol. 17, no. 11, pp. 490-505, November 1946.
- [125] "Precise Determination of the Magnetic Moment of the Deuteron," *Physical Review*, vol. 83, no. 4, pp. 812-821, August 1951.
- [126] Gary C. Bjorklund, "Frequency-modulation spectroscopy: a new method for measuring weak absorptions and dispersions," *Optics letters*, vol. 5, no. 1, pp. 15-17, January 1980.
- [127] RWP Drever et al, "Laser Phase and Frequency Stabilization Using an Optical Resonator," *Applied Physics B*, vol. 31, pp. 97-105, February 1983.
- [128] David W. Allan, "Statistics of Atomic Frequency Standards," *Proceedings of the IEEE*, vol. 54, no. 2, pp. 221-230, February 1966.
- [129] J.A. Barnes et al, "Characterization of frequency stability," *IEEE Transactions on Instrumentation and Measurements*, vol. IM-20, no. 2, pp. 105-120, May 1971.
- [130] Jacques Rutman, F. L. Walls, "Characterization of Frequency Stability In Precision Frequency Sources," *Proceedings of the IEEE*, vol. 79, no. 6, pp. 952-960, June 1991.

- [131] Ayan Ray, "Study of the frequency fluctuations of a semiconductor diode laser," *Canadian Journal of Physics*, vol. 86, pp. 351-358, 2008.
- [132] Alok Chakrabarti, Vaishali Naik, Arup Bandyopadhyay Rakesh Bhandari, "Rare ion beams - the new road to understand the universe," *Current Science*, vol. 108, no. 1, pp. 22-29, January 2015.
- [133] Alok Chakrabarti, "Radioactive ion beams programme at VECC-Kolkata, Indian efforts," in *Proceedings of HIAT2015*, Yokohama, Japan, 2015, pp. 300-303.
- [134] A. Chakrabarti, "The radioactive ion beam project at VECC, Kolkata-Its present status and future plans," *Nuclear Instruments and Methods in Physics Research B*, vol. 261, pp. 1018-1022, 2007.
- [135] Vaishali Naik et al, "First online production of radioactive ion beams at VECC," *Nuclear Instruments and Methods in Physics Research B*, vol. 317, pp. 227-230, June 2013.
- [136] V. Naik et al, "A gas-jet transport and catcher technique for on-line production of radioactive ion beams using an electron cyclotron resonance ion-source," *Review of Scientific Instruments*, vol. 84, no. 033301, pp. 1-7, February 2013.
- [137] V Naik et al, "VECC-TRIUMF injector for the e-Linac project," *Proceedings of Linear Accelerator Conference LINAC2010*, Tsukuba, Japan, pp. 727-729, 2010.
- [138] Alok Chakrabarti et al, "The ANURIB project at VECC-Plans and preparations," *Nuclear Instruments and Methods in Physics Research B*, vol. 317, pp. 253-256, 2013.
- [139] Alok Chakrabarti et al, "33.7 MHz heavy-ion radio frequency quadrupole linac at VECC KOLkata," *Review of Scientific Instruments*, vol. 78, no. 043303, pp. 1-5, April

2007.

- [140] Alok Chakrabarti et al, "The design of a four-rod RFQ LINAC for VEC-RIB facility," *Nuclear Instruments and Methods in Physics Research A*, vol. 535, pp. 599-605, August 2004.
- [141] Arup Bandyopadhyay et al, "Design of LINAC post-accelerator for VECC RIB facility using realistic field," *Nuclear Instruments and Methods in Physics Research A*, vol. 560, pp. 182-190, January 2006.
- [142] Matthew Himsworth, "Coherent manipulation of ultracold Rubidium," PhD Thesis 2009.
- [143] Julio Gea-Banacloche, Yong-qing Li, Shao-zheng Jin, Min Xiao, "Electromagnetically induced transparency in ladder-type inhomogeneously broadened media: Theory and experiment," *Physical Review A*, vol. 51, no. 1, pp. 576-584, January 1995.
- [144] Yong-qing Li, Min Xiao, "Transient properties of an electromagnetically induced transparency in three-level atoms," *Optics Letters*, vol. 20, no. 13, pp. 1489-1491, July 1995.
- [145] M. S. Safronova, Carl J. Williams, Charles W. Clark, "Relativistic many-body calculations of electric-dipole matrix elements, lifetimes, and polarizabilities in rubidium," *Physical Review A*, vol. 69, no. 022509, pp. 1-8, February 2004.
- [146] S. Shepherd, D. J. Fulton, M. H. Dunn, "Wavelength dependence of coherently induced transparency in a Doppler-broadened cascade medium," *Physical Review A*, vol. 54, no. 6, pp. 5394-5399, December 1996.
- [147] Shin-ichi Ohshima, Harald Schnatz, "Optimization of injection current and feedback

- phase of an optically self-locked laser diode," *Journal of Applied Physics*, vol. 71, no. 7, pp. 3114-3117, December 1991.
- [148] Heung-Ryoul Noh, Han Seb Moon, "Calculation of line shapes in double-resonance optical pumping," *Physical Review A*, vol. 80, no. 022509, pp. 1-5, August 2009.
- [149] S. Wielandy, Alexander L. Gaeta, "Investigation of electromagnetically induced transparency in the strong probe regime," *Physical Review A*, vol. 58, no. 3, pp. 2500-2505, September 1998.
- [150] Ayan Ray, Md. Sabir Ali, Alok Chakrabarti, "Optical switching in a Ξ system: A comparative study on DROP and EIT," *The European Physical Journal D*, vol. 97, no. 78, pp. 1-9, April 2013.
- [151] Shuangqiang Liu, Yundong Zhang, Daikun Fan, Hao Wu, Ping Yuan, "Selective optical pumping process in Doppler-broadened atoms," *Applied Optics*, vol. 50, no. 11, pp. 1620-1624, April 2011.
- [152] E. Arimondo G. Orriols, "Nonabsorbing Atomic Coherences by Coherent Two-Photon Transitions in a Three-Level Optical Pumping.," *Lettere Al Nuovo Cimento*, vol. 17, no. 10, pp. 333-338, November 1976.
- [153] Shaozheng Jin, Yongqing Li, Min Xiao, "Hyperfine spectroscopy of highly-excited atomic states based on atomic coherence," *Optics communications*, vol. 119, pp. 90-96, August 1995.
- [154] Han Seb Moon, Heung-Ryoul Noh, "Resonant two-photon absorption and electromagnetically induced transparency in open ladder-type atomic system," *Optics Express*, vol. 21, no. 6, pp. 7447-7455, March 2013.

- [155] Wei Jiang, Qun-feng Chen, Yong-sheng Zhang, G.C. Guo, "Optical pumping-assisted electromagnetically induced transparency," *Physical Review A*, vol. 73, no. 053804, pp. 1-7, May 2006.
- [156] Ayan Ray, Md. Sabir Ali, Alok Chakrabarti, "Study of the effect of repump laser on atomic line filter," *Journal of the Optical Society of America B*, vol. 30, no. 9, pp. 2436-2442, September 2013.
- [157] Ayan Ray, Md. Sabir Ali, Alok Chakrabarti, "Application of repumping laser in optical switching," *Journal of Optics & Laser Technology*, vol. 60, pp. 107-110, January 2014.
- [158] S.H. Autler, C.H. Townes, "Stark Effect in Rapidly Varying Fields," *Physical Review*, vol. 100, no. 2, pp. 703-722, October 1955.
- [159] M. Fleischhaue et al, "Lasing without inversion: interference of radiatively broadened resonances in dressed atomic systems," *Optics Communications*, vol. 94, pp. 599-608, April 1992.
- [160] Ali Javan, Olga Kocharovskaya, Hwang Lee, Marlan O. Scully, "Narrowing of electromagnetically induced transparency resonance in a Doppler-broadened medium," *Physical Review A*, vol. 66, no. 013805, pp. 1-4, July 2002.
- [161] G. S. Agarwal, W. Harshawardhan, "Inhibition and Enhancement of Two Photon Absorption," *Physical Review Letters*, vol. 77, no. 6, pp. 1039-1042, August 1996.
- [162] Han Seb Moon, Lim Lee, Jung Bog Kim, "Double-resonance optical pumping of Rb atoms," *Journal of the Optical Society of America B*, vol. 24, no. 9, pp. 2157-2164, September 2007.
- [163] T. Meijer, J. D. White, B. Smeets, M. Jeppesen, R. E. Scholten, "Blue five-level

- frequency-upconversion system in rubidium," *Optics Letters*, vol. 31, no. 7, pp. 1002-1004, April 2006.
- [164] Heung-Ryoul Noh, Han Seb Moon, "Transmittance signal in real ladder-type atoms," *Physical Review A*, vol. 85, no. 033817, pp. 1-5, March 2012.
- [165] Md Sabir Ali, Ayan Ray, Alok Chakrabarti, "Tunable offset locking in a ladder system: an experimental study on the rubidium atom," *Physica Scripta*, vol. 88, no. 065301, pp. 1-9, October 2013.
- [166] A.K. Mohapatra, T.R. Jackson, C.S. Adams, "Coherent Optical Detection of Highly Excited Rydberg States Using Electromagnetically Induced Transparency," *Physical Review Letters*, vol. 98, no. 113003, pp. 1-4, March 2007.
- [167] L.J. Wang, A. Kuzmich, A. Dogariu, "Gain-assisted superluminal light propagation," *Nature*, vol. 406, pp. 277-279, July 2000.
- [168] Per Arve, Peter Janes, Lars Thylen, "Propagation of two-dimensional pulses in electromagnetically induced transparency media," *Physical Review A*, vol. 69, no. 063809, pp. 1-8, June 2004.
- [169] Suguru Sangu, Kiyoshi Kobayashi, Akira Shojiguchi, Motoichi Ohtsu, "Logic and functional operations using a near-field optically coupled quantum-dot system," *Physical Review B*, vol. 69, no. 115334, pp. 1-13, March 2004.
- [170] Jian Qi Shen, Pu Zhang, "Double-control quantum interferences in a four-level atomic system," *Optics Express*, vol. 15, no. 10, pp. 6484-6493, May 2007.
- [171] Md. Sabir Ali, Ayan Ray, Alok Chakrabarti, "Control of coherence in a ladder type system with double resonance optical pumping and electromagnetically induced

- transparency," *The European Physical Journal D*, vol. 69, no. 41, pp. 1-10, February 2015.
- [172] E.A. Donley, T.P. Heavner, F. Levi, M. O. Tataw, S.R. Jefferts, "Double-pass acousto-optic modulator system," *Review of Scientific Instruments*, vol. 76, no. 063112, pp. 1-6, June 2005.
- [173] Armen Sargsyan, David Sarkisyan, Ulrich Krohn, James Keaveney, Charles Adams, "Effect of buffer gas on an electromagnetically induced transparency in a ladder system using thermal rubidium vapor," *Physical Review A*, vol. 82, no. 045806, pp. 1-4, October 2010.
- [174] H. Lee, Y. Rostovtsev, C. J. Bednar, A. Javan, "From laser-induced line narrowing to electromagnetically induced transparency: closed system analysis," *Applied Physics B: Lasers and Optics*, vol. 76, pp. 33-39, January 2003.
- [175] Liang Zhang, Junxiong Tang, "Experimental study on optimization of the working conditions of excited state Faraday filter," *Optics communications*, vol. 152, pp. 275-279, July 1998.
- [176] R. I. Billmers et al, "Experimental demonstration of an excited-state Faraday filter operating at 532 nm," *Optics Letters*, vol. 20, no. 1, pp. 106-108, January 1995.
- [177] H. Chen et al, "Sodium-vapor dispersive Faraday filter," *Optics Letters*, vol. 18, no. 12, pp. 1019-1021, June 1993.
- [178] Alessandro Cere et al, "Narrowband tunable filter based on velocity-selective optical pumping in an atomic vapor," *Optics Letters*, vol. 34, no. 7, pp. 1012-, April 2009.
- [179] Yanfei Wang, Shengnan Zhang, Dongying Wang, Zhiming Tao, Yelong Hong,

- Jingbiao Chen, "Nonlinear optical filter with ultranarrow bandwidth approaching the natural linewidth," *Optics Letters*, vol. 37, no. 19, pp. 4059-4061, October 2012.
- [180] Shuangqiang Liu, Yundong Zhang, "Incoherent pump assisted atomic filter based on laser-induced optical anisotropy," *Applied Optics*, vol. 51, no. 30, pp. 7183-7187, October 2012.
- [181] Zhusong He, Yundong Zhang, Hao Wu, Ping Yuan, Shuangqiang Liu, "Theoretical model for an atomic optical filter based on optical anisotropy," *Journal of the Optical Society of America B*, vol. 26, no. 9, pp. 1755-1759, September 2009.
- [182] A. Perez Galvan, D. Sheng, L.A. Orozco Y. Zhao, "Two-color modulation transfer spectroscopy," *Canadian Journal Of Physics*, vol. 87, pp. 95-100, 2009.
- [183] Yifu Zhu , T. N. Wasserlauf, "Sub-Doppler linewidth with electromagnetically induced transparency in rubidium atoms," *Physical Review A*, vol. 54, no. 4, pp. 3653-3656, October 1996.
- [184] B.R. Mollow, "Power Spectrum of Light Scattered by Two-Level Systems," *Physical Review*, vol. 188, no. 5, pp. 1969-1975, December 1969.
- [185] C. Y. Ye, A. S. Zibrov, "Width of the electromagnetically induced transparency resonance in atomic vapor," *Physical Review A*, vol. 65, no. 023806, pp. 1-5, January 2002.
- [186] Yong-qing Li, Shao-zheng Jin, Min Xiao, "Observation of an electromagnetically induced change of absorption in multilevel rubidium atoms," *Physical Review A*, vol. 51, no. 3, pp. R1754-R1757, March 1995.
- [187] Th. Udem, J. Reichert, R. Holzwarth, T. W. Hänsch, "Absolute Optical Frequency

Measurement of the Cesium D1 Line with a Mode-Locked Laser," *Physical Review Letters*, vol. 82, no. 18, pp. 3568-3571, May 1999.

- [188] Andy W. Brown, Min Xiao, "Modulation transfer in an electromagnetically induced transparency system," *Physical Review A*, vol. 70, no. 053830, pp. 1-7, November 2004.
- [189] Arup Bandyopadhyay et al, "A helium jet coupled on-line isotope separator facility at Variable Energy Cyclotron Centre, Kolkata," *Nuclear Instruments and methods in Physics Research A*, vol. 562, pp. 41-47, 2006.
- [190] A. Chakrabarti et. al, "The helium-jet coupled ISOL facility at VECC, Calcutta," *Nuclear Instruments and Methods in Physics Research B*, vol. 70, pp. 254-258, 1992.
- [191] A. Chakrabarti et al, "Helium-jet Recoil Transport Set-up for Chemistry and Nuclear Applications at VECC," *Nuclear Instruments and Methods in Physics Research A*, vol. 263, pp. 421-426, 1988.
- [192] U. Rohrer, "PSI Graphic Transport Framework by U. Rohrer based on a CERN-SLAC-FERMILAB version by K.L. Brown et al.," 2006.
- [193] Arup Bandyopadhyay et al, "A helium jet coupled on-line isotope separator facility at Variable Energy Cyclotron Centre, Kolkata," *Nuclear Instruments and methods in Physics Research A*, vol. 562, pp. 41-47, 2006.
- [194] A. Klose et al, "Tests of atomic charge exchange cells for collinear laser spectroscopy," *Nuclear Instruments and Methods in Physics Research A*, vol. 678, pp. 114-121, March 2012.
- [195] M. Bacal, A. Truc, H. J. Doucet, H. Lamain, M. Chretien, "Charge Exchange Cell with

- Cesium Recycling," *Nuclear Instruments and Methods*, vol. 114, pp. 407-409, 1974.
- [196] Jorg Kramer, "Construction and Commissioning of a Collinear Laser Spectroscopy Setup at TRIGA Mainz and Laser Spectroscopy of Magnesium Isotopes at ISOLDE (CERN)," Johannes Gutenberg Universitat Mainz, Mainz, Germany, PhD Thesis 2010.
- [197] Sophia Vinnikova, "Development and Commissioning of a Photon Detection System for Collinear Laser Spectroscopy at NSCL," Michigan State University , East Lansing, Masters Thesis 2011.
- [198] K.D. Kreim, "Collinear Laser Spectroscopy of Potassium," Thesis 2013.
- [199] G. D. Sprouse, J. F. Sell K. Gulyuz, "Collinear laser spectroscopy of francium using online rubidium vapor neutralization and amplitude modulated lasers," *Review of Scientific Instruments*, vol. 80, no. 123108, pp. 1-5, December 2009.
- [200] Annika Voss et al, "First use of high-frequency intensity modulation of narrow-linewidth laser light and its application in determination of $^{206,205,204}\text{Fr}$ ground-state properties," *Physical Review Letters*, vol. 111, no. 122501, pp. 1-5, September 2013.
- [201] A. Bandyopadhyay, "Design and Development of Isotope Separator and LINAC Post-Accelerator for the RIB facility at VECC, Kolkata," Variable Energy Cyclotron Centre, Kolkata, PhD Thesis 2006.
- [202] J. F. Sell, K. Gulyuz, G. D. Sprouse, "Collinear laser spectroscopy of francium using online rubidium vapor neutralization and amplitude modulated lasers," *Review of Scientific Instruments*, vol. 80, no. 123108, pp. 1-5, December 2009.
- [203] D. A. Steck. (2008) Rubidium 85 data. [Online]. <http://steck.us/alkalidata/>

[204] J. Perel et al, "Measurement of Cesium and Rubidium Charge Transfer Cross Sections,"

The Physical Review, vol. 138, no. 4A, pp. A937-A946, May 1965.